

Strain Rate Effects on a Ductile Moment Resisting Frame with RBS
Connection Subjected to Seismic Ground Motions

by

Tarundeep Singh

A thesis submitted to the Faculty of Graduate and Postdoctoral
Affairs in partial fulfillment of the requirements
for the degree of

Master of Applied Science

in

Civil Engineering

Carleton University

Ottawa, Ontario

© 2019

Tarundeep Singh

ABSTRACT

A numerical study that considers strain rate dependency of material behaviour has been carried out to assess the performance of a ductile moment resisting frame (MRF) with reduced beam section (RBS) subjected to seismic ground motion. The structural components of an MRF can experience a significantly high rate of deformation during seismic ground motion, which can vary the mechanical properties of the steel. Hence, quasi-static material properties used in the design of steel structures are not representative of the material dynamic behaviour during an earthquake.

A procedure has been developed to generate stress versus strain curves for mixed-mode hardening plasticity model using the test data by other researchers conducted at strain rate ranging from 0.00005 s^{-1} to 1.0 s^{-1} for two grades (ASTM A572 grade 50 and CAN/CSA G40.20/21 300W) of steel coupons (specimens). The strain rate dependent material properties for these materials are used in different combinations on beams and columns of MRF with RBS to conduct the non-linear dynamic analyses subjected to a suite of earthquake records at different seismic hazard levels in finite element software, ABAQUS. The maximum bending moment and maximum base shear are found to increase by up to 8% when strain rate dependent material properties are used in the analyses. However, there is only a slight decrease in the mean predicted inter-storey drift when strain rate dependent material properties are considered. It is observed that the MRF with RBS connections can experience a maximum strain rate of up to 0.30 s^{-1} . The strain hardening factor at the RBS center has been found to be much greater than the prescribed value in the design specification. A strain hardening of at least 1.2 should be used for a ductile moment resisting frame when inter-storey drift limit is ignored in the design.

ACKNOWLEDGEMENT

First and foremost, I would like to thank almighty Waheguru for providing me the knowledge, strength and resources to help me complete my degree.

I would like to express my gratitude to my supervisor Dr. Heng Aik Khoo for his unwavering support and guidance throughout the duration of this thesis. This thesis would not have been possible without his active involvement and advise to solve the problems encountered during the project. He is a great teacher and his doors were always open if I had any questions. His prompt replies to the emails even during university holidays helped in the progression of this work.

I would also like to humbly acknowledge my mother, Manjit Kaur and my father, Upkar Singh for their unconditional emotional and financial support throughout my life and during this project. Without their love, sacrifice, patience and motivation, this study would not have been feasible.

I would like to extend my profound gratitude to Mr. Cuckoo Kochar for providing Kochar family scholarship which made life easier throughout the development of this thesis. I would also like to extend my appreciation to the department of Civil and Environmental Engineering for providing the teaching assistantship and departmental scholarship during my stay at Carleton University which helped in making this project possible.

I would like to extend my thanks to my thesis committee members, Dr. Magdi Mohareb and Dr. Jefferey Erochko for their insightful comments.

I would also like to extend my thanks to my university professors back in India, Dr. Naveen Kwatra, Dr. Shweta Goyal and Dr. Gurbir Kaur who provided the letter of

recommendations for me to secure admission in the master's program at Carleton University.

Finally, I sincerely thank many individuals who have given freely of their time, acquaintance and resources to help me during the project. That list includes Dr. David Lau, Mr. Inderpreet Singh, Dr. M.P. Singh, Joshua Woods, Nabeel Khan, and Ryan Brouwer.

TABLE OF CONTENTS

ABSTRACT	ii
ACKNOWLEDGEMENT	iii
TABLE OF CONTENTS	v
LIST OF TABLES	viii
LIST OF FIGURES	xii
LIST OF ABBREVIATIONS AND SYMBOLS	xxiii
Chapter 1: Introduction	1
1.1 Objective of the Thesis	2
1.2 Methodology Used in the Research.....	2
1.3 Organization of the Thesis.....	3
Chapter 2: Literature Review	5
2.1 Strain Rate	5
2.2 Plasticity	6
2.3 Modelling of Strain Rate Effects	9
2.4 Effects of Strain Rate due to Seismic Excitation.....	12
2.5 Moment Resisting Frames	15
2.6 Capacity Design Approach and Reduced Beam Section.....	17
2.7 Concluding Remarks	21
Chapter 3: Calibration of Material Properties	26
3.1 Monotonic Tensile and Cyclic Tests by Chen (2010) and Walker (2012).....	26
3.2 Modified Cowper-Symonds Amplification Equation.....	28

3.3	Calibration of Material Properties for Mixed-Mode Hardening Material Model for Different Strain Rates	29
3.3.1	Calibration of Kinematic Hardening Parameters	30
3.3.2	Static Stress-Strain Curve and Stress Amplification at Different Strain Rates	32
3.3.3	Generating Isotropic Yield Stress-Plastic Strain Curves for Different Strain Rates	35
3.4	Generated Material Properties for Material G	36
3.5	Validation of Calibrated and Generated Material Properties	38
Chapter 4: Numerical Modelling of Ductile Moment Resisting Frame.....		75
4.1	Moment Resisting Frame	75
4.2	Numerical Modelling of Moment Resisting Frame.....	76
4.3	Interface between Beam and Shell Elements.....	77
4.4	Modelling of Moment Resisting Frame using Hybrid Model	79
4.5	Mesh Convergence Study for Hybrid Model	80
4.6	Modelling of Moment Resisting Frame with Entirely Beam Elements.....	81
4.7	Model Convergence Study for Frame Composed of Beam Elements	82
4.8	Comparisons between Hybrid Model and Beam Element Only Model	83
Chapter 5: Numerical Simulations of MRF with RBS.....		99
5.1	Dynamic Non-Linear Time history Analysis	99
5.2	Scaling of Earthquake Records.....	100
5.3	Numerical Simulations	104
5.3.1	Maximum Strain Rate	104
5.3.2	Bending Moment in MRF	106
5.3.3	Strain Hardening	109
5.3.4	Maximum Inter-Story Drift.....	109
5.3.5	Maximum Base Shear	111

5.4	Numerical Simulations using Hybrid Model.....	112
Chapter 6: Conclusions and Recommendations for Future Studies.....		138
6.1	Conclusions	138
6.2	Recommendations	142
References.....		144
APPENDICES.....		153
Appendix A Design of Ductile Moment Resisting Frame with Reduced Beam Section		153
A.1	Gravity Loads for Seismic Load Calculations	153
A.2	Design Base Shear.....	154
A.3	Reduced Beam Section	156
Appendix B Validation of the Shell and Beam Element Interface		172
Appendix C Example of Moment Versus Curvature Curves		178

LIST OF TABLES

Table	Page
Table 2.1 Comparative study of Eq. (2.12) to Eq. (2.17) (Salahi and Othman 2016)	22
Table 3.1 Parameters for generating monotonic true flow stress versus true plastic strain curves at different strain rates (Walker 2012).....	40
Table 3.2 Kinematic hardening parameters from Walker (2012)	41
Table 3.3 Data points of isotropic yield stress (MPa) at rate of 0.00005 s^{-1} from Walker (2012) used for calibration of kinematic hardening terms.....	41
Table 3.4 Calibrated kinematic hardening parameters for material G and H	41
Table 3.5 Material H isotropic yield stress at various plastic strains for different strain rates	42
Table 3.6 Calibrated values of constants I and J for materials G and H.....	42
Table 3.7 Calibrated values of A and B for material G and H	42
Table 3.8 Material H isotropic yield stress at various plastic strains for different strain rates using Eq. (3.13).....	43
Table 3.9 Parameters for Eq. (3.15) for static isotropic stress curve for materials G and H	43
Table 3.10 Material G isotropic yield stress at various plastic strains for different strain rates	44
Table 3.11 Material G isotropic yield stress at various plastic strains for different strain rates using Eq. (3.13)	44
Table 4.1 Meshing scheme for the RBS at first floor modelled using shell elements (S4R)	85

Table 4.2 Comparisons of RBS modelled using shell elements for coarse and fine meshes	85
Table 4.3 Comparisons of the results for beam element only MRF model for different meshes.....	86
Table 4.4 Number of elements for rest of the beam in beam element only model with 52 elements in RBS segment. (See Fig. 4.16).....	86
Table 4.5 Comparisons of the results for hybrid and beam element only models.....	87
Table 5.1 Ground motions records from FEMA P695 (FEMA 2009).....	113
Table 5.2 Maximum strain rate (s^{-1}) at first floor RBS center for different material combinations with strain rate dependent material properties	114
Table 5.3 Maximum strain rate (s^{-1}) at roof RBS center for different material combinations with strain rate dependent material properties	115
Table 5.4 Maximum strain rate (s^{-1}) at first floor and roof RBS center for MATG and MATH with and without rate dependent material properties at MCE hazard level	116
Table 5.5 Mean predicted maximum moment (kN.m) at the first floor RBS center with and without strain rate dependent material properties, and probable maximum moment, M_{pr} (1405 kN.m).....	117
Table 5.6 Mean predicted maximum moment (kN.m) at the first floor column face with and without strain rate dependent material properties, and probable maximum moment, M_{cf} (1641 kN.m).....	118
Table 5.7 Mean predicted maximum moment (kN.m) at the first floor column centerline with and without strain rate dependent material properties and, probable maximum moment, M_c (1841 kN.m).....	119

Table 5.8 Mean predicted maximum moment (kN.m) at the roof RBS center with and without strain rate dependent material properties, and probable maximum moment, M_{pr} (353 kN.m).....	120
Table 5.9 Mean predicted maximum moment (kN.m) at the roof column face with and without strain rate dependent material properties, and probable maximum moment, M_{cf} (391 kN.m).....	121
Table 5.10 Mean predicted maximum moment (kN.m) at the roof column centerline with and without strain rate dependent material properties, and probable maximum moment, M_c (439 kN.m).....	122
Table 5.11 Mean predicted strain hardening factor at the roof and first-floor RBS center for MATG and MATH with static material properties.....	122
Table 5.12 Predicted maximum inter-storey drift (%) for individual earthquake record at first floor for MATG and MATH at MCE hazard level	123
Table 5.13 Predicted maximum inter-storey drift (%) for individual earthquake record at first floor for MATG and MATH at DBE hazard level	124
Table 5.14 Mean predicted maximum inter-storey drifts (%) for the suite of earthquake records with and without strain rate dependent material properties	125
Table 5.15 Mean predicted maximum base shear (kN) for different material combinations with and without strain rate dependent material properties, and design base shear, V_d (440 kN)	125
Table 5.16 The results for hybrid model for acceleration time history (Fig 5.19) for MATH at MCE hazard level.....	126

Table 5.17 The results for hybrid model for acceleration time history (Fig 5.20) for MATH at MCE hazard level.....	126
Table A.1 Seismic weight at roof and first floor (Metten and Driver 2015)	160
Table A.2 Snow load.....	160
Table A.3 Design spectrum for Victoria, British Columbia (site class D)	161
Table A.4 Shear force distribution at each storey of MRF	161
Table A.5 Sectional properties.....	162
Table A.6 Design summary of RBS at first floor and roof of the MRF	162
Table A.7 Design of column.....	163
Table A.8 Comparison of base shear, distributed force, elastic drift and moment at RBS center.....	163
Table B.1 Vertical deflection and bending rotation at the middle of the beam at free end and section S-2500.....	173

LIST OF FIGURES

Figure	Page
Figure 2.1 Isotropic and kinematic hardening (Kelly 2013).....	23
Figure 2.2 Idealized stress-strain curve of steel (Wakabayshi et. al 2015).....	23
Figure 2.3 Stress versus strain relationship curve of steel Tian et al. (2011).....	24
Figure 2.4 Typical MRF connection with the beam web (a) bolted to the column flanges (b) welded to the column flange. (Lau 2017)	24
Figure 2.5 RBS connection (AISC 2016)	25
Figure 2.6 Reduced beam section connection in field (Metten and Driver 2015).....	25
Figure 3.1 True flow stress versus true plastic strain curves at various strain rates for material H (Walker 2012).....	45
Figure 3.2 True flow stress versus true plastic strain curves at various strain rates for material G (Walker 2012).....	45
Figure 3.3 Back stress versus true plastic strain curves for material H (Walker 2012)....	46
Figure 3.4 Back stress versus true plastic strain curves for material G (Walker 2012)....	46
Figure 3.5 Relationship between true flow stress, isotropic yield stress and back stress.	47
Figure 3.6 Isotropic yield stress versus true plastic strain curves at different strain rates for material H (Walker 2012).....	47
Figure 3.7 Isotropic yield stress versus true plastic strain curves at different strain rates for material G (Walker 2012).....	48
Figure 3.8 Isotropic yield stress amplification factors at different strain rates for material H from Walker (2012).	48

Figure 3.9 Isotropic yield stress amplification factors at different strain rates for material G from Walker (2012)	49
Figure 3.10 Flow stress amplification factors at different strain rates for material H from Walker (2012).....	49
Figure 3.11 Flow stress amplification factors at different strain rates for material G from Walker (2012).....	50
Figure 3.12 Isotropic yield stress versus true plastic strain at the strain rate of 0.00005 s^{-1} for material H (Walker 2012)	50
Figure 3.13 Isotropic yield stress versus true plastic strain curves at strain rate of 0.00005 s^{-1} for different iterations for material H compared with that obtained from Walker (2012)	51
Figure 3.14 Isotropic yield stress-plastic strain curves at strain rate of 0.00005 s^{-1} for different iteration for material H magnified near the end of yield plateau	51
Figure 3.15 Comparisons between isotropic yield stress versus true plastic strain for 4 back stress terms and 2 back stress terms from Walker (2012) for material H at the strain rate of 0.00005 s^{-1}	52
Figure 3.16 Comparisons between isotropic yield stress versus true plastic strain for 4 back stress terms and 2 back stress terms from Walker (2012) for material H at strain rate of 0.00005 s^{-1} (Fig. 3.15 magnified near the end of yield plateau).....	52
Figure 3.17 Comparisons between calibrated back stress (4 terms) versus plastic strain and back stress versus plastic strain curve from Walker (2012) for material H.....	53
Figure 3.18 Isotropic yield stress versus true plastic strain curves for material H from Walker (2012) and from 4 kinematic hardening terms.....	53

Figure 3.19 Comparisons of calibrated back stress (3 terms) versus plastic strain and back stress versus plastic strain curve from Walker (2012) for material H	54
Figure 3.20 Isotropic yield stress versus true plastic strain curves for material H from Walker (2012) and from 3 kinematic hardening terms.....	54
Figure 3.21 Comparisons of isotropic yield stress versus true plastic strain with different number of back stress terms for material H at a strain rate of 0.00005 s^{-1}	55
Figure 3.22 Amplification factor for isotropic yield stress at true plastic strain of 0.75 for material H.....	55
Figure 3.23 Amplification factors of isotropic yield stress calculated with Eq. (3.3) and tests for material H.....	56
Figure 3.24 Amplification factor of flow stress calculated with Eq. (3.6) and tests for material H.....	57
Figure 3.25 Generated static isotropic yield stress-true plastic strain curve for material H with Eqs. (3.13) and (3.15)	58
Figure 3.26 Generated isotropic yield stress versus true plastic strain curves for material H at different strain rates	58
Figure 3.27 Comparisons of generated flow stress versus true plastic strain curve for material H at different strain rates by Walker (2012) and Eqs. (3.6, 3.14 and 3.15) with 4 kinematic hardening terms.....	59
Figure 3.28 Comparisons between isotropic yield stress versus true plastic strain for 4 back stress terms and 2 back stress terms from Walker (2012) for material G at the strain rate of 0.00005 s^{-1}	59

Figure 3.29 Comparisons between calibrated back stress (4 terms) versus plastic strain and back stress versus plastic strain curve from Walker (2012) for material G.....	60
Figure 3.30 Isotropic yield stress versus true plastic strain curve for material G from Walker (2012) and from 4 kinematic hardening term	60
Figure 3.31 Amplification factor of isotropic yield stress at true plastic strain of 0.75 for material G.....	61
Figure 3.32 Amplification factor of isotropic yield stress calculated with Eq. (3.3) and tests for material G.....	62
Figure 3.33 Amplification factor of flow stress calculated with Eq. (3.6) and tests for material G.....	63
Figure 3.34 Generated static isotropic yield stress-true plastic strain curve for material G with Eqs. (3.13) and (3.15)	64
Figure 3.35 Generated isotropic yield stress versus true plastic strain curve for material G at different strain rates	64
Figure 3.36 Comparisons of generated flow stress versus true plastic strain curve for material G at different strain rates by Walker (2012) and Eqs. (3.6, 3.14 and 3.15) with 4 kinematic hardening terms.....	65
Figure 3.37 The half gauge length model of tapered specimen modelled in ABAQUS by Chen (2010) and Walker (2012)	65
Figure 3.38 Test and predicted engineering stress versus engineering strain curve for material H for the cyclic test by Walker (2012) at a strain rate of 0.0001 s^{-1}	66
Figure 3.39 Test and predicted engineering stress versus engineering strain curve for material H for the cyclic test by Walker (2012) at a strain rate of 0.001 s^{-1}	66

Figure 3.40 Test and predicted engineering stress versus engineering strain curve for material H for the cyclic test by Walker (2012) at a strain rate of 0.01 s^{-1}	67
Figure 3.41 Test and predicted engineering stress versus engineering strain curve for material H for the cyclic test by Walker (2012) at a strain rate of 0.1 s^{-1}	67
Figure 3.42 Test and predicted engineering stress versus engineering strain curve for material G for the cyclic test by Walker (2012) at a strain rate of 0.0001 s^{-1}	68
Figure 3.43 Test and predicted engineering stress versus engineering strain curve for material G for the cyclic test by Walker (2012) at a strain rate of 0.001 s^{-1}	68
Figure 3.44 Test and predicted engineering stress versus engineering strain curve for material G for the cyclic test by Walker (2012) at a strain rate of 0.01 s^{-1}	69
Figure 3.45 Test and predicted engineering stress versus engineering strain curve for material G for the cyclic test by Walker (2012) at a strain rate of 0.1 s^{-1}	69
Figure 3.46 Test and predicted engineering stress versus cross-section area ratio curve for material H for monotonic tensile test by Chen (2010) at a strain rate of 0.0001 s^{-1}	70
Figure 3.47 Test and predicted engineering stress versus cross-section area ratio curve for material H for monotonic tensile test by Chen (2010) at a strain rate of 0.001 s^{-1}	70
Figure 3.48 Test and predicted engineering stress versus cross-section area ratio curve for material H for monotonic tensile test by Chen (2010) at a strain rate of 0.01 s^{-1}	71
Figure 3.49 Test and predicted engineering stress versus cross-section area ratio curve for material H for monotonic tensile test by Chen (2010) at a strain rate of 0.1 s^{-1}	71
Figure 3.50 Test and predicted engineering stress versus cross-section area ratio curve for material H for monotonic tensile test by Chen (2010) at a strain rate of 1.0 s^{-1}	72

Figure 3.51 Test and predicted engineering stress versus cross-section area ratio curve for material G for monotonic tensile test by Chen (2010) at a strain rate of 0.0001 s^{-1}	72
Figure 3.52 Test and predicted engineering stress versus cross-section area ratio curve for material G for monotonic tensile test by Chen (2010) at a strain rate of 0.001 s^{-1}	73
Figure 3.53 Test and predicted engineering stress versus cross-section area ratio curve for material G for monotonic tensile test by Chen (2010) at a strain rate of 0.01 s^{-1}	73
Figure 3.54 Test and predicted engineering stress versus cross-section area ratio curve for material G for monotonic tensile test by Chen (2010) at a strain rate of 0.1 s^{-1}	74
Figure 3.55 Test and predicted engineering stress versus cross-section area ratio curve for material G for monotonic tensile test by Chen (2010) at a strain rate of 1.0 s^{-1}	74
Figure 4.1 Building plan dimensions	88
Figure 4.2 Elevation view of the moment resisting frame	88
Figure 4.3 Details of reduced beam section (RBS) connections	89
Figure 4.4 Hybrid cantilever beam model	90
Figure 4.5 Connection of shell and beam elements. (a) Nodes constrained on the flanges (b) nodes constrained on the web (c) kinematic coupling (d) beam to shell connection..	91
Figure 4.6 Schematic representation of the elements and constraints for the hybrid model of MRF	92
Figure 4.7 Hybrid model of ductile MRF (leaning column has not been shown here for clarity)	93
Figure 4.8 Dimensions of shell element portions of hybrid model	93
Figure 4.9 RBS modelled using shell elements with different meshes (a) mesh-1 (coarse mesh) (b) mesh-2 (fine mesh)	94

Figure 4.10 Acceleration time history (Northridge 1994 scaled to PGA of 0.57g) for mesh convergence study of the hybrid model	94
Figure 4.11 Base shear versus roof displacement for fine and coarse mesh of hybrid model	95
Figure 4.12 Schematic representation of the frame modelled using B31OS elements.....	95
Figure 4.13 Beam element flange with varying width at the RBS	96
Figure 4.14 Acceleration time history (Landers 1992 scaled to PGA of 0.83g) for mesh convergence study of the beam element only model	96
Figure 4.15 Comparisons of base shear versus roof displacement for different meshing schemes at RBS.....	97
Figure 4.16 Modelling scheme for beam only model with 52 elements in RBS segment (See Table 4.4)	97
Figure 4.17 Moment time history at the center of first floor RBS with different mesh schemes for the rest of the model	98
Figure 4.18 Comparisons of base shear versus roof displacement for hybrid and beam element only model.....	98
Figure 5.1 Combinations used to conduct non-linear dynamic analyses for an earthquake record	127
Figure 5.2 Spectral acceleration for MCE hazard level	128
Figure 5.3 Spectral acceleration for DBE hazard level.....	128
Figure 5.4 The loading and mass on the MRF of the two storey building from Chapter 4	129

Figure 5.5 Strain rate versus time for MATG at first floor RBS center for earthquake record 8 at MCE and DBE hazard level.....	129
Figure 5.6 Strain rate versus time for MATH at the first floor RBS center for earthquake record 8 at MCE and DBE hazard level.....	130
Figure 5.7 Ground acceleration time history for earthquake record 8 at MCE and DBE hazard levels.....	130
Figure 5.8 Maximum moment at the first floor RBS center with and without strain rate dependent material properties for MATH at MCE hazard level.....	131
Figure 5.9 Maximum moment at the first floor RBS center with and without strain rate dependent material properties for MATH at DBE hazard level	131
Figure 5.10 Maximum moment at the first floor RBS center with and without strain rate dependent material properties for MATG at MCE hazard level.....	132
Figure 5.11 Maximum moment at the first floor RBS center with and without strain rate dependent material properties for MATG at DBE hazard level	132
Figure 5.12 Increase (%) in the maximum moment with strain rate dependent material properties for MATG and MATH at first floor RBS center at DBE and MCE hazard levels.	133
Figure 5.13 Predicted strain hardening factor at the first floor RBS center for MATG and MATH with static material properties at MCE hazard level	133
Figure 5.14 Percentage change in the peak inter-storey drift for first storey with strain rate dependent material properties for MATG and MATH at DBE and MCE hazard levels.	134
Figure 5.15 Average peak inter-storey drift with and without rate dependent properties for MATG and MATH at DBE hazard level.....	134

Figure 5.16 Average peak inter-storey drift with and without rate dependent properties for MATG and MATH at MCE hazard level	135
Figure 5.17 Average peak inter-storey drift with and without rate dependent properties for the suite of earthquake for COMBH and COMBG at DBE hazard level	135
Figure 5.18 Average peak inter-storey drift with and without rate dependent properties for the suite of earthquake for COMBH and COMBG at MCE hazard level	136
Figure 5.19 Ground acceleration time history for ground motion record 7 at MCE hazard level.....	136
Figure 5.20 Ground acceleration time history for ground motion record 8 at MCE hazard level.....	137
Figure 5.21 Comparisons of base shear versus roof displacement for hybrid and beam element only models for acceleration time history shown in Fig. 5.19	137
Figure A.1 Building plan dimensions from Christopoulos and Filiatrault (2006).....	164
Figure A.2 Six-storey building elevation from Christopoulos and Filiatrault (2006)	164
Figure A.3 Building plan dimensions	165
Figure A.4 Elevation view of the moment resisting frame of the modified building.....	165
Figure A.5 Seismic hazard map (Geological Survey of Canada 2015)	166
Figure A.6 Design Spectrum for Victoria, British Columbia for site class D	166
Figure A.7 Lateral forces on the ductile MRF	167
Figure A.8 The applied loads on the ductile MRF.....	167
Figure A.9 (a) Final member sizes of ductile MRF (b) bending moment diagram (c) shear force diagram (d) axial force diagram	168
Figure A.10 Details of RBS connections	169

Figure A.11 Free-body diagram of beam segment between plastic hinges at RBS center	169
Figure A.12 Free body diagram of beam segment between RBS center at (a) first floor and (b) roof	170
Figure A.13 Maximum moment due to plastic hinging of RBS at (a) column face (b) column centerline (Moment Connections for Seismic Application, CISC 2014)	170
Figure A.14 RBS design summary	171
Figure B.1 Sections at which bending and axial stresses are evaluated.....	174
Figure B.2 Comparisons of stresses at section S-5000 and S-2500 of the cantilever beam for hybrid and beam element only models.....	175
Figure B.3 Comparisons of stresses at section S-3500 and S-3000 of the cantilever beam for hybrid and beam element only models.....	176
Figure B.4 Comparisons of stresses at section S-4500 and S-4000 of the cantilever beam for hybrid and beam element only models.....	177
Figure C.1 Ground acceleration time history for earthquake record 4 at MCE hazard level.....	178
Figure C.2 Ground acceleration time history for earthquake record 4 at DBE hazard level.....	178
Figure C.3 Moment versus curvature at first floor RBS center for earthquake record 4 for MATH at MCE hazard level.....	179
Figure C.4 Moment versus curvature at roof RBS center for earthquake record 4 for MATH at MCE hazard level.....	179

Figure C.5 Moment versus curvature at first floor RBS center for earthquake record 4 for MATG at MCE hazard level.....	180
Figure C.6 Moment versus curvature at roof RBS center for earthquake record 4 for MATG at MCE hazard level.....	180
Figure C.7 Moment versus curvature at first floor RBS center for earthquake record 4 for MATH at DBE hazard level.....	181
Figure C.8 Moment versus curvature at roof RBS center for earthquake record 4 for MATH at DBE hazard level.....	181
Figure C.9 Moment versus curvature at first floor RBS center for earthquake record 4 for MATG at DBE hazard level.....	182
Figure C.10 Moment versus curvature at roof RBS center for earthquake record 4 for MATG at DBE hazard level.....	182

LIST OF ABBREVIATIONS AND SYMBOLS

A	-	modified amplification equation constant
AISC	-	American Institute of Steel Construction
ASTM	-	American Society for Testing and Materials
B	-	modified amplification equation constant
B31OS	-	linear 3D beam element with open section
BFP	-	bolted flange plate connection
BSEP	-	bolted stiffened end plate connection
BUEP	-	bolted unstiffened end plate connection
$b(z)$	-	flange width along the longitudinal axis
c	-	depth of the cut at the center of reduced beam section
[C]	-	damping matrix for multiple degree of freedom system
CISC	-	Canadian Institute of Steel Construction
COMBG	-	MRF with material G in beams and material H in columns
COMBH	-	MRF with material H in beams and material G in columns
CSA	-	Canadian Standard Association
D_a	-	dynamic amplification factor
DBE	-	design basis earthquake
DOFs	-	degrees of freedoms
FEA	-	finite element analysis
FEMA	-	Federal Emergency Management Agency
IDA	-	incremental dynamic analysis

I	-	Cowper-Symonds equation constant
I_e	-	earthquake importance factor of a structure
J	-	Cowper-Symonds equation constant
[K]	-	stiffness matrix for multiple DOF system
L_r	-	original length
$L(t)$	-	length at any time t .
[M]	-	mass matrix
MATG	-	MRF with frame members composed of material G
MATH	-	MRF with frame members composed of material H
MCE	-	maximum credible earthquake
MPC	-	multi-point constraint
MRF	-	moment resisting frame
n	-	number of kinematic hardening terms
NBCC	-	National Building Code of Canada
RBS	-	reduced beam section connection
R_d	-	ductility related force modification factor
R_o	-	overstrength- related modification factor
s	-	length of reduced beam section
S4R	-	4-noded shell element with reduced integration
K_0	-	parameter defining the size of yield surface
T_r	-	room temperature
T_m	-	melting temperature
T^*	-	temperature of a material as a function of its melting point

C_m	-	kinematic hardening moduli
$\dot{\varepsilon}$	-	strain rate in s^{-1}
σ_i	-	isotropic yield stress
$\sigma^i(\dot{\varepsilon})$	-	isotropic yield stress at a strain rate
σ_s^i	-	isotropic yield stress at zero strain rate
σ_t^F	-	true flow stress at zero strain rate
$\sigma_t^F(\dot{\varepsilon})$	-	true flow stress at a strain rate
σ_y	-	static yield stress
σ_{eq}^i	-	equivalent isotropic yield stress
α	-	back stress/Rayleigh damping coefficient
β	-	Rayleigh damping coefficient
γ_m	-	rate of C_n reduction with increasing plastic strain
ε_t^p	-	true plastic strain
ε_0^p	-	true plastic strain at the end of yield plateau
$\dot{\varepsilon}^{pl}$	-	equivalent plastic strain rate
ε	-	critical damping ratio
s_{ij}	-	deviatoric stress tensor
V_0	-	activation volume constant
k	-	Boltzmann constant
f_{ys}	-	static yield strength
f_{yd}	-	dynamic yield strength
ω_i	-	frequency for the mode considered in damping

Chapter 1: Introduction

One of the more severe dynamic loading that can be experienced by civil engineering structures comes from earthquake ground motions. The loading on a structure due to an earthquake ground motions can be quite complex. One way to assess the response of a structure due to this loading is through numerical simulation by subjecting the structure to the recorded time histories of ground acceleration.

A thorough understanding of the material behaviour is required for the design and analysis of a structure. Generally, quasi-static material properties are used in the design of steel structures. However, these properties are not representative of the dynamic behaviour of the material during an earthquake. Structures can experience considerably high rate of deformation (straining) during a seismic event. Tian et. al (2014) stated that the loading imparted on a steel building during an earthquake can produce a deformation/strain rate up to 1.0 s^{-1} in the structural components. Various researchers (Cowper-Symonds 1957, Wakabayashi et. al 1980, Suita et. al 1992, Elghazouli et al. 2004, Walker 2012) have shown that the yield and flow stress of steel increases with increasing strain rate. Hence, using strain rate dependent material properties in the numerical simulations can produce results that are more representative of the actual behaviour of a structure during a seismic event.

Although numerous numerical studies have been conducted to study the effect of strain rate on steel structures due to seismic excitation, no study has been found to investigate the effect on ductile moment resisting frames (MRFs) with reduced beam section (RBS) connections. Moreover, not many studies can be found in the literature that have used the actual material properties for a combined isotropic/kinematic hardening model to carry out non-linear dynamic time history analyses of ductile MRFs with RBS.

1.1 Objective of the Thesis

The objective of the thesis is to assess the performance of a ductile moment resisting frame with reduced beam section subjected to seismic ground motions that considers strain rate dependency of material behaviour. Numerical simulations are carried out using the actual strain rate dependent material properties calibrated from monotonic tensile tests by Chen (2010) and cyclic tests by Walker (2012) of round steel coupons (specimens) at different strain rates. A procedure is being developed to enable properties of materials with different strain rate sensitivity to be generated for use in the numerical simulations.

1.2 Methodology Used in the Research

The material properties to be used in the numerical simulations are calibrated using the experimental data from monotonic tensile tests by Chen (2010) and cyclic tests by Walker (2012) for two grades (ASTM A572 grade 50 and CAN/CSA G40.20/21 300W) of steel coupons (specimens) conducted at different strain rates. A procedure is being developed and used to calibrate the parameters and generate the stress versus strain curves of these two materials for a mixed-mode hardening plasticity model. In the process, existing material models are modified to permit the back stress versus true plastic strain curves and isotropic yield stress versus true plastic strain curves at different strain rates to be generated easily, which allows properties for materials with different strain rate sensitivity to be generated if needed. The generated curves are validated through numerical simulations against tests results of monotonic tensile and cyclic tests from Chen (2010) and Walker (2012).

A ductile moment resisting frame (MRF) with reduced beam section (RBS) connections of a two-storey building in Victoria, BC is being considered in the study. The frame is designed according to NBCC (2015) and CSA S16-14 (CSA 2014). A simple finite element model of the frame is created to carry out the numerical simulations with finite element software

ABAQUS (Dassault Systèmes 2017). The generated isotropic yield stress versus plastic strain curves at different strain rates and back stress curves for the materials of Chen (2010) and Walker (2012) are used as the material properties input in the numerical simulations. Non-linear dynamic time-history analyses with and without strain rate dependent material properties are conducted using a suite of scaled earthquake ground motion records at two seismic hazard levels. Different material combinations in the beams and columns of the frame are considered in the simulations. Bending moment, strain hardening, strain rate, base shear and inter-storey drift from the numerical simulations are analysed and studied, in particular for effects due to strain rate dependency of material properties.

1.3 Organization of the Thesis

Chapter 2 presents a brief literature review on effects of strain rate, plasticity models for metals, constitutive equations used by various researchers to relate the stress amplification due to strain rate to the quasi-static stress and summarizes a few studies conducted to investigate effects of strain rate on various structures. Some background information on moment resisting frames, reduced beam section connections and capacity design approach has also been provided.

Chapter 3 consists of details on the calibration of parameters for the mixed-mode hardening model plasticity model. An existing equation has been modified to relate the isotropic yield stress amplification at different strain rates as a ratio to the static isotropic yield stress. Material properties for different strain rates to be used in the numerical simulations are generated. A procedure to simplify the generation of strain rate dependent material properties has been developed. The generated strain rate dependent material properties (stress versus strain curves) are validated against tests results through numerical simulations

Chapter 4 consists of the design and numerical modelling of a moment resisting frame with RBS connections. A combination shell and beam elements model, and a beam element only model of the frame are explored. Mesh sensitivity study has been conducted for two models. Comparisons are made between these models to come up with an efficient method to conduct non-linear dynamic analyses using rate dependent material properties.

Chapter 5 presents non-linear dynamic time history analyses carried out using different combinations of material properties on beams and columns of the MRF subjected to a suite of earthquake ground motion records. Bending moment, strain hardening, strain rate, base shear and inter-storey drift from the analyses are analysed and studied. Effects of strain rate dependency of material properties on the response and performance of the frame are assessed and discussed

Chapter 6 contains conclusions and recommendations for future studies

Supplementary analyses and results are provided in the appendices

Chapter 2: Literature Review

There are many systems that can be used to resist the lateral forces on a building. One among the systems being a moment resisting frame with reduced beam section that is used specifically to resist the seismic load. The accuracy of the numerical simulation to predict the response of the frame depends on the correct modelling of the material load-deformation behaviour. Thus, the dynamic material properties are required in the simulation to predict the response due to earthquake ground motions. In order to facilitate the discussions, brief reviews of moment resisting frames and on the effects of strain rate on the material load-deformation response are provided. Various constitutive equations used to incorporate the effects of strain rate, metal plasticity, and as well as capacity design approach and reduced beam sections will be discussed.

2.1 Strain Rate

The change in the deformation or strain with respect to time is termed as strain rate. It can be defined as the change in length with respect to time divided by the length.as

$$\dot{\epsilon}(t) = \frac{d}{dt} \left(\frac{L(t) - L_r}{L_r} \right) = \frac{1}{L_r} \times \frac{dL(t)}{dt} \quad (2.1)$$

where $\dot{\epsilon}(t)$ represents the rate of change of engineering strain, L_r is the original length and $L(t)$ represents the length at any time t .

Mechanical properties of many construction materials, such as steel and concrete, are sensitive to the rate of deformation (straining). There is very little change in the material stress-strain curve of most metals when subjected to quasi-static loading (Meyers 1994). However, their mechanical properties vary considerably when the loading rate is high. Hence, it is imperative to account for effects of strain rate on the mechanical properties of structural steel when assessing the safety of the steel structures subjected to loading that may induce

significantly high deformation rate such as earthquake ground motions. Various researchers have conducted studies to examine the effects of strain rate on the mechanical properties of structural steel (Manjoine 1944, Soroushian and Choi 1987, Suita 1992, Chen 2010, Tian et al. 2011, Walker 2012, Ritchie 2017). It has been found that the yield and ultimate strengths of the steel increase with increasing strain rate. At the same strain rate, the percentage increase in the yield strength has been found to be higher than in the ultimate strength. However, the elastic modulus remains unaffected by the change in strain rate. In essence, only plastic deformation is affected by strain rate. It has also been found that different grades of steel exhibit different strain rate sensitivity. Steel with a lower yield strength is generally more sensitive to strain rate than steel with a higher yield strength.

An earthquake ground motion cannot be considered as quasi-static loading. According to Ngo et al. (2007), a structure may experience the deformation up to a maximum strain rate of 10^{-1} s^{-1} during a seismic event. Chang and Lee (1987) stated that a maximum strain rate up to 10^{-1} s^{-1} can be attained in a steel building frame but not likely will be exceeded (Tian et al. 2011). The effect of strain rate becomes significantly more important when the rate reaches 10^{-1} s^{-1} to 1 s^{-1} as the rate of strength increase in steel increases with increasing strain rate.

2.2 Plasticity

There have been many plasticity constitutive models proposed to model metals (steel). For a metal under cyclic loading, the flow stress is commonly modelled with kinematic hardening or combined isotropic and kinematic hardening. One of the models used is a combined hardening model by Armstrong and Frederick (1966) and modified by Chaboche et al. (1979). The yield surface of the model can be defined by von Mises yield criterion as

$$f(\sigma_{ij} - \alpha_{ij}) = \sqrt{\frac{3}{2}(s_{ij} - \alpha_{ij})(s_{ij} - \alpha_{ij})} - K_0 = 0 \quad (2.2)$$

where σ_{ij} is the stress tensor, α_{ij} is the back stress that represents the translation of the yield surface, s_{ij} is the deviatoric stress tensor, and K_0 is the parameter defining the size of yield surface. The evolution of plastic strain tensor is given by

$$de_{mn}^p = \frac{\partial f(\sigma_{ij} - \alpha_{ij})}{\partial \sigma_{mn}} d\lambda \quad (2.3)$$

where $d\lambda$ is the constant of proportionality. The back stress tensor is the summation of M number of back stress tensor terms according to

$$\alpha_{ij} = \sum_{m=1}^M \alpha_{ijm} \quad (2.4)$$

with m^{th} term back stress tensor evolves as

$$\dot{\alpha}_{ijm} = C_m \frac{1}{K_0} (\sigma_{ij} - \alpha_{ij}) \dot{\epsilon}^{pl} - \gamma_m \alpha_{ijm} \dot{\epsilon}^{pl} \quad (2.5)$$

where C_m (kinematic hardening moduli) and γ_m (rate of reduction of α_{ijm} with increasing plastic strain) are the constants that characterize the m^{th} term back stress tensor evolution and the equivalent plastic strain rate given by

$$\dot{\epsilon}^{pl} = \sqrt{\frac{2}{3} \dot{\epsilon}_{mn}^p \dot{\epsilon}_{mn}^p} \quad (2.6)$$

For uniaxial monotonic tension condition and zero initial back stress tensor, Eq. (2.5) reduces to

$$\dot{\alpha}_m = C_m \dot{\epsilon}_t^p - \gamma_m \alpha_m \dot{\epsilon}_t^p \quad (2.7)$$

where α_m is the m^{th} term uniaxial equivalent back stress defined by

$$\alpha_m = \sqrt{\frac{3}{2} \alpha_{ij_m} \alpha_{ij_m}} \quad (2.8)$$

and ε_t^p is the uniaxial true plastic strain reduced from Eq. (2.6) for monotonic uniaxial tension.

Equation (2.7) can be integrated to give

$$\alpha_m = \frac{C_m}{\gamma_m} \left(1 - e^{-\gamma_m \varepsilon_t^p} \right) \quad (2.9)$$

The equivalent isotropic yield stress is given by

$$\sigma_{eq}^i = \sqrt{\frac{3}{2} (s_{mn} - \alpha_{mn})(s_{mn} - \alpha_{mn})} \quad (2.10)$$

The flow stress for uniaxial tension is the combination of isotropic yield stress and back stress defined as

$$\sigma_t^F = \sigma^i + \alpha \quad (2.11)$$

where σ_t^F is a function of true plastic strain ε_p^t , σ^i is the isotropic yield stress for uniaxial condition and α is $\sum_{m=1}^M \alpha_m$. Under uniaxial condition, σ^i is equal to σ_{eq}^i

Krempf (1979) conducted monotonic and cyclic uniaxial tests on 304 stainless steel, while Chang and Lee (1987) performed cyclic tests on A36 structural steel tubing at constant and varying strain rate to study the strain rate history effects. It was found that cyclic flow stress is independent of strain rate history and is affected by current strain rate only. Hence, kinematic hardening can be considered to be independent of strain rate. Lemaitre and Chaboche (1990) also found that that strain rate mainly affects the size of yield surface (isotropic hardening) and not the evolution of back stress (kinematic hardening). Walker (2012) found that the constants that characterize the evolution of back stress given in Eq. (2.9) can be assumed to be independent of strain rate. Chun et al. (2002) examined the plasticity model proposed by Chaboche (1979) by conducting tension-compression and multi-cycle bend

tests of sheet metals and validating it through finite element analyses. It was found that the numerical simulations were able to capture the Bauschinger effect consistently over multiple cycles. Figure 2.1 gives the diagrammatic representation of isotropic and kinematic hardening.

2.3 Modelling of Strain Rate Effects

Modelling of the effects of strain rate on the strength (flow stress) of steel becomes quite important at intermediate to high rates of 10^{-3} s^{-1} to 10^3 s^{-1} as there is a sharp increase in the strength with strain rate. Various researchers have developed many equations that takes effects of strain rate into consideration in modelling the material behaviour. Some of these are discussed here.

Cowper and Symonds (1957) studied the effects of strain hardening and strain rate on a cantilever beam made up of mild steel, and as well as copper by subjecting it to impact loading. A power law equation was proposed to relate the yield stress at different strain rates to the static yield stress as a ratio of the static yield stress as

$$\frac{\sigma(\dot{\varepsilon})}{\sigma_y} = 1 + \left(\frac{\dot{\varepsilon}}{D}\right)^q \quad (2.12)$$

where $\sigma(\dot{\varepsilon})$ is the yield stress at $\dot{\varepsilon}$ strain rate, σ_y is the static yield stress, D and q are constants.

Johnson and Cook (1985) studied the behaviour of three metals namely, OFHC copper, Armco iron and AISI 4340 steel under dynamic loading conditions. The differences in the dynamic and static properties were found to be affected by strain, strain rate, temperature and pressure. The flow stress was proposed to vary with strain, strain rate and temperature as

$$\sigma = [A + B\varepsilon^n] \left[1 + C \ln \frac{\dot{\varepsilon}}{\dot{\varepsilon}_0}\right] [1 - (T^*)^m] \quad (2.13)$$

where ε is the equivalent plastic strain, $\dot{\varepsilon}$ is the strain rate, $\dot{\varepsilon}_0$ is taken as 1.0 s^{-1} , A , B , C , n and m are material constants, and T^* is homologous temperature (temperature of a material as a function of its melting point) given by $\left[\frac{T-T_r}{T_m-T_r}\right]$ where T is the temperature, T_r is the room

temperature, T_m is the melting temperature. Hence, a linear variation of flow stress with the logarithm of strain rate was assumed. Effects of strain hardening, strain rate and thermal softening are assumed to occur independently. Tuazon et al. (2014) modified the Eq. (2.13) (Johnson-Cook equation) by introducing an exponential relationship between the flow stress and the logarithmic strain rate as

$$\sigma = [A + B\varepsilon^n] \left[1 + C \left(\ln \frac{\dot{\varepsilon}}{\dot{\varepsilon}_0} \right)^p \right] [1 - T^{*m}] \quad (2.14)$$

where p is a constant. This equation can capture the increase in the strain rate sensitivity of the material at high strain rates

Couque (2014) developed a material model that incorporated a more refined strain rate effect on the Johnson-Cook (1985) model. This model has the capability of reproducing the test results up to the strain rate of $2 \times 10^4 \text{ s}^{-1}$ at room temperature. In this model, an additional material constant has been added by introducing an additional new power-law term on strain rate as given in

$$\sigma = [A + B\varepsilon^n] \left[1 + C \ln \frac{\dot{\varepsilon}}{\dot{\varepsilon}_0} + D \left(\frac{\dot{\varepsilon}}{\dot{\varepsilon}_1} \right)^k \right] (1 - T^{*m}) \quad (2.15)$$

where D and k are constants, $\dot{\varepsilon}_0$ and $\dot{\varepsilon}_1$ are taken as 1.0 s^{-1} and 10^3 s^{-1} respectively. This model was able to capture the stress versus strain rate test data for nickel, aluminum and stainless steel at low, and as well as high strain rates.

Othman (2015) makes use of a modified Eyring equation to model the yield and flow stresses of the metals considering a wide range of strain rates. Modified Eyring equation (Othman 2015) was an improvement to the proposed Eyring (1936) equation of

$$\sigma_y^E = \sigma_0 + \frac{kT}{V_0} \ln \left(\frac{\dot{\varepsilon}}{\dot{\varepsilon}_0} \right) \quad (2.16)$$

where σ_y^E and σ_0 are the yield stress and yield stress at a strain rate $\dot{\varepsilon}$, $\dot{\varepsilon}_0 = 1 \text{ s}^{-1}$, V_0 is a constant related to the activation volume and k is Boltzmann constant. In the modified Eyring equation,

an additional exponential on the strain rate was added as

$$\sigma_y^E = \sigma_0 + \frac{kT}{V^*} \ln\left(\frac{\dot{\epsilon}}{\dot{\epsilon}_0}\right) \quad (2.17)$$

where V^* is given by

$$V^* = V_0 \exp\left(-\sqrt{\frac{\dot{\epsilon}}{\dot{\epsilon}_c}}\right) \quad (2.18)$$

where $\dot{\epsilon}_c$ is the critical strain rate

Salahi and Othman (2016) have conducted a comparative study of Eq. (2.12) to Eq. (2.17) by fitting the compression yield stress of copper and steel at two temperatures and at strain rates ranging from 10^{-4} to $5 \times 10^4 \text{ s}^{-1}$. The experimental data were obtained from Couque (2014) and Clarke et al. (2008). Equation (2.12) by Cowper and Symonds (1957) was found to be able to fit the experimental data well with 95% accuracy. Johnson-Cook model using Eq. (2.13) could not capture the increase in the yield stress at high strain rates of 10^3 to $5 \times 10^4 \text{ s}^{-1}$, while fitted well for strain rates lower than 10^3 s^{-1} . Equation (2.14) by Tuazon et al. (2014) was found to be able to capture the rise of yield stress at high strain rates but was unable to capture the rise at low strain rates. This equation was considered to be beneficial when considering strain rates higher than 10^{-2} s^{-1} . Equation (2.15) by Couque (2014) and Eq. (2.17) by Othman (2015) fitted well for the experimental data of steel and copper over the entire strain rate range considered in the study. The study concluded that the fitting provided by Eq. (2.12) (Cowper-Symonds 1957), Eq. (2.15) (Couque 2014), and Eq. (2.17) (Othman 2015) to be satisfactory. However, it was recommended that only either Eq. (2.12) or Eq. (2.17) be used to model the effects of strain rate as these equations have fewer material constants compared to Eq. (2.15). Table 2.1 summarizes the comparative study of Eq. (2.12) to Eq. (2.17) by Salahi and Othman (2016).

2.4 Effects of Strain Rate due to Seismic Excitation

The effects of strain rate due to seismic ground motion excitations have been studied for different types of structures. Experimental testing and numerical modelling have been carried out on the reinforced concrete (RC) structures and, as well as steel frames to understand the effects of strain rate.

Wakabayashi et. al (1980) found that the yield moment of reinforced concrete beams and steel beams increased significantly in monotonic loading tests at different strain rates ranging between 0.005 s^{-1} to 0.1 s^{-1} . It was concluded that the compressive strength and elastic modulus of concrete, and yield stress of steel increases linearly with the logarithmic strain rate. Dynamic response analyses were conducted on single-storey steel frame using earthquake excitations to find out the magnitude of strain rate experienced by the structure during an earthquake event. A tri-linear stress strain relationship shown in Fig. 2.2 with a characteristic line prescribing the expansion of hysteresis loop that represent elastic modulus, softening due to Bauschinger effect and strain-hardening curve respectively, was used to model steel. The yield stress (σ_y) was assumed to increase linearly with the logarithm of the strain rate as

$$\frac{\sigma_y}{\sigma_{y_0}} = 1 + 4.73 \times \log_{10} \left| \frac{\dot{\epsilon}}{\dot{\epsilon}_0} \right| \quad (2.19)$$

where σ_{y_0} is the quasi-static yield stress at the rate of $\dot{\epsilon}_0 = 5 \times 10^{-5} \text{ s}^{-1}$. The maximum strain up to 0.5 s^{-1} was found at the critical section of the column. Moreover, it was found that the maximum strain rate increases with the increase in the deformation (flexibility).

Suita et al. (1992) conducted an experimental study on three steel connections where the structural joints were subjected to high speed loading. The connections were butt welded joint, friction and bearing type bolted connections. These specimens were subjected to tensile monotonic loading, and as well as cyclic loading of 5 cycles at a constant amplitude of 4 mm. The cyclic tests were conducted at the strain rate range of 0.05 to 0.35 s^{-1} . The experiments

showed that there was an increase in the yield stress of welded joints with strain rate under monotonic and cyclic loading.

Elghazouli et al. (2004) conducted experiments on concentrically braced steel frames with tubular cold formed steel as bracing members. The experiments on the frames subjected to the seismic ground motions were carried out using a shake table. The braces were connected to the bottom flange of the transverse beam at the top and to a table platform at the bottom. Both coupon test and section tensile test for the steel members used in the frame were conducted. The frames were subjected to the El Centro earthquake record to determine inelastic response. In order to examine effects of strain hardening and strain rate, maximum tensile force measured in the braces during each test was normalized by actual yield and ultimate strengths obtained in monotonic tensile section tests. It was found that the tensile capacity calculated based on actual yield strength can underestimate the maximum tensile force transferred from the braces to other frame members by 30% due to combination of strain hardening and effects of strain rate. On the other hand, if the tensile capacity is calculated using the ultimate material strength, maximum tensile force transferred to other frame members is still underestimated by 10 % due to effects of strain rate.

Bhowmick et al. (2009) showed the need for the inclusion of strain rate effect in the modelling of steel plate shear wall. A four and fifteen storey steel plate shear walls were designed according to NBCC (2005) and CAN/CSA S16-01 (CSA 2001). Various earthquake records were scaled to design spectrum of Vancouver, BC, Canada, for the analyses of these shear walls. An elasto-plastic stress strain curve was adopted with Eq. (2.12) (Cowper-Symonds 1957) used to model the change in the flow stress with strain rate. The flexural demand for the shear wall was found to increase by an average of 11% when effects of strain rate were included in the material model. Moreover, it was found that the strain rate effect on the seismic demand at the base of steel plate shear wall increases with the intensity of the

earthquake. The deformation of the steel plate shear wall was found to decrease with the higher strain rate.

Zhang and Li (2011) investigated the effect of strain rate on the dynamic behaviour of reinforced concrete structures subjected to earthquake loading. Finite element software ABAQUS was used to analyze the dynamic response of a single bay 3-floor reinforced concrete frame and shear wall. Drucker-Prager model (1952) and concrete damaged plasticity model were used for concrete in the dynamic analyses in the study. Effects of strain rates on the yield strength of steel bars were defined as

$$f_{yd} = \left(1 + c_f \log \frac{\dot{\varepsilon}}{\dot{\varepsilon}_o}\right) f_{ys} \quad (2.20)$$

where f_{ys} , and f_{yd} are static yield strength and dynamic yield strength respectively, $\dot{\varepsilon}_o$ is quasi-static strain rate and c_f is a parameter given by

$$c_f = 0.1709 - 3.289 \times 10^{-4} f_{ys} \quad (2.21)$$

It was found through dynamic analyses that the load carrying capacity and stiffness of the shear wall increase with the inclusion of effects of strain rate on the material properties. The reinforced concrete frame was subjected to the El Centro earthquake record with peak ground accelerations of 0.4g and 0.6g. There was increase in the maximum value of base shear and base moment when strain rate dependent material properties were included in the simulations.

Tian et al. (2014) investigated the influence of including the strain rate effect in the analysis of power transmission tower under different ground motion intensities. A subroutine was developed in ABAQUS to model the progressive collapse in the simulation. To model progressive collapse, the stiffness of the of the element is set to zero once the strain in that element exceeds ultimate strain. Incremental dynamic analysis (IDA) method was adopted to calculate the seismic response of the tower with and without the consideration of the strain rate effect. Elastic-perfectly plastic material model, shown Fig. 2.3, was used. The dynamic yield

stress was assumed to vary with strain rate according to Eq. (2.20). The dynamic analyses were carried out using 3 earthquake records and these records were scaled up until progressive collapse of the structure occurred. At the ground motion intensity close to resulting in a collapse of the transmission tower, the maximum displacement at the top of the tower decreases, and the maximum base shear increases when effects of strain rate were included in the analyses. However, for weak ground motions, the maximum displacement at the top of the tower still decreases and the maximum base shear increases when the effects of strain rate are included for most of the earthquakes, but maximum base shear decreased and maximum displacement at the top of tower increased for a few cases.

2.5 Moment Resisting Frames

Moment resisting frame (MRFs) is commonly used framing system that provides resistance to lateral loads in a structure that are subjected to severe ground motions. They are one of the most ductile seismic resisting systems, thus making them quite popular among structural engineers designing buildings in areas of high seismicity. The load resistance of these frames is based on the plastic moment capacity of the beam and the capacity of the connection such that the plastic hinge formation is away from the face of the column thus forming a weak beam-strong column situation. Due to their high ductility, design specification codes have assigned a large force reduction factor to be used in calculating the equivalent static design load for these frames. Furthermore, they can provide an open layout that serves the functional requirements of a building that provides large unobstructed spaces throughout the building plan. However, due to this framing arrangement, MRFs require large member sizes in order to keep the drift within the limits. The columns and beams in a moment resisting frames are usually connected using full restrained moment connections. In these frames, flanges of the wide flange beams can be connected to the column flanges using complete joint penetration

weld along with either the beam web bolted or welded to the column flanges. Figure 2.4 shows a typical MRF connection where the beam web has been either bolted or welded to the column flange. Moment resisting frames can be used in low, medium and high-rise steel buildings.

Redwood et al. (1989) attributed the higher flexibility of MRFs to produce forces in the structure that are lower compared to a stiffer concentrically braced seismic resisting. Moreover, the lower forces produced by MRF can be partially attributed to its high redundancy, which allows the redistribution of loads after yielding. In addition, structural elements are detailed such that an MRF can undergo high ductile deformation. Chen et al. (1996) stated that the input energy of severe ground motions can be absorbed and dissipated by plastic hinges formed at the beam-column connection of the moment resisting frames. Hence, the amount of energy dissipated by these MRFs will be dependent on the rotational capacity of these connections. A proper design of the connections is critical for MRFs to function in resisting the lateral loads

Aksoylar et al. (2011) stated that the high ductility along with the economic viability have allowed the moment resisting frame to be used in low and medium rise structures in intense seismic zones. Moment resisting frames that are designed using the strong column-weak beam philosophy have large column sections in low rise long span buildings. Hence, these frames are used on the periphery of the building. Fadden and McCormick (2012) recommended MRFs to be used in high seismic regions due to their intrinsic capability of providing resistance to the lateral loads coming from the bending resistance of columns, girder and joints (rigid frame action) that enable the seismic energy to be dissipated in a ductile manner.

Some prequalified moment connections have been specified in the Moment Connection for Seismic Application by CISC (2014). This document serves as an alternative to the physical testing that is mandatory as the basis for the design of beam-column connection for ductile (Type D), moderately ductile (Type MD) and low ductile (Type LD) moment resisting frames.

The connections specified by the guidelines for connecting the beam to column flanges are reduced beam section (RBS) connection, bolted unstiffened end plate (BUEP) connection, bolted stiffened end plate (BSEP) connection and bolted flange plate (BFP) connection. In the seismic applications, these connections types are considered to be fully restrained with beams and columns conforming to appropriate requirements of CSA S16-14 (CSA 2014). BUEP and BSEP connections are primarily composed of an extended end plate that is first welded to the beam of the moment resisting frame and then bolted to the column flange. For the inelastic deformation to take place in the beam, sufficient strength is required in the connection to allow flexural yielding of beam section or end-plates or column panel zone. BFP connections consists of the flange plates welded to the column flanges using complete joint penetration weld. These plates are then connected to the beam flanges using the high strength bolts with beam web bolted to the column flange using shear tab. The unwelded portion of the flange plate serves as the location for the initial yielding and formation of plastic hinge. Another connection, an RBS connection will be discussed in greater detail in the following section

2.6 Capacity Design Approach and Reduced Beam Section

The extensive damage experienced by MRFs during the 1994 Northridge earthquake and 1995 Kobe Earthquake was a matter of great concern for the structural engineers. There were some unexpected failures at the beam-column connection. The local brittle damage at the interface of the beam-column connections of steel MRF has led to an extensive research to solve this problem in the MRF. Two methods have been proposed to address this problem. One by strengthening the beam-column joints with additional bolts, welds or stiffeners, and the other by reducing the flexural capacity of the beam or some portion of the beam that framed into the column. Strengthening the beam-column connections, even though effective, is not an economically viable option for large projects.

Moore et al. (1999) stated that the moment frames constructed before Northridge earthquake were designed with the beam web connected to the column transferring the beam shear to the column, while the moment is transferred through the beam flanges. However, this assumption was disputed by a number of researchers due to widespread damage of these moment connections which led to the adoption of a design philosophy that is known as capacity design approach. Leslie et al. (2008) stated that capacity design approach is a method in seismic design of members in steel structures wherein a pecking order of strength is established within the structure. In this method, some of the ductile members are designed to yield while safeguarding some other members from yielding. The design of these protected members is based on the maximum force that is generated by the yielding members. The strength of the protected members is governed by multiplying the over-strength factor (OF) with the specified or nominal strength of the yielding members. In capacity design approach of structural system, yielding location is deliberately defined such that yielding occurs at a required force level at that location. The other members that are linked to the yielding members are designed to be stronger than the yielding members. Yielding members act as fuse that protects the less ductile sections of the structure. In capacity design, the forces in structural members are obtained and calculated from yielding elements. According to CSA S16-14 (CSA 2014), capacity design approach shall be adopted to design the members and connections of the seismic force resisting systems. In this approach, identified members of the structure are designed to dissipate energy along with proper detailing. Other members are designed sufficiently strong to allow the designated members (components) to achieve the energy dissipation. This led to introduction of RBS connections in the design of MRF.

RBS connections or “dog-bone” are a part of prequalified moment connections that can be used in the moment frames without any prior physical testing. The strategy employed in these connections is to deliberately reduce the flexural capacity of the beam at a specific

location for yielding and plastic hinge formation to take place in the beam. The main characteristic of these connection is the reduction in the size of beam top and bottom flanges with cuts (generally semi-circular shapes) near the beam-column connections as shown in Fig. 2.5. The intention is to allow the plastic hinge formation and yielding to occur away from the beam-column interface at the center of the RBS. Since inelastic deformation takes place mainly in the RBS only, minimal effort is required in designing of the beam-column connection. The weak beam-strong column connections are made possible by the introduction of a smaller moment at the face of the column due to RBS. It is an economically viable connection as no additional plates, weld or fastener is required. Figure 2.6 shows an RBS connection in the field.

The performance of reduced beam section is dependent on its shape, size and location. Various studies have been conducted to study the performance of RBS with different shapes, which include semi-circular cut, tapered cut and straight cut. RBS with radius cut or the semi-circular cut has been listed as one of the prequalified moment connections in Moment Connection for Seismic Application (CISC 2014) and ANSI/AISC 358-16 (AISC 2016). Moreover, Sofias et al. (2014) recommended radius cut RBS because of its highest rotational capacity. Figure 2.5 shows the parameters used in the design of RBS with “a” represents the distance of RBS from the face of the column, “s” is the length of RBS and “c” is the depth of the cut at RBS center (radius cut RBS will be designated as RBS henceforth). Engelhardt (1999) stated that to minimize the growth of moment from the plastic hinge forming at RBS center to column face, distance “a” (shown in Fig. 2.5) should be kept as small as possible. However, the distance should be large enough to allow the stress from RBS to spread uniformly across the flange width at the face of the column. The moment developed at the centerline of the column is dependent on the depth of the cut at the center of the RBS as this depth dictates the maximum moment that can be developed at the center of the RBS. Hence, it is the most important dimension that requires the utmost attention in the design of RBS. Englehart (1999)

recommended that the flange width reduction should not be greater than the 50 percent of the flange width as excessive reduction in the flange area could lead to untimely local lateral torsional buckling that could lead to adverse effects on the frame.

Kitjasateanphun et al. (2001) stated that the performance and efficiency of the RBS is dependent on its proper design. Insufficient or inadequate reduction of the flange width will not be able to sufficiently reduce the stress at the column face and allow for proper yielding of RBS. The location of the RBS cut also plays a pivotal role in its performance. The cut carved out too close to the column face might result in the failure of the connection. According to Moment Connection for Seismic Application (CISC 2014), the cut should be in the range of 20% to 50% of the beam flange width. Similar depth of cut has also been recommended by ANSI/AISC 358-16 (AISC 2016).

Sofias et al. (2014) studied the behaviour of RBS with end plates subjected to cyclic loading with tests and numerical simulations. The profile recommended by the EC-8, Part-3 (Eurocode 2005) was used to design the RBS. Coupon tests were conducted for the steel used in the RBS to define elastic-plastic material properties for the finite element analyses. The beam-column connection with the same RBS dimension but different mechanical properties was subjected to cyclic loading and plastic hinge was able to form in the RBS. This protected the beam-column connection from plastification and hence failure. It was also stated that the maximum permissible depth of the cut at the center of RBS is dependent on the ductility of steel. The RBS specimen made of steel with better ductility can prevent the brittle fracture of the tensile region at an extremely high load.

Kitjasateanphun et al. (2001) studied modelling issues associated with inelastic behaviour of RBS experimentally and numerically. An FEA model was built to study the performance of RBS over a range of RBS location and flange reduction . A trilinear stress-strain curve on the coupon test was used for the analyses. The specimen tested consists of a

beam with reduced beam section connected to a column. It is subjected to cyclic displacement time history at the free end of the beam with increasing cyclic amplitudes up to 200 mm displacement. A good agreement has been found between the experimental and finite element analysis hysteretic force of the connection versus tip displacement.

The reduction in the beam strength due to introduction of RBS has only a small impact on the overall lateral stability of the MRF. Grub (1997) analyzed moment resisting frame with varying height and different flange reduction in a radius cut RBS. The elastic stiffness reduction of these frame was found to be in order of 4 to 7% for flange reduction ranging from 40 to 50%. Moore et al. (1999) stated that even though the beam is weakened with introduction of the RBS, it has only a small effect on the lateral stability and stiffness of a steel moment frame.

2.7 Concluding Remarks

Although numerous studies have been conducted to investigate effects of strain rate on steel structures, none of the studies have been found to study these effects on ductile moment resisting frame (MRF) with reduced beam sections (RBS) connections. Moreover, none of the studies have employed realistic material properties in the analyses. Hence, the performance of ductile MRF with RBS connections that considers strain rate dependency of material behaviour can be investigated by employing actual strain rate dependent material properties in numerical simulations.

Table 2.1 Comparative study of Eq. (2.12) to Eq. (2.17) (Salahi and Othman 2016)

Strain Rate Model	Constitutive Equation	Fitting results with experimental data
Cowper-Symonds (1957)	Eq. (2.12)	Fits well at strain rates ranging from 10^{-4} to 50000 s^{-1} with 95% accuracy.
Johnson-Cook (1985)	Eq. (2.13)	Could not capture increase in yield stress at high strain rates of 10^3 to 50000 s^{-1}
Tuazon (2014)	Eq. (2.14)	Unable to capture increase in yield stress at strain rates lower than 10^{-2} s^{-1}
Couque (2014)	Eq. (2.15)	Fits well at the strain rates ranging from 10^{-4} to 5000 s^{-1}
Othman (2015)	Eq. (2.17)	Fits well at the strain rates ranging from 10^{-4} to 50000 s^{-1}

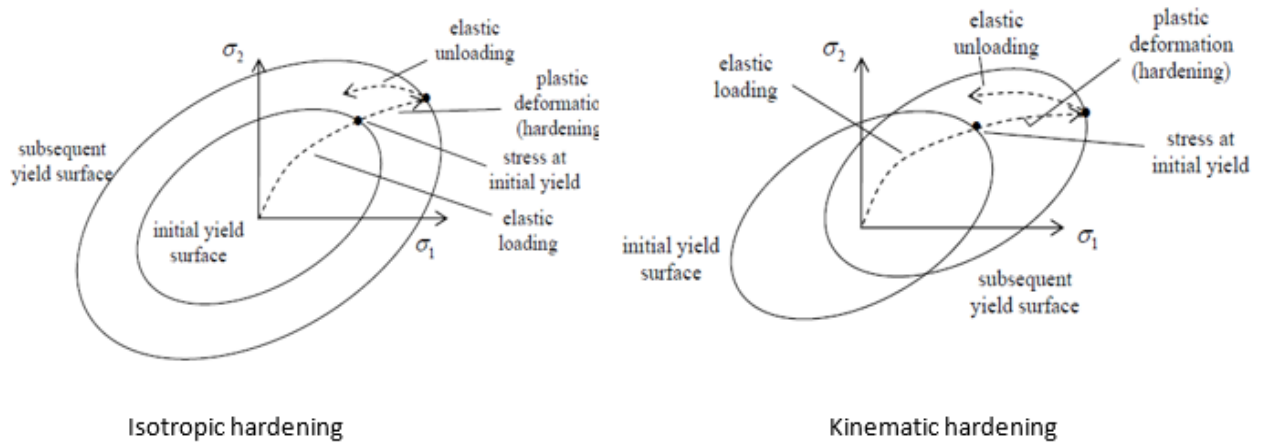


Figure 2.1 Isotropic and kinematic hardening (Kelly 2013)

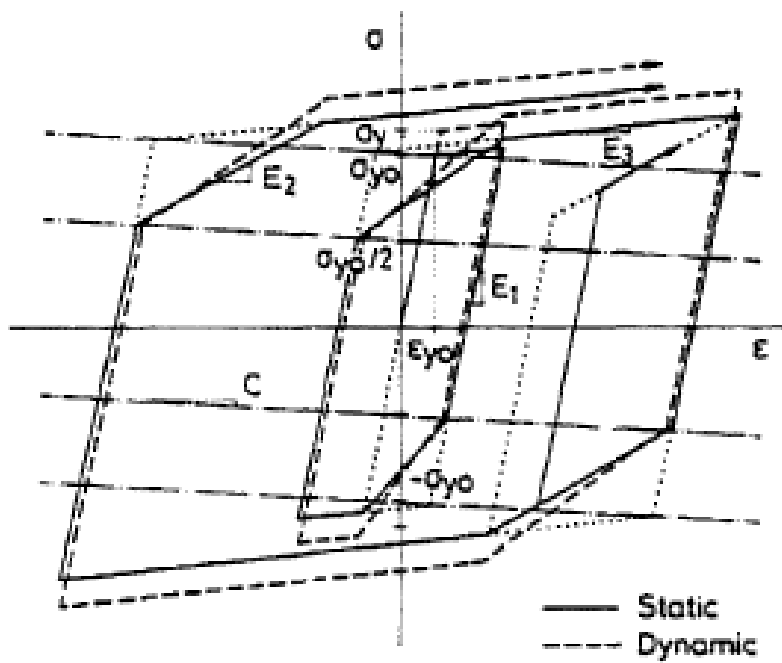


Figure 2.2 Idealized stress-strain curve of steel (Wakabayshi et. al 2015)

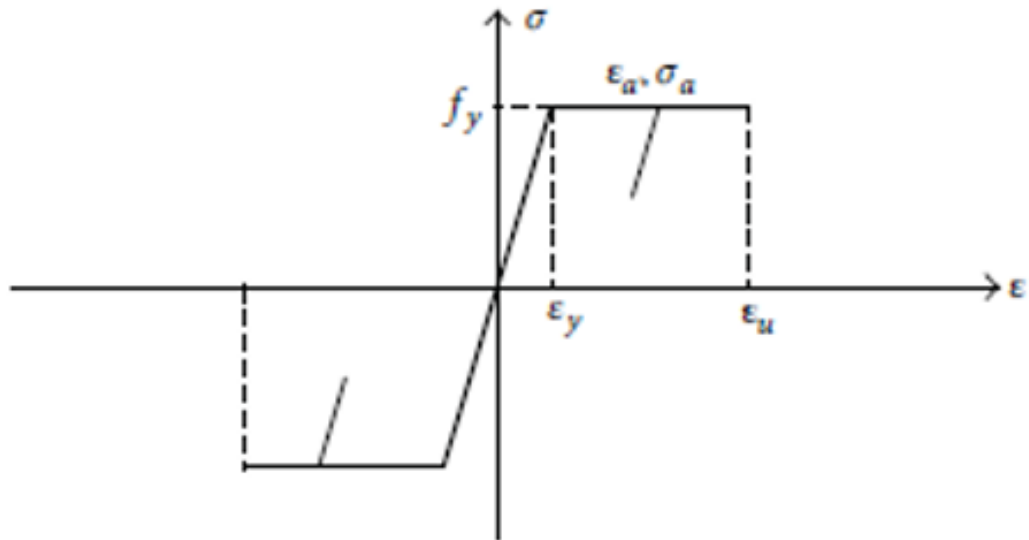


Figure 2.3 Stress versus strain relationship curve of steel Tian et al. (2011)



Figure 2.4 Typical MRF connection with the beam web (a) bolted to the column flanges (b) welded to the column flange. (Lau 2017)

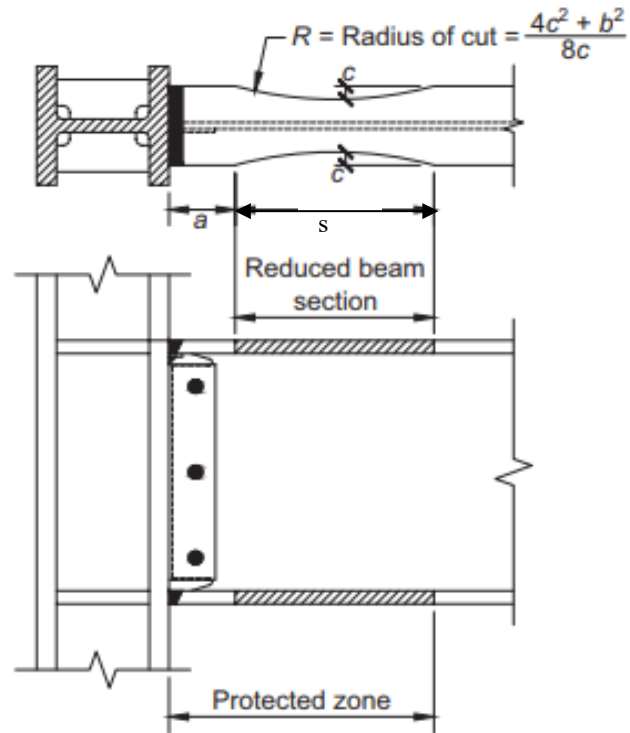


Figure 2.5 RBS connection (AISC 2016)



Figure 2.6 Reduced beam section connection in field (Metten and Driver 2015)

Chapter 3: Calibration of Material Properties

Using realistic material properties and proper constitutive model in numerical simulations of a structure can produce results that are more representative of the actual behaviour. The appropriate material properties to be used in carrying out the analyses to assess effect of strain rate dependency of the material strength (behaviour) on the performance of a structure subjected to seismic ground motions can be obtained from the tests of steel coupons (specimens) at different strain rates. Chen (2010) and Walker (2012) have respectively conducted monotonic tensile and cyclic tests of steel coupons (specimens) for two grades of steel at different strain rates. Results of these tests can be used to generate the material properties input for the numerical simulations. A simple procedure has also been proposed to allow for a material with different stress amplification factors to be generated. The strain rate amplification factor by Cowper-Symonds (1957) in Eq. (2.12) has been modified and improved on and validated against tests results. This will allow material properties used in the numerical simulations to be varied in order to study the response and performance of structures with various material strain rate sensitivity. All numerical analyses have been carried out with ABAQUS (Dassault Systèmes 2017) with elastic modulus of 200 GPa and Poisson's ratio of 0.3.

3.1 Monotonic Tensile and Cyclic Tests by Chen (2010) and Walker (2012)

Monotonic tensile tests at constant strain rates from of 10^{-5} s^{-1} to 1 s^{-1} were conducted by Chen (2010) for rectangular and round specimens of ASTM A572 grade 50 and CAN/CSA G40.20/21 300W steel. Results of the tests show that the amplification of true stress with strain rate was found to be higher at the initial stage of strain hardening and diminishing with

deformation. To facilitate the discussions, ASTM A572 grade 50 and CAN/CSA G40.20/21 300W steel used in these tests will be referred to respectively as material H and material G

Walker (2012) also carried out tests on the round specimens of materials G and H with tapered and notched profiles subjected to a variety of cyclic loading at constant strain rates from 10^{-4} to 10^{-1} s^{-1} . The loading applied to the tapered specimens consisted of a combination of predefined number of loading cycles at specified strain ranges that was followed by pulling the specimen to fracture. A positive rate sensitivity on flow stress has been found for both these materials during initial cyclic loading. However, with continuous loading, tests performed at the strain rates of 10^{-2} and 10^{-1} s^{-1} were found to show negative flow stress rate sensitivity due to adiabatic heating. Walker (2012) has developed a procedure to generate strain rate dependent input material properties for numerical simulations under a general loading condition for strain rate ranging from 0.00005 s^{-1} to 1.0 s^{-1} using the mixed-mode hardening model by Lemaitre and Chaboche (1990). An exponential-law based equation

$$\sigma_t^F = \sigma_t^y + \sigma_1 \left[1 - \exp\left(\frac{-(\varepsilon_t^p - \varepsilon_t^o)^d}{\varepsilon_c}\right) \right] \text{ for } (\varepsilon_t^p - \varepsilon_t^o) > 0 \quad (3.1)$$

was used by Walker (2012) to generate flow stress versus true plastic strain curves at different strain rates, where ε_t^o is the true plastic strain at the end of the yield plateau, σ_t^y is the yield stress, σ_1 is saturated yield stress at the plastic strain of 5.0, ε_c and d are constants. The generated curves for materials H and G at different strain rates are respectively shown in Figs. 3.1 and 3.2. Table 3.1 shows the parameters used to generate these monotonic true flow stress versus true plastic strain curves at different strain rates by Walker (2012). Walker (2012) also calibrated the kinematic hardening parameters for two back stress terms. The generated back stress versus true plastic strain curves with calibrated parameters in Table 3.2 are shown in

Figs. 3.3 and 3.4 for materials H and G. Rearranging Eq. (2.11), the isotropic yield stress versus plastic strain curves at different strain rates were obtained for both materials by subtracting the back stress from the flow stress as

$$\sigma^i = \sigma_t^F - \alpha \quad (3.2)$$

Figure 3.5 gives the general relationship between the flow stress, isotropic yield stress and back stress. Figures 3.6 and 3.7 show the isotropic yield stress curves at different strain rates generated by Walker (2012) for materials H and G. Walker (2012) carried out the numerical simulations of the round specimen tests using mixed-mode hardening plasticity model by Lemaitre and Chaboche (1990) at different constant strain rates from 10^{-4} to 10^{-1} s^{-1} with the generated isotropic hardening curves and back stress curves. Good agreement was achieved between the results of the simulations and cyclic tests.

3.2 Modified Cowper-Symonds Amplification Equation

Cowper-Symonds (1957) proposed an equation based on power-law relationship shown in Eq. (2.12) to calculate the amplification factor that relates the yield stress at different strain rates as a ratio to the static yield stress. Taking the isotropic yield stress and flow stress from Walker (2012), calculated amplification factors for materials H and G at different strain rates and strains are shown in Figs. 3.8 to 3.11. The isotropic yield stress and flow stress at the strain rate of 0.00005 s^{-1} are taken as the static stresses in calculating the amplification factors in Figs. 3.8 to 3.11 as static stresses were not given by Walker (2012). It can be seen that the amplification factor is higher at the initial stage of strain hardening and decreases with strain. However, Eq. (2.12) is independent of plastic strain. Hence, a modified Eq. (2.12) has been

proposed to approximate the amplification factor on the isotropic yield stress that decreases with increasing plastic strain as

$$D_a = \frac{\sigma^i(\dot{\varepsilon})}{\sigma_s^i} = 1 + S(\dot{\varepsilon}) \xi_{pl} \quad (3.3)$$

where D_a is the dynamic amplification factor, σ_s^i is the static isotropic yield stress and $\sigma^i(\dot{\varepsilon})$ is the isotropic yield stress at a specified strain rate, $S(\dot{\varepsilon})$ is the term from Cowper-Symonds (1957) given as

$$S(\dot{\varepsilon}) = \left(\frac{\dot{\varepsilon}}{I}\right)^{\frac{1}{J}} \quad (3.4)$$

where I and J are constants, and ξ_{pl} is the term that approximates the reduction in the stress amplification with increasing plastic strain given by

$$\xi_{pl} = \left(1 + A e^{-B(\varepsilon_t^p - \varepsilon_0^p)}\right) \quad (3.5)$$

where A and B are the constants, ε_t^p is true plastic strain and ε_0^p is true plastic strain at the end of yield plateau. Hence, the true flow stress at different strain rates for uniaxial monotonic can be expressed using Eq. (3.3) as

$$\sigma_t^F(\dot{\varepsilon}) = \left[(1 + S(\dot{\varepsilon}) \xi_{pl}) \sigma_s^i\right] + \alpha \quad (3.6)$$

In a simpler form, Eq. (3.6) can be written as

$$\sigma_t^F(\dot{\varepsilon}) = (D_a \times \sigma_s^i) + \alpha \quad (3.7)$$

The constants A , B , I and J are simply referred to as amplification constants in the discussions.

3.3 Calibration of Material Properties for Mixed-Mode Hardening Material Model for Different Strain Rates

The isotropic stress-strain curves generated by Walker (2012) in Figs. 3.6 and 3.7 show a considerable hump at close to a plastic strain of 0.2 for both materials. However, the isotropic yield stress is expected to always increase with strain. These humps were produced because

only two kinematic hardening terms for back stress were used by Walker (2012). It is expected that the hump in the isotropic stress-strain curve to become less distinct or be eliminated as more kinematic hardening terms are used to better represent the back stress evolution. Hence, a procedure has been adopted to extend the calibration by Walker (2012) to use more kinematic hardening terms. These back stress terms are then used to calculate the isotropic stress amplification factors at different strain rates along with the static isotropic yield stress-true plastic strain curve using modified amplification equation, Eq. (3.3). This forms a two-step procedure in which the first step involves calibrating the kinematic hardening parameters and the second step consists of calculating the static isotropic yield stress and the isotropic yield stress amplification factors at different strain rates and strains. These two steps are explained further in the following sections. Since both materials G and H are calibrated using the same procedure, only the calibration of material H is presented in the discussions

3.3.1 Calibration of Kinematic Hardening Parameters

According to Krempl (1979), Chang and Lee (1987) and Lemaitre and Chaboche (1990), only the size of yield surface (isotropic yield stress) is affected by strain rate while evolution of back stress can be considered to be unaffected. Since the flow stress-true plastic strain curve at zero strain rate (static curve) has not been provided by Walker (2012), the kinematic hardening parameters are calibrated using the isotropic yield stress versus plastic strain curve at a strain rate of 0.00005 s^{-1} shown in Fig. 3.12. It can be seen in Figs. 3.3 and 3.4 that the first kinematic hardening term reaches saturation at a strain less than 0.04. Thus, the hump in the isotropic yield stress-plastic strain curve at around plastic strain of 0.2 is due to the second back stress term. For this reason, the second back stress term is being replaced with more than one back stress term in an attempt to eliminate the hump. The process of calibrating of kinematic hardening parameters for more back stress terms involves re-calculating the

isotropic yield stress based on the flow stress given by Walker (2012) for p number of back stress terms as

$$\sigma^i = \sigma_t^F(0.00005) - \frac{C_1}{\gamma_1} \left(1 - e^{-\gamma_1 \varepsilon_t^p}\right) + \sum_{m=2}^p \frac{C_m}{\gamma_m} \left(1 - e^{-\gamma_m \varepsilon_t^p}\right) \quad (3.8)$$

where $\sigma_t^F(0.00005)$ represents flow stress at strain rate of 0.00005 s^{-1} , C_1 and γ_1 are kinematic hardening parameters for the first back stress term from Walker (2012). The derivative of isotropic yield stress with strain is constrained to be positive such that

$$\frac{d}{d\varepsilon} \left(\sigma_t^F(0.00005) - \frac{C_1}{\gamma_1} \left(1 - e^{-\gamma_1 \varepsilon_t^p}\right) + \sum_{m=2}^p \frac{C_m}{\gamma_m} \left(1 - e^{-\gamma_m \varepsilon_t^p}\right) \right) > 0 \quad (3.9)$$

to ensure that the hump to be less distinct or be eliminated. Another condition is that the saturated isotropic yield stress versus plastic strain curve by Walker (2012) in Fig. 3.13 does not change.

The kinematic hardening parameters are calibrated by the least square error fitting of the isotropic yield stress versus plastic strain curve by Walker (2012) shown in Fig. 3.12 and the data points listed in Table 3.3 by varying the isotropic stress at the end of yield plateau such that the isotropic stress-plastic strain curve obtained using Eq. (3.2) does not exhibit any hump or there is a significant reduction in the hump at close to plastic strain of 0.2. The isotropic yield stress at the end of yield plateau ($\varepsilon_0^p = 0.006$) for strain rate of 0.00005 s^{-1} has been found to be equal to 279 MPa based on the kinematic hardening parameters by Walker (2012). Setting the isotropic yield stress at the end of yield plateau any higher than 279 MPa will increase the hump. Hence, the isotropic yield stress at the end of yield plateau has to be lower than 279 MPa in the least square error fitting. Using four kinematic hardening terms, Figs. 3.13 and 3.14 show the isotropic yield stress versus plastic strain curves of iterations with isotropic yield stresses of 230, 245 and 265 MPa at the end of yield plateau. It can be seen that a higher isotropic yield stress produces a higher saturated isotropic yield stress. Thus, the trial isotropic yield stress at the end of yield plateau is iterated between 245 and 265 MPa until the saturated isotropic yield

stress matches that from Walker (2012) shown in Fig. 3.13. The isotropic yield stress at the end of yield plateau is iterated to 260 MPa for the resulted isotropic yield stress versus true plastic strain curve shown in Figs. 3.15 and 3.16, and the calibrated parameters for 4 kinematic hardening terms listed in Table 3.4. Back stress and isotropic yield stress versus plastic strain curves calculated based on parameters in Tables 3.1 and 3.4 are shown in Fig. 3.17 and 3.18. The back stress with 4 kinematic hardening terms is higher at small strain compared to that with 2 kinematic hardening terms as can be seen in Fig. 3.17 and is able to eliminate the hump in the isotropic yield stress versus plastic strain curve as shown in Fig. 3.18.

Three kinematic hardening terms have also been considered. Figures 3.19 and 3.20 show the back stress and isotropic yield stress versus true plastic strain curves with calibrated parameters listed in Table 3.4 for three kinematic hardening terms. It can be seen that the increase in the back stress at low strain for 3 kinematic hardening terms over back stress for two kinematic hardening terms is not as high as the increase with four kinematic hardening terms. Consequently, hump in the isotropic yield stress versus true plastic strain curves at around the strain of 0.2 has not been as effectively eliminated with 3 kinematic hardening terms as shown in Fig. 3.20 and 3.21 and compared to Fig. 3.18 for 4 kinematic hardening term. Although further improvement on the elimination of the hump can be expected with more kinematic hardening terms, only 4 kinematic hardening terms will be considered as to limit the complexity in the calibration of the kinematic hardening parameters. It is decided that the improvement provided with 4 kinematic hardening terms is sufficient

3.3.2 Static Stress-Strain Curve and Stress Amplification at Different Strain Rates

In the studies by Chen (2010) and Walker (2012), the true stress versus true strain curves at different strain rates have been measured and generated for materials G and H. Chen (2010) paused monotonic tension tests at the strain rate of 10^{-4} s^{-1} for around half a minute at

regular intervals to take the reading. While this gives the reading at a zero loading rate after some relaxation due to the pause, it cannot be considered to be a true static (extremely low strain rate) reading. Walker (2012) also did not provide a true true stress versus true strain curve (static) at zero strain rate. Instead, numerical simulations carried out by Walker (2012) were using the true stress-strain curve at the strain rate of 0.00005 s^{-1} as the static curve. Since there is no data available lower than the strain rate of 0.00005 s^{-1} , the true stress-true strain curve at the strain rate of 0.00005 s^{-1} by Walker (2012) will be used as the basis to calculate the static stress versus strain curve and constants A , B , I and J for the modified amplification equation, Eq. (3.6).

The flow (true) stress at the strain rate of 0.00005 s^{-1} according to Eq. (3.6) can be expressed as

$$\sigma_t^F(0.00005) = [(1 + S(0.00005) \xi_{pl}) \sigma_s^i] + \alpha \quad (3.10)$$

where $S(0.00005)$ is

$$S(0.00005) = \left(\frac{0.00005}{I} \right)^{\frac{1}{J}} \quad (3.11)$$

Rearranging Eq. (3.10) as

$$\sigma_s^i = \frac{\sigma_t^F(0.00005) - \alpha}{(1 + S(0.00005) \xi_{pl})} \quad (3.12)$$

and substituting for the isotropic static stress, Eq. (3.6) can be rearranged to give the isotropic yield stress at different strain rates according to Eq. (3.2) as

$$\sigma^i(\dot{\epsilon}) = \sigma_t^F(\dot{\epsilon}) - \alpha = \left((1 + S(\dot{\epsilon}) \xi_{pl}) \times \frac{[\sigma_t^F(0.00005) - \alpha]}{(1 + [S(0.00005)] \xi_{pl})} \right) \quad (3.13)$$

Constants A , B , I and J are determined through least-square error fitting of the amplification factor at different strain rates and strains for isotropic yield stress in Table 3.5. The parameters for the kinematic hardening (back stress) are shown in Table 3.4. The isotropic yield stresses in Table 3.5 are calculated with the flow stresses using Eq. (3.1) from the parameters by Walker

(2012) in Table 3.1 and back stress by Eq. (2.9) with parameters for 4 kinematic hardening terms in Table 3.4.

There is a two-step process involving calibrating the constants A , B , I and J . The constants I and J are first calibrated for the amplification factors at a large strain. This is followed by calibrating constants A and B using the amplification factors at all strains. At a large strain, the term ξ_{pl} is assumed to approach 1.0 and thus Eq. (3.3) converges to Eq. (2.12).

Rearranging Eq. (3.3) as

$$\sigma^i(\dot{\epsilon}) = \sigma_s^i(1 + S(\dot{\epsilon})\xi_{pl}) \quad (3.14)$$

and taking $\xi_{pl}=1.0$ at a plastic strain of 0.75, the constants I and J for Eq. (3.4) are calibrated through least square error fitting of the isotropic stress amplification factor of isotropic yield stresses in Table 3.5 at strain of 0.75. The result of the fitting is shown in Fig. 3.22 for material H and calibrated values of I and J in Table 3.6. Constants A and B are then calibrated through the least square error fitting of the isotropic stress amplification factor obtained using all the data in Table 3.5 and calibrated values of I and J from Table 3.6. Even though the length of yield plateau varies with strain rate in the tests, a constant plastic strain at the end of yield plateau of 0.006 from the tests at a strain rate of 0.00005 s^{-1} is adopted. Calibrated values of A and B are shown in Table 3.7. Calculated isotropic yield stress based on calibrated constants A , B , I and J are shown in Table 3.8. The static isotropic yield stress σ_s^i is determined from the isotropic yield stress at the strain rate of 0.00005 s^{-1} through Eq. (3.12). Comparisons of the fit of Eq. (3.3) to the amplification of the measured isotropic yield stress and flow stress (calculated and generated) at various strain rates are shown in Figs. 3.23 and 3.24 for material H. The proposed modified Cowper-Symonds amplification equation, Eq. (3.6), appears to be able to give a reasonable prediction of the stress amplification. The calculated static isotropic yield stress versus plastic strain curves from Eqs. (3.1) and (3.13) are shown in Fig. 3.25.

3.3.3 Generating Isotropic Yield Stress-Plastic Strain Curves for Different Strain Rates

Static isotropic yield stress versus plastic strain curves has been calculated in Section 3.3.2. It is expected that the hardening rate of isotropic yield stress to decrease with plastic strain. While four kinematic hardening is able to reduce or eliminate the hump in the calculated static isotropic yield stress versus plastic strain curves, it does not always give a calculated isotropic yield stress versus true plastic strain curve that show a decreasing hardening rate with plastic strain, which will be shown in the following section for material G. In order to facilitate the generation of the isotropic yield stress at different strain rates and to partially correct this deficiency, a smoother curve is fitted over the calculated static isotropic yield stress curve in Fig. 3.25. A modified Eq. (3.1) for generating the flow stress is being used to fit the calculated static isotropic yield stress versus true plastic strain curve. The equation can be expressed as

$$\sigma_s^i = \sigma_s^{yp} + \sigma_1 [1 - \exp(-a (\varepsilon_t^p - \varepsilon_t^o)^b)] \text{ for } (\varepsilon_t^p - \varepsilon_t^o) > 0 \quad (3.15)$$

where σ_s^i is the isotropic yield stress, σ_s^{yp} is the isotropic yield stress at the end of yield plateau, σ_1 is additional increase in the yield stress over σ_s^{yp} at the infinite finite plastic strain such that $\sigma_s^{yp} + \sigma_1$ is equal to saturated yield stress, (the upper limit in Fig 3.25), ε_t^o is plastic strain at the end of yield plateau, a and b are constants. Using Eq. (3.15) to generate the static isotropic yield stress versus plastic strain curve also allows material properties used in the numerical simulations to be varied in a study to investigate the response and performance of structures with different strain rate sensitivity in the material properties.

The constants a and b are determined by least square error of fitting of Eq. (3.15) through a few points in the calculated static isotropic yield stress versus plastic strain curve shown in Fig. 3.25. Comparisons of the fitted and calculated static isotropic yield stress versus true plastic strain curves are shown in Fig. 3.25, and parameters calibrated and used in Eq.

(3.15) are listed in Table 3.9. The isotropic yield stress versus plastic strain curves at different strain rates can be generated from the static isotropic yield stress versus plastic strain curve according to Eq. (3.14) and the flow stress versus plastic strain curves according to Eq. (3.6). Using the calibrated values in Tables 3.4 (4 kinematic hardening terms), 3.6, 3.7 and 3.9, generated isotropic yield stress versus true plastic strain curves and flow stress versus true plastic strain curves for different strain rates for material H are shown in Figs 3.26 and 3.27 respectively. Comparisons of generated flow stress versus true plastic strain curves by Walker (2012) and Eqs. (3.6, 3.14 and 3.15) with four kinematic terms are shown in Fig. 3.27 for material H. Note that the yield plateau length of the flow stress versus true plastic strain curves by Walker (2012) varies with strain rate, while a constant yield plateau length of 0.006 from the tests at a strain rate of 0.00005 s^{-1} is adopted when generated with Eqs. (3.6, 3.14 and 3.15). Nevertheless, the difference between the generated curves by Walker (2012) and Eq. (3.6) is not big.

3.4 Generated Material Properties for Material G

Using procedure outlined in Section 3.3, parameters and material properties for mixed mode hardening for different strain rates are calibrated and generated for material G. Similar to material H, the calibration is carried out mainly with data from the monotonic tension test at strain rate of 0.00005 s^{-1} . Table 3.4 shows the parameters for kinematic hardening parameters calibrated for 3 and 4 back stress terms. Together with the data points used in the curve fitting, comparisons of calculated isotropic yield stress versus plastic strain curve with 4 kinematic hardening terms and 2 terms from Walker (2012) are shown in Fig. 3.28. Parameters for 4 kinematic hardening terms have been calibrated with the isotropic yield stress of 205 MPa at the end of yield plateau ($\varepsilon_0^p = 0.013$). Figure 3.29 compares the back stress versus plastic strain curves with 2 and 4 kinematic hardening terms. The higher back stress at small strain translates

to a reduction or elimination of the hump in the isotropic yield stress versus true plastic strain curves for 4 kinematic hardening terms as compared to that for 2 terms, as can be seen in Fig. 3.30. Results of the calibration of the modified Cowper-Symonds amplification Eq. (3.3) are shown Fig. 3.31 for the isotropic yield stress at the plastic strain of 0.75, and Figs. 3.32 and 3.33 for the isotropic yield stress and flow stress at various plastic strains. Isotropic yield stress at various strains and strain rates used in the calibration are listed in Table 3.10, and the isotropic yield stress calculated based on the calibrated parameters in Tables 3.4, 3.6 and 3.7 for Eqs. (3.3) to (3.5) of Eq. (3.3) are listed in Table 3.11. As can be seen in Figs. 3.31 to 3.33, reasonably good representation can be achieved using Eq. (3.3) to calculate the stress amplification where the amplification is significantly higher at the beginning of strain hardening (small strain).

Figure 3.34 shows the comparison of the static isotropic yield stress versus plastic strain curve calculated with Eq. (3.13) and the fitted curve with Eq. (3.15) together with the data points used in the least square error fitting. Parameters used and calibrated for Eq. (3.15) are listed in Table 3.9. It can be seen in Fig. 3.34 that the rate of hardening of curve with Eq. (3.13) does not always decrease with plastic strain unlike to the fitted curve. The isotropic yield stress versus plastic strain curves at different strain rates generated from static isotropic yield stress versus plastic strain curve using Eq. (3.14) and the flow stress versus plastic strain curves using Eq. (3.6) from parameters listed in Tables 3.4 (4 kinematic hardening term), 3.6, 3.7 and 3.9 are shown in Figs. 3.35 and 3.36 respectively.

Generated flow stress versus true plastic strain curves using Eqs. (3.6), (3.14) and (3.15) are compared to that from Walker (2012) in Fig. 3.36. Similar to material H, the differences between the generated curves by Walker (2012) and Eq. (3.6) are not big even though the yield plateau length varies with strain rate (Walker 2012) while it is taken to be constant at a plastic strain of 0.13 for curves generated with Eqs. (3.6), (3.14) and (3.15).

3.5 Validation of Calibrated and Generated Material Properties

Round specimens of material G and H of 14mm in diameter with a tapered profile were tested for different strain rates under monotonic tension by Chen (2010) and cyclic loading by Walker (2012). One set of cyclic loading tests consisted of specimens cyclically loaded at decreasing engineering strain ranges of $\pm 2\%$ and $\pm 0.5\%$ for 10 cycles at each range and then pulled to fracture. These tests were performed at strain rates of 0.0001 s^{-1} , 0.001 s^{-1} , 0.01 s^{-1} and 0.1 s^{-1} . Monotonic tension tests by Chen (2010) were carried out at a constant strain rates ranging from 10^{-4} s^{-1} to 1.0 s^{-1} . The half gauge length finite element model by Walker (2012) shown in Fig. 3.37 is being used to carry out the numerical simulation of the tests with kinematic hardening parameters (4 back stress terms) in Table 3.4 and generated isotropic yield stress versus true plastic strain curves in Figs. 3.26 (material H) and 3.35 (material G).

Comparisons of test and predicted engineering stress versus engineering strain curves at different strain rates for cyclic tests by Walker (2012) are shown in Fig. 3.38 to 3.41 for material H and Fig 3.42 to 3.45 for material G. Overall there is a good agreement between the test and predicted curves except at the end of tests for the strain rate of 0.1 s^{-1} where the numerical simulations predicted a higher stress. This is due to adiabatic heating of the specimen and the reduction in the yield stress with increase in the temperature that are not accounted for in the numerical simulations.

Comparisons of test and predicted engineering stress versus cross-section ratio curves at different strain rates for monotonic tension tests by Chen (2010) are shown in Fig. 3.46 to 3.50 for material H and Fig. 3.51 to 3.55 for material G. There is a good agreement between tests and predicted curves at strain rates of 10^{-3} s^{-1} and 10^{-2} s^{-1} . Numerical simulations slightly over-predicted the stress after the peak load at the strain rate of 10^{-4} s^{-1} and significantly more for strain rates of 0.1 s^{-1} and 1.0 s^{-1} . Walker (2012) postulated that the test stress and cross section area ratio curves at the strain rate of 10^{-4} s^{-1} is lower due to slight misplacement of the

diametral extensometer in the tests, while the lower test curves at the strain rate of 0.1 s^{-1} and 1.0 s^{-1} are attributed to adiabatic heating. The over-prediction by the numerical simulations is higher for strain rate of 1.0 s^{-1} than 0.1 s^{-1} , which corresponds to a larger temperature increase for 1.0 s^{-1} rate tests.

Table 3.1 Parameters for generating monotonic true flow stress versus true plastic strain curves at different strain rates (Walker 2012)

Material	Strain rate (s ⁻¹)	σ_t^y (MPa)	σ_1 (MPa)	ε_c	d	ε_t^o	True stress at a true plastic strain of 5.0 (MPa)
Material G	0.00005	353	412	0.229	0.691	0.013	765
	0.0001	354	413	0.215	0.716	0.013	767
	0.001	360	414	0.223	0.693	0.014	775
	0.01	382	402	0.254	0.625	0.018	785
	0.1	399	399	0.232	0.667	0.021	798
	1	420	395	0.214	0.702	0.024	815
Material H	0.00005	383	398	0.236	0.66	0.006	781
	0.0001	383	399	0.231	0.665	0.006	782
	0.001	388	398	0.197	0.716	0.006	786
	0.01	397	397	0.218	0.678	0.006	794
	0.1	416	392	0.196	0.722	0.0062	809
	1	439	395	0.211	0.689	0.012	834

Table 3.2 Kinematic hardening parameters from Walker (2012)

	C_1	γ_1	C_2	γ_2
Material G	19852	175.2	1997	6.17
Material H	27427	199.3	1383	5.35

Table 3.3 Data points of isotropic yield stress (MPa) at rate of 0.00005 s^{-1} from Walker (2012)

used for calibration of kinematic hardening terms

Isotropic yield stress (MPa)	$\epsilon_t^p=0.05$	$\epsilon_t^p=0.10$	$\epsilon_t^p=0.20$	$\epsilon_t^p=0.30$	$\epsilon_t^p=0.60$	$\epsilon_t^p=0.75$
Material H	351	373	379	376	375	377
Material G	302	319	317	313	316	319

Table 3.4 Calibrated kinematic hardening parameters for material G and H

Material G			Material H		
Parameters	Number of Back Stress Terms		Parameters	Number of Back Stress Terms	
	3	4		3	4
C_1	19852	19852	C_1	27427	27427
γ_1	175.2	175.2	γ_1	199.3	199.3
C_2	1666	1874	C_2	818	692
γ_2	5.86	6.71	γ_2	6.62	5.35
C_3	2127	222.7	C_3	872	42976
γ_3	53.2	9.73	γ_3	6.53	2466
C_4	----	24610	C_4	----	1016
γ_4		1222	γ_4		9.26

Table 3.5 Material H isotropic yield stress at various plastic strains for different strain rates

Plastic strain	0	0.006	0.1	0.2	0.3	0.6	0.75
$\dot{\epsilon} = 0.00005$	383.4	260.0	342.8	353.8	359.5	372.8	377.1
$\dot{\epsilon} = 0.0001$	383.2	259.8	344.7	356.3	362.0	374.8	378.9
$\dot{\epsilon} = 0.001$	388.4	265.0	355.3	371.2	377.2	386.0	388.3
$\dot{\epsilon} = 0.01$	396.6	273.2	361.6	373.9	379.3	390.0	393.4
$\dot{\epsilon} = 0.1$	416.2	292.8	377.7	393.4	399.4	408.2	410.4
$\dot{\epsilon} = 1$	438.7	315.2	396.8	413.4	419.3	430.9	433.9

Table 3.6 Calibrated values of constants I and J for materials G and H

	I	J
Material G	4684	5.04
Material H	10573	5.49

Table 3.7 Calibrated values of A and B for material G and H

	A	B
Material G	1.13	13.1
Material H	0.39	8.00

Table 3.8 Material H isotropic yield stress at various plastic strains for different strain rates using Eq. (3.13)

Plastic strain	0	0.006	0.1	0.2	0.3	0.6	0.75
$\dot{\epsilon} = 0.00005$	383.4	260.0	342.8	353.8	359.5	372.8	377.1
$\dot{\epsilon} = 0.0001$	384.8	261.4	344.4	355.3	361.0	374.3	378.6
$\dot{\epsilon} = 0.001$	391.1	267.7	351.4	362.0	367.5	380.8	385.2
$\dot{\epsilon} = 0.01$	400.6	277.1	362.2	372.1	377.4	390.7	395.3
$\dot{\epsilon} = 0.1$	415.0	291.5	378.5	387.6	392.4	405.9	410.5
$\dot{\epsilon} = 1$	436.9	313.5	403.2	411.1	415.3	428.9	433.7

Table 3.9 Parameters for Eq. (3.15) for static isotropic stress curve for materials G and H

	Material G	Material H
σ_s^{yp}	194.1	249.4
σ_1	125.9	125.6
a	5.40	4.50
b	0.54	0.53
ϵ_0^t	0.013	0.006

Table 3.10 Material G isotropic yield stress at various plastic strains for different strain rates

Plastic strain	0	0.013	0.1	0.2	0.3	0.6	0.75
$\dot{\epsilon} = 0.00005$	352.9	226.2	318.9	317.5	313.5	315.9	319.1
$\dot{\epsilon} = 0.0001$	353.8	227.1	320.6	322.2	319.0	320.6	323.2
$\dot{\epsilon} = 0.001$	360.1	233.4	329.1	329.1	325.2	326.8	329.7
$\dot{\epsilon} = 0.01$	382.3	255.7	345.7	338.2	330.8	331.3	335.1
$\dot{\epsilon} = 0.1$	399.4	272.7	355.9	354.1	348.7	349.0	351.9
$\dot{\epsilon} = 1$	420.0	293.4	369.2	373.2	369.6	369.5	371.8

Table 3.11 Material G isotropic yield stress at various plastic strains for different strain rates using Eq. (3.13)

Plastic strain	0	0.013	0.1	0.2	0.3	0.6	0.75
$\dot{\epsilon} = 0.00005$	352.9	226.2	318.9	317.5	313.5	315.9	319.1
$\dot{\epsilon} = 0.0001$	354.5	227.8	320.4	318.8	314.7	317.0	320.3
$\dot{\epsilon} = 0.001$	361.7	235.0	327.2	324.4	320.0	322.4	325.8
$\dot{\epsilon} = 0.01$	373.1	246.4	338.0	333.2	328.3	330.8	334.3
$\dot{\epsilon} = 0.1$	391.0	264.4	354.9	347.1	341.4	344.1	347.8
$\dot{\epsilon} = 1$	419.4	292.8	381.7	369.2	362.2	365.2	369.2

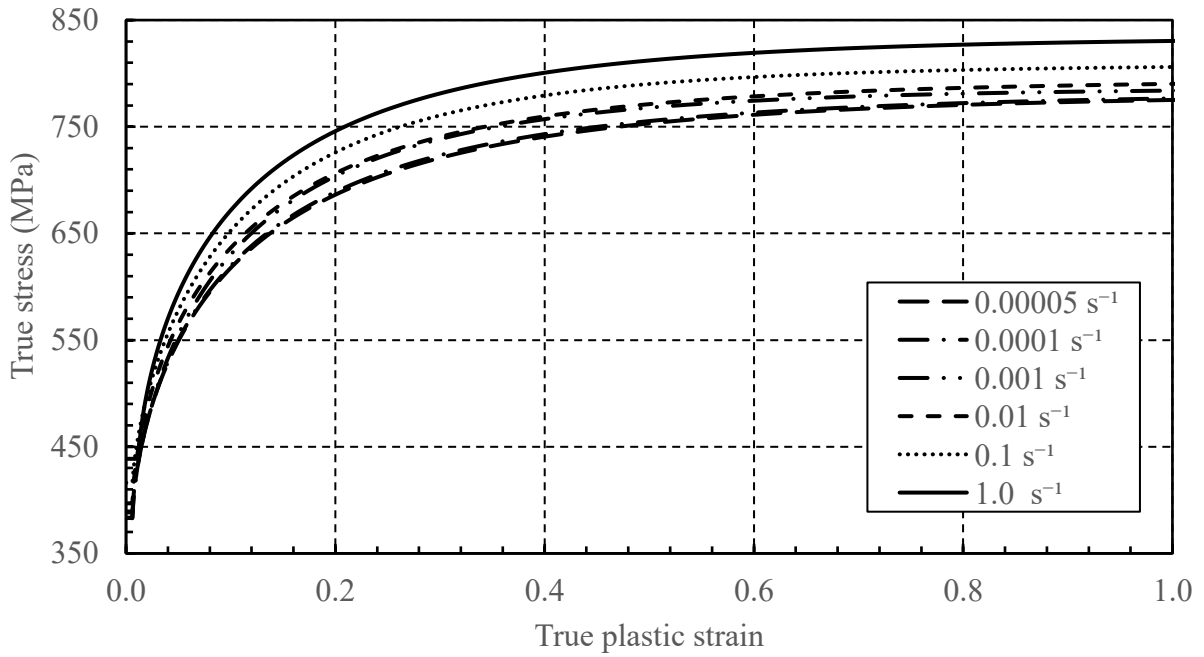


Figure 3.1 True flow stress versus true plastic strain curves at various strain rates for material H (Walker 2012)

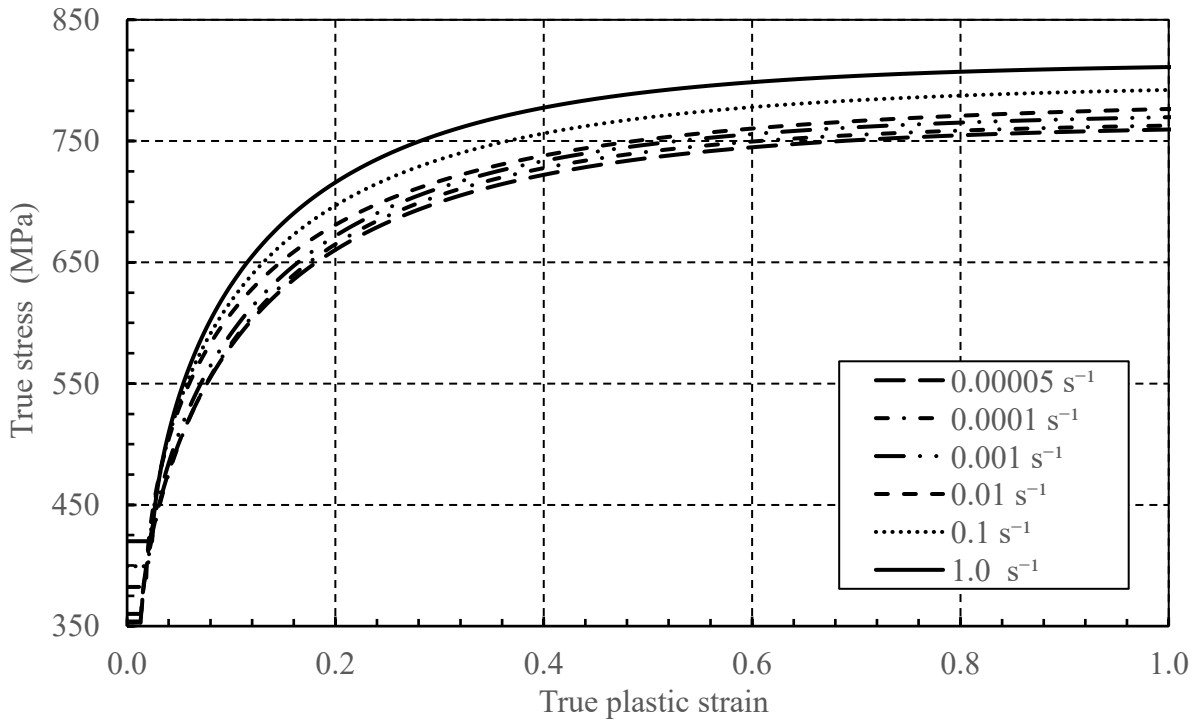


Figure 3.2 True flow stress versus true plastic strain curves at various strain rates for material G (Walker 2012)

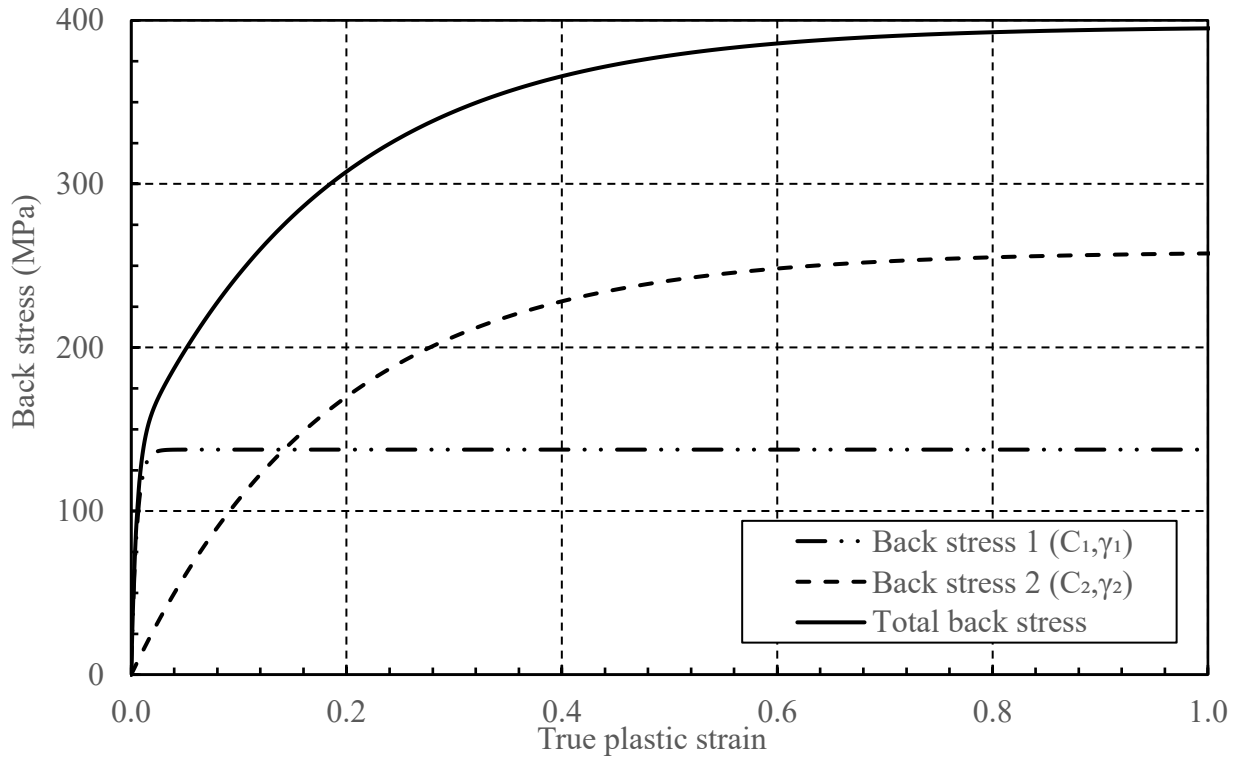


Figure 3.3 Back stress versus true plastic strain curves for material H (Walker 2012)

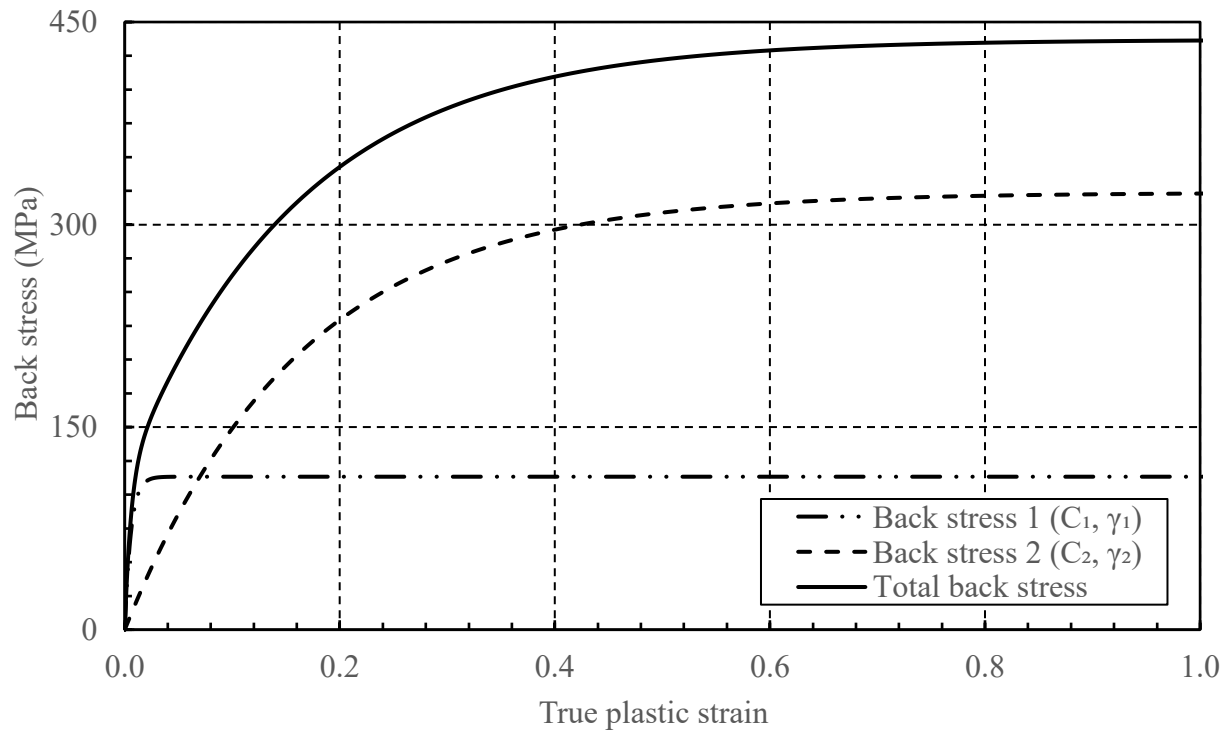


Figure 3.4 Back stress versus true plastic strain curves for material G (Walker 2012)

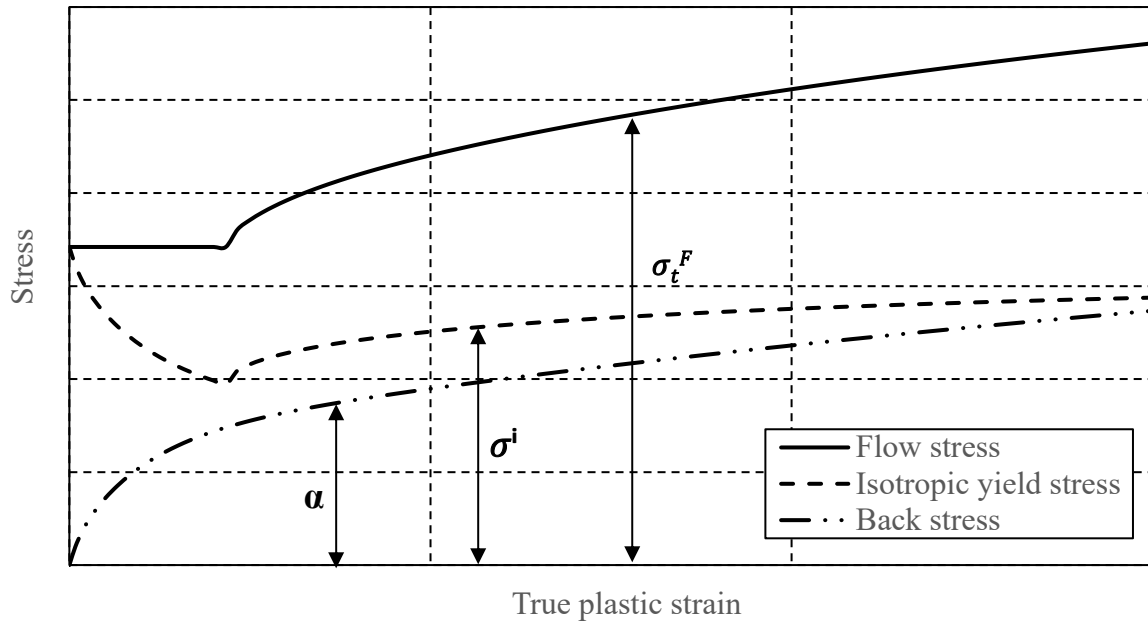


Figure 3.5 Relationship between true flow stress, isotropic yield stress and back stress

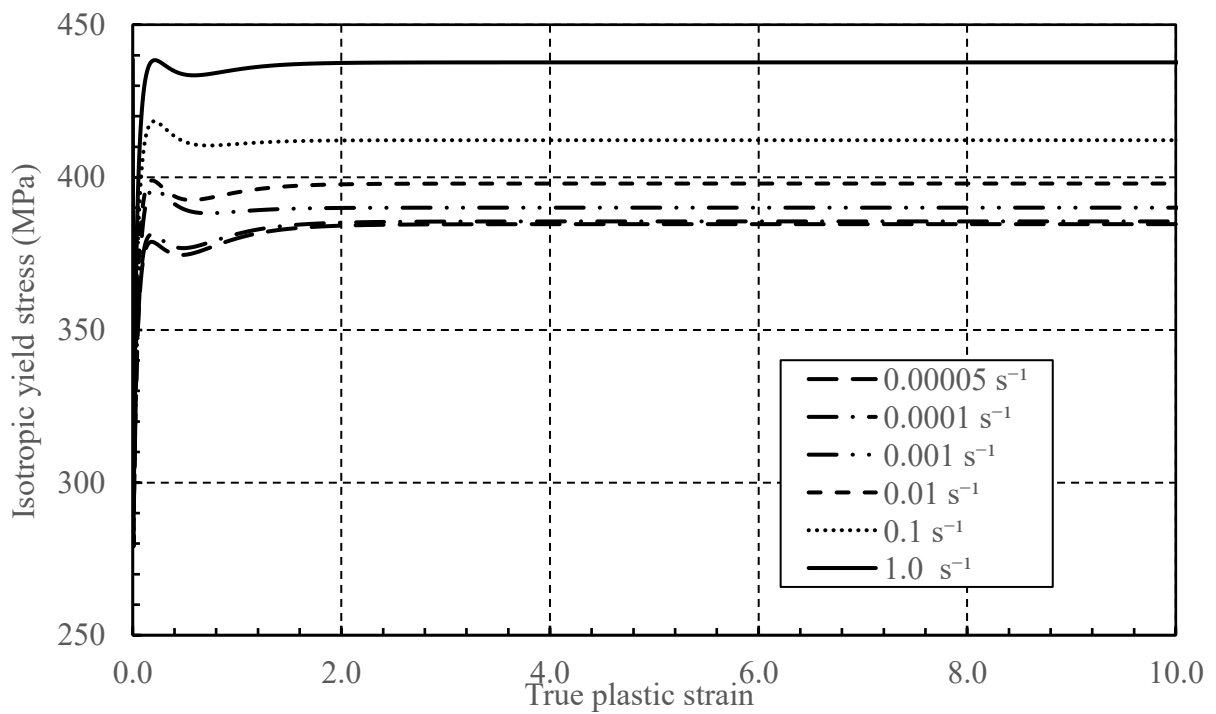


Figure 3.6 Isotropic yield stress versus true plastic strain curves at different strain rates for material H (Walker 2012)

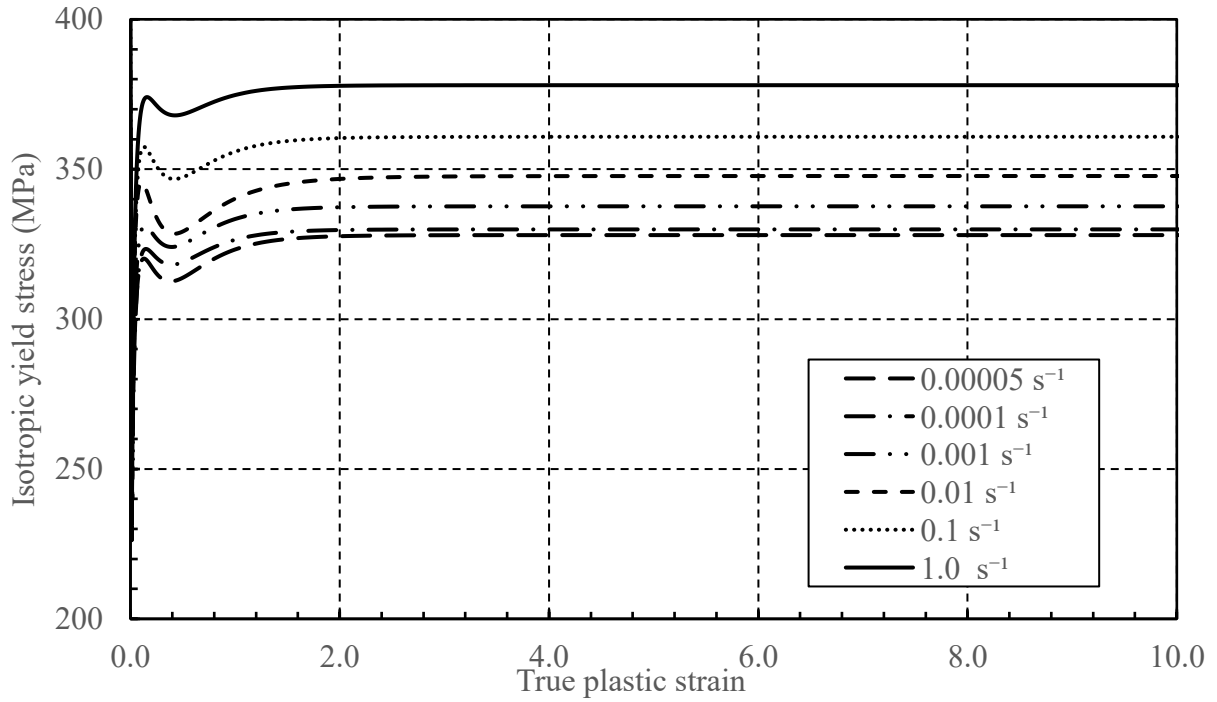


Figure 3.7 Isotropic yield stress versus true plastic strain curves at different strain rates for material G (Walker 2012)

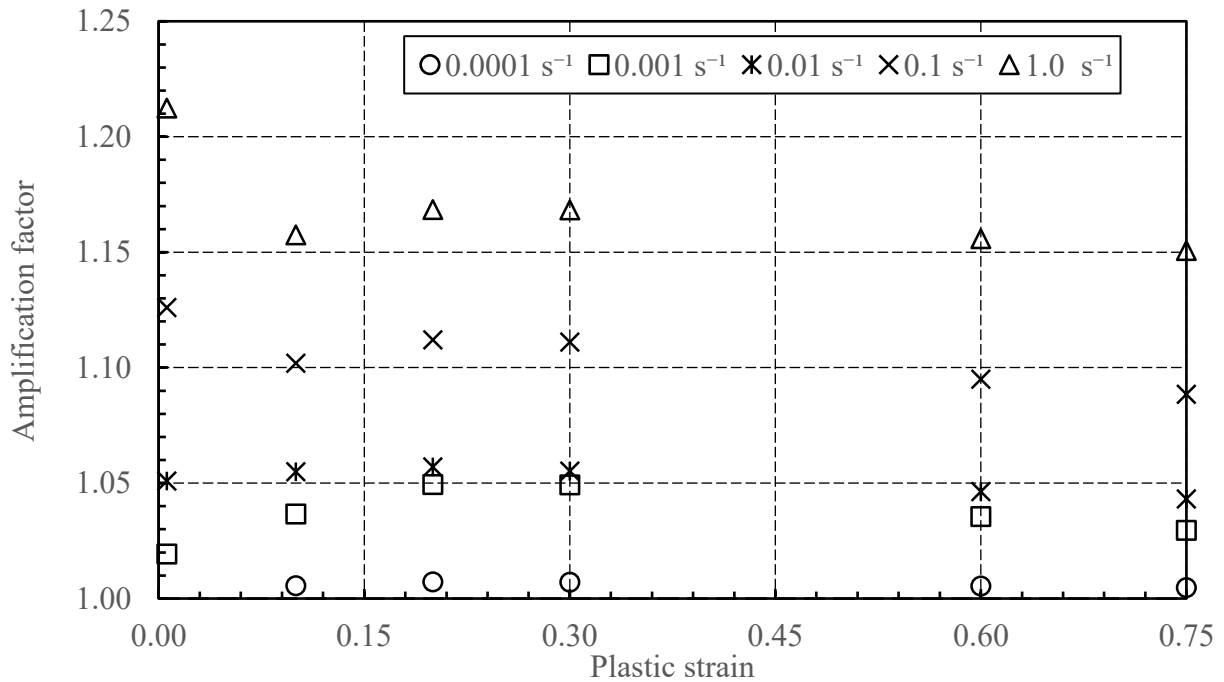


Figure 3.8 Isotropic yield stress amplification factors at different strain rates for material H from Walker (2012).

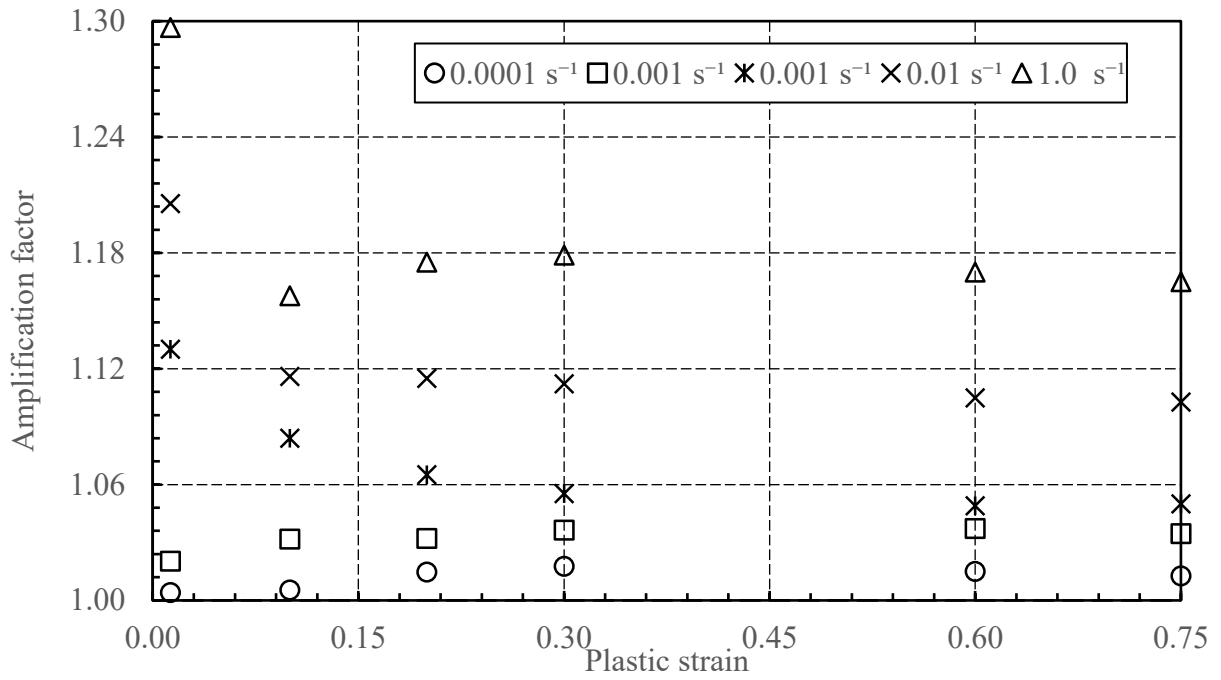


Figure 3.9 Isotropic yield stress amplification factors at different strain rates for material G from Walker (2012)

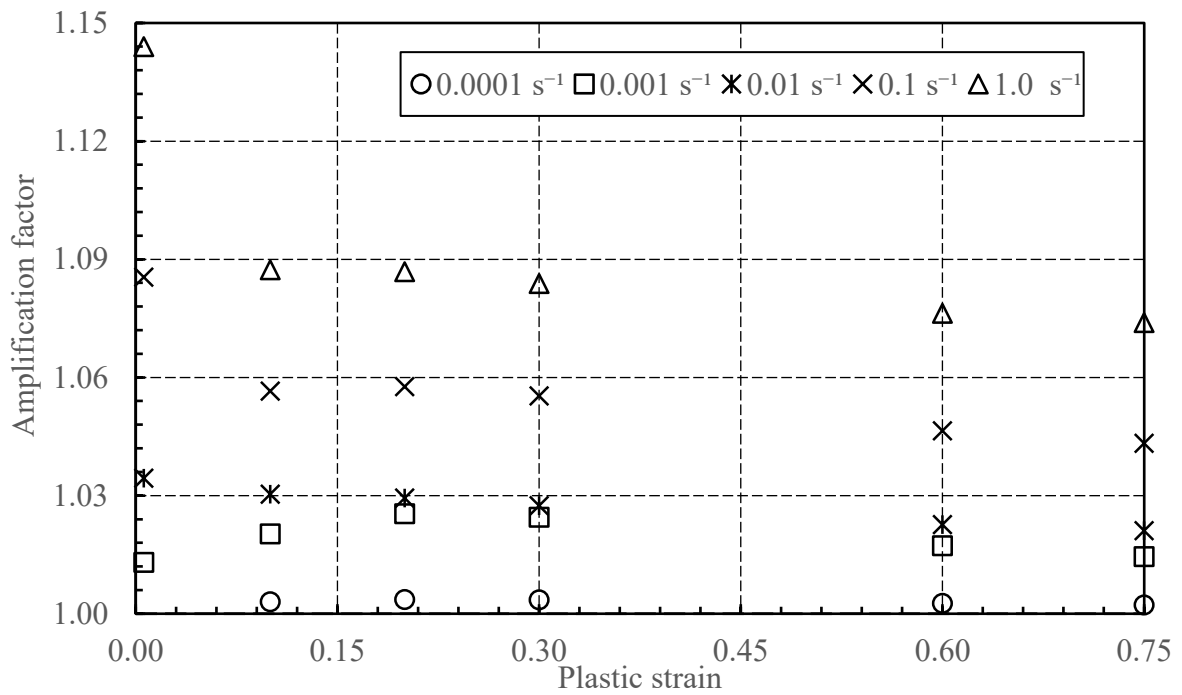


Figure 3.10 Flow stress amplification factors at different strain rates for material H from Walker (2012)

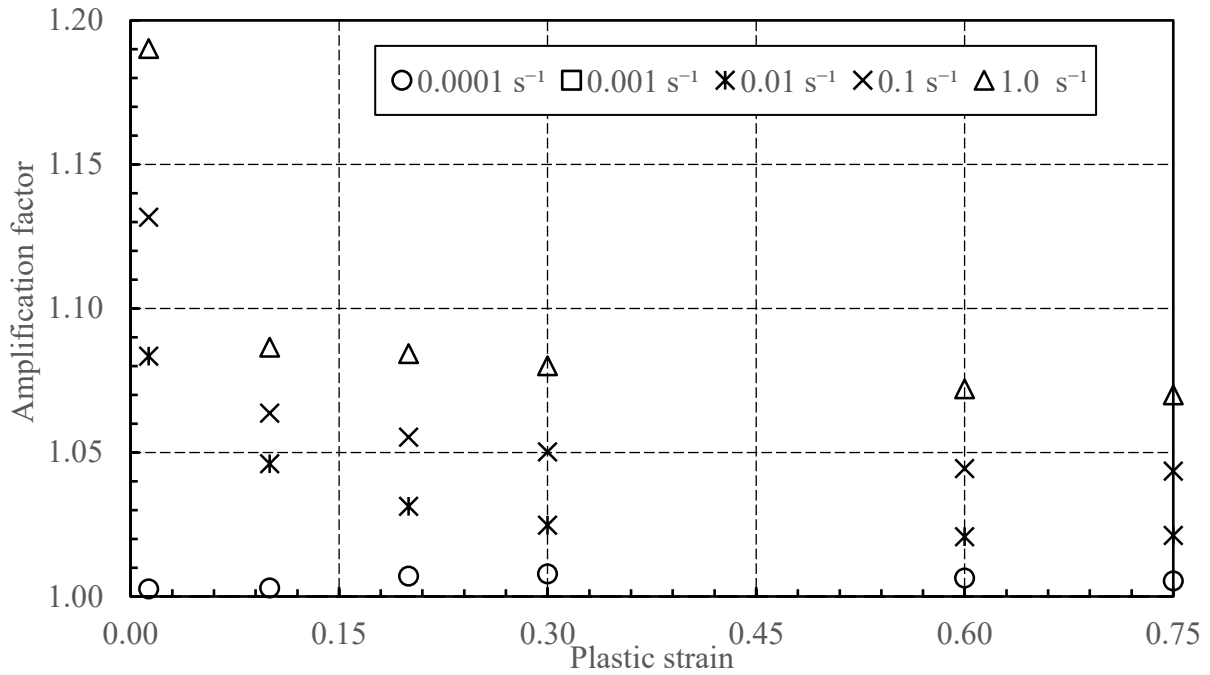


Figure 3.11 Flow stress amplification factors at different strain rates for material G from Walker (2012)

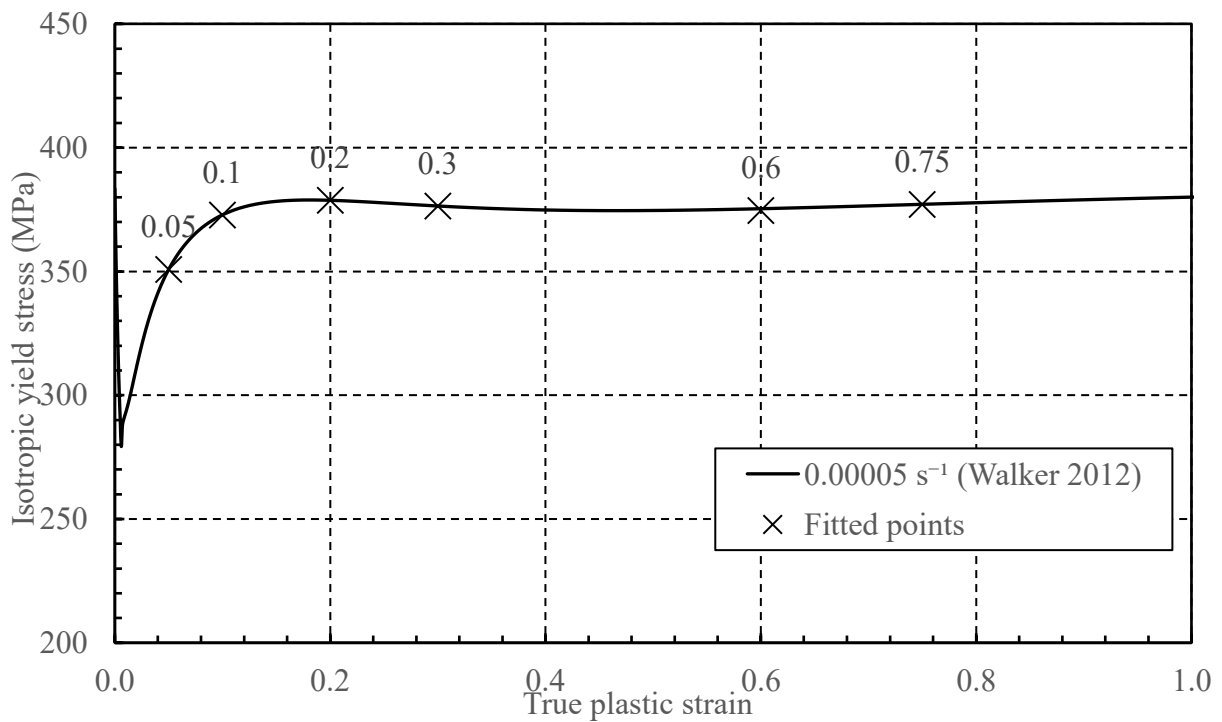


Figure 3.12 Isotropic yield stress versus true plastic strain at the strain rate of 0.00005 s⁻¹ for material H (Walker 2012)

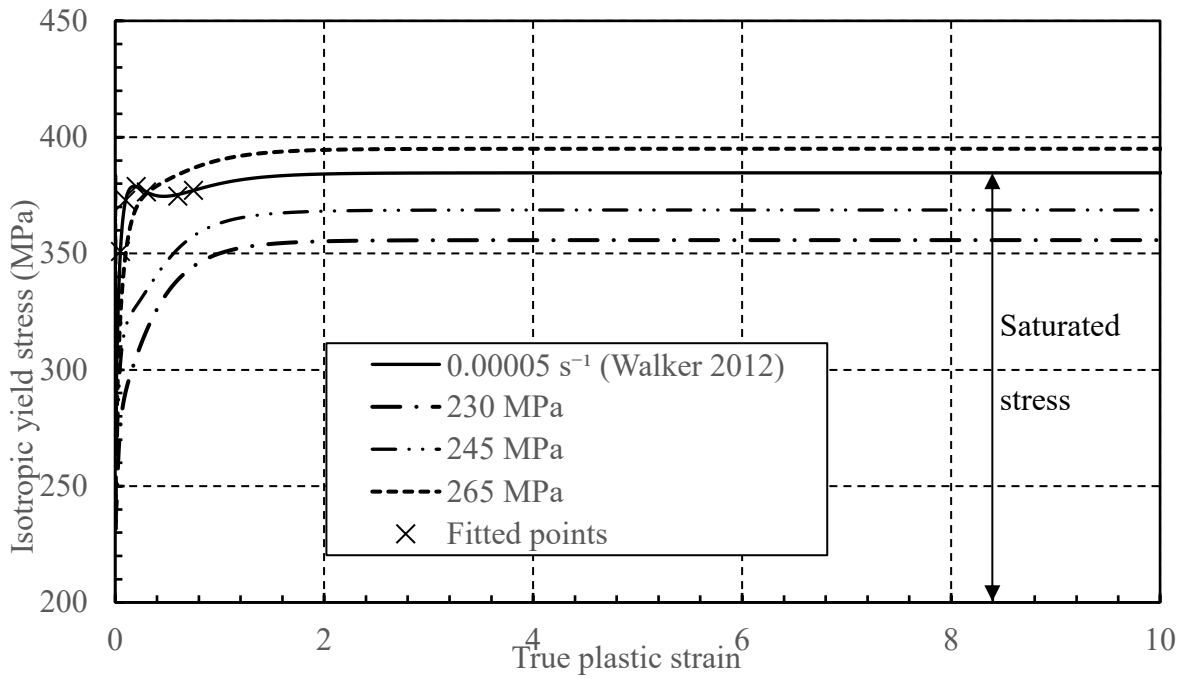


Figure 3.13 Isotropic yield stress versus true plastic strain curves at strain rate of 0.00005 s⁻¹ for different iterations for material H compared with that obtained from Walker (2012)

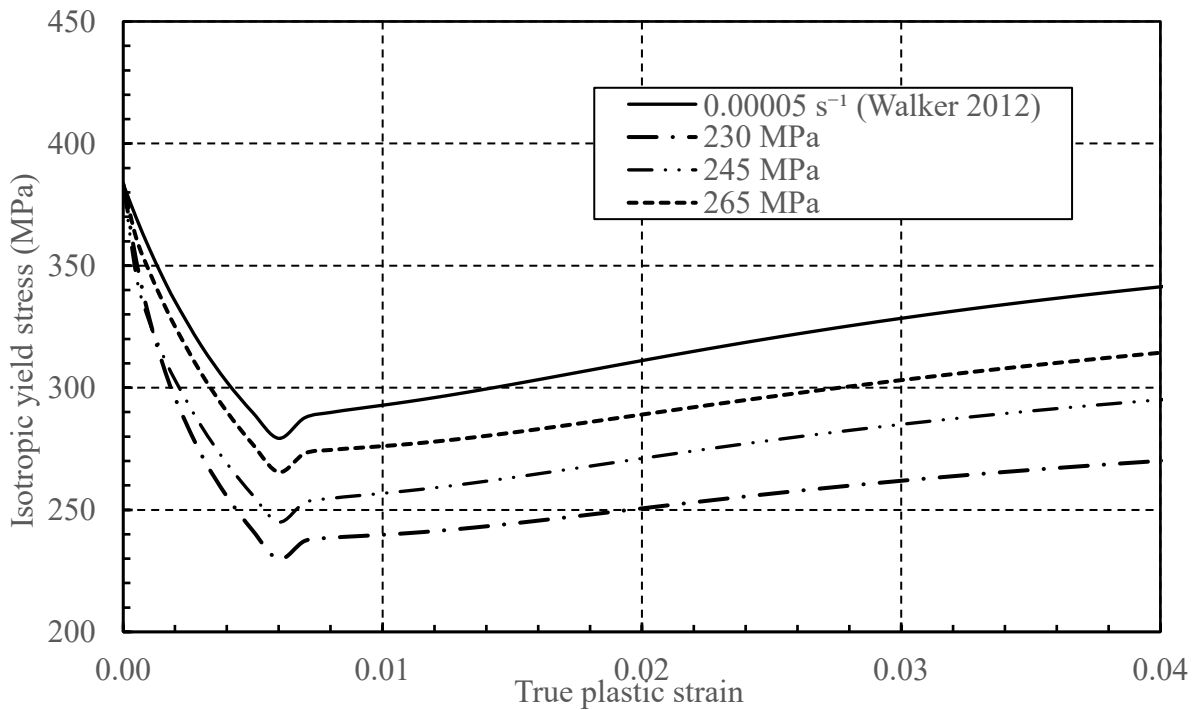


Figure 3.14 Isotropic yield stress-plastic strain curves at strain rate of 0.00005 s⁻¹ for different iteration for material H magnified near the end of yield plateau

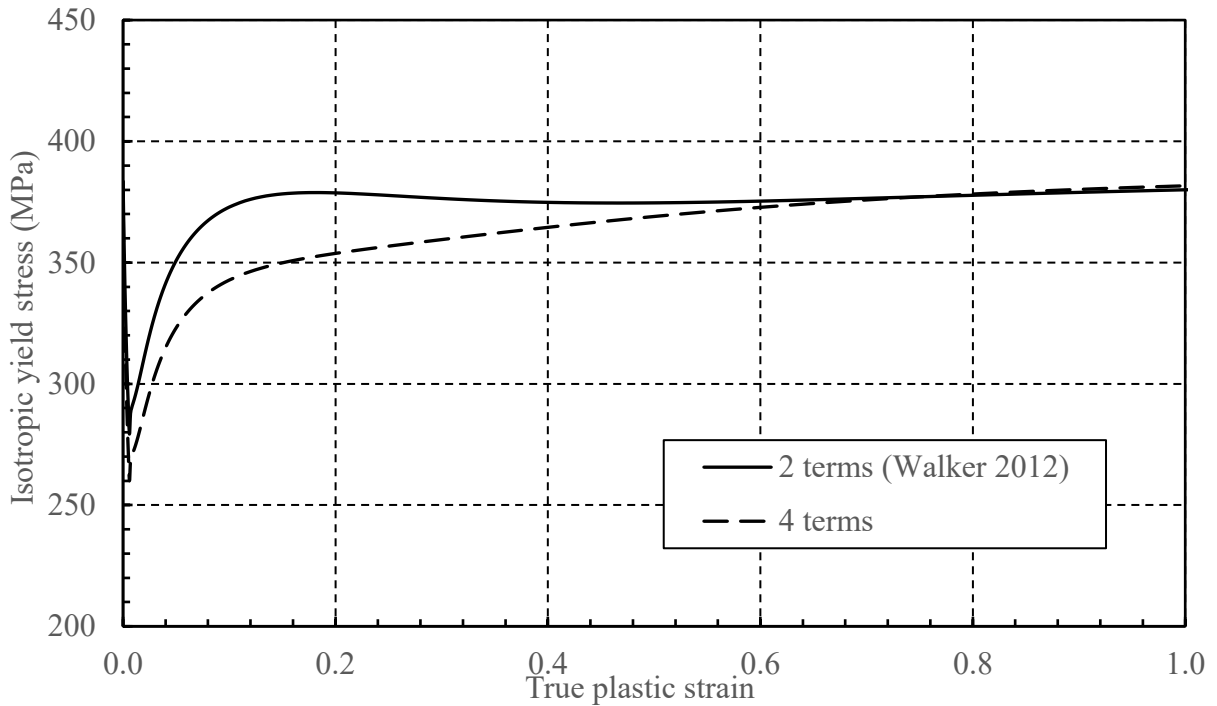


Figure 3.15 Comparisons between isotropic yield stress versus true plastic strain for 4 back stress terms and 2 back stress terms from Walker (2012) for material H at the strain rate of 0.00005 s^{-1}

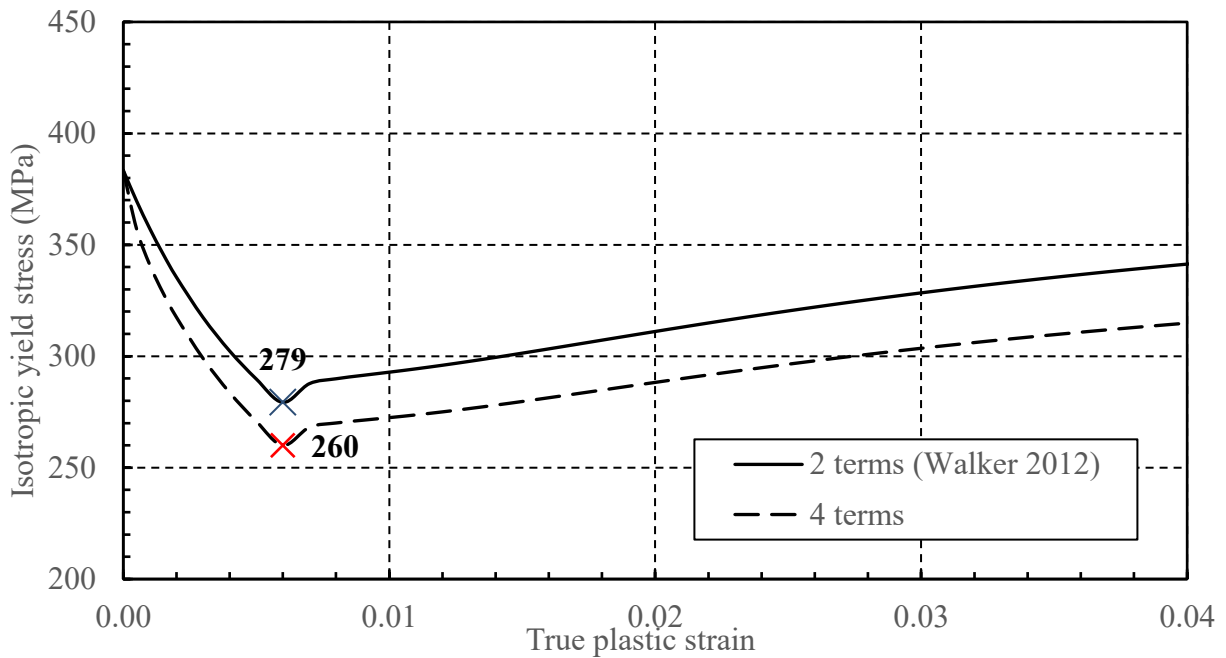


Figure 3.16 Comparisons between isotropic yield stress versus true plastic strain for 4 back stress terms and 2 back stress terms from Walker (2012) for material H at strain rate of 0.00005 s^{-1} (Fig. 3.15 magnified near the end of yield plateau)

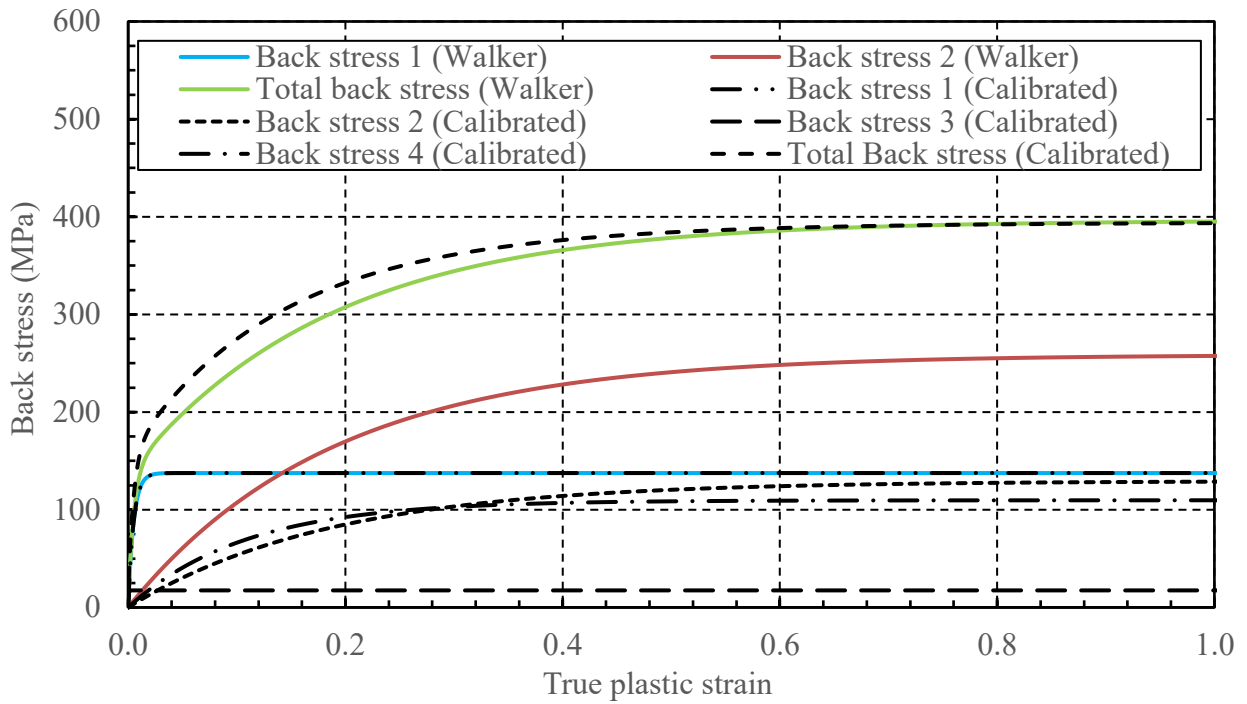


Figure 3.17 Comparisons between calibrated back stress (4 terms) versus plastic strain and back stress versus plastic strain curve from Walker (2012) for material H

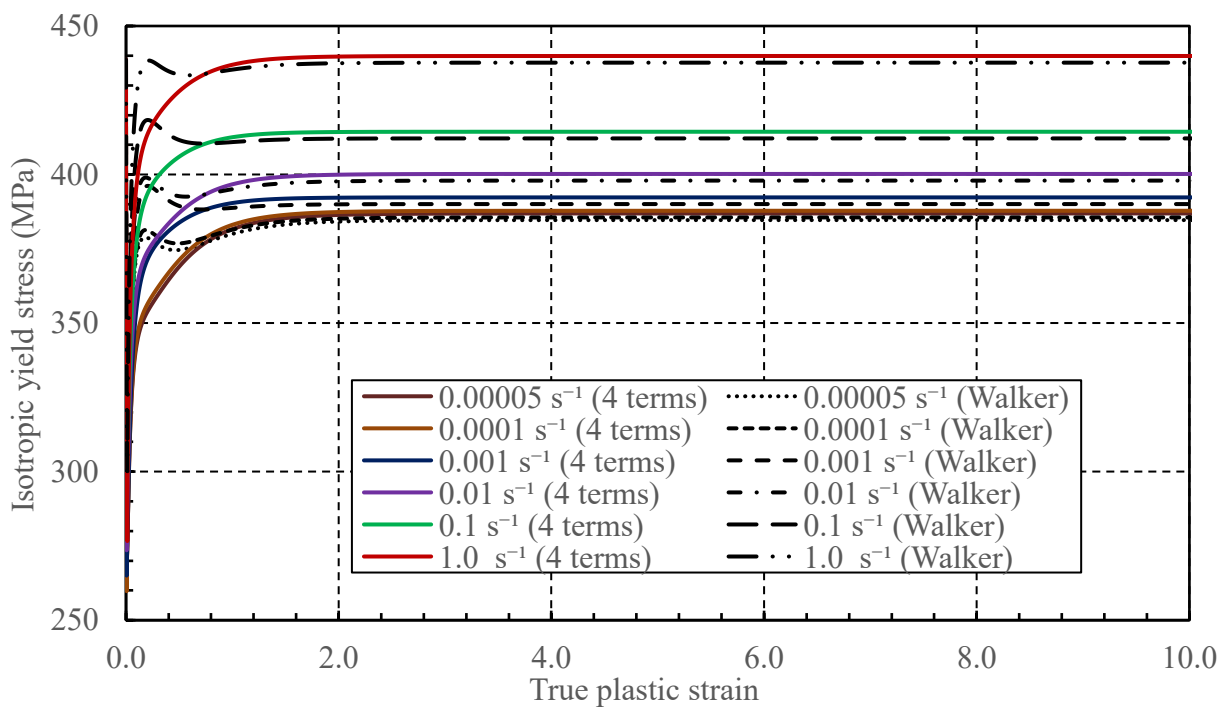


Figure 3.18 Isotropic yield stress versus true plastic strain curves for material H from Walker (2012) and from 4 kinematic hardening terms

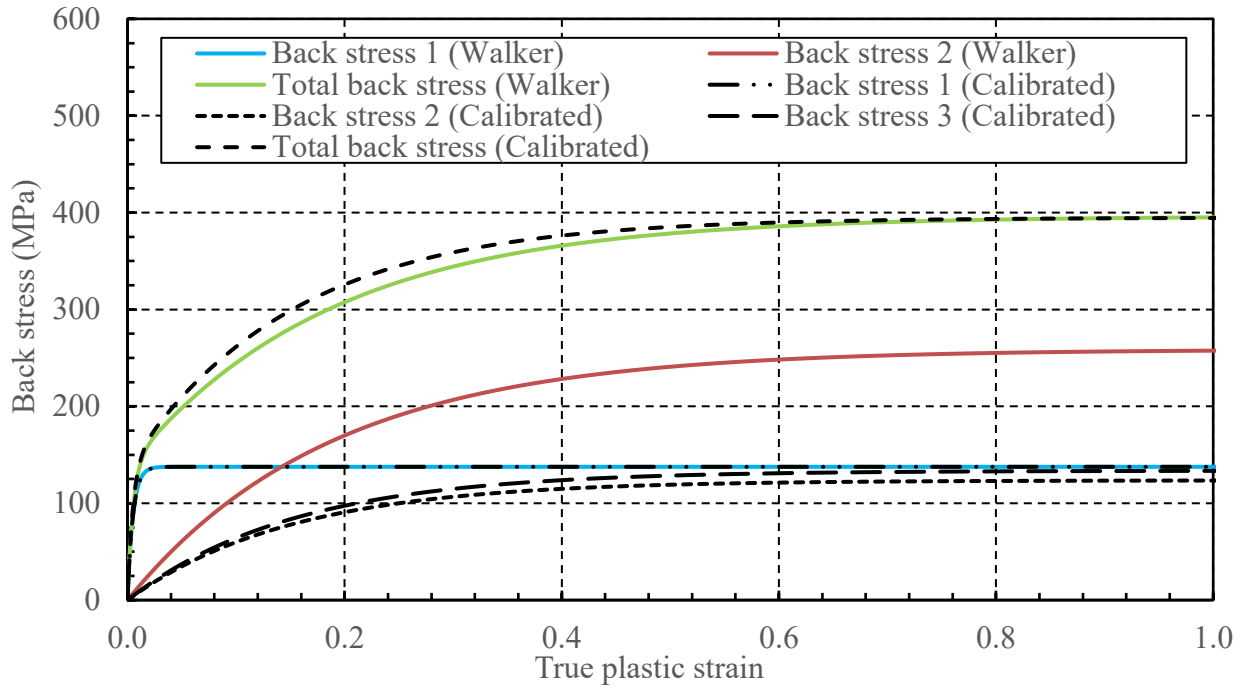


Figure 3.19 Comparisons of calibrated back stress (3 terms) versus plastic strain and back stress versus plastic strain curve from Walker (2012) for material H

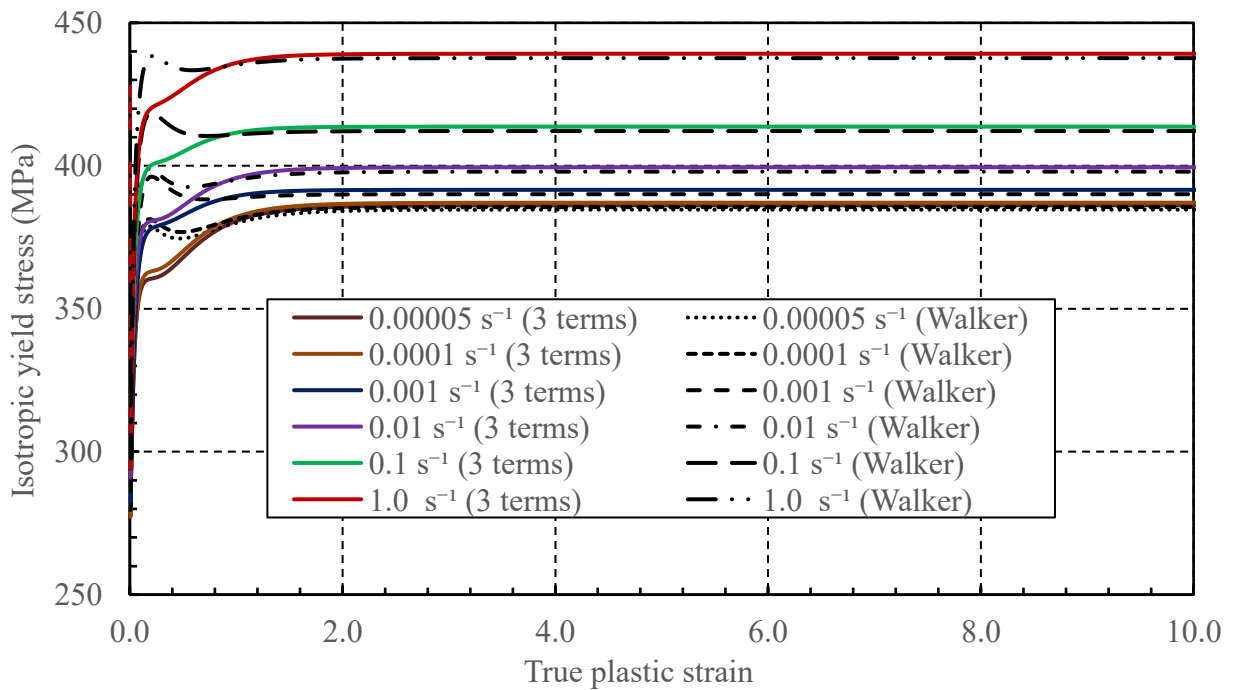


Figure 3.20 Isotropic yield stress versus true plastic strain curves for material H from Walker (2012) and from 3 kinematic hardening terms

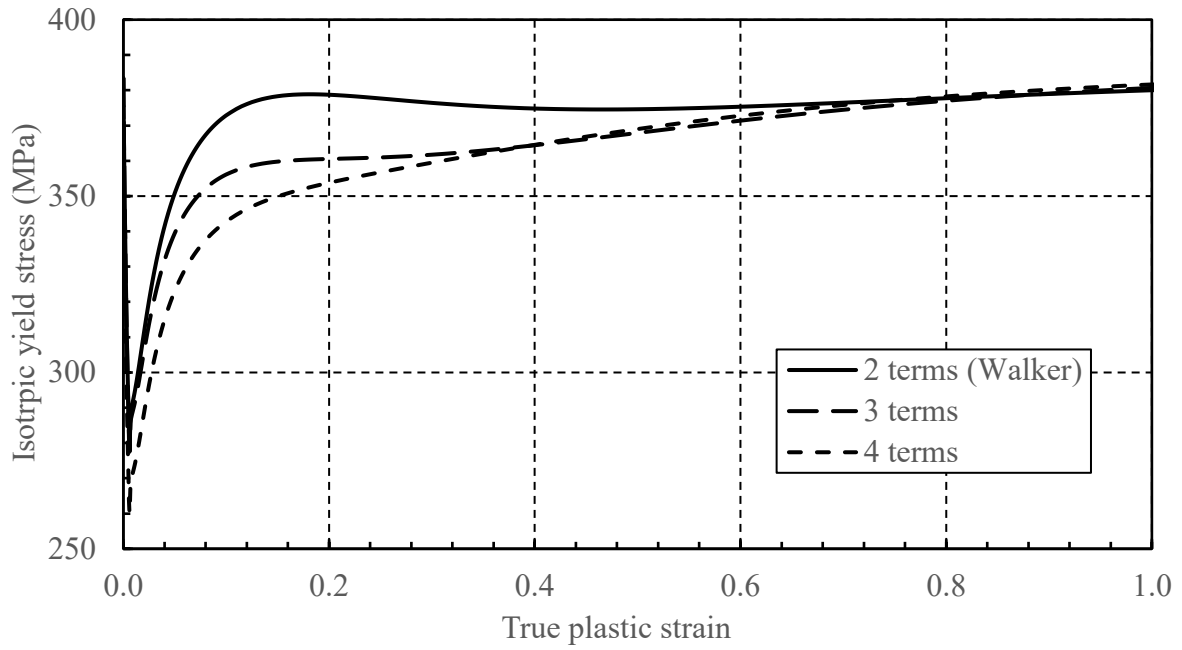


Figure 3.21 Comparisons of isotropic yield stress versus true plastic strain with different number of back stress terms for material H at a strain rate of 0.00005 s^{-1}

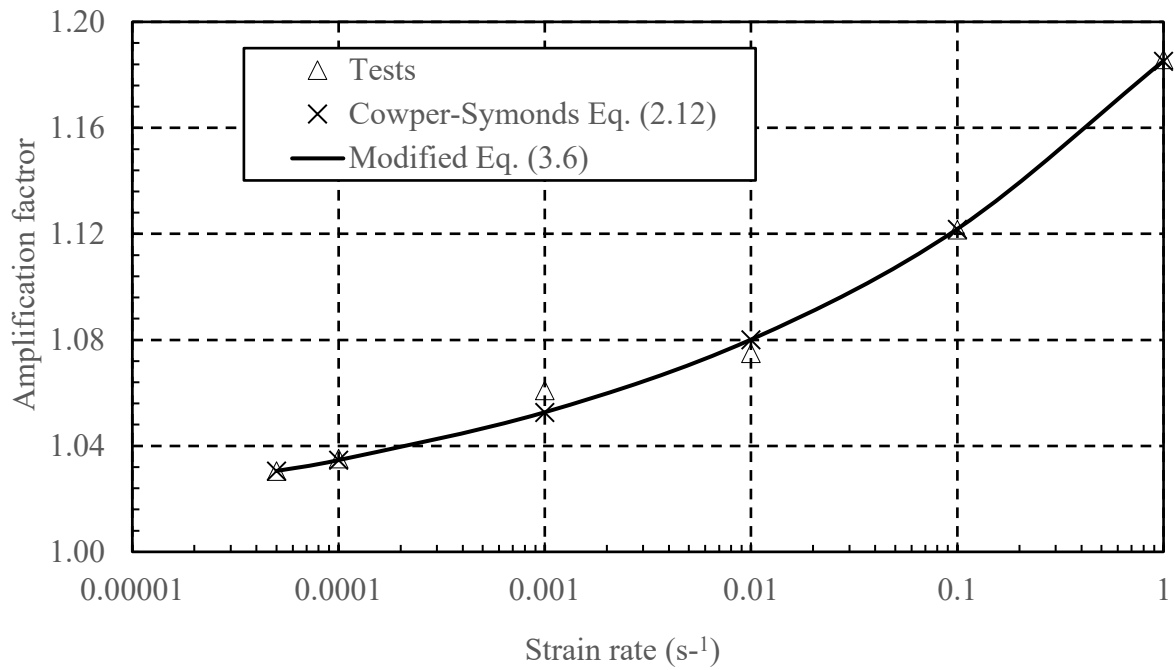


Figure 3.22 Amplification factor for isotropic yield stress at true plastic strain of 0.75 for material H

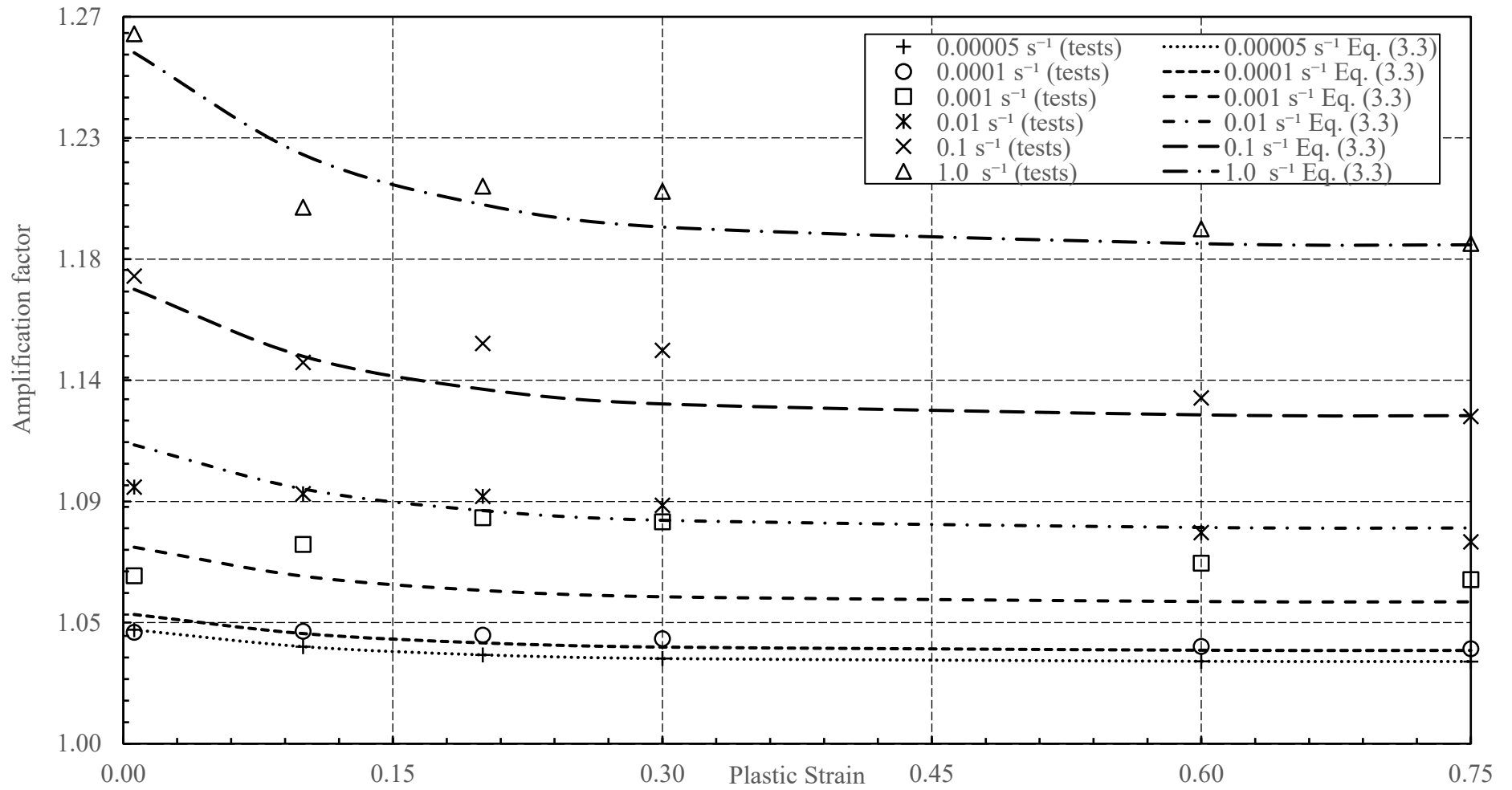


Figure 3.23 Amplification factors of isotropic yield stress calculated with Eq. (3.3) and tests for material H

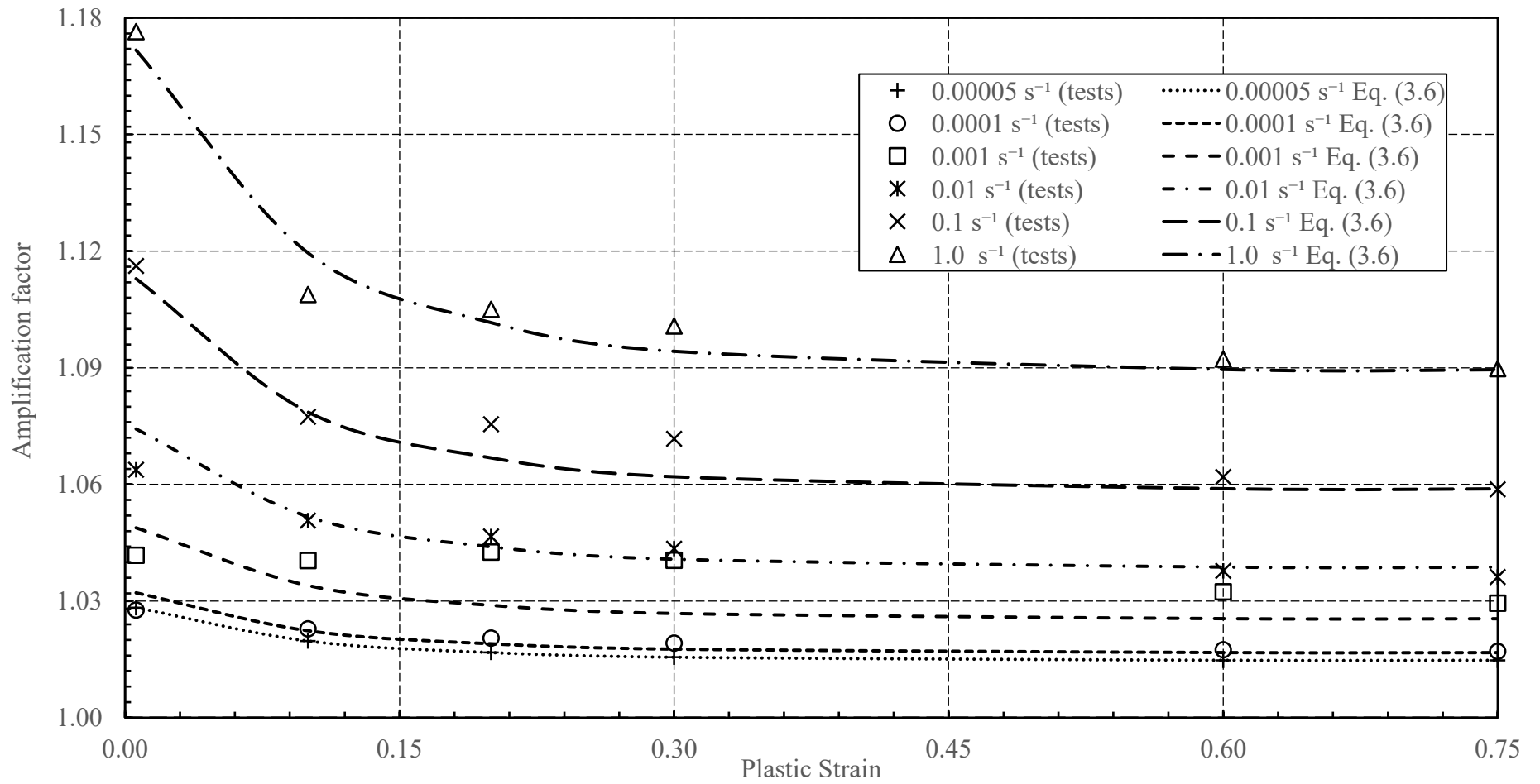


Figure 3.24 Amplification factor of flow stress calculated with Eq. (3.6) and tests for material H

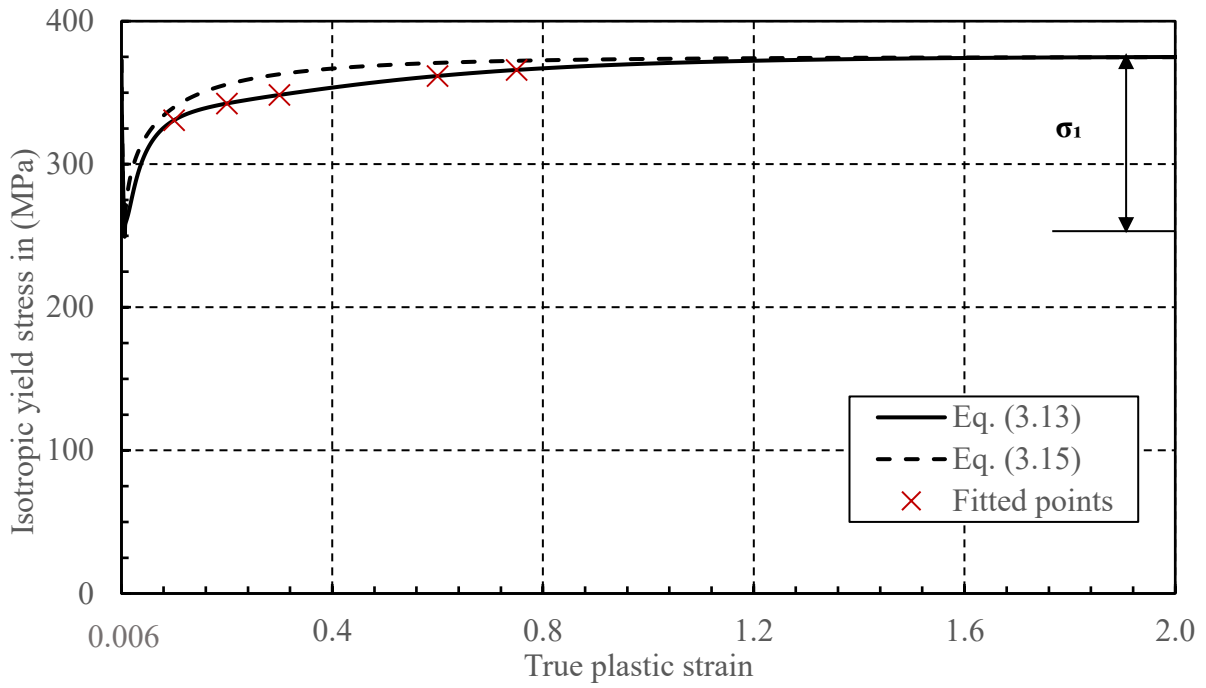


Figure 3.25 Generated static isotropic yield stress-true plastic strain curve for material H with Eqs. (3.13) and (3.15)

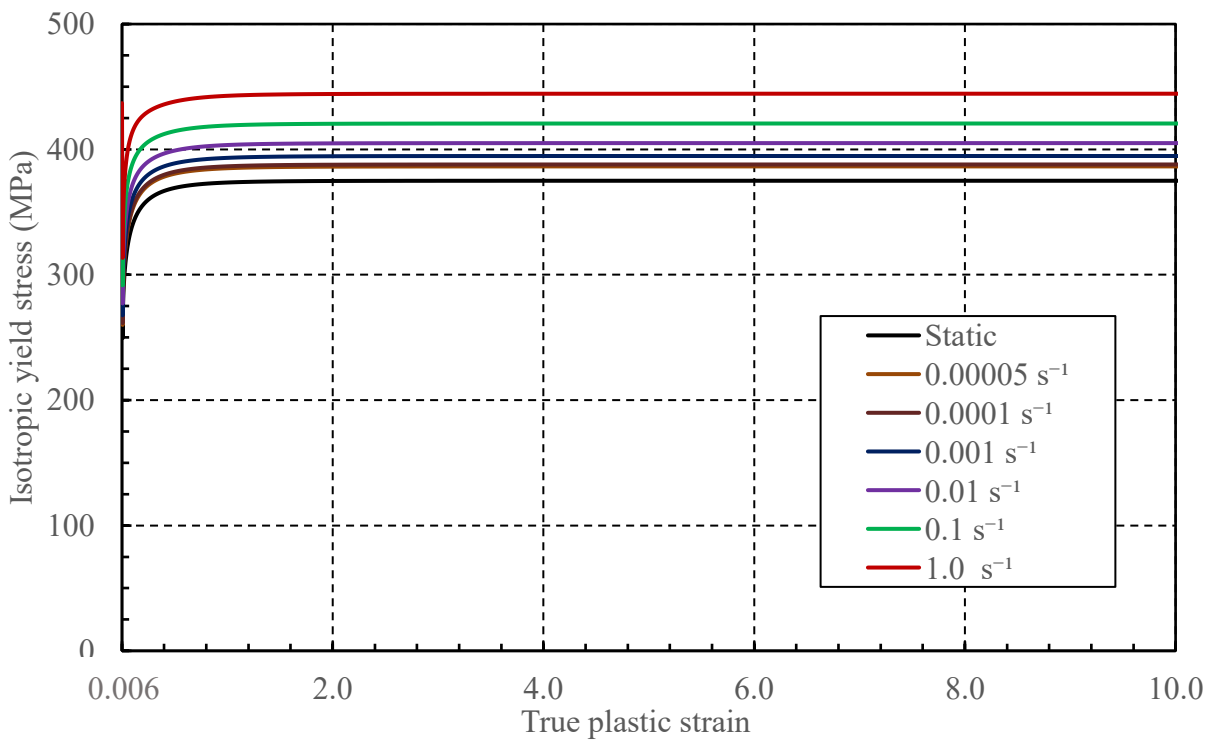


Figure 3.26 Generated isotropic yield stress versus true plastic strain curves for material H at different strain rates

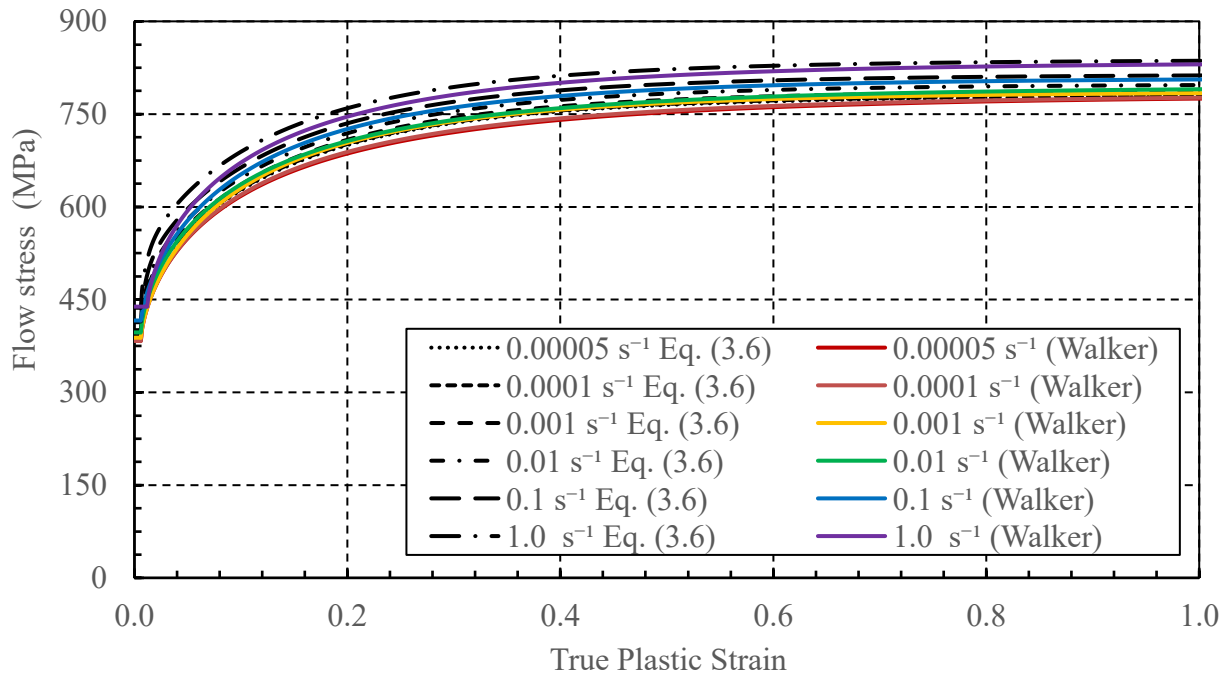


Figure 3.27 Comparisons of generated flow stress versus true plastic strain curve for material H at different strain rates by Walker (2012) and Eqs. (3.6, 3.14 and 3.15) with 4 kinematic hardening terms

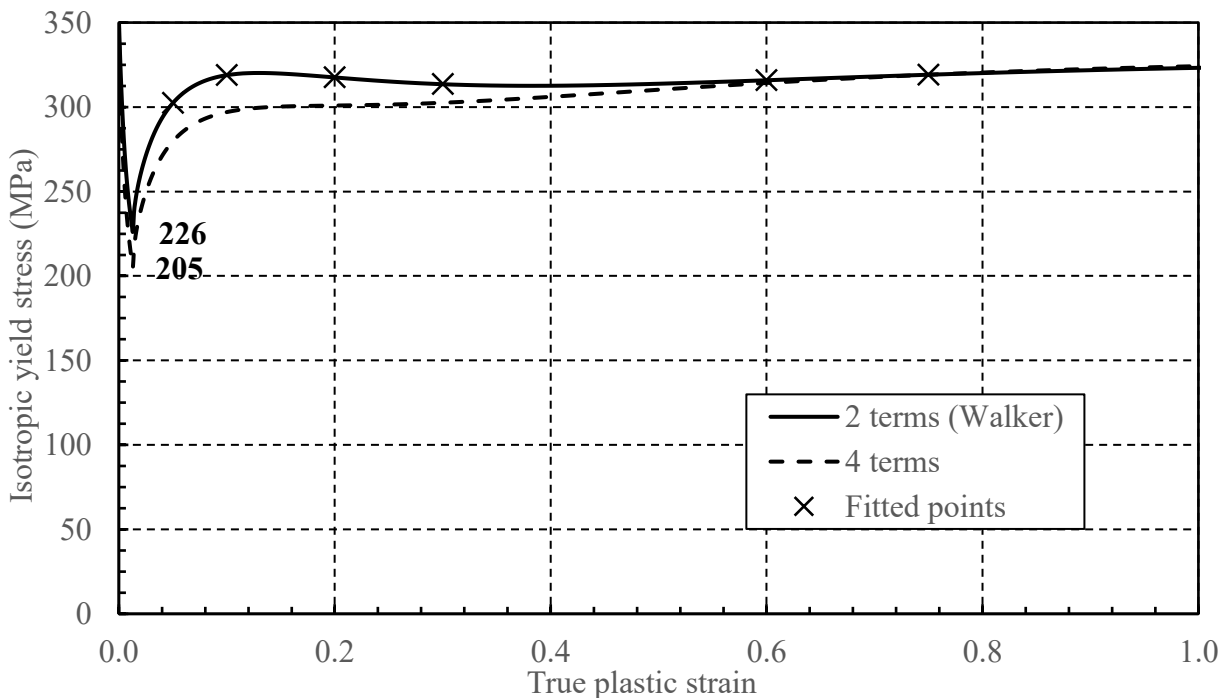


Figure 3.28 Comparisons between isotropic yield stress versus true plastic strain for 4 back stress terms and 2 back stress terms from Walker (2012) for material G at the strain rate of 0.00005 s^{-1}

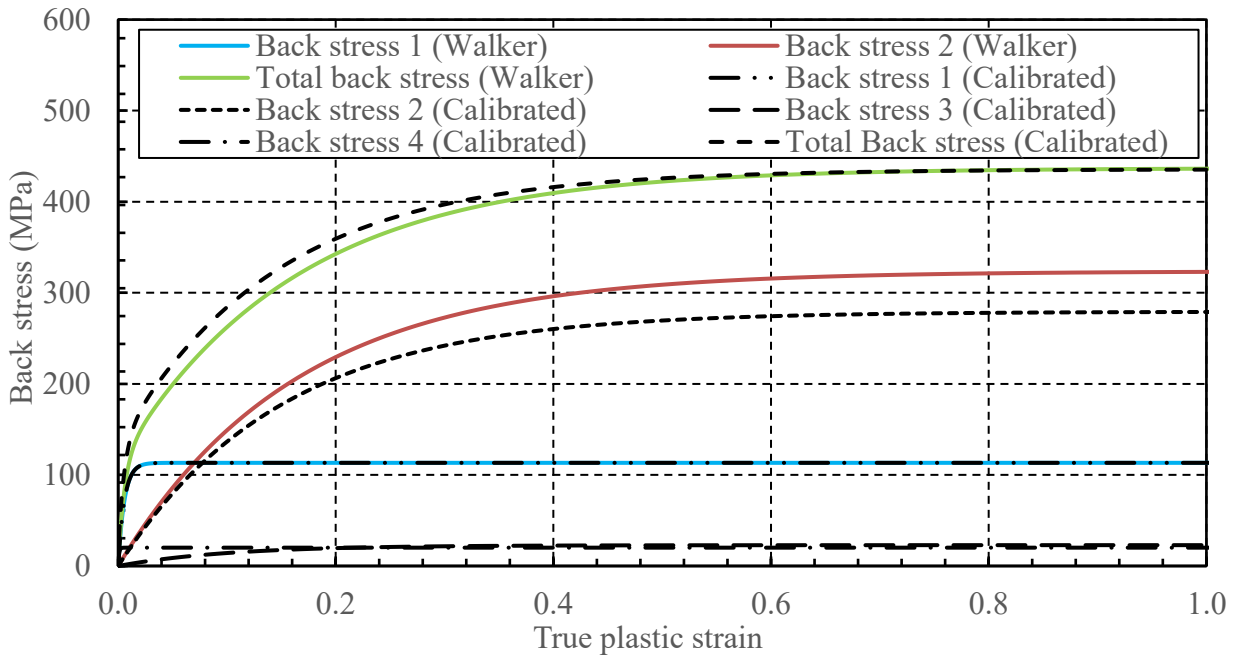


Figure 3.29 Comparisons between calibrated back stress (4 terms) versus plastic strain and back stress versus plastic strain curve from Walker (2012) for material G

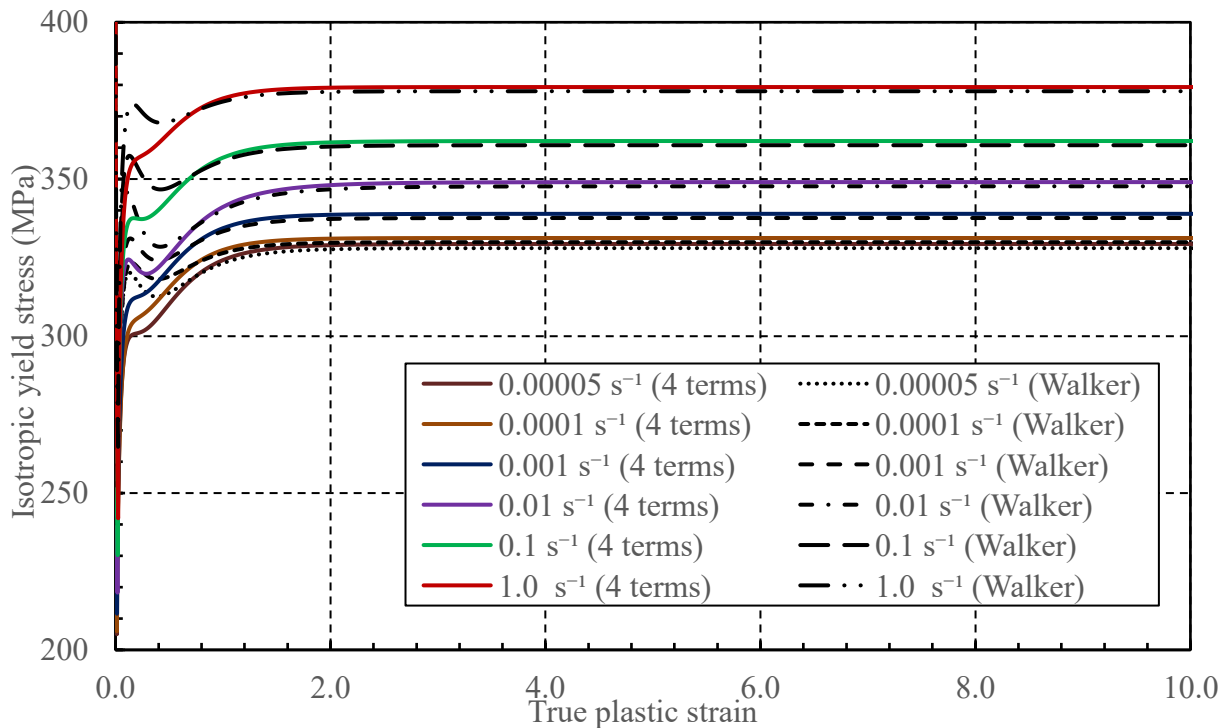


Figure 3.30 Isotropic yield stress versus true plastic strain curve for material G from Walker (2012) and from 4 kinematic hardening term

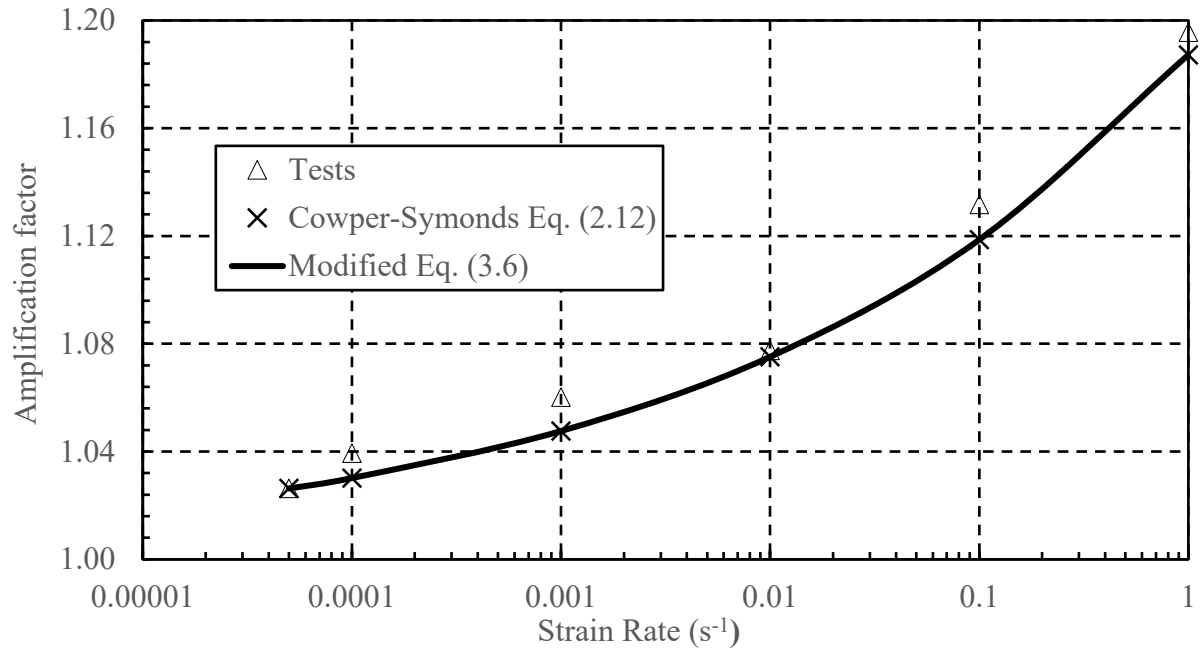


Figure 3.31 Amplification factor of isotropic yield stress at true plastic strain of 0.75 for material G

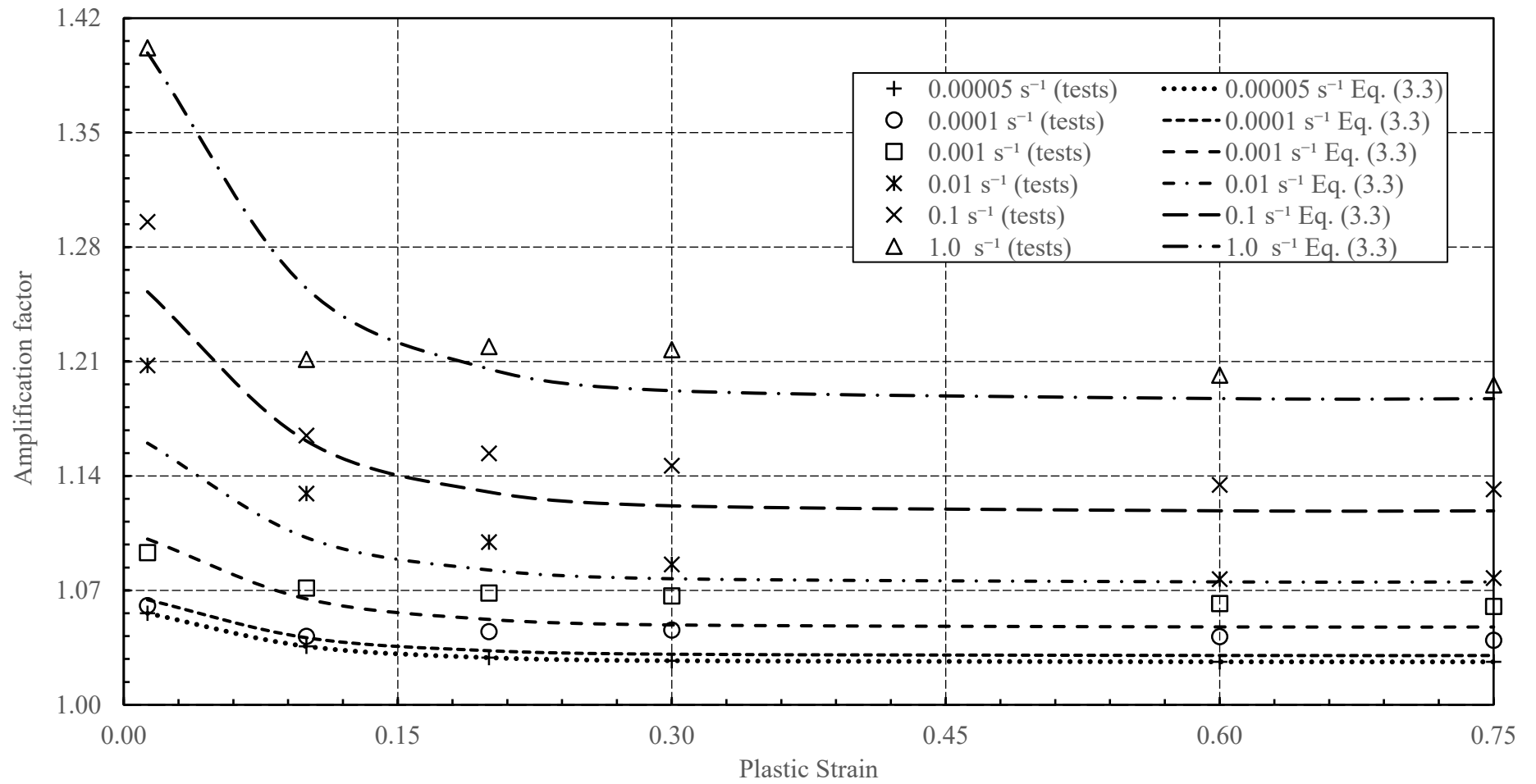


Figure 3.32 Amplification factor of isotropic yield stress calculated with Eq. (3.3) and tests for material G

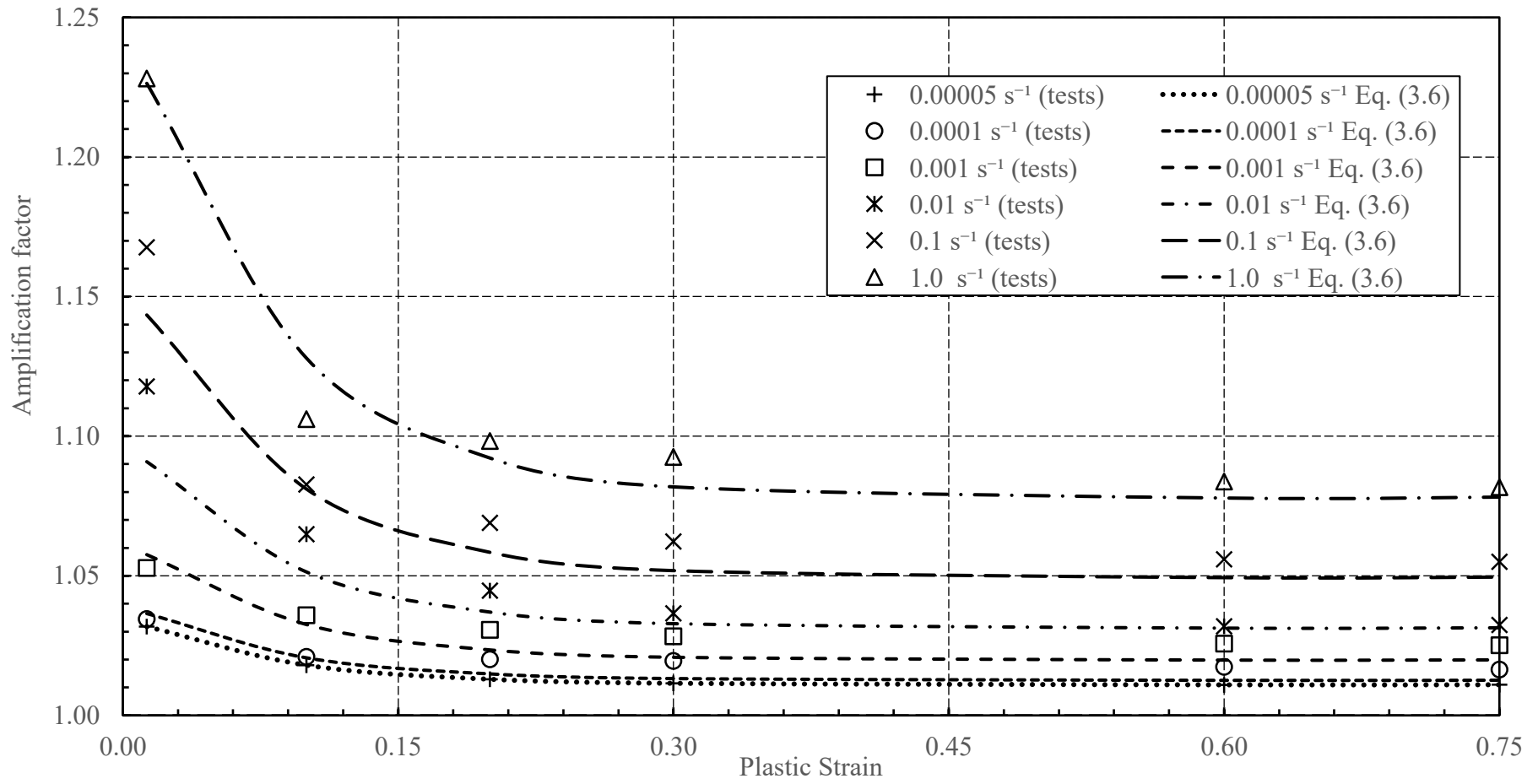


Figure 3.33 Amplification factor of flow stress calculated with Eq. (3.6) and tests for material G

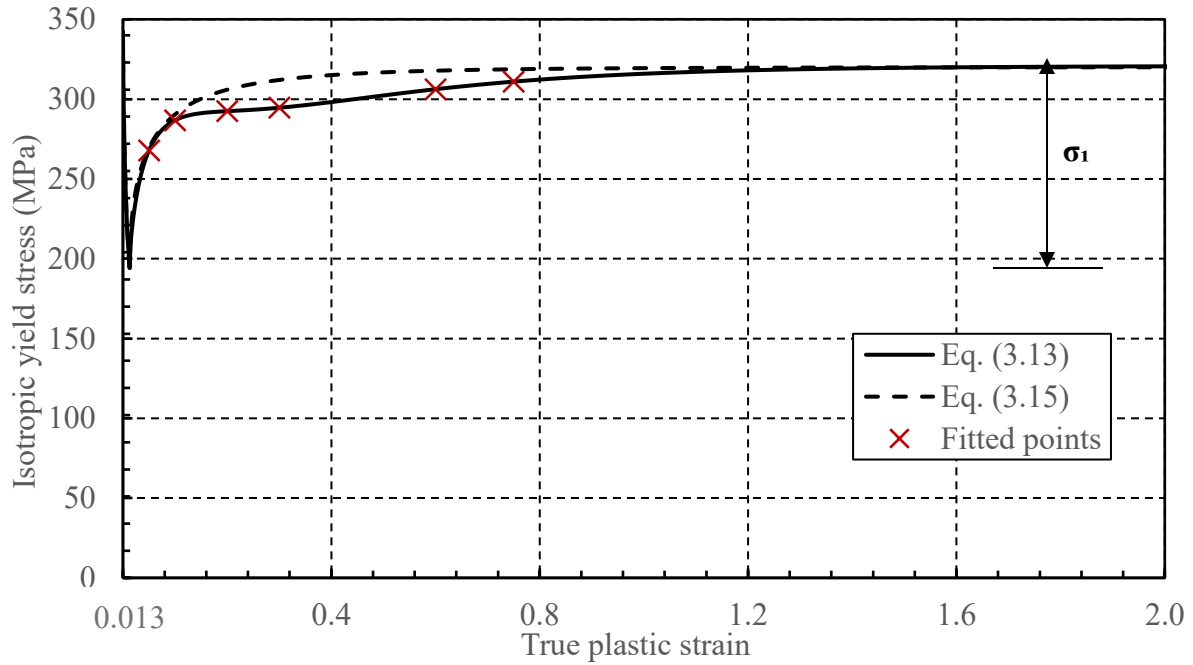


Figure 3.34 Generated static isotropic yield stress-true plastic strain curve for material G with Eqs. (3.13) and (3.15)

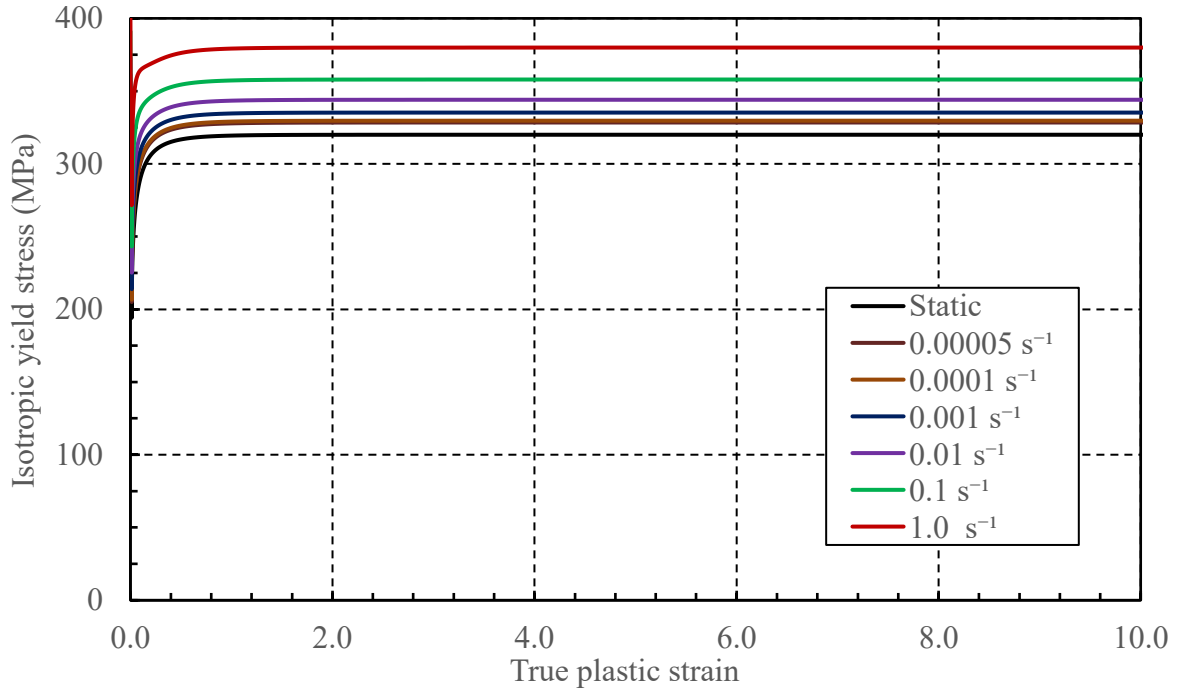


Figure 3.35 Generated isotropic yield stress versus true plastic strain curve for material G at different strain rates

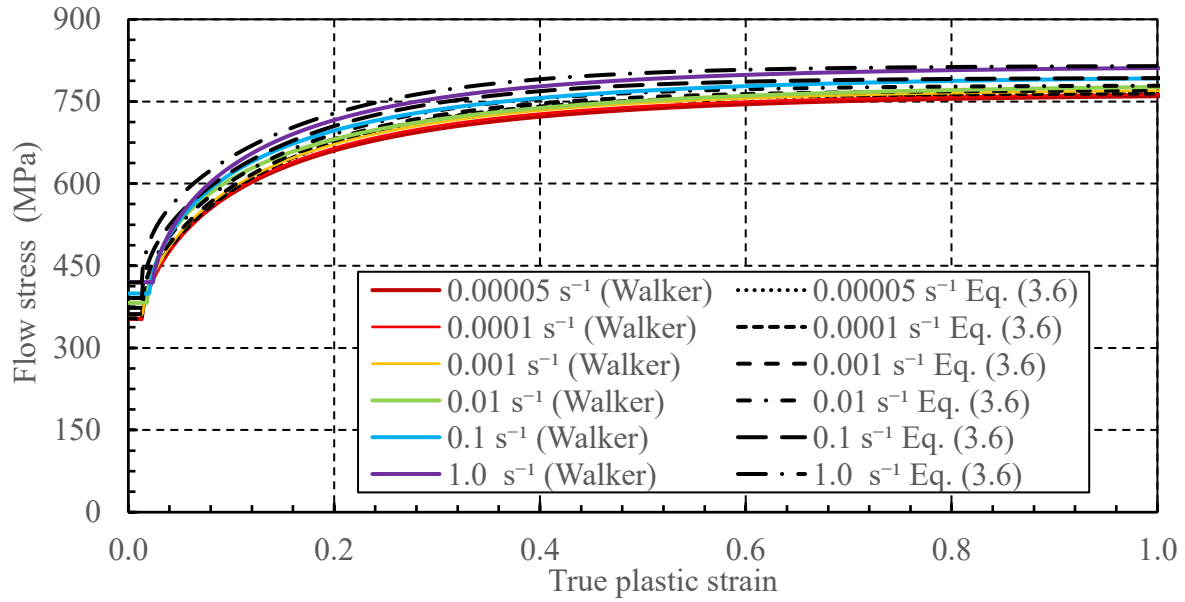


Figure 3.36 Comparisons of generated flow stress versus true plastic strain curve for material G at different strain rates by Walker (2012) and Eqs. (3.6, 3.14 and 3.15) with 4 kinematic hardening terms

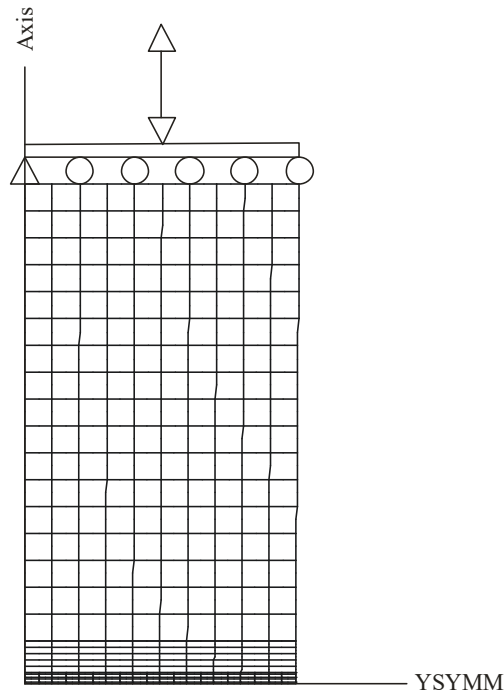


Figure 3.37 The half gauge length model of tapered specimen modelled in ABAQUS by Chen (2010) and Walker (2012)

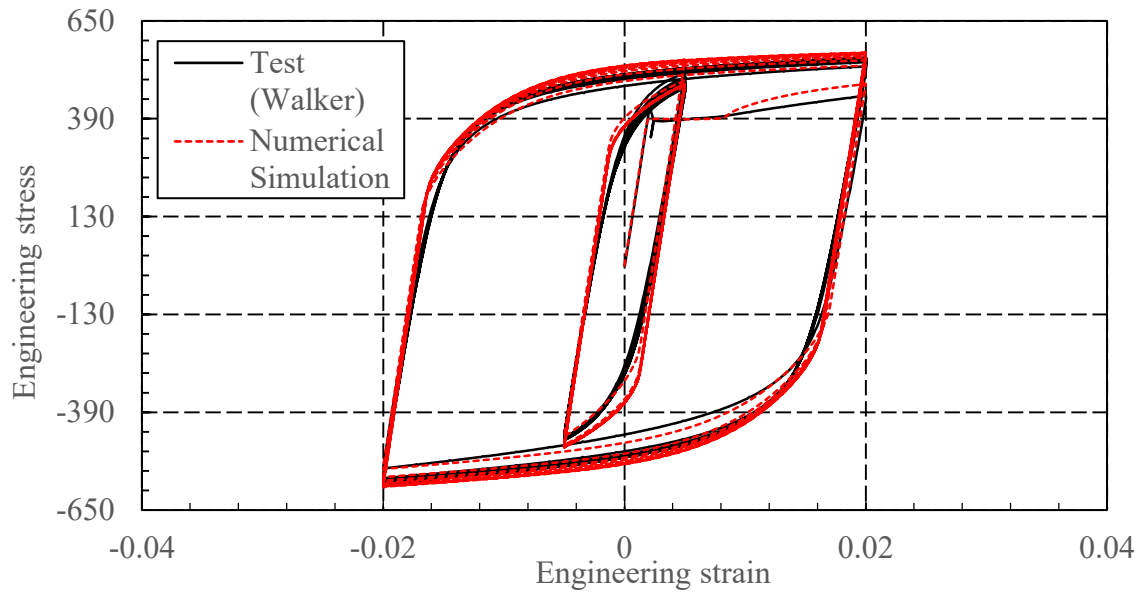


Figure 3.38 Test and predicted engineering stress versus engineering strain curve for material H for the cyclic test by Walker (2012) at a strain rate of 0.0001 s^{-1}

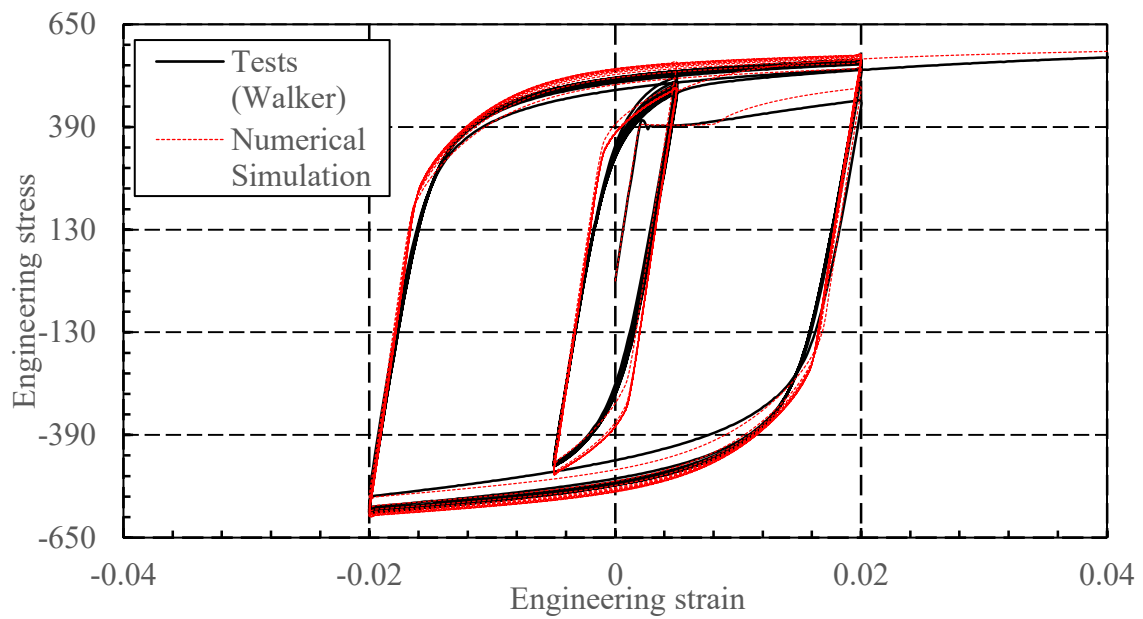


Figure 3.39 Test and predicted engineering stress versus engineering strain curve for material H for the cyclic test by Walker (2012) at a strain rate of 0.001 s^{-1}

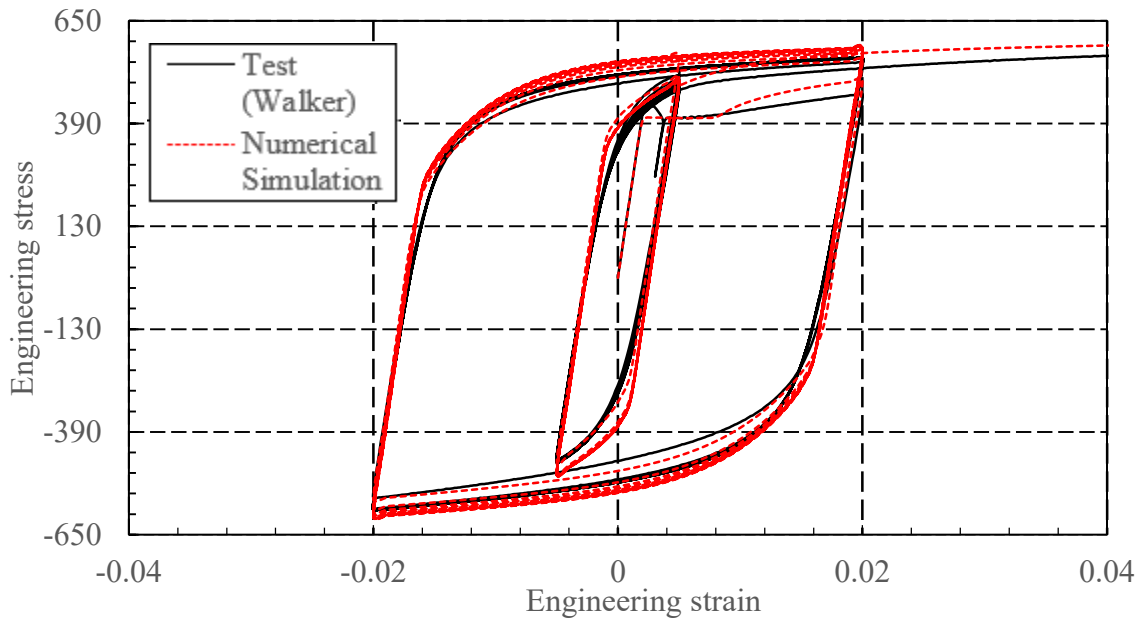


Figure 3.40 Test and predicted engineering stress versus engineering strain curve for material H for the cyclic test by Walker (2012) at a strain rate of 0.01 s^{-1}

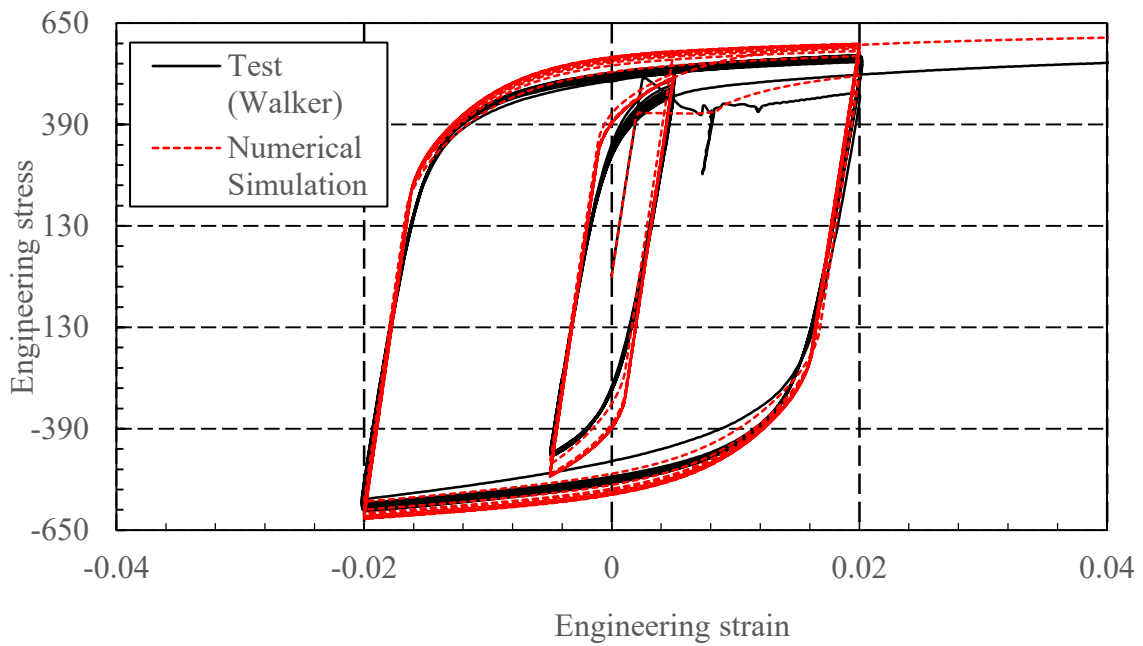


Figure 3.41 Test and predicted engineering stress versus engineering strain curve for material H for the cyclic test by Walker (2012) at a strain rate of 0.1 s^{-1}

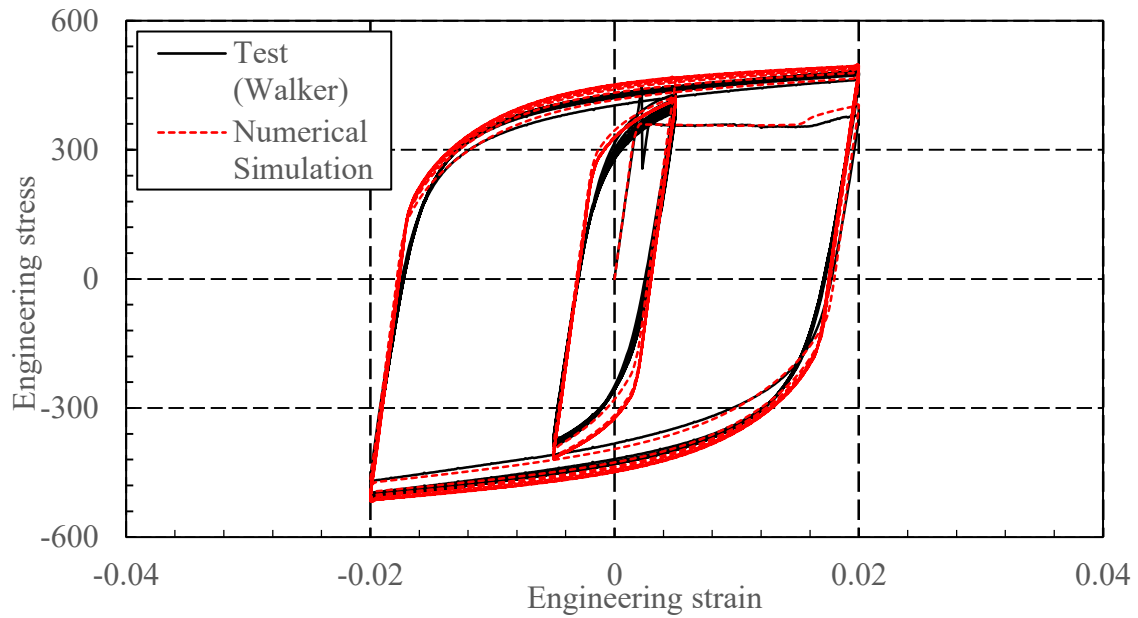


Figure 3.42 Test and predicted engineering stress versus engineering strain curve for material G for the cyclic test by Walker (2012) at a strain rate of 0.0001 s^{-1}

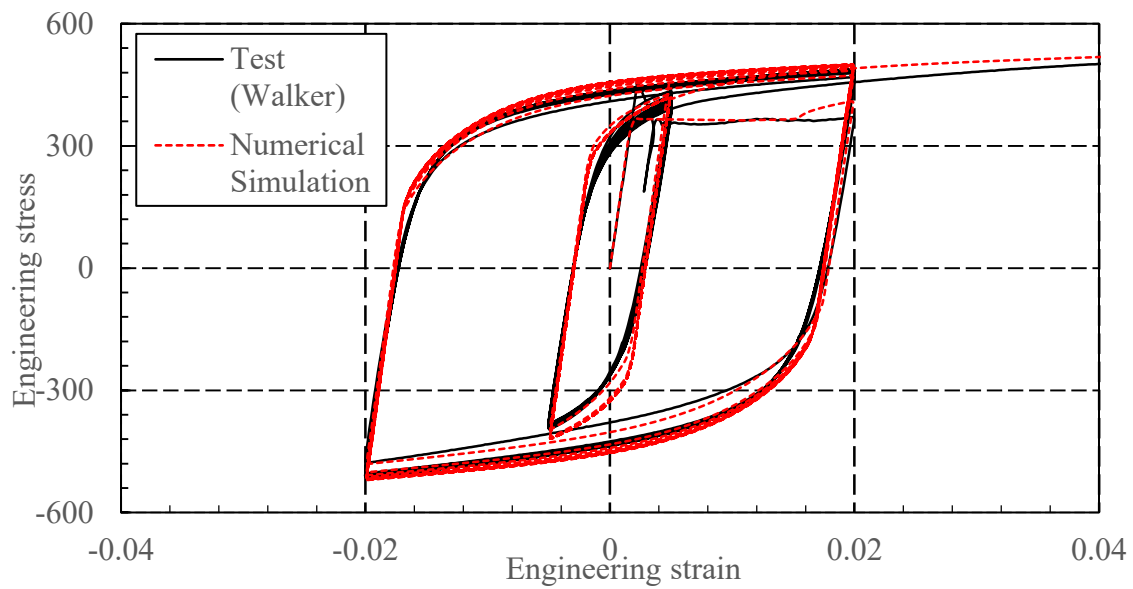


Figure 3.43 Test and predicted engineering stress versus engineering strain curve for material G for the cyclic test by Walker (2012) at a strain rate of 0.001 s^{-1}

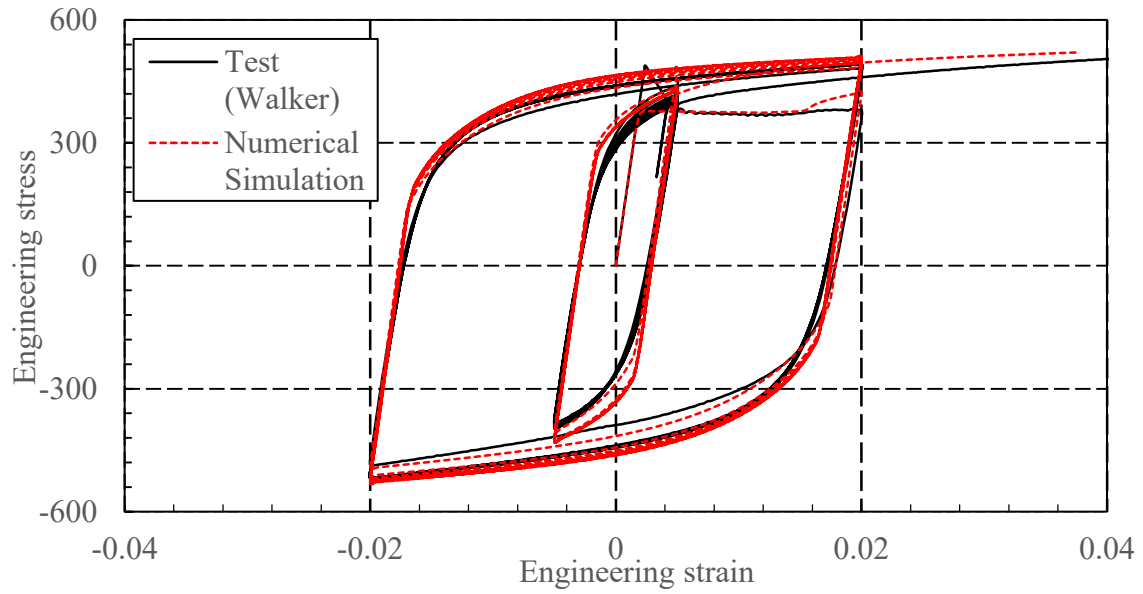


Figure 3.44 Test and predicted engineering stress versus engineering strain curve for material G for the cyclic test by Walker (2012) at a strain rate of 0.01 s^{-1}

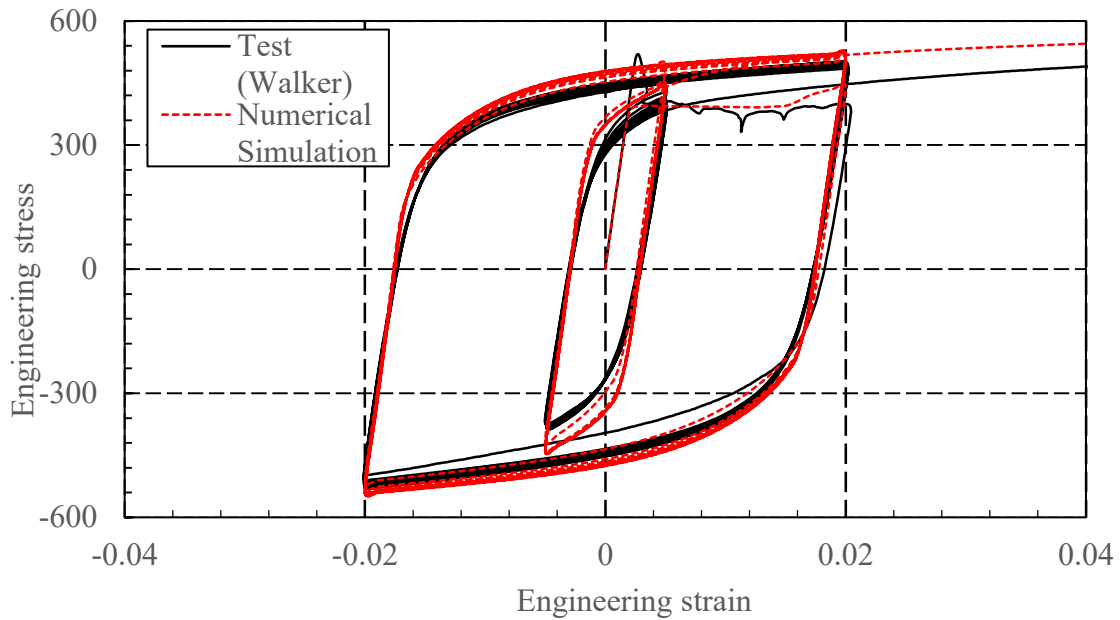


Figure 3.45 Test and predicted engineering stress versus engineering strain curve for material G for the cyclic test by Walker (2012) at a strain rate of 0.1 s^{-1}

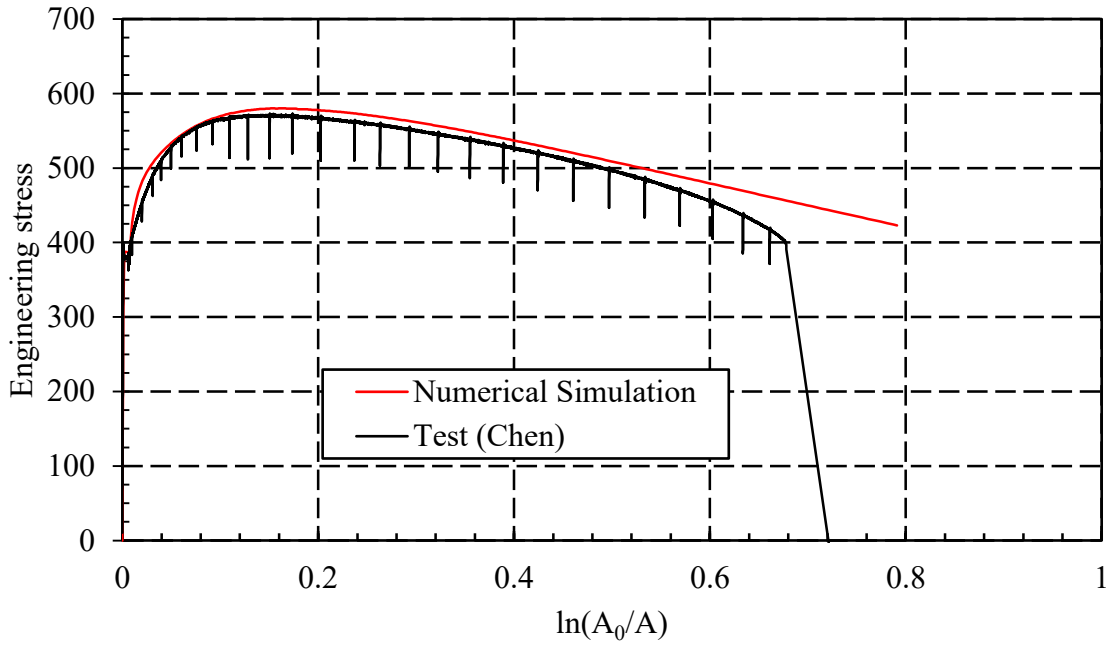


Figure 3.46 Test and predicted engineering stress versus cross-section area ratio curve for material H for monotonic tensile test by Chen (2010) at a strain rate of 0.0001 s^{-1}

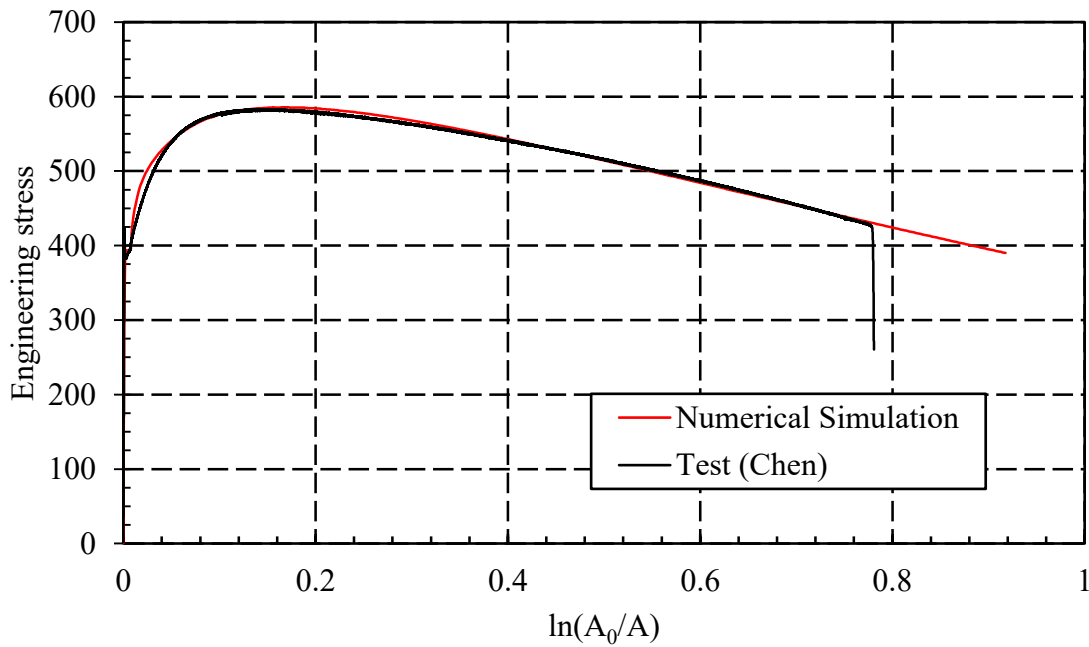


Figure 3.47 Test and predicted engineering stress versus cross-section area ratio curve for material H for monotonic tensile test by Chen (2010) at a strain rate of 0.001 s^{-1}

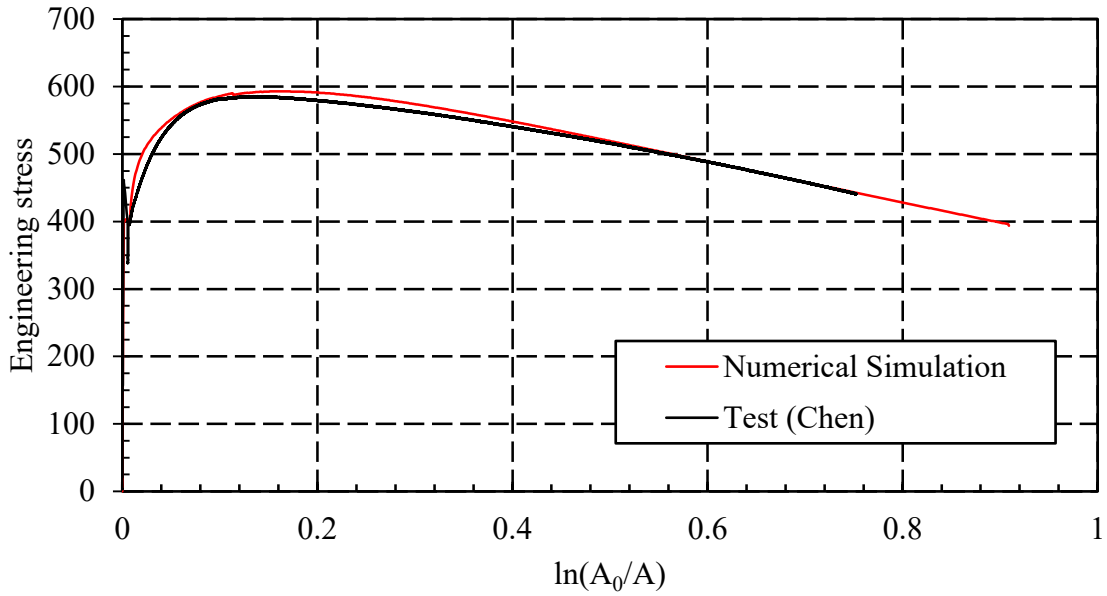


Figure 3.48 Test and predicted engineering stress versus cross-section area ratio curve for material H for monotonic tensile test by Chen (2010) at a strain rate of 0.01 s^{-1}

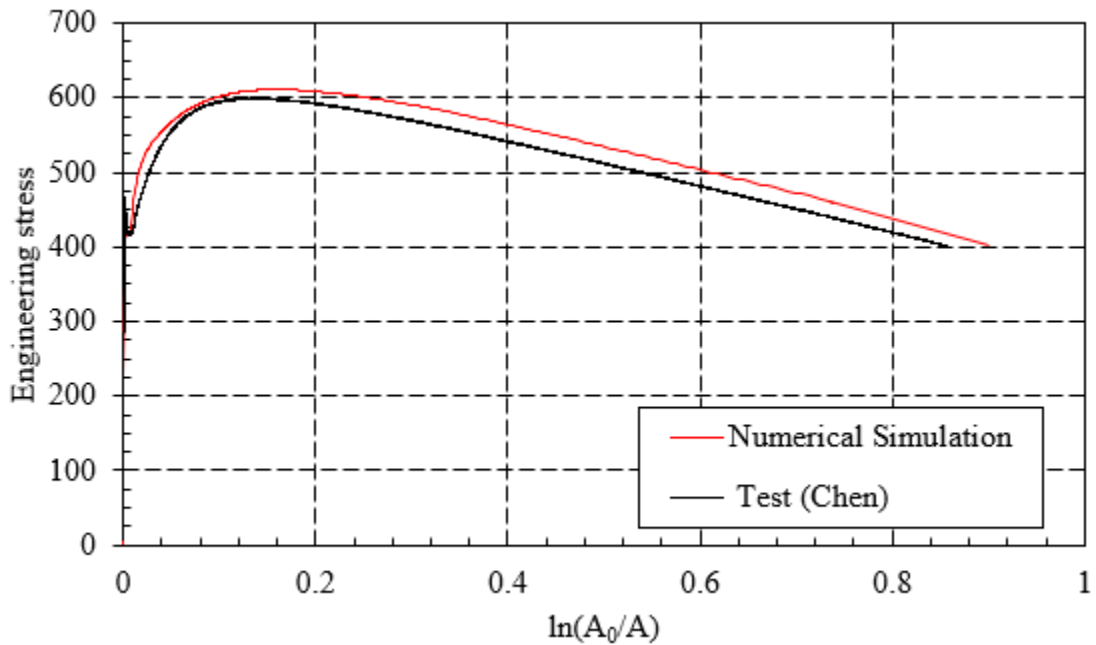


Figure 3.49 Test and predicted engineering stress versus cross-section area ratio curve for material H for monotonic tensile test by Chen (2010) at a strain rate of 0.1 s^{-1}

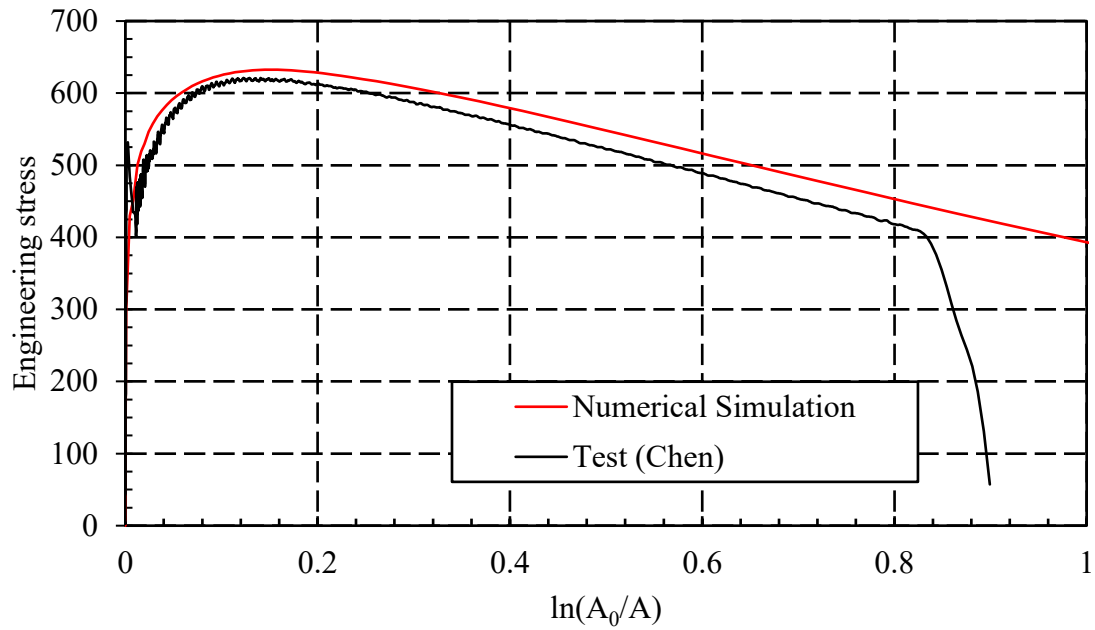


Figure 3.50 Test and predicted engineering stress versus cross-section area ratio curve for material H for monotonic tensile test by Chen (2010) at a strain rate of 1.0 s^{-1}

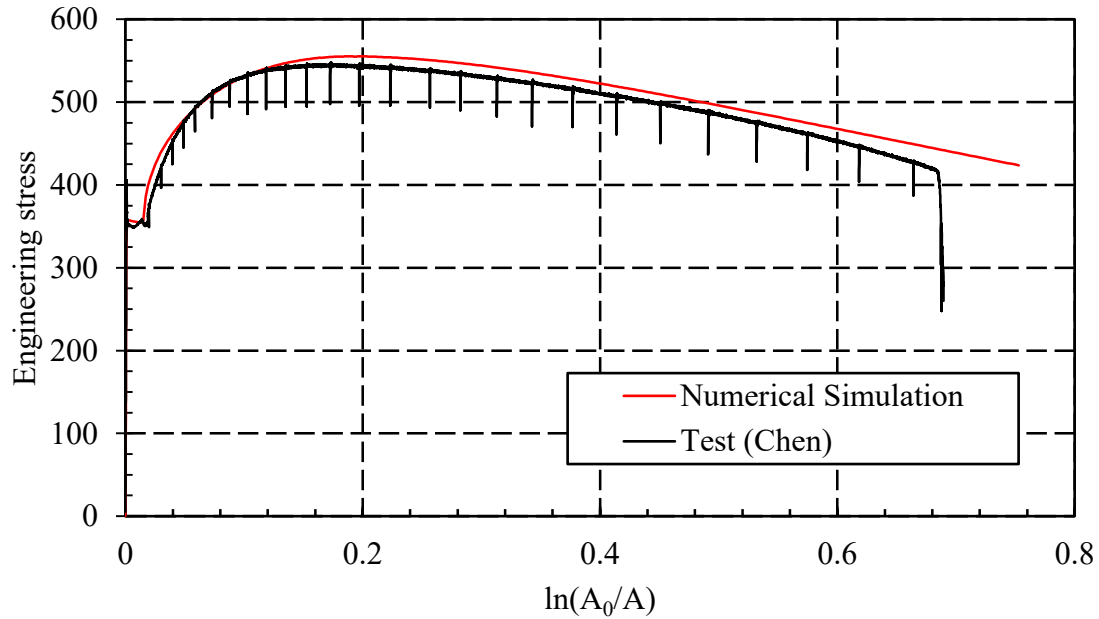


Figure 3.51 Test and predicted engineering stress versus cross-section area ratio curve for material G for monotonic tensile test by Chen (2010) at a strain rate of 0.0001 s^{-1}

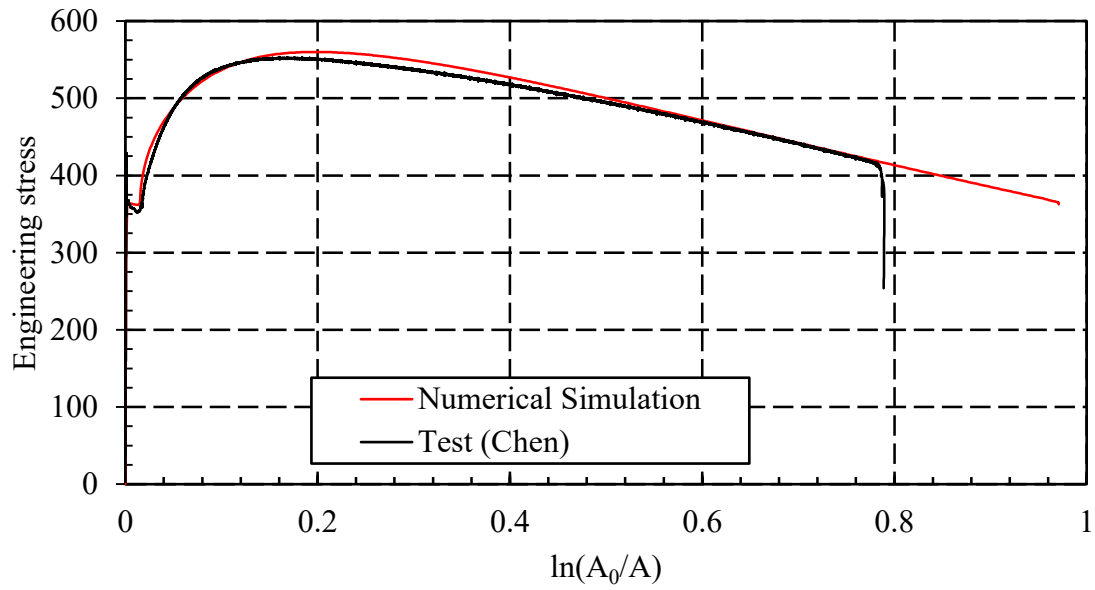


Figure 3.52 Test and predicted engineering stress versus cross-section area ratio curve for material G for monotonic tensile test by Chen (2010) at a strain rate of 0.001 s^{-1}

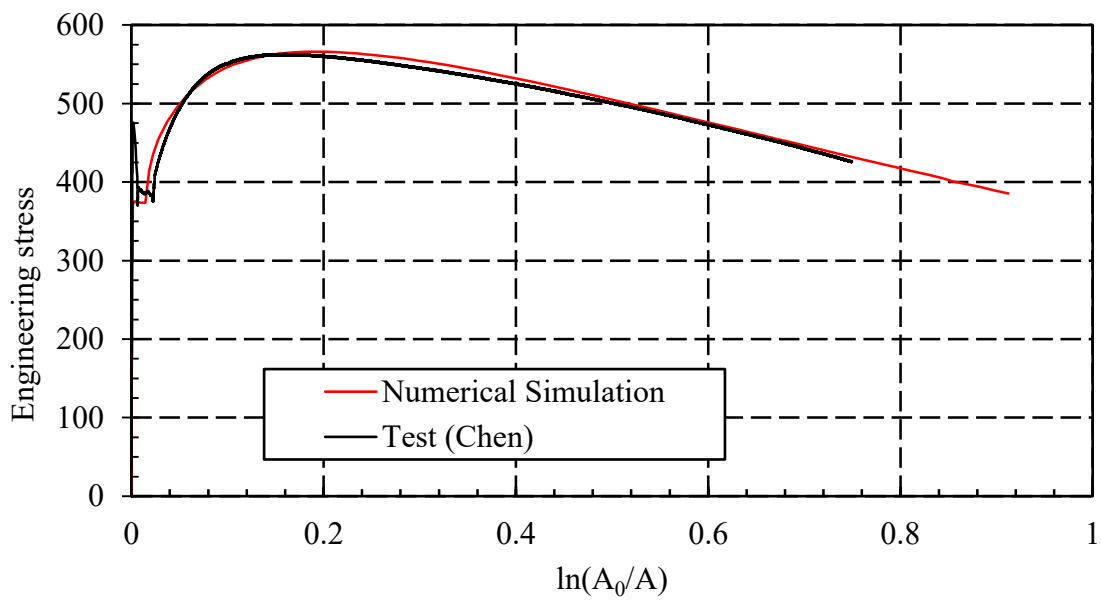


Figure 3.53 Test and predicted engineering stress versus cross-section area ratio curve for material G for monotonic tensile test by Chen (2010) at a strain rate of 0.01 s^{-1}

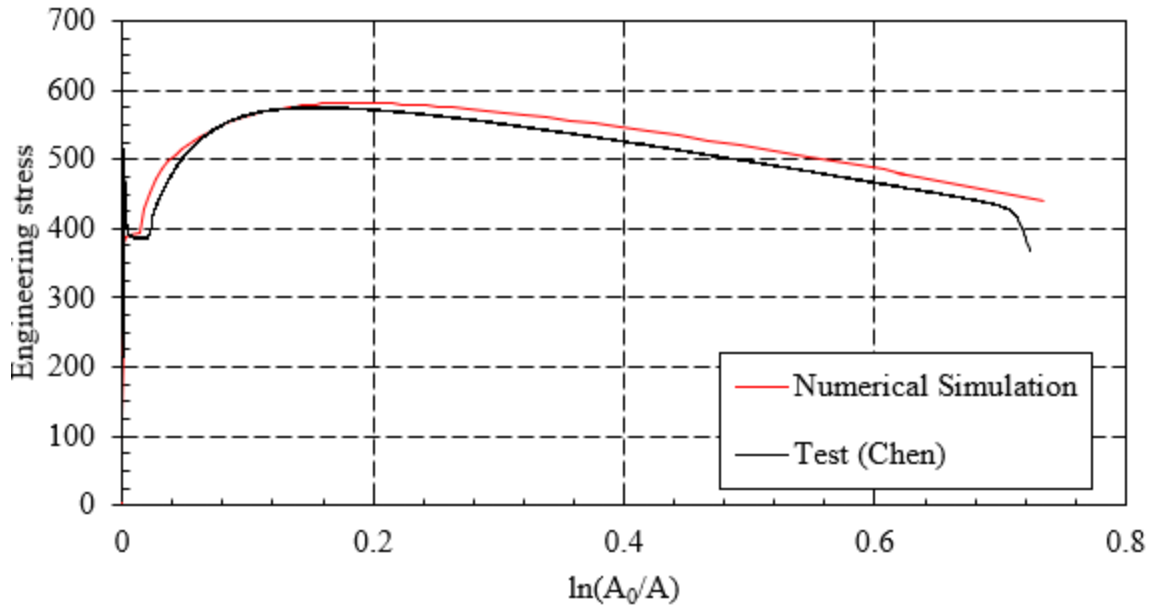


Figure 3.54 Test and predicted engineering stress versus cross-section area ratio curve for material G for monotonic tensile test by Chen (2010) at a strain rate of 0.1 s^{-1}

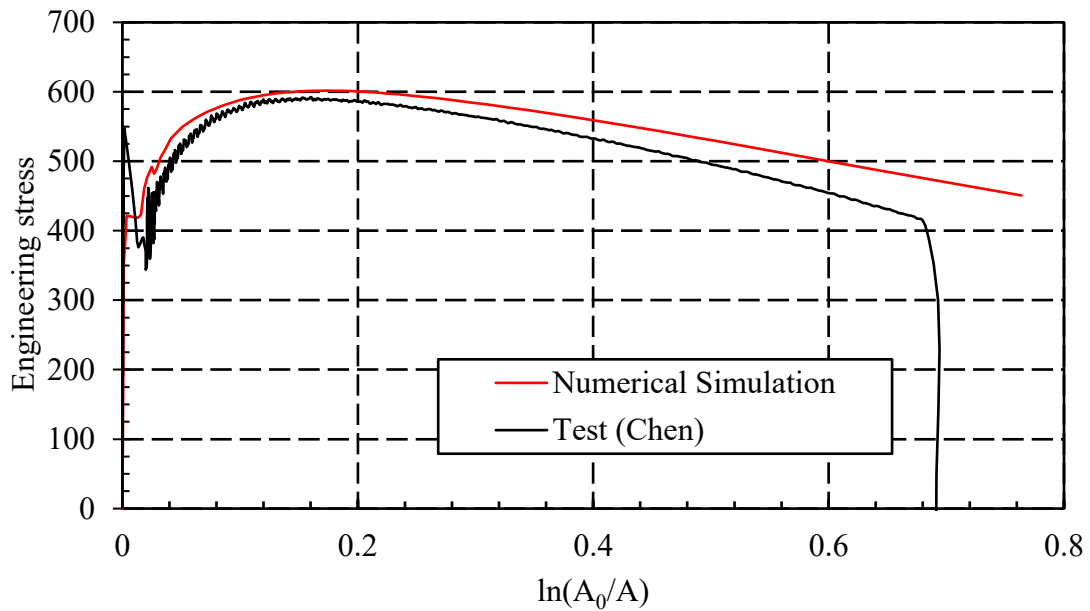


Figure 3.55 Test and predicted engineering stress versus cross-section area ratio curve for material G for monotonic tensile test by Chen (2010) at a strain rate of 1.0 s^{-1}

Chapter 4: Numerical Modelling of Ductile Moment Resisting Frame

In shake table tests, Elghazouli et al. (2004) have found that forces induced in the brace of a concentrically braced steel frame due to seismic ground motion can be 30% and 10% higher than that calculated using the yield and ultimate strengths respectively. These higher forces were partly attributed to the increase in the flow stress with strain rate for the steel brace. There have been many numerical studies carried out to investigate effects of material properties strain rate dependency on the response of the steel structures under seismic ground motions. However, none of the studies employed realistic strain rate dependent material properties in the analyses.

One of the seismic-force-resisting-systems (SFRS) used in a building is a moment resisting frame (MRF) with reduced beam section (RBS) connection. A simple finite element model of MRF with RBS connection has been developed to assess effects of material properties strain rate dependency on the response of the frame. Strain rate dependent material properties calibrated from tests by Chen (2010) and Walker (2012) are being employed in the numerical simulations in order to predict a more realistic response of the frame. All finite element analyses have been conducted with ABAQUS (Dassault Systèmes 2017).

4.1 Moment Resisting Frame

A six storey building with moment resisting frames by Christopoulos and Filiatrault (2006) has been used as the basis to design the MRF with RBS connection. In order to simplify the analyses in the study to assess effects of material properties strain rate dependency, a modified version of this building that has the same plan dimensions but only two storeys of equal height is being considered. The roof is assumed to be steel deck and the floor to be concrete slab. Thus, the beam can be considered to be laterally supported against lateral torsional buckling. In addition,

only one bay on each side of the perimeter has the moment resisting frame while the remaining bays consist of simply supported beams. Normally there are more than one bay of moment resisting frame in the building. Figures 4.1 and 4.2 show the plan and elevation of the modified building with the ductile MRF in the north-south direction (noted in Fig. 4.1) being considered in the numerical simulations.

The ductile moment resisting frame with RBS has been designed according to National Building Code of Canada (NBCC 2015) and CSA S16-14 (CSA 2014) for Victoria, British Columbia, Canada with stiff soil (site class D) condition. Lateral seismic forces imposed on the frame are calculated using the equivalent static method of seismic designs. The frame is considered to be pinned supported and designed only for strength in order to assess for possible maximum effects of material properties strain rate dependency. Thus, it is expected that the inter-storey drift limit to be exceeded. The inter-storey drift limit is ignored in the design so that the effects can be evaluated for maximum ductility of the ductile moment resisting frame. The RBS connections are designed according to Moment Connection for Seismic Application (CISC 2014). Details of the design of the ductile moment resisting frame with RBS are provided in Appendix A. The member sizes of the MRF and details of RBS are shown in Figs. 4.2 and 4.3 respectively. The frame has a first mode time period of 1.1 seconds, and inter-storey drift of 8.9% for first storey and 5.9% for the roof due to the seismic load from the equivalent static method.

4.2 Numerical Modelling of Moment Resisting Frame

There are many element types that can be used to model a structure. It is possible to model the ductile moment resisting frame using shell element or beam element entirely, or a combination of both. The analyses carried out using shell elements are more accurate, but they are

computationally more expensive. Hence, numerical modelling of the MRF using a combination of shell and beam elements or using beam element entirely have been explored.

Wide flange beams or columns modelled with beam elements are unable to capture stress concentration or other local phenomena of RBS accurately. While shell elements are better able to capture local phenomena, they are computationally more expensive. In order to increase the efficiency of the finite element analysis, shell elements can be used in regions where local effect is prominent and beam elements are used for the rest of the model. Hence, a proper interface between beam and shell elements is required to transfer the forces and maintain continuity. To facilitate the discussion, a finite element model that uses a combination of beam and shell elements will be referred to henceforth as hybrid model. Section properties of all the beam elements are integrated over the section using 5 integration points each along the web and across the flange.

4.3 Interface between Beam and Shell Elements

A 5 meter wide flange I-section ($W610 \times 174$) cantilever beam has been used to develop and verify shell to beam element interface for the hybrid model. The beam is modelled using four-node shell elements with reduced integration (S4R) and two- node 3D open section (B31OS) beam element. Half of the beam is modelled using S4R shell element and the other half using B31OS beam element as shown in Fig. 4.4. B31OS beam element is the only 3D beam element that can be used with mixed-mode isotropic/kinematic hardening metal plasticity material model. Multiple point constraints (MPC) and other constraints are used to connect the beam and shell elements, and as well as to enable the fixed support for the cantilever beam to be imposed by prescribing the restraints on a single node connected to shell elements.

It is assumed that the plane at both ends of half the beam modelled with shell elements remain plane after deformation. The orientation of the coordinate axes with y-axis in the vertical direction (along the web) and z-axis in the longitudinal direction, shown in Fig. 4.4 is adopted in the following discussions. Nodes on each flange are constrained to move in a straight line using MPC SLIDER with corner nodes and the node at the intersection of web and flange on each flange acting as the master nodes. Corner nodes and the node at the web-flange intersection of each flange are further constrained using linear constraint equations (*EQUATION) to have same nodal displacements in y-direction and z-direction. Thus, all the nodes at each flange are constrained to displace the same amount in both vertical and longitudinal directions. Figure 4.5 (a) shows the nodes involved in these constraints for the upper and lower flanges with U_{yt} and U_{zt} , and U_{yb} and U_{zb} representing the nodal displacements.

As shown in Fig. 4.5 (b), nodes along the web are constrained using MPC BEAM with the node at the middle of the web considered as the master node to displace and rotate as a rigid body. Finally, KINEMATIC COUPLING is used to couple the rotational degrees of freedom (DOFs) of the end nodes of the flanges to that of the node at the center of the web. Thus, all these nodes will have the same rotation. Figure 4.5 (c) shows the kinematic coupling scheme between the nodes on the flanges and the web at the section with R_x , R_y and R_z represent the rotations. However, only the rotation about x-axis (R_x) is coupled as there is no rotation about the other two axes. The node at the center of the web is tied to the node of the beam elements using MPC TIE according to Fig. 4.5 (d), thus connecting the shell elements to the beam element. The fixed support condition is imposed by restraining the node at the center of the web against all displacements and rotations, as shown in Fig. 4.5 (d). In order to prevent local torsional buckling, all the nodes at the web and flange intersections along the length are restrained against displacement in x-direction and rotation

in z-direction. Similarly, nodes of beam elements are restrained against displacement in x-direction and rotation in z-direction to prevent lateral torsional buckling. The established shell and beam interface scheme has been validated in Appendix B with comparisons of the results from hybrid model and beam element only model.

4.4 Modelling of Moment Resisting Frame using Hybrid Model

A combination of shell and beam elements is being used to model the ductile MRF with RBS connection. The RBS portion is being modelled with S4R shell elements and the rest of the frame with B31OS beam elements. The RBS segment and beam elements are connected using the interface scheme described in Section 4.3, and as shown in Fig. 4.5. Figure 4.6 gives the schematic representation of the hybrid model of the MRF. Dimensions of the frame are shown in Fig. 4.2. Figure 4.7 shows the hybrid model of the MRF with details of the RBS shell segments shown in Fig. 4.8. Additional respective length of 180 mm and 110 mm on both the ends of the RBS at the first floor and roof are modelled with shell elements to better replicate the non-uniform stress distribution at the transition to the RBS.

The seismic masses are placed at each corner of the frame. A leaning column has been added to model the P-delta effects of the gravity loads from the rest of the building. The leaning column is modelled with extremely stiff B31 beam elements that is hinged at the base and pinned connected at the first floor. Lateral displacement of the leaning column is constrained (or attached) to the main frame using *EQUATION, and thus transferring the lateral load effect to the frame. Orban (2011) stated that the damping ratio for steel structures subjected to earthquakes is between 2-5%. Kudu et. al (2015) specified a damping ratio of 2-2.5% for steel frames while Goehlich

(2015) stated that most of steel structure have damping ratio equal to 3%. Hence, Rayleigh damping of 3% is considered for the MRF model. The damping matrix of structure is defined as

$$[C] = \alpha [M] + \beta [K] \quad (4.1)$$

where $[C]$, $[M]$ and $[K]$ are the damping, mass and stiffness matrices respectively, and α and β represent the mass and stiffness proportional damping coefficients. These coefficients are defined by Song and Su (2017) as

$$\begin{Bmatrix} \alpha \\ \beta \end{Bmatrix} = \frac{2\varepsilon}{\omega_i + \omega_j} \begin{Bmatrix} \omega_i \omega_j \\ 1 \end{Bmatrix} \quad (4.2)$$

where ε is the damping ratio, and ω_i and ω_j are frequencies of the mode considered in the damping. The damping is applied through material properties definition in the numerical model of the MRF with the input values of α and β .

4.5 Mesh Convergence Study for Hybrid Model

A mesh convergence study has been conducted to improve the efficiency of the finite element model. When the MRF is subjected to seismic ground motions, plastic hinge forms at the RBS of the frame. RBS is a region with highly non-uniform stress and strain distribution. Hence, a sufficiently fine finite element mesh is required to capture these effects at the RBS. However, an excessively fine mesh can increase the computational time without significantly improve the accuracy of the results.

Different meshing schemes considered involve changing the mesh size in the RBS region of the model while 100 beam elements are used to model each storey of the column and beam segment between the RBS and, 10 beam elements are used to model the segment between column and RBS segment at each storey. Figure 4.9 (a) and (b) shows the finite element meshes and Table 4.1 gives the number of elements and element sizes of these meshes for the RBS at first floor. The

same meshing schemes in terms of number of elements shown in Fig 4.9 are used for the finite element meshes for the RBS at the roof. The element size in the coarser mesh (mesh-1) is 1.6 times the element size in the finer mesh (mesh-2). Non-linear dynamic analyses with rate dependent material properties of material H are used in the numerical simulations of the hybrid model in the mesh convergence study. Rayleigh damping of 3% has been used for first 2 lateral modes of translation with input values of $\alpha = 0.27 \text{ rad s}^{-1}$ and $\beta = 2.4 \times 10^{-3} \text{ s rad}^{-1}$ obtained using Eq. (4.2) with $\omega_i = 5.57 \text{ rad/s}$ and $\omega_j = 24.2 \text{ rad/s}$. The hybrid model is subjected to Northridge 1994 earthquake scaled to peak ground acceleration (PGA) of 0.57g shown in Fig. 4.10. Figure 4.11 shows a good agreement in the predicted base shear versus roof displacement plotted from results of mesh-1 and mesh-2. Comparisons of peak first floor acceleration and displacement, peak roof acceleration and displacement and maximum base shear from these meshes are shown in Table 4.2. There is no significant difference in the results from both meshes. The processing time for the analysis using mesh-1 with 8 central processing units (CPUs) is about 16 hours and 50 minutes, while the processing time for the same analysis using mesh-2 with two CPUs is 128 hours (i.e. 5 days and 8 hours). Hence, mesh-1 is used for subsequent analyses as mesh-2 increases the computational time using approximately 47 hours with 8 CPUs (there is a reduction of processing time by a factor of 0.6 for every doubling of the number of CPUs) without providing any significant improvement in the results. A coarser mesh scheme has not been considered as it was deemed to be too coarse.

4.6 Modelling of Moment Resisting Frame with Entirely Beam Elements

Although a hybrid model is an improvement over an entirely shell element model in efficiency, it can still be computationally expensive. Thus, a scheme that models the moment

resisting frame with entirely B31OS beam elements shown in Fig. 4.12 is also being explored. Instead of shell elements, the RBS is modelled with beam elements of varying flange width to approximate the flange profile of the RBS. The equivalent width for any beam element segment is the average width taken as

$$b_i = \frac{1}{z_{i+1} - z_i} \int_{z_i}^{z_{i+1}} b(z) dz \quad (4.3)$$

where $b(z)$ is the flange width along the longitudinal axis, z_i and z_{i+1} are the longitudinal coordinates at the start and end of the i^{th} beam element segment. Figure 4.13 shows beam elements of varying flange width superimposed on the flange of an RBS.

4.7 Model Convergence Study for Frame Composed of Beam Elements

A model convergence study has been carried out for MRF with RBS modelled entirely using beam element to find out the optimum finite element model configuration. The number of elements in the RBS varies from 26 elements in model-1 to 52 elements in model-2 and 104 elements in model-3. 100 beam elements are used to model each storey of the column and the beam between the RBS. 10 beam elements are used to model the portion between column and RBS segment at each storey. Mixed-mode hardening material behaviour and strain rate dependent material properties of material H calibrated in Chapter 3 are used in the non-linear dynamic analyses. For the purpose of this study, the frame is subjected to the seismic ground motion from Landers,1992 earthquake with scaled PGA of 0.83g shown in Fig. 4.14. Predicted base shear versus roof displacement from the results of these meshing schemes are shown in Fig. 4.15. It can be seen that there is a good agreement between results of model-2 and model-3. Comparisons of the peak first floor acceleration and displacement, peak roof acceleration and displacement, maximum base shear, maximum moment at first floor and roof column centerline from these

models are shown in Table 4.3. The differences among the results of these three models are small. The processing time to complete the analyses using 2 CPUs is 80 minutes, 95 minutes and 125 minutes with model-1, model-2 and model-3 respectively. Hence, based on the comparisons in Fig. 4.15 and Table 4.3, model-2 with the RBS modelling with 52 elements is chosen to be used in the beam element only model for all subsequent analyses

With 52 elements in the RBS segment of the beam element only model, the mesh sensitivity study has also been conducted to investigate the number of elements to be used for the rest of the beam using non-linear dynamic analyses with rate dependent material properties of material H subjected to seismic ground motion shown in Fig. 4.14. Three modelling schemes representing scheme-1, scheme-2 and scheme-3 for the rest of the beam are shown in Table 4.4 and Fig. 4.16. The moment time history plots at the center of first floor RBS for three schemes are shown in Fig. 4.17. It can be seen that there is very little or no difference between the results of the three schemes. Even though any scheme appears to be acceptable, model with scheme-2 has nevertheless been chosen to be used in subsequent analyses. Based on the comparisons in Fig. 4.17, 100 beam elements for each storey of the column and 10 beam elements between the column and RBS in the hybrid model can be considered to be adequate.

4.8 Comparisons between Hybrid Model and Beam Element Only Model

Comparisons made between the results of the analyses from the hybrid and beam element only models subjected to ground motion shown in Fig. 4.14 are shown in Table 4.5 and Fig. 4.18. The predicted peak acceleration and displacement at both first floor and roof, the predicted maximum base shear and column centerline maximum moment at the first floor between the two models differ by less than 2%. However, there is a larger percentage difference in the predicted

column centerline maximum moment at the roof because the magnitude of the column centerline moment at the roof is significantly smaller than that at the first floor. Thus, any change in the difference in column centerline moment at the first floor due to moment redistribution will affect the column moment at the roof disproportionately percentage wise, even though the change in the moment is of comparable magnitude. Figure 4.18 shows that the base shear versus roof displacement predicted by the beam element only model closely tracks that of the hybrid model. Thus, based on the overall good agreement between results of the analyses from both models, it is decided that the beam element only model which is significantly less computationally expensive will be used predominantly in the analyses to study the effects of strain rate dependent material properties on the MRF with RBS. Nevertheless, hybrid models will be used in a few parametric combinations to get more precise results.

Table 4.1 Meshing scheme for the RBS at first floor modelled using shell elements (S4R)

Mesh scheme	Number of elements			Element size (mm)	
	N _L	N _W	N _H	Flange	Web
Mesh-1	40	10	28	25.4 × 23.4	23.8 × 23.4
Mesh-2	64	16	44	15.9 × 14.6	15.1 × 14.6

Table 4.2 Comparisons of RBS modelled using shell elements for coarse and fine meshes

	Peak acceleration (g)		Displacement (mm)		Maximum base shear (kN)
	First floor	Roof	First floor	Roof	
Mesh-1	0.61	1.16	193	354	858
Mesh-2	0.61	1.16	193	354	858

Table 4.3 Comparisons of the results for beam element only MRF model for different meshes

	Model-1	Model-2	Model-3
Peak first floor acceleration (g)	1.00	1.03	1.04
Peak roof acceleration (g)	0.97	0.99	1.01
Peak first floor displacement (mm)	229	231	231
Peak roof displacement (mm)	417	419	419
Maximum base shear (kN)	851	852	852
Column centerline max moment at first floor (kN.m)	2137	2139	2139
Column centerline max moment at roof (kN.m)	563	561	560

Table 4.4 Number of elements for rest of the beam in beam element only model with 52 elements in RBS segment. (See Fig. 4.16)

	N ₁ elements (element size)	N ₂ elements (element size)	N ₃ elements (element size)	N ₄ elements (element size)
Scheme-1	6 (82 mm)	70 (80 mm)	7 (80 mm)	64 (80 mm)
Scheme-2	12 (41 mm)	140 (40 mm)	15 (38 mm)	128 (39 mm)
Scheme-3	24 (20 mm)	280 (20 mm)	30 (19 mm)	256 (20 mm)

Table 4.5 Comparisons of the results for hybrid and beam element only models

	Hybrid	Beam	Relative difference (%)
Peak first floor acceleration (g)	1.04	1.03	0.91
Peak roof acceleration (g)	1.00	0.99	0.88
Peak first floor displacement (mm)	232	231	0.03
Peak roof displacement (mm)	421	419	0.03
Maximum base shear (kN)	846	852	0.72
Column centerline max moment at first floor (kN.m)	2098	2139	1.92
Column centerline max moment at roof (kN.m)	597	561	6.23

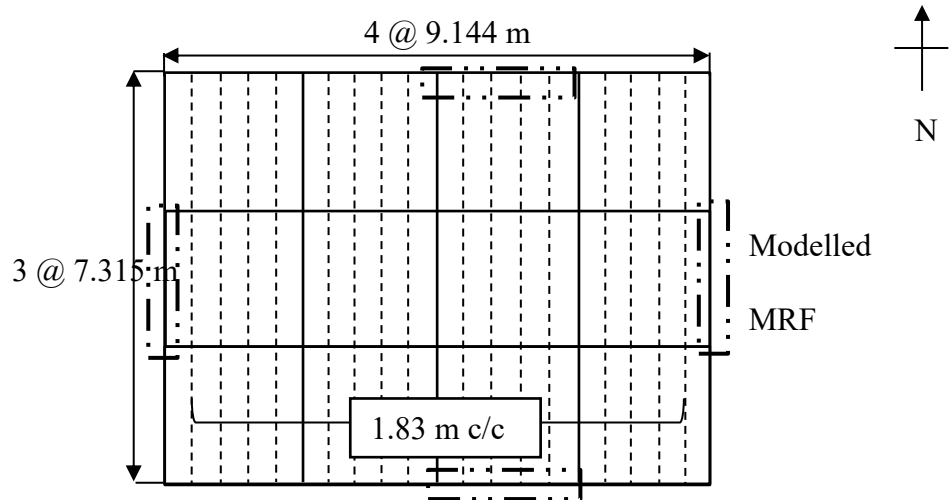


Figure 4.1 Building plan dimensions

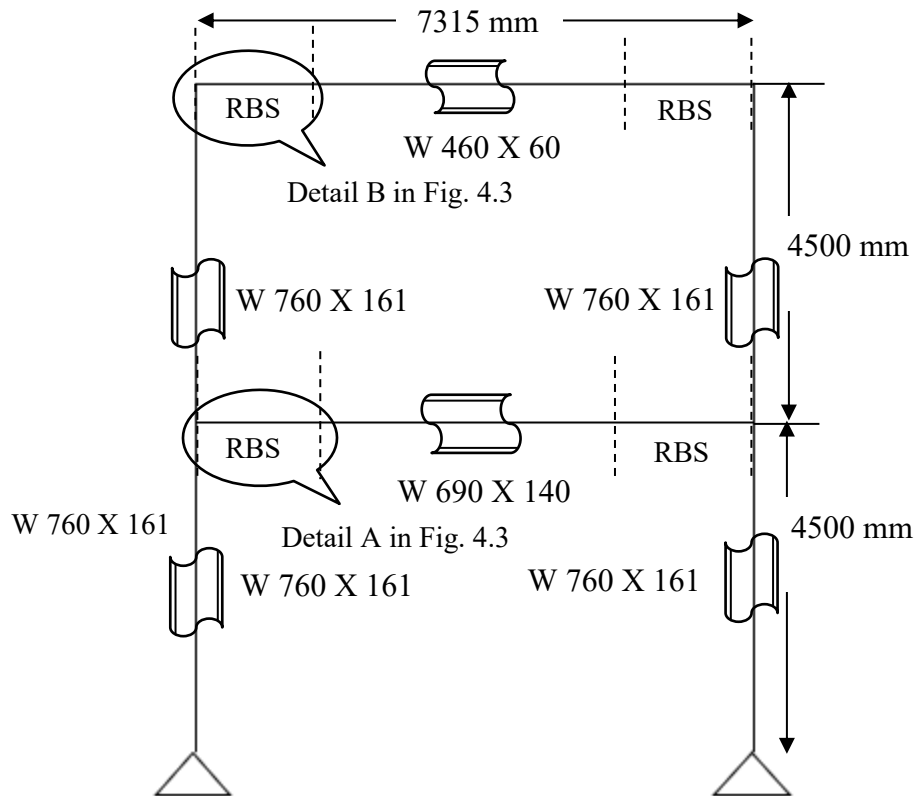
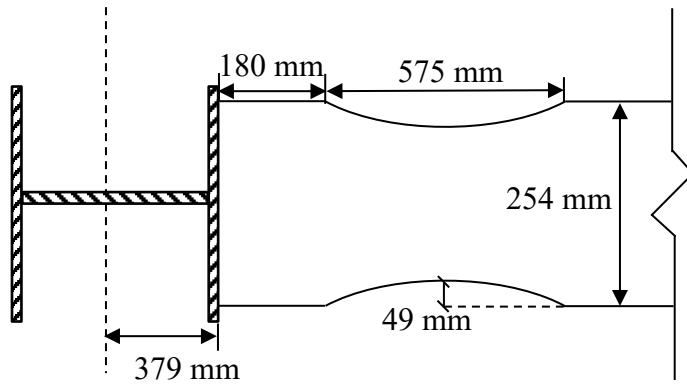
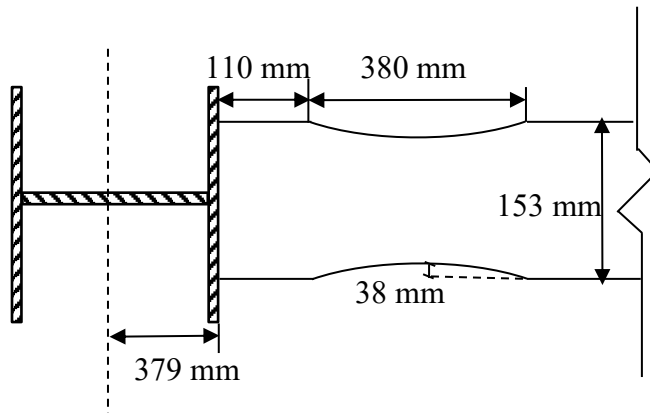


Figure 4.2 Elevation view of the moment resisting frame



(a) Detail A of Fig. 4.2



(b) Detail B of Fig. 4.2

Figure 4.3 Details of reduced beam section (RBS) connections

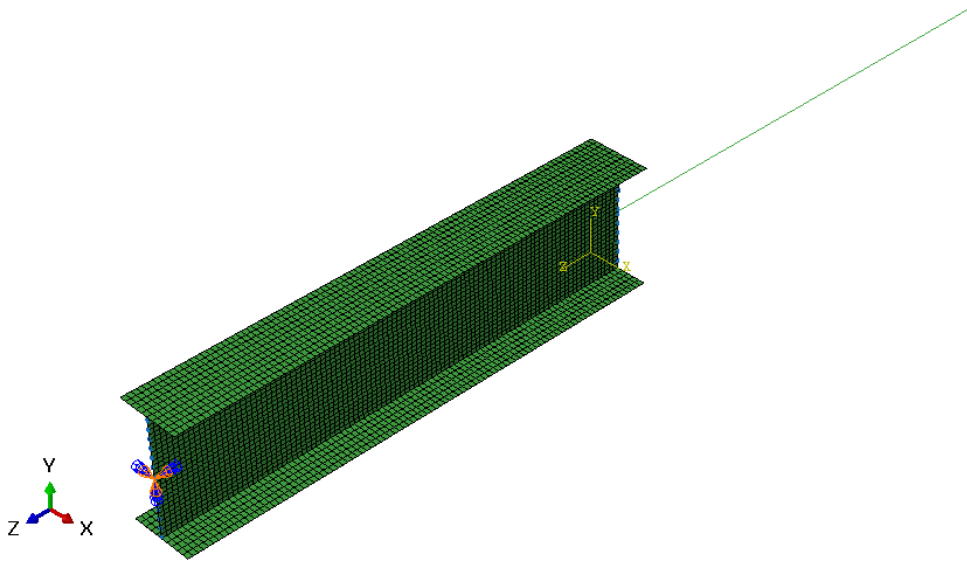
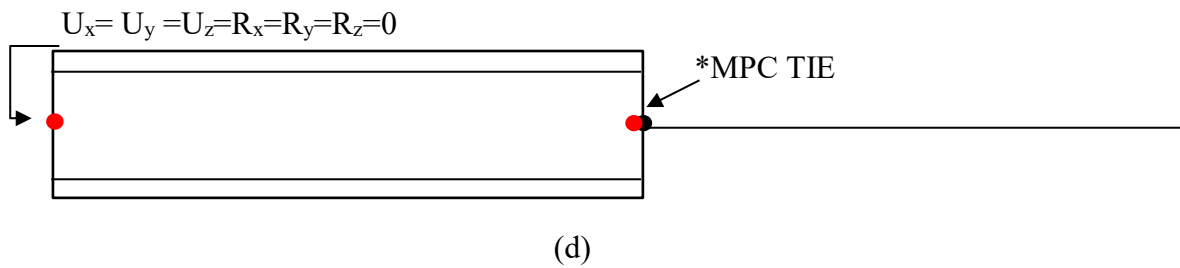
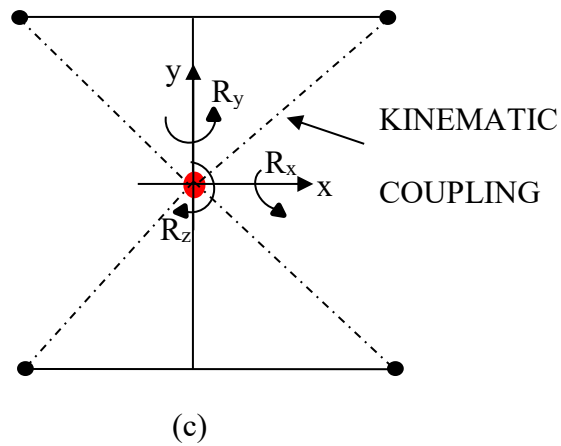
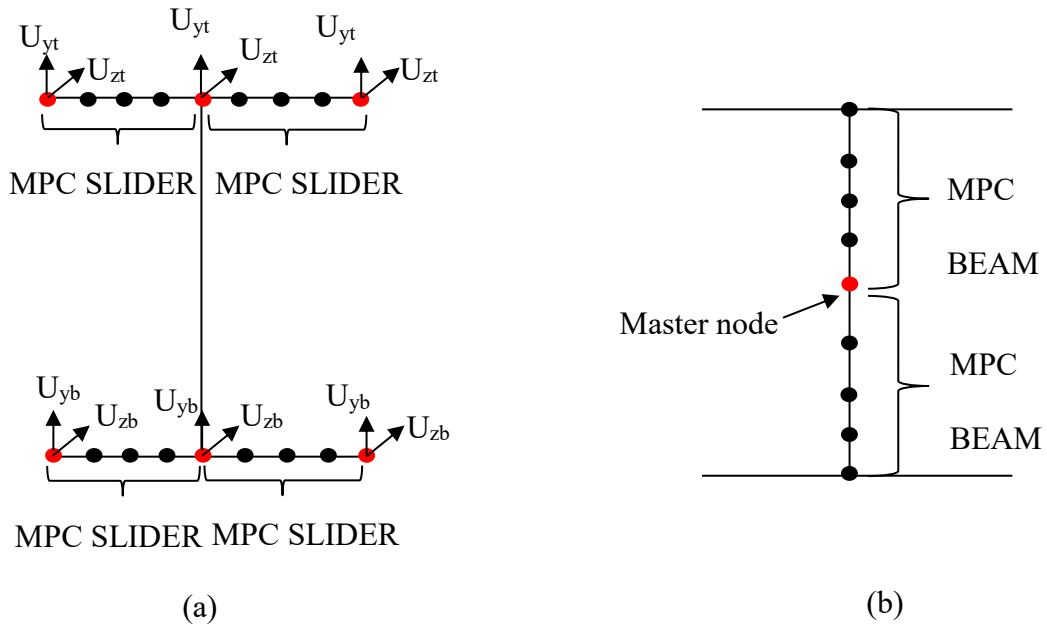


Figure 4.4 Hybrid cantilever beam model



● - Represents the master node/nodes

Figure 4.5 Connection of shell and beam elements. (a) Nodes constrained on the flanges (b) nodes constrained on the web (c) kinematic coupling (d) beam to shell connection

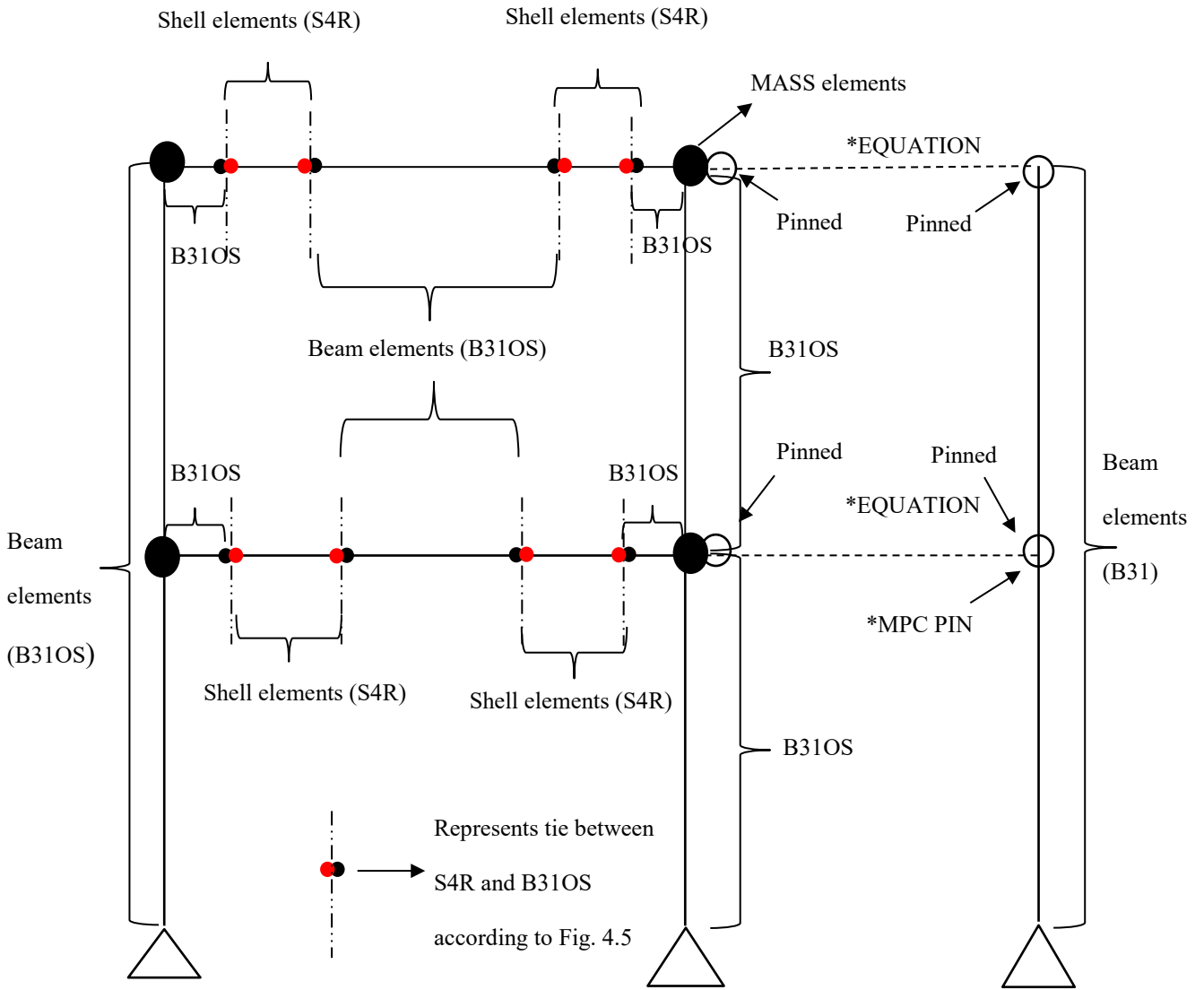


Figure 4.6 Schematic representation of the elements and constraints for the hybrid model of MRF

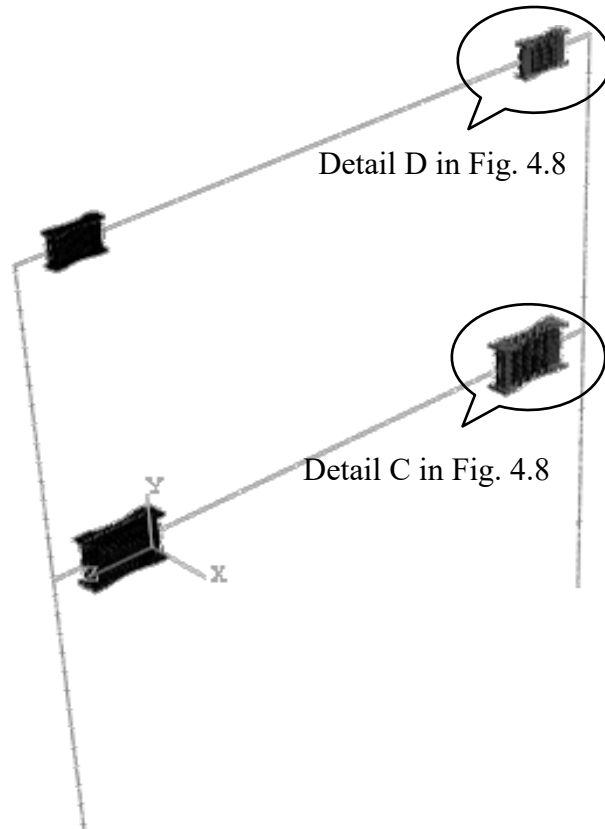


Figure 4.7 Hybrid model of ductile MRF (leaning column has not been shown here for clarity)

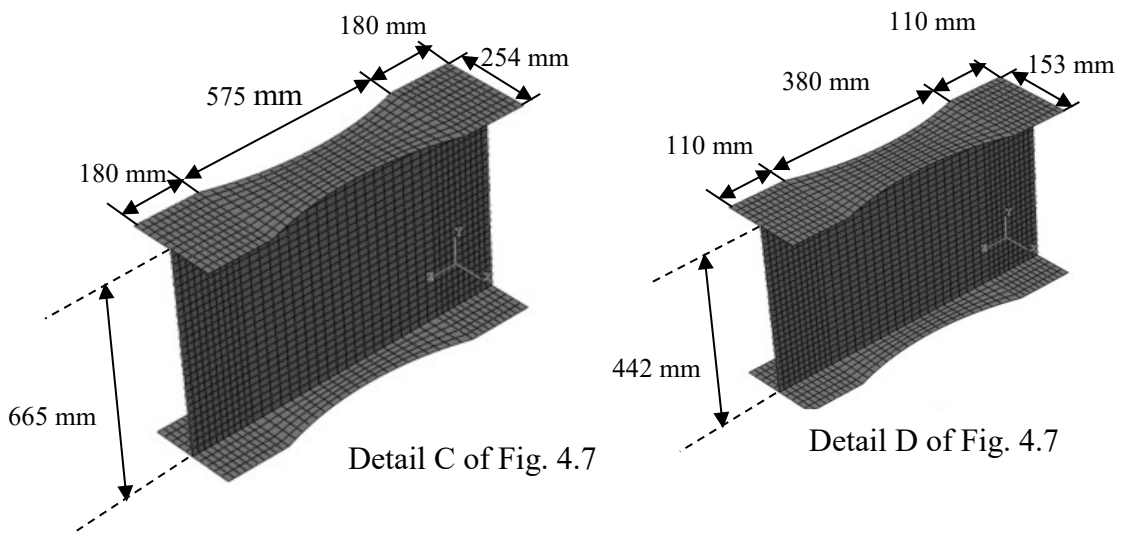


Figure 4.8 Dimensions of shell element portions of hybrid model

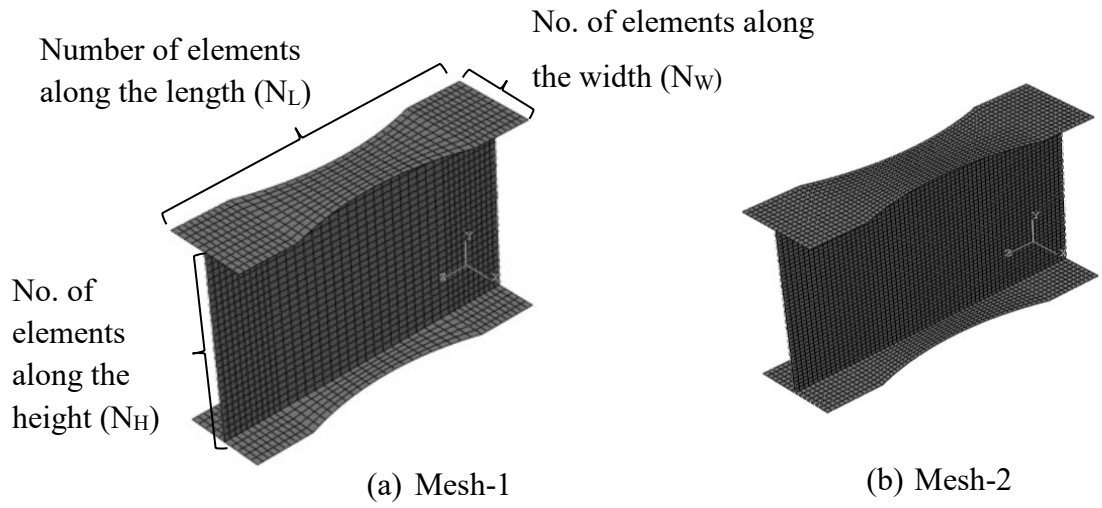


Figure 4.9 RBS modelled using shell elements with different meshes (a) mesh-1 (coarse mesh) (b) mesh-2 (fine mesh)

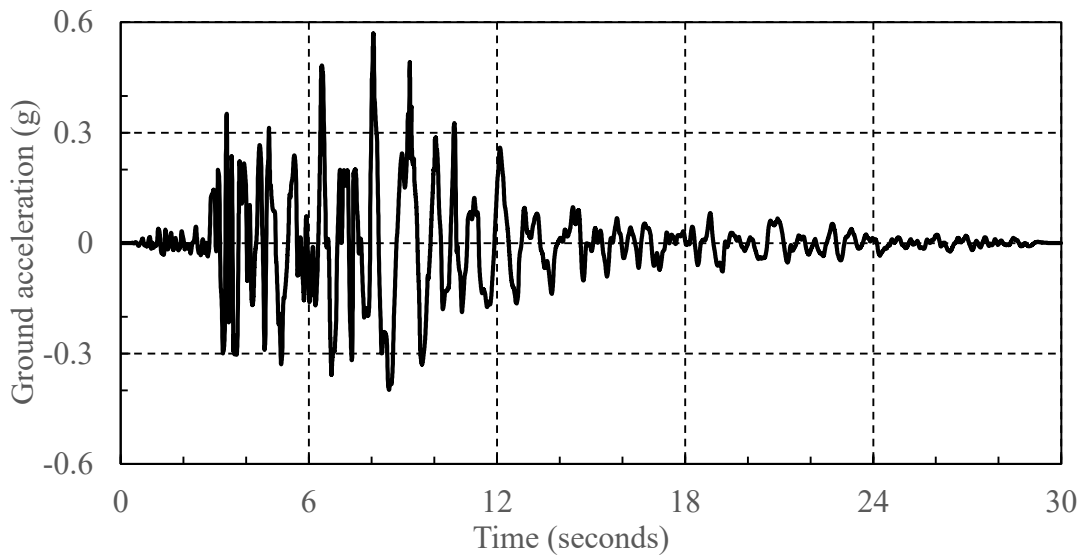


Figure 4.10 Acceleration time history (Northridge 1994 scaled to PGA of 0.57g) for mesh convergence study of the hybrid model

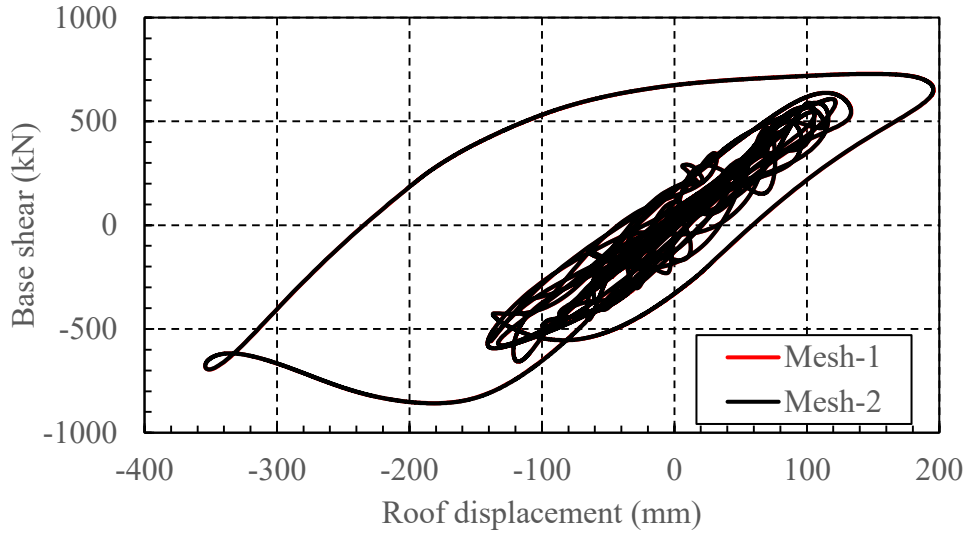


Figure 4.11 Base shear versus roof displacement for fine and coarse mesh of hybrid model

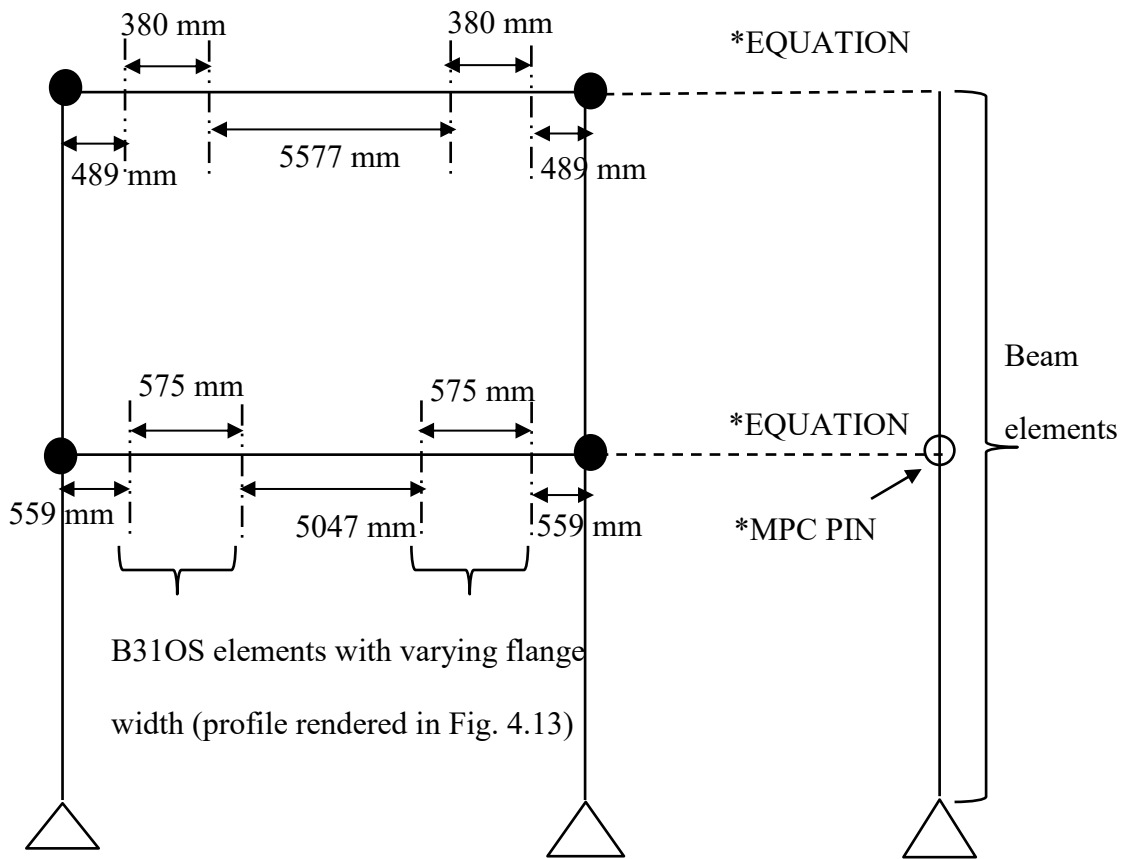


Figure 4.12 Schematic representation of the frame modelled using B31OS elements

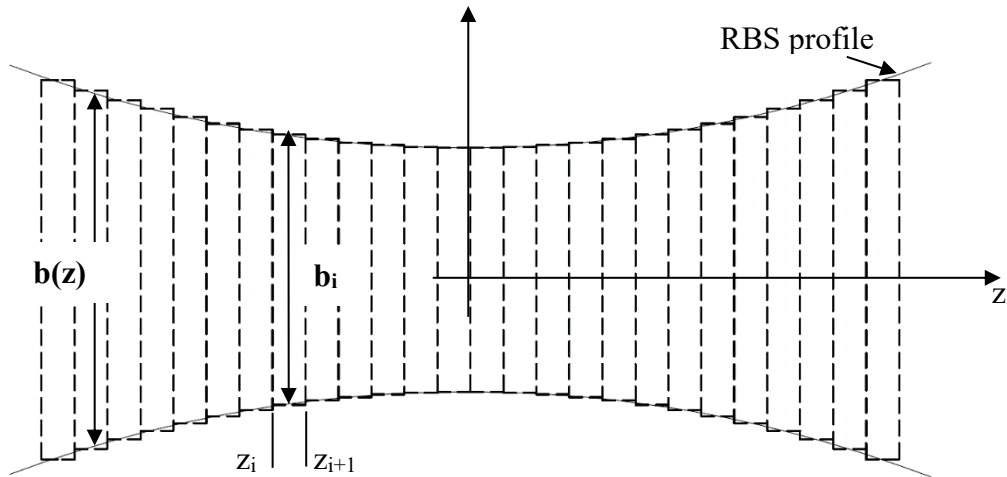


Figure 4.13 Beam element flange with varying width at the RBS

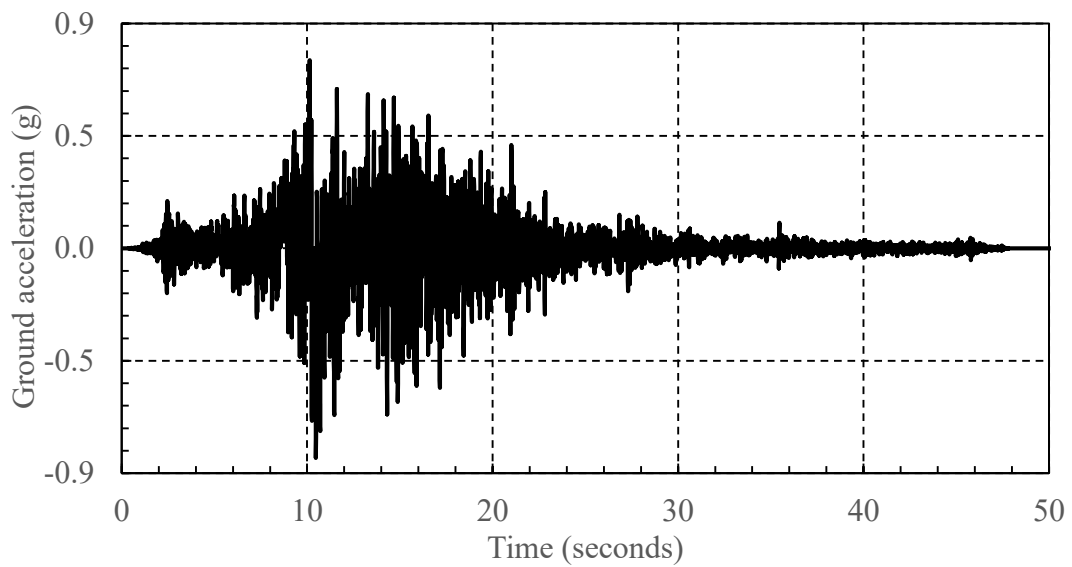


Figure 4.14 Acceleration time history (Landers 1992 scaled to PGA of 0.83g) for mesh convergence study of the beam element only model

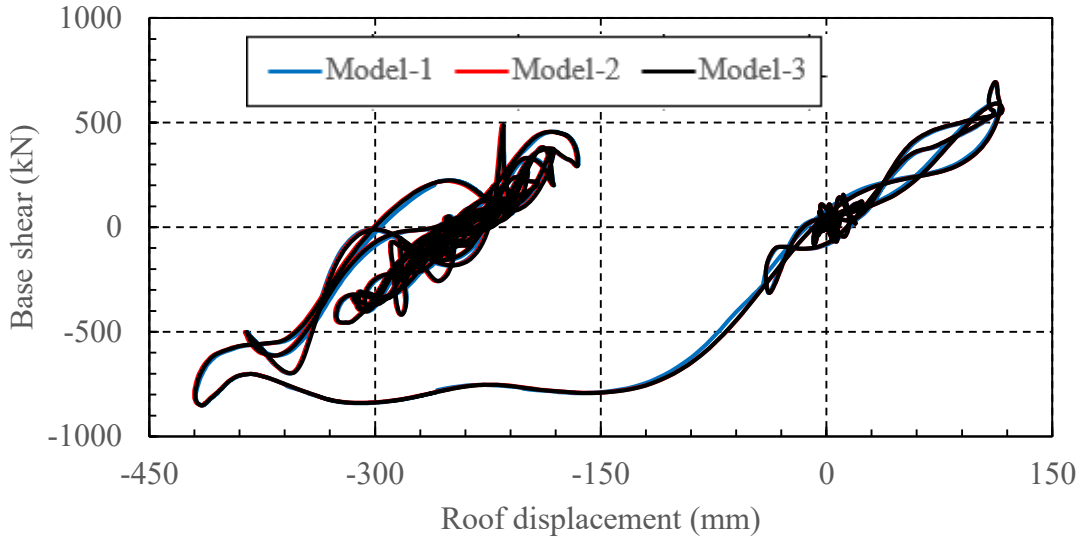


Figure 4.15 Comparisons of base shear versus roof displacement for different meshing schemes at RBS.

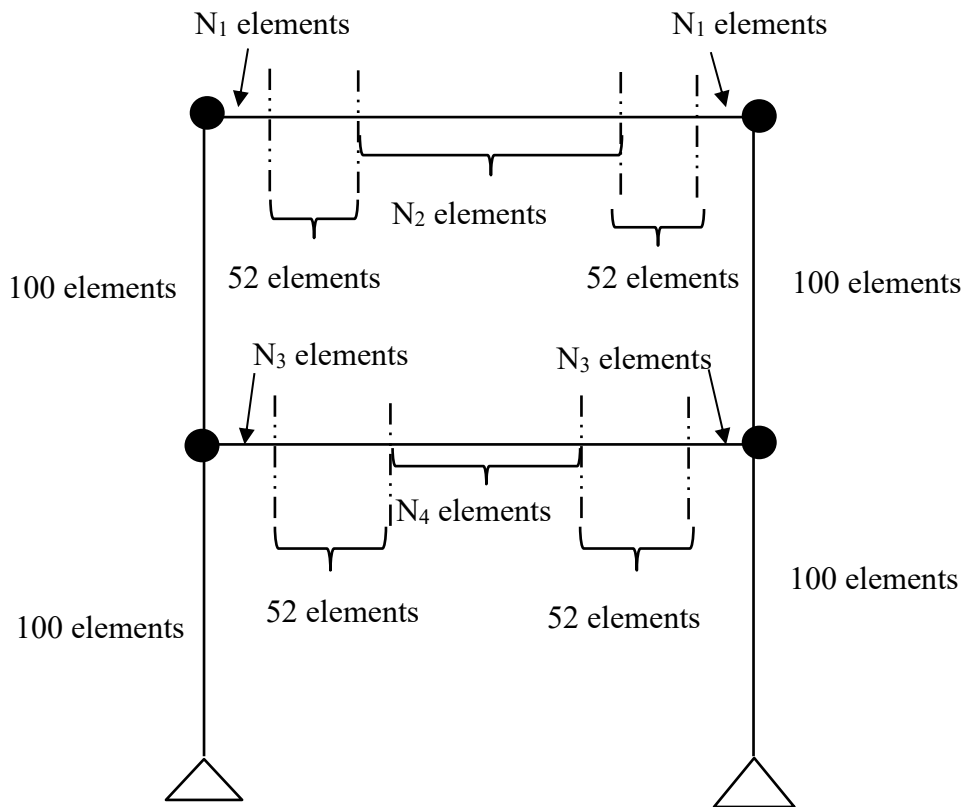


Figure 4.16 Modelling scheme for beam only model with 52 elements in RBS segment (See Table 4.4)

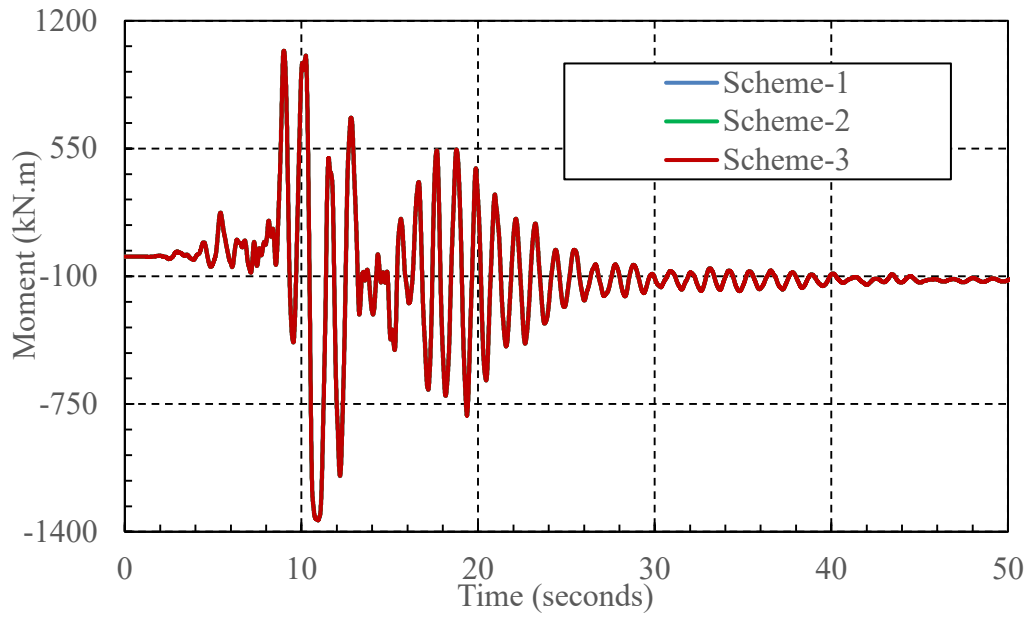


Figure 4.17 Moment time history at the center of first floor RBS with different mesh schemes for the rest of the model

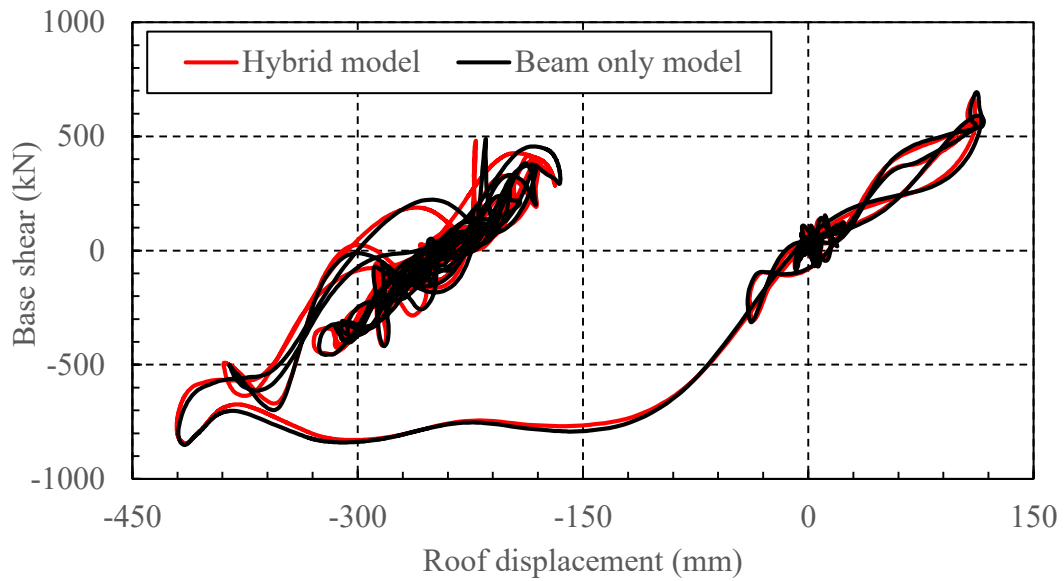


Figure 4.18 Comparisons of base shear versus roof displacement for hybrid and beam element only model

Chapter 5: Numerical Simulations of MRF with RBS

The displacements and forces used in the design of a structure can be obtained from non-linear dynamic analyses subjected to a suite of earthquake ground motion records that are compatible with target response spectrum of the site. However, there is a scarcity of these earthquake ground motion records. As a result, a suite of earthquake ground motion records is obtained by scaling the existing ground motion records such that their response spectrums match or exceed the target spectrum. A linear scaling method is adopted to scale a suite of earthquake ground motion records to match the target spectrum at the time period of the MRF with RBS connection detailed in Chapter 4. These records are then used to conduct non-linear dynamic analyses of the MRF at two different seismic hazard levels of maximum credible earthquake (MCE) and design basis earthquake (DBE). An MCE has a 2% probability of being exceeded in 50 years while a DBE has 10% probability of exceedance in 50 years. A parametric study using different combinations of material properties calibrated in Chapter 3 for the beams and columns of MRF are carried out to study effects strain rate dependent material properties have on the base shear, inter-storey drift and maximum moment at various locations of the MRF.

5.1 Dynamic Non-Linear Time history Analysis

Non-Linear dynamic time history analyses are performed on the proposed moment resisting frame using the scaled acceleration time histories at MCE and DBE hazard levels in finite element software ABAQUS (Dassault Systèmes 2017). The static and rate dependent material properties of materials G and H calibrated in Chapter 3 are assigned to the frame members in different combinations to carry out the analyses of the MRF. Material G and material H have static yield

strengths of 342 MPa and 373 MPa respectively. While material H has a higher strength, material G on the other hand has a higher strain rate amplification of the flow stress. Material G can be taken to represent steel at the nominal yield strength of 350 MPa and material H for steel at the probable yield strength of $R_y F_y$ of 385 MPa. The Rayleigh damping is calculated by using the first two translation modes having frequencies of 0.9 and 3.4 rad/s from the eigen value analyses of the MRF. Using Eq. (4.2) and a damping ratio (ε) of 3%, values of alpha (α) and beta (β) come out to be 0.27 s^{-1} and $2.4 \times 10^{-3} \text{ s}$ respectively.

In total, four combinations of material properties are used in the analyses of MRF; entire moment frame composed of material G (referred to as MATG), entire moment frame composed of material H (referred to as MATH), columns in the moment frame composed of material G while beams composed of material H (referred to as COMBH) and columns in the moment frame composed of material H while beams composed of material G (referred to as COMBG). A total of 192 analyses are performed with the material combinations, earthquake hazard levels, rate dependent and independent material properties. Figure 5.1 shows these combinations used to conduct the non-linear dynamic analyses of the ductile MRF for an earthquake record. The time to complete non-linear dynamic analysis of the MRF is 160 hours and 40 hours respectively for analyses with and without strain rate dependent material properties for all parametric combinations considered in this study.

5.2 Scaling of Earthquake Records

One of the important steps involved in conducting any non-linear dynamic time history analysis of a structure for design is the scaling of the earthquake records. This is due to the scarcity of the site-specific earthquake records and necessity to match the earthquake response spectrum to

the design hazard spectrum of the location for the time-period of interest. Linear scaling and spectral matching are two methods which are currently used to match the ground motion records to the target spectrum. In general, the linear scaling method applies a constant scaling factor to match the design spectrum such that the frequency content of the ground motions remains unchanged. Spectral matching is a technique which modifies the ground motion records in frequency or time domain to match their response spectrum to the target spectrum over a range of periods. There is not much guidance available to use spectral matching for non-linear dynamic analyses.

NBCC (2015) specifies a method of scaling wherein the ground motion spectrums are scaled to match the target spectrum at the defined period range. The ground motion records are first scaled individually over that period range and are followed by a second scaling with a factor based on the mean of the records in the suite of ground motion records. The period range is chosen to cover all the structural periods that contribute to the dynamic response of the structure. A minimum of five records have to be considered for that period range.

There is a complex arrangement of tectonic plates in British Columbia (specifically near the south-west) which results in three types of ground motions from crustal, sub-crustal and subduction earthquakes. Mario (2015) stated that in southwest BC, subduction earthquake controls the hazard for structures with the period greater than 1.5s. The contribution from crustal and sub-crustal earthquakes is dominant for the structures with time period less than 0.7s. The scaling method prescribed in NBCC (2015) try to deal with a wide variety of structures with different geometries and heights, and the chosen period range for scaling must cover all the structural periods contributing to the dynamic response of the structure. Thus, in order to match the design spectrum, records from all these three earthquake sources are needed. Nevertheless, if the

earthquake records are scaled to the design spectrum at the fundamental time period of the structure, the analyses with these ground motions can be expected to give results that are representative of the response since the first mode is the primary contributor to the dynamic response of the MRF for a simple two storey building with regular geometry modelled in Chapter 4. Hence a simpler scaling method from FEMA P695 (FEMA 2009) is chosen to scale the selected ground motion records in this study to investigate the effects of material properties strain rate dependency due to seismic earthquake ground motions.

Ground motion records have been selected from FEMA P695 (FEMA 2009) for scaling. A total number of 12 acceleration time histories with 8 far-field ground motion and 4 near-field ground motions from Los Angeles, California have been selected. This set contains 6 seismic events with their acceleration time histories in two perpendicular horizontal directions. Table 5.1 gives a summary of these records with their names, magnitude, time-step and peak ground acceleration (PGA).

The unscaled earthquake records are obtained from PEER NGA database (peer.berkeley.edu/ngawest2) and a two-step scaling method from FEMA P695 (FEMA 2009) has been adopted to scale these records. Each individual earthquake records are normalized by the geometric mean of the peak ground velocity of the two horizontal components. The median peak ground velocity of the suite of earthquake records is used to obtain a normalization factor using the following expression

$$N_i = \frac{\text{Median}(PGV_{set})}{PGV_{NM}} \text{ for } PGV_{NM} = \sqrt{PGV_{Fn,i} \times PGV_{Fp,i}} \quad (5.1)$$

where N_i is the normalization factor for i^{th} seismic event, $\text{Median}(PGV_{set})$ is the median of the peak ground velocities of the earthquake record set and PGV_{NM} is the geometric mean of peak ground velocity of the two horizontal components of a seismic event, $PGV_{Fn,i}$ and $PGV_{Fp,i}$. The

subscript F_n and F_p denote the normal and perpendicular directions of the i^{th} seismic event. The normalized acceleration time histories for the earthquake records in the normal and perpendicular directions are scaled with the normalization factors as

$$A_{Fn,i} = N_i \times AH_{Fn,i} \quad (5.2)$$

$$A_{Fp,i} = N_i \times AH_{Fp,i} \quad (5.3)$$

where $AH_{Fn,i}$ and $AH_{Fp,i}$ are the unnormalized horizontal acceleration components for i^{th} seismic event in the normal and perpendicular directions. The normalization procedure helps in removing any variability in the records due to the difference in magnitude, source type, distance to source and site conditions while preserving the overall ground motion strength of the record set.

The acceleration time histories in the record sets are then scaled to match the design spectrum of Victoria, British Columbia site class D from NBCC (2015) with a single scaling factor obtained by matching the median spectral acceleration of the earthquake record set at the fundamental time period of the proposed MRF, as shown in Fig.5.2. The scaling factor is given by

$$F_s = \frac{S(a)_{T_1}}{S(a)_{median,set}} \quad (5.4)$$

where $S(a)_{T_1}$ is the spectral acceleration of the design spectrum at the fundamental time period T_1 of the proposed MRF and $S(a)_{median,set}$ is median spectral acceleration of the earthquake record set.

The scaling factor calculated from Eq. (5.4) is 1.88, which represents the scaling for MCE hazard level. To analyze the MRF at the DBE hazard level, the ground motions are scaled by a factor of 1.26, which is 67 % of the factor for MCE hazard level. Figure 5.3 shows the spectral acceleration spectrum for DBE hazard level.

5.3 Numerical Simulations

Dynamic non-linear time history analyses on the MRF with RBS of the two storey building in Chapter 4 are carried out for the scaled ground motions records in Table 5.1 and parametric combinations in Fig. 5.1. The loading and the mass on the frame used in the simulations are shown in Fig. 5.4. Effects of strain rate dependent material properties on the response of the MRF are assessed and discussed. Results of the analyses on the strain rate, storey drifts and bending moments are analyzed and studied.

5.3.1 Maximum Strain Rate

Table 5.2 shows the maximum strain rate at the center of first floor RBS from the analyses with strain rate dependent material properties. The strain is taken at the top and bottom flanges at the RBS center. It can be seen that the maximum strain rate experienced at the first-floor RBS center is between 0.06 s^{-1} to 0.15 s^{-1} at MCE hazard level and 0.03 s^{-1} to 0.14 s^{-1} at DBE hazard level. The maximum strain rate for MATG and COMBG ranges from 0.06 s^{-1} to 0.15 s^{-1} and 0.03 s^{-1} to 0.12 s^{-1} at MCE and DBE hazard levels respectively. As expected, the maximum strain rate at MCE hazard level is generally higher than DBE hazard level, but not for every ground motion. However, the mean maximum strain rate at MCE hazard level is only slightly higher than at DBE level, even though the intensity at MCE is 50% higher than DBE level. The same trend can be seen for MATH and COMBH. There is only a small difference in the maximum strain rate between MATG and MATH for every earthquake record, and there is hardly any difference in the mean maximum strain rate. Since the plastic deformation mainly occurs at the RBS, MATG and COMBG with the material at the RBS also have almost the same maximum strain rate. Similarly,

it can be observed for MATH and COMBH as well. Overall, there is not much difference in the maximum strain rate between the four material combinations.

Results of the maximum strain rate at the roof RBS center in Table 5.3 also show the same characteristic as that for the first floor RBS center albeit with a higher magnitude. It can be seen that the maximum strain rate experienced at the roof RBS center is between 0.09 s^{-1} to 0.27 s^{-1} at MCE hazard level and 0.06 s^{-1} to 0.24 s^{-1} at DBE hazard level. Table 5.4 shows the maximum strain rate at the first floor and roof RBS center for MATG and MATH from analyses with and without strain rate dependent material properties at MCE hazard level. The maximum strain rate can go up to 0.30 s^{-1} at MCE hazard level without strain rate dependent material properties. There is not much difference in the predicted maximum strain rate between analyses conducted with and without strain rate dependent material properties.

Figures 5.5 and 5.6 shows the strain rate versus time at the first floor RBS center for analyses for MATG and MATH subjected to ground motion shown in Fig. 5.7 for earthquake record 8 at MCE and DBE hazard levels with strain rate dependent material properties at MCE and DBE hazard level. It can be seen that the maximum strain rate occurs at about the same time as the peak ground acceleration. The RBS experiences strain rate higher than 0.1 s^{-1} for one cycle and 0.01 s^{-1} only for a short duration, which implies that there is only very little adiabatic heating occurring to have any significant temperature rise to affect the material properties. With a few exceptions, the magnitude of the strain rate is generally higher at the MCE hazard level as compared to DBE level throughout the whole duration of earthquake ground motion excitation.

5.3.2 Bending Moment in MRF

It is expected that the bending moment generated in the frame is affected with the consideration of strain rate dependent material properties in the non-linear dynamic analyses. Moments from the analyses with and without rate dependent material properties at MCE and DBE hazard levels for different material combinations are compared and discussed. The probable moment (M_{pr}) calculated based on CSA S16-14 (CSA 2014) and Moment Connections for Seismic Application (CISC 2014) at first floor RBS center is 1405 kN.m and at the roof RBS center is 353 kN.m.

Figures 5.8 to 5.11 shows that the predicted maximum moment at first floor RBS center for material combination MATH and MATG at MCE and DBE hazard levels with and without strain rate dependent material properties. Table 5.5 shows the mean predicted maximum moment at the first floor RBS center. It can be seen that the predicted maximum moment at the first floor RBS center increases when material properties are considered to be strain rate dependent. As expected, the predicted maximum moment for MATH is higher than MATG, since MATH has a higher strength. Similarly, the predicted maximum moment is higher at MCE hazard level than DBE level. At MCE hazard level, the predicted maximum moment with and without strain rate dependent material properties of MATH is higher than the design probable maximum moment for all except two earthquake records. Even at DBE level, the predicted maximum moment for MATH exceeds the design probable moment for many of the earthquake records. For MATG, the predicted maximum moment for most of the earthquakes records still exceeds the design probable moment when strain rate material properties are considered in the analyses at MCE hazard level, but lower for most of the earthquake records when only static material properties are considered. The

predicted maximum moment are lower than the design probable moment for most or all earthquake records at DBE hazard level with and without strain rate dependent material properties.

The mean predicted maximum moment increases by 8.3% and 7.7% for MATG and MATH at MCE hazard levels, and 7.2% and 5.3% at DBE hazard level when material properties are considered to be strain rate dependent. Since, MATG with material G is more strain rate sensitive (higher isotropic yield stress amplification with strain rate), the rate of increase is higher for MATG than MATH. The rate of increase is lower at DBE than MCE hazard level as ground motion intensity is lower. As can also be observed in Figs 5.8 to 5.11, the mean predicted maximum moment exceeds the design probable moment at MCE hazard level for MATH with and without strain rate dependent material properties by 15% and 7%, and it slightly exceeds by 3% for MATG when strain rate dependent material properties are considered. At DBE hazard level, the mean predicted maximum moment only slightly exceeds the design probable moment for MATH when strain rate dependent material properties are considered. Since the response of the frame is governed mainly by the plastic hinge at the RBS, frame with similar material at RBS are expected to have similar response. It can be seen in Table 5.5 that analyses with MATG and COMBG, and MATH and COMBH, have comparable mean predicted maximum moment and rate of increase in the mean predicted maximum moment when strain rate dependent material properties are considered. Trends similar to Table 5.5 can be seen in Tables 5.6 and 5.7 for mean predicted maximum moment at first floor column face and centerline. Figure 5.12 shows the rate of increase in the mean predicted maximum moment at the first floor RBS center for MATG and MATH when strain rate dependent material properties are considered. Overall, the increase is slightly higher for MATG than MATH at MCE hazard level, but difference in the increase between MATG and MATH is slightly larger at DBE hazard level. This can be seen in Table 5.5 that the

difference of the increase in the mean predicted maximum moment is 0.6% at MCE hazard level and 1.9% at DBE hazard level. As observed in Chapter 3, the amplification factor on the isotropic yield stress decreases with strain, and thus does the difference in the amplification factor between material G and H also decreases with strain. Since the level of plastic strain is higher at MCE hazard level than DBE hazard level, the difference in the rate of increase between MATG and MATH is lower at MCE hazard level than DBE hazard level.

Table 5.8 shows the mean predicted maximum moment at the roof RBS center exceeds the probable maximum moment for all parametric combinations except MATG and COMBG with static material properties at DBE hazard level. The predicted maximum moment at the roof RBS center is much higher than expected. This could be result of high cyclic deformation strain range due to strain localization at RBS center where the cut in the flange width is close to 50%. However, no definite reason has yet been found to explain for this high predicted maximum moment. Further investigation is needed to look into the high predicted moment. Besides the high predicted maximum moment, other characteristics of the mean predicted maximum moment observed for the first floor RBS center are applicable to the roof RBS center. Trends similar to that at the roof RBS center in Table 5.8 in Tables 5.9 and 5.10 can be seen for the mean predicted maximum moment at the roof column face and centerline. Examples of moment versus curvature curves at the first floor and roof RBS center for MATH and MATG subjected to earthquake record 4 at DBE and MCE hazard level. with and without considering strain rate dependent material properties in the analyses are shown in Appendix C.

5.3.3 Strain Hardening

In the design of ductile moment resisting frame, the probable moment at the plastic hinge is calculated based on the strain hardening factor of 1.1 due to significant plastic deformation developed at the plastic hinge. The strain hardening factor can be calculated as

$$F_{sh} = \frac{M}{Z_x F_y} \quad (5.5)$$

where M is the moment, Z_x is the plastic section modulus about the axis of bending and F_y is the initial yield stress. Materials G and H considered in the numerical simulations have static initial yield stress of 342 MPa and 373 MPa respectively.

Figure 5.13 shows the strain hardening factor at the first floor RBS center with static material properties of MATG and MATH at MCE hazard level. It can be seen that the strain hardening factor is higher than 1.1 for all but two of the earthquake records with MATH having slightly higher factor than MATG. Table 5.11 shows the strain hardening factor at the roof and first floor RBS center for MATG and MATH with static material properties at DBE and MCE hazard level.

At MCE hazard level, the mean strain hardening factors are 1.18 and 1.22 for MATG and MATH at the first floor RBS center, and 1.31 and 1.33 at the roof RBS center. The factor is significantly higher than 1.1 specified in the design specification. With a lower ground intensity at DBE hazard level, the strain hardening factor is close to 1.1. Thus, a strain hardening factor greater than 1.1 should be considered for ductile moment resisting frame when drift limits are ignored.

5.3.4 Maximum Inter-Story Drift

The moment resisting frame in this study has been designed for strength and no deflection limit has been considered. Thus, the inter-storey drift is expected to be greater than the design limit

of 2.5%. The inter-storey drifts for the first-storey is 8.9% and second storey is 5.9% due to the seismic load calculated according to the equivalent static method with the initial estimated fundamental period of 0.44s, but the inter-storey drift are respectively 5.6% and 3.8% when calculated using the actual fundamental period of 1.1s.

Tables 5.12 and 5.13 shows the inter-storey drift for MATG and MATH, and MCE and DBE hazard levels at first floor. The mean maximum inter-storey drift of 4.1 to 4.3% at MCE hazard level clearly exceeds the design limit of 2.5% but is lower than the 8.9% calculated for fundamental period 0.44s and 5.6% for fundamental period 1.1s based on the equivalent static method seismic load. Overall, there is slight reduction in the inter-storey drift when strain rate dependent material properties are considered. Similarly, there is only a slight reduction at DBE hazard level when strain rate dependent material properties are considered albeit the inter-storey drift around 2.7% is much lower at DBE than MCE hazard level. However, inter-storey drift for all the earthquakes records does not consistently decrease when strain rate dependent material properties are considered, as seen in Fig. 5.14 on the percentage change in the peak inter-storey drift at first storey with strain rate dependent material properties.

Table 5.14, Figs. 5.15 and 5.16 shows the mean maximum inter-storey drift for MATG and MATH. The inter-storey drift for second storey of 3.3 to 3.6% is significantly lower than that for the first storey of 4.1 to 4.3% since the column at the second storey was way over designed. In general, considering the material properties to be strain rate dependent in the numerical simulations only slightly reduces the mean maximum inter-storey drift. MATG being weaker (less stiff) than MATH, also gives a higher inter-storey except for first storey at DBE hazard level where MATH gives a slightly higher mean maximum inter-storey drift.

Figures 5.17 and 5.18 show mean maximum inter-storey drift for COMBG and COMBH

material combinations. Similar to the mean maximum moment at the RBS center, the mean maximum inter-storey drift is governed by the material at the RBS. Thus, having the same materials at the RBS, the inter-storey drift for COMBG closely follows that for MATG, and COMBH for MATH.

5.3.5 Maximum Base Shear

A base shear of 440 kN is considered in the design based on the equivalent static method for calculating the seismic load based on the initial estimate fundamental period of 0.44s (239 kN based on the actual fundamental period of 1.1s). Comparisons are made on the maximum base shear from analyses with and without strain rate dependent material properties at MCE and DBE hazard levels for MATG, MATH, COMBH and COMBG. In Table 5.15, it shows that there is an increase in the mean maximum base shear when strain rate dependent material properties are used in the non-linear dynamic analyses. There is an increase of 7.1% and 5.4 % respectively at MCE and DBE hazard levels for MATG, and 5.9% and 4.5% for MATH. As expected, the mean maximum base shear is higher for MATH than MATG as material H is stronger than material G.

Similar to the mean maximum moment at the RBS center, the maximum base shear of COMBG closely follows that for MATG, and COMBH that of MATH, for having the same material at RBS. The predicted base shear is much higher than the design base shear, with difference at a ratio of 1.84 at MCE hazard level, and 1.62 at DBE hazard level for MATG. For MATH, the ratio is 1.98 at MCE hazard level and 1.71 at DBE hazard level. Even with static material properties, the difference is at a ratio of 1.70 at MCE hazard level and 1.54 at DBE hazard level for MATG. The difference at a ratio 1.88 at MCE hazard level and, 1.64 at DBE hazard level for MATH is observed for the numerical simulations. Further study is required to investigate the

big difference in the predicted and design base shear.

5.4 Numerical Simulations using Hybrid Model

Beam element only model of the frame has been used in all numerical simulations for efficiency. However, unlike the hybrid model (Chapter 4), beam element only model cannot replicate the non-uniaxial stress at the flange of RBS. Thus, analyses are carried out with the hybrid model and MATH for one pair of earthquake motions to study the differences in the results compared to beam element only model. Earthquake records 7 and 8 at MCE hazard level, shown in Figs. 5.19 and 5.20 are used in the numerical simulations.

It can be seen in Tables 5.16 and 5.17 that the predicted peak acceleration and displacement at both first floor and roof, the predicted maximum base shear and column centerline maximum moment at the first floor by the two models differ by no greater than 2.5%. However, there is a larger percentage difference in the predicted column centerline maximum moment at the roof because the magnitude of the column centerline moment at the roof is significantly smaller than that at the first floor. Thus, any change in the difference in column centerline moment at the first floor due to moment redistribution will affect the column moment at the roof disproportionately percentage wise, even though the change in the moment is of comparable magnitude. Figure 5.21 shows that the base shear versus roof displacement predicted by the beam element only model closely tracks that of the hybrid model that is subjected to the same acceleration time history shown in Fig. 5.19. Based on the overall small difference between results from hybrid and beam element only models, beam element only model can be considered to be adequate to be used in the numerical simulations in place of hybrid model while recognizing that there is a larger uncertainty in the moment predicted for the members at the roof level.

Table 5.1 Ground motions records from FEMA P695 (FEMA 2009).

EQ Code	Description	Recording station	Magnitude	Time Step	PGA(g)
1	F _n Northridge	Beverly Hills- Mulhol	6.7	0.005 s	0.41
2	F _p Northridge		6.7	0.005 s	0.52
3	F _n Hector	Hector	7.1	0.005 s	0.27
4	F _p Hector		7.1	0.005 s	0.34
5	F _n Loma Prieta	Gilroy Array #3	6.9	0.005 s	0.55
6	F _p Loma Prieta		6.9	0.005 s	0.37
7	F _n Cape Mendocino	Rio Dell Overpass	7.0	0.005 s	0.40
8	F _p Cape Mendocino		7.0	0.005 s	0.57
9	F _n Imperial Valley	El Centro Array #6	6.5	0.005 s	0.33
10	F _p Imperial Valley		6.5	0.005 s	0.44
11	F _p Landers	Lucerne	7.3	0.005 s	0.70
12	F _n Landers		7.3	0.005 s	0.79

Table 5.2 Maximum strain rate (s^{-1}) at first floor RBS center for different material combinations with strain rate dependent material properties

Eq. record	MATG		COMBG		MATH		COMBH	
	DBE	MCE	DBE	MCE	DBE	MCE	DBE	MCE
1	0.10	0.10	0.10	0.10	0.07	0.13	0.07	0.13
2	0.11	0.11	0.12	0.10	0.10	0.13	0.10	0.09
3	0.08	0.09	0.08	0.09	0.07	0.09	0.07	0.08
4	0.09	0.13	0.09	0.13	0.08	0.09	0.08	0.09
5	0.04	0.06	0.04	0.06	0.03	0.05	0.02	0.05
6	0.12	0.10	0.14	0.10	0.09	0.09	0.09	0.09
7	0.12	0.10	0.12	0.10	0.10	0.11	0.09	0.11
8	0.07	0.13	0.07	0.13	0.06	0.13	0.06	0.13
9	0.08	0.13	0.11	0.13	0.07	0.09	0.08	0.10
10	0.10	0.15	0.12	0.15	0.09	0.15	0.11	0.15
11	0.09	0.14	0.09	0.14	0.14	0.15	0.09	0.15
12	0.04	0.06	0.04	0.07	0.03	0.07	0.03	0.06
Mean	0.09	0.11	0.09	0.10	0.08	0.11	0.07	0.10

Table 5.3 Maximum strain rate (s^{-1}) at roof RBS center for different material combinations with strain rate dependent material properties

Eq. record	MATG		COMBG		MATH		COMBH	
	DBE	MCE	DBE	MCE	DBE	MCE	DBE	MCE
1	0.15	0.17	0.15	0.17	0.13	0.23	0.14	0.22
2	0.19	0.17	0.19	0.18	0.24	0.25	0.18	0.24
3	0.14	0.19	0.14	0.19	0.13	0.18	0.12	0.18
4	0.16	0.17	0.16	0.17	0.14	0.15	0.14	0.16
5	0.07	0.12	0.07	0.13	0.06	0.09	0.06	0.09
6	0.18	0.19	0.18	0.19	0.16	0.20	0.19	0.16
7	0.14	0.18	0.14	0.19	0.21	0.22	0.20	0.22
8	0.15	0.27	0.11	0.27	0.14	0.22	0.14	0.24
9	0.11	0.20	0.10	0.20	0.09	0.15	0.09	0.19
10	0.15	0.22	0.15	0.22	0.15	0.21	0.22	0.18
11	0.13	0.21	0.13	0.21	0.20	0.23	0.20	0.22
12	0.01	0.10	0.03	0.11	0.02	0.09	0.02	0.09
Mean	0.13	0.18	0.13	0.19	0.14	0.19	0.14	0.18

Table 5.4 Maximum strain rate (s^{-1}) at first floor and roof RBS center for MATG and MATH with and without rate dependent material properties at MCE hazard level

Eq. record	MATG		MATH		MATG		MATH	
	First floor				Roof			
	Static	Rate	Static	Rate	Static	Rate	Static	Rate
1	0.10	0.10	0.10	0.13	0.17	0.17	0.16	0.23
2	0.11	0.11	0.12	0.13	0.16	0.17	0.14	0.25
3	0.09	0.09	0.09	0.09	0.21	0.19	0.19	0.18
4	0.14	0.13	0.10	0.09	0.17	0.17	0.15	0.15
5	0.10	0.06	0.08	0.05	0.15	0.12	0.12	0.09
6	0.11	0.10	0.10	0.09	0.19	0.19	0.18	0.20
7	0.12	0.10	0.10	0.11	0.14	0.18	0.14	0.22
8	0.15	0.13	0.14	0.13	0.30	0.27	0.26	0.22
9	0.11	0.13	0.11	0.09	0.19	0.20	0.17	0.15
10	0.17	0.15	0.15	0.15	0.24	0.22	0.19	0.21
11	0.12	0.14	0.11	0.15	0.23	0.21	0.17	0.23
12	0.09	0.06	0.06	0.07	0.12	0.10	0.09	0.09
Mean	0.12	0.11	0.11	0.11	0.18	0.18	0.16	0.19

Table 5.5 Mean predicted maximum moment (kN.m) at the first floor RBS center with and without strain rate dependent material properties, and probable maximum moment, M_{pr} (1405 kN.m)

Material Combinations	Predicted mean maximum moment (kN.m)			$\frac{M_s}{M_{pr}}$	$\frac{M_r}{M_{pr}}$
	Static, M_s	Rate, M_r	% increase		
MCE					
MATG	1340	1452	8.3	0.95	1.03
MATH	1509	1626	7.7	1.07	1.16
COMBG	1342	1454	8.3	0.96	1.03
COMBH	1522	1618	6.3	1.08	1.15
DBE					
MATG	1247	1337	7.2	0.89	0.95
MATH	1386	1460	5.3	0.99	1.04
COMBG	1247	1337	7.2	0.89	0.95
COMBH	1383	1458	5.4	0.98	1.04

Table 5.6 Mean predicted maximum moment (kN.m) at the first floor column face with and without strain rate dependent material properties, and probable maximum moment, M_{cf} (1641 kN.m)

Material Combinations	Predicted mean maximum moment (kN.m)			$\frac{M_s}{M_{cf}}$	$\frac{M_r}{M_{cf}}$
	Static, M_s	Rate, M_r	% increase		
MCE					
MATG	1562	1692	8.3	0.95	1.03
MATH	1759	1894	7.7	1.07	1.15
COMBG	1564	1694	8.3	0.95	1.03
COMBH	1773	1885	6.3	1.08	1.15
DBE					
MATG	1454	1559	7.3	0.88	0.95
MATH	1615	1701	5.3	0.98	1.03
COMBG	1454	1560	7.3	0.88	0.95
COMBH	1612	1699	5.4	0.98	1.03

Table 5.7 Mean predicted maximum moment (kN.m) at the first floor column centerline with and without strain rate dependent material properties and, probable maximum moment, M_c (1841 kN.m)

Material Combinations	Predicted mean maximum moment (kN.m)			$\frac{M_s}{M_c}$	$\frac{M_r}{M_c}$
	Static, M_s	Rate, M_r	% increase		
MCE					
MATG	1746	1891	8.3	0.95	1.03
MATH	1965	2117	7.7	1.07	1.16
COMBG	1749	1893	8.3	0.96	1.03
COMBH	1981	2106	6.3	1.08	1.15
DBE					
MATG	1625	1742	7.2	0.89	0.95
MATH	1805	1901	5.3	0.99	1.04
COMBG	1626	1743	7.2	0.89	0.95
COMBH	1801	1901	5.4	0.98	1.04

Table 5.8 Mean predicted maximum moment (kN.m) at the roof RBS center with and without strain rate dependent material properties, and probable maximum moment, M_{pr} (353 kN.m)

Material Combinations	Predicted mean maximum moment (kN.m)			$\frac{M_s}{M_{pr}}$	$\frac{M_r}{M_{pr}}$
	Static, M_s	Rate, M_r	% increase		
MCE					
MATG	372	405	8.7	1.05	1.15
MATH	411	439	6.7	1.16	1.24
COMBG	374	407	8.7	1.06	1.15
COMBH	410	435	6.1	1.16	1.23
DBE					
MATG	341	364	6.9	0.97	1.03
MATH	373	390	4.7	1.06	1.10
COMBG	341	365	6.9	0.97	1.03
COMBH	371	389	4.7	1.05	1.10

Table 5.9 Mean predicted maximum moment (kN.m) at the roof column face with and without strain rate dependent material properties, and probable maximum moment, M_{cf} (391 kN.m)

Material Combinations	Predicted mean maximum moment (kN.m)			$\frac{M_s}{M_{cf}}$	$\frac{M_r}{M_{cf}}$
	Static, M_s	Rate, M_r	% increase		
MCE					
MATG	411	447	8.8	1.05	1.14
MATH	454	486	7.0	1.16	1.24
COMBG	412	449	8.8	1.05	1.15
COMBH	453	482	6.7	1.16	1.23
DBE					
MATG	378	405	7.0	0.97	1.03
MATH	413	433	4.9	1.06	1.10
COMBG	378	405	7.0	0.97	1.03
COMBH	412	432	4.9	1.05	1.10

Table 5.10 Mean predicted maximum moment (kN.m) at the roof column centerline with and without strain rate dependent material properties, and probable maximum moment, M_c (439 kN.m)

Material Combination	Predicted mean maximum moment (kN.m)			$\frac{M_s}{M_c}$	$\frac{M_r}{M_c}$
	Static, M_s	Rate, M_r	% increase		
MCE					
MATG	465	505	8.7	1.05	1.14
MATH	513	548	6.9	1.16	1.24
COMBG	466	507	8.7	1.05	1.15
COMBH	512	544	6.3	1.16	1.23
DBE					
MATG	428	457	6.8	0.97	1.03
MATH	467	489	4.8	1.06	1.10
COMBG	428	458	6.9	0.97	1.03
COMBH	466	488	4.8	1.05	1.10

Table 5.11 Mean predicted strain hardening factor at the roof and first-floor RBS center for MATG and MATH with static material properties

Material Combinations	MCE		DBE	
	First floor	Roof	First floor	Roof
MATG	1.18	1.31	1.10	1.20
MATH	1.22	1.33	1.12	1.20
COMBH	1.18	1.32	1.11	1.19
COMBG	1.22	1.31	1.10	1.21

Table 5.12 Predicted maximum inter-storey drift (%) for individual earthquake record at first floor for MATG and MATH at MCE hazard level

EQ. records	MATG			MATH		
	Static	Rate	% change	Static	Rate	% change
1	4.5	4.4	-2.4	4.4	4.2	-3.9
2	5.5	5.7	4.2	5.8	5.80	-0.4
3	2.9	3.2	13	3.4	3.6	6.2
4	7.2	6.6	-7.6	6.5	5.3	-18.3
5	2.2	2.2	0.0	2.2	2.2	0.0
6	6.2	5.8	-6.1	5.8	5.5	-5.1
7	3.8	4.0	2.6	3.9	4.1	3.0
8	3.9	3.8	-2.9	3.8	3.7	-2.6
9	3.1	3.2	4.2	3.2	3.2	1.6
10	5.1	4.8	-5.9	4.8	4.6	-4.8
11	5.8	5.4	-5.3	5.4	5.1	-5.8
12	1.6	1.7	3.6	1.7	1.7	1.2
Mean	4.3	4.2	-1.7	4.3	4.1	-2.4

Table 5.13 Predicted maximum inter-storey drift (%) for individual earthquake record at first floor for MATG and MATH at DBE hazard level

EQ. records	MATG			MATH		
	Static	Rate	% change	Static	Rate	% change
1	2.6	2.9	10	3.1	3.2	4.5
2	3.9	3.5	-4.7	3.5	3.4	-3.2
3	2.7	2.6	-2.0	2.8	2.7	-2.2
4	3.6	3.5	-3.1	3.7	3.6	-0.2
5	1.5	1.5	0.0	1.5	1.5	0.0
6	3.8	3.7	-2.2	3.7	3.6	-2.4
7	3.2	3.3	3.7	3.3	3.4	1.9
8	2.41	2.41	-0.3	2.4	2.4	-0.1
9	2.2	2.2	-0.7	2.2	2.17	-0.5
10	2.8	2.7	-4.6	2.7	2.6	-1.4
11	2.9	2.7	-6.8	2.7	2.7	-1.7
12	1.3	1.3	1.6	1.3	1.3	1.2
Mean	2.7	2.7	-0.7	2.7	2.7	-0.3

Table 5.14 Mean predicted maximum inter-storey drifts (%) for the suite of earthquake records with and without strain rate dependent material properties

Material Combinations	MCE			DBE		
	Static	Rate	% decrease	Static	Rate	% decrease
First floor						
MATG	4.3	4.2	1.7	2.7	2.7	0.7
MATH	4.3	4.1	2.4	2.7	2.7	0.3
COMBH	4.3	4.2	1.7	2.7	2.6	0.4
COMBG	4.3	4.1	3.0	2.7	2.7	0.7
Roof						
MATG	3.6	3.5	2.8	2.3	2.2	2.7
MATH	3.5	3.3	5.9	2.2	2.1	3.3
COMBH	3.7	3.6	2.2	2.3	2.2	3.1
COMBG	3.4	3.3	3.6	2.2	2.1	2.8

Table 5.15 Mean predicted maximum base shear (kN) for different material combinations with and without strain rate dependent material properties, and design base shear, V_d (440 kN)

Combinations	Predicted mean maximum base shear (kN)			$\frac{V_s}{V_d}$	$\frac{V_r}{V_d}$
	Static, V_s	Rate, V_r	% increase		
MCE					
MATG	759	813	7.1	1.70	1.84
MATH	826	875	5.9	1.88	1.98
COMBG	776	826	6.4	1.76	1.88
COMBH	802	856	6.7	1.82	1.95
DBE					
MATG	677	714	5.4	1.54	1.62
MATH	720	753	4.5	1.64	1.71
COMBG	713	716	5.6	1.62	1.63
COMBH	680	748	4.8	1.55	1.70

Table 5.16 The results for hybrid model for acceleration time history (Fig 5.19) for MATH at MCE hazard level

	Hybrid	Beam	Relative difference (%)
Peak first floor acceleration (g)	0.80	0.82	2.50
Peak roof acceleration (g)	1.32	1.34	1.52
Peak first floor displacement (mm)	183	183	0.33
Peak roof displacement (mm)	337	338	0.30
Maximum base shear (kN)	939	946	0.75
Column centerline max moment at first floor (kN.m)	2078	2111	1.60
Column centerline max moment at roof (kN.m)	598	551	-7.86

Table 5.17 The results for hybrid model for acceleration time history (Fig 5.20) for MATH at MCE hazard level

	Hybrid	Beam	Relative difference (%)
Peak first floor acceleration (g)	1.14	1.14	2.50
Peak roof acceleration (g)	2.14	2.14	1.52
Peak first floor displacement (mm)	168	168	0.33
Peak roof displacement (mm)	292	292	0.30
Maximum base shear (kN)	936	943	0.75
Column centerline max moment at first floor (kN.m)	2002	2037	1.72
Column centerline max moment at roof (kN.m)	593	549	-7.42

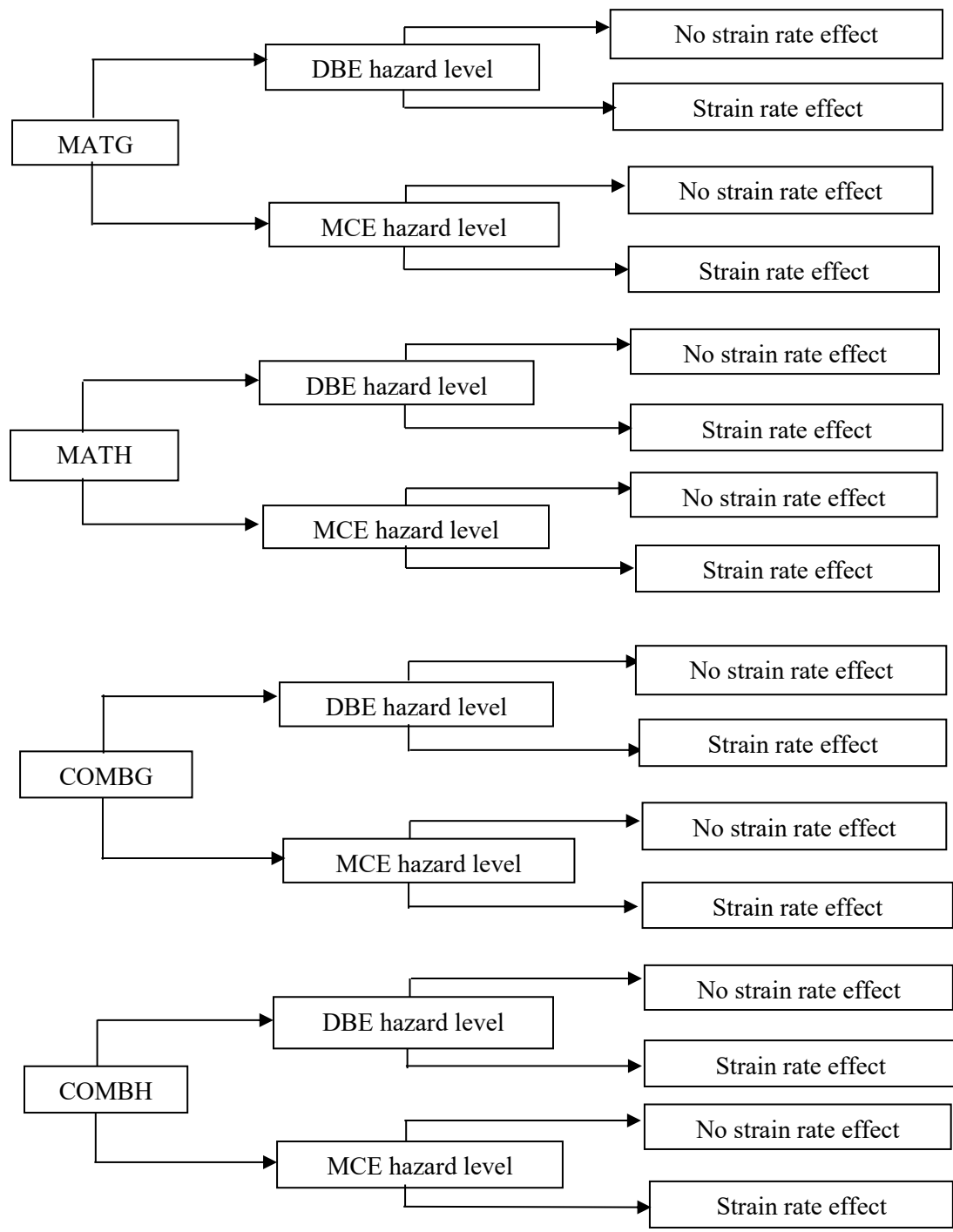


Figure 5.1 Combinations used to conduct non-linear dynamic analyses for an earthquake record

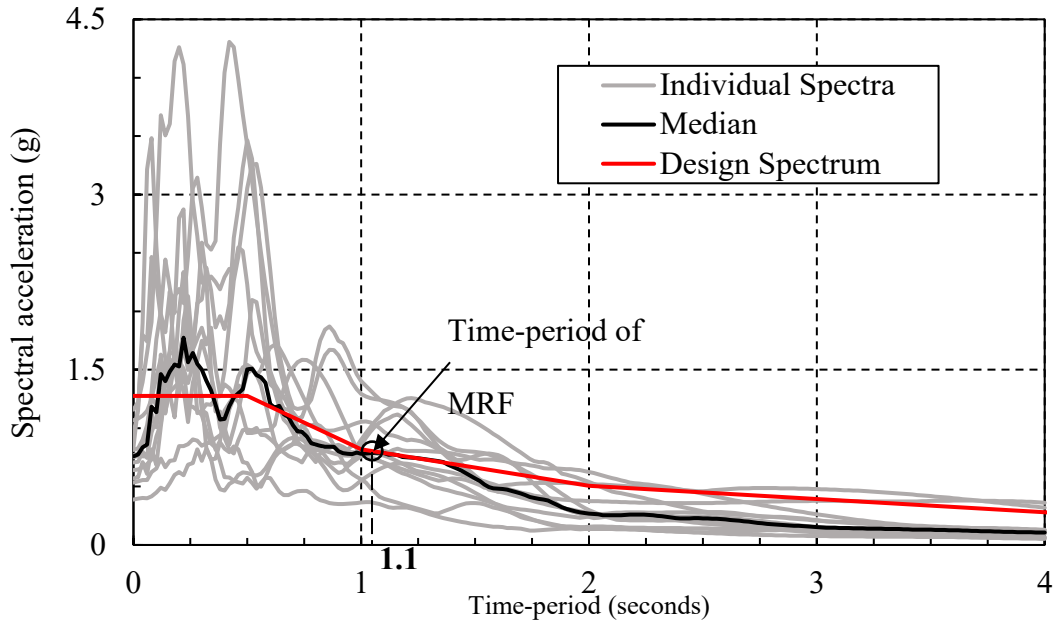


Figure 5.2 Spectral acceleration for MCE hazard level

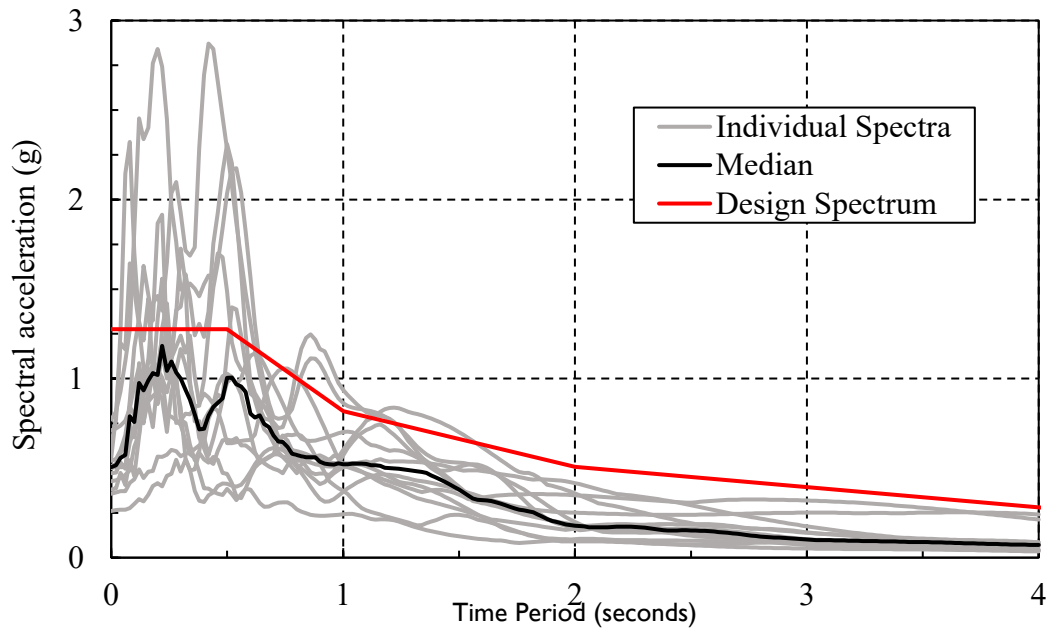


Figure 5.3 Spectral acceleration for DBE hazard level

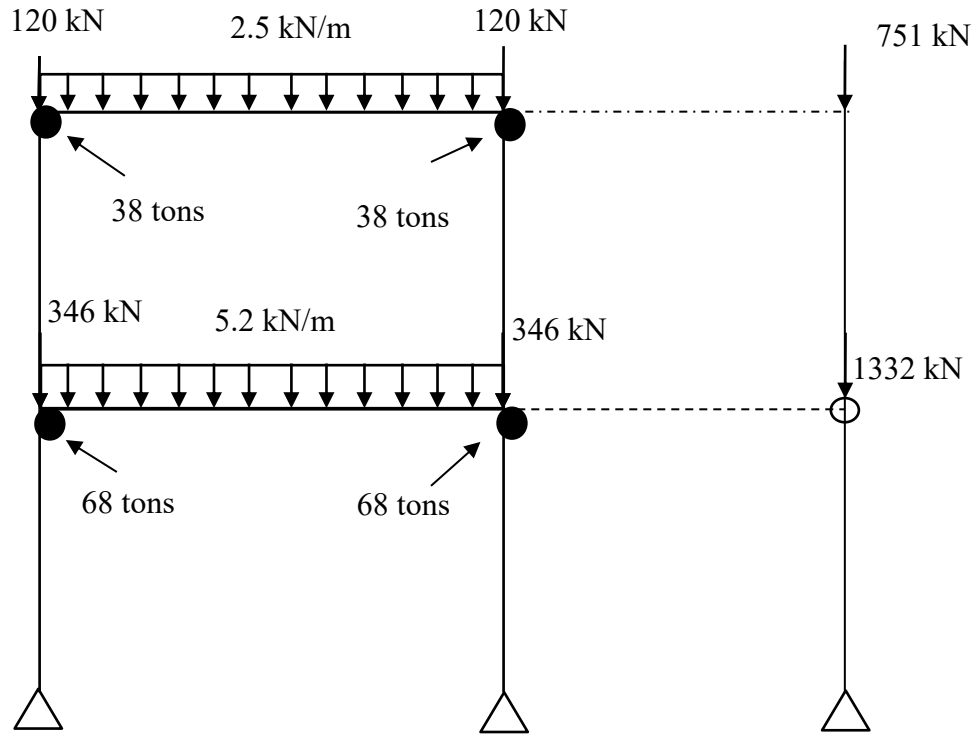


Figure 5.4 The loading and mass on the MRF of the two storey building from Chapter 4

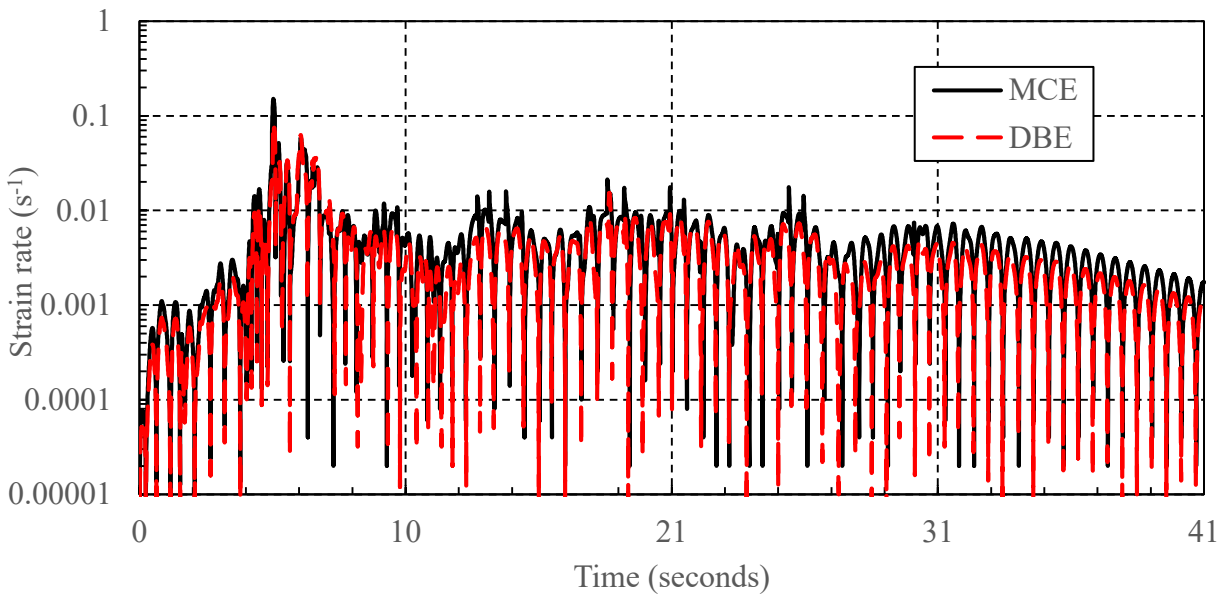


Figure 5.5 Strain rate versus time for MATG at first floor RBS center for earthquake record 8 at MCE and DBE hazard level

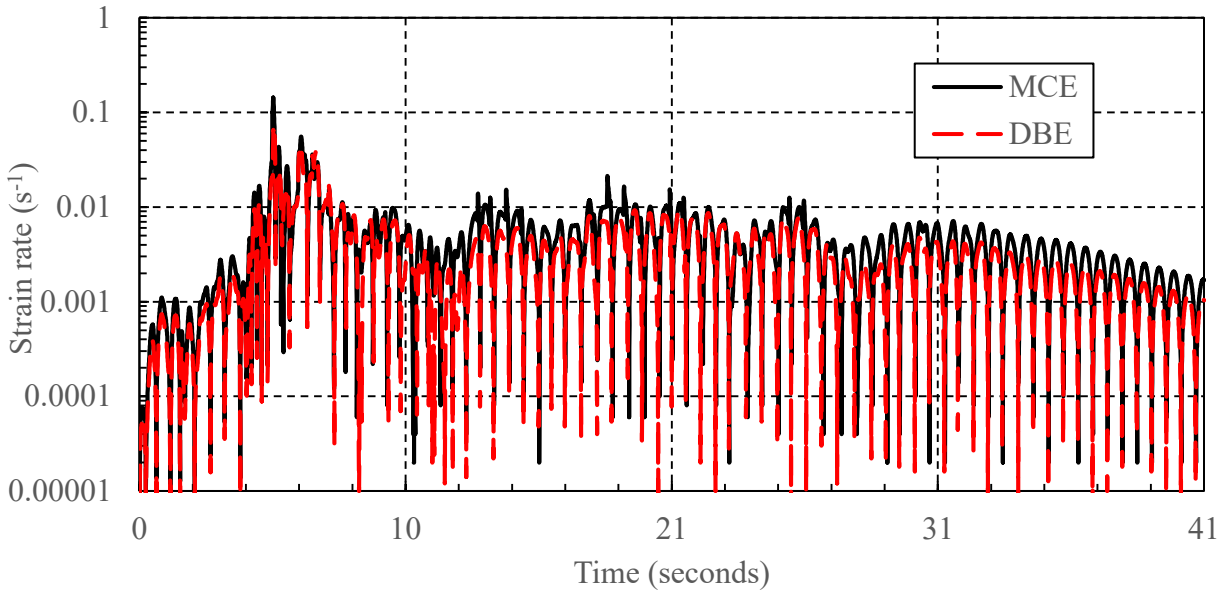


Figure 5.6 Strain rate versus time for MATH at the first floor RBS center for earthquake record 8 at MCE and DBE hazard level

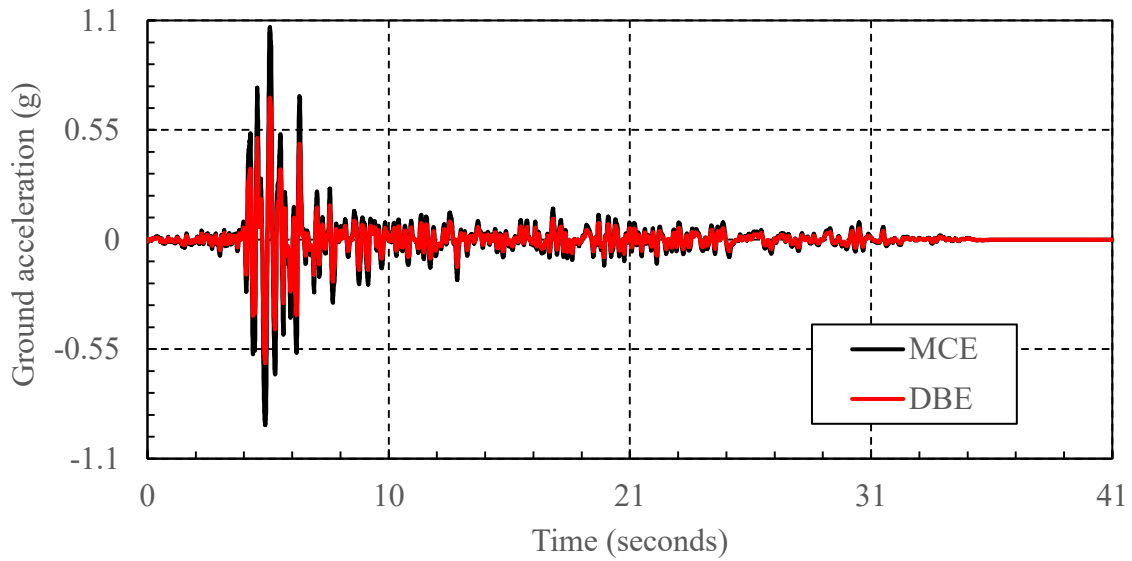


Figure 5.7 Ground acceleration time history for earthquake record 8 at MCE and DBE hazard levels.

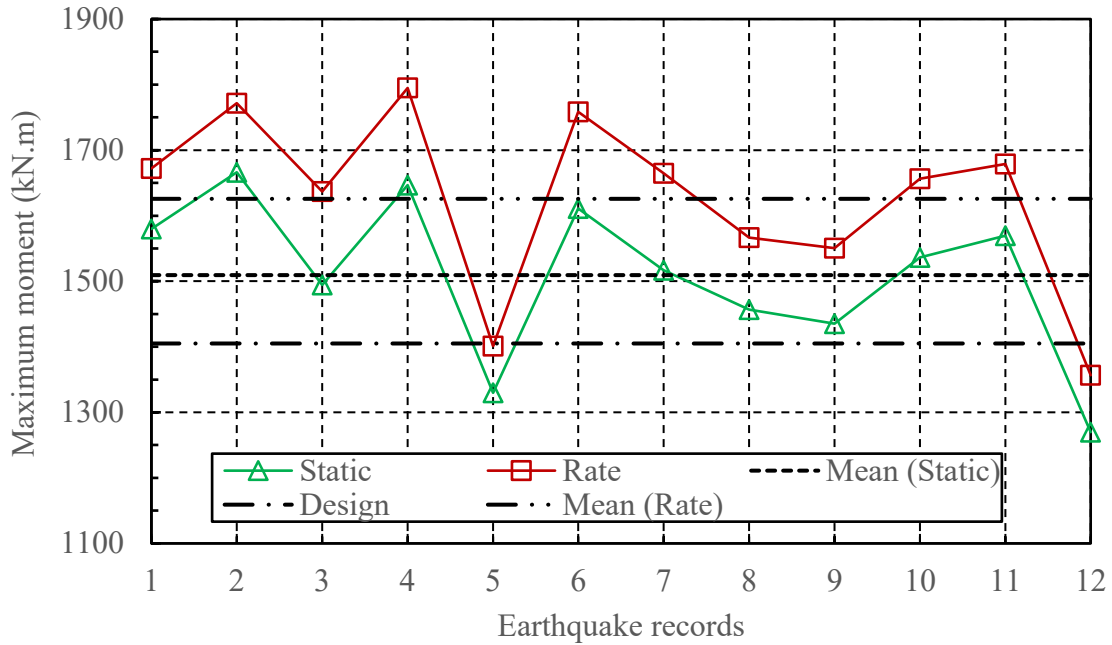


Figure 5.8 Maximum moment at the first floor RBS center with and without strain rate dependent material properties for MATH at MCE hazard level.

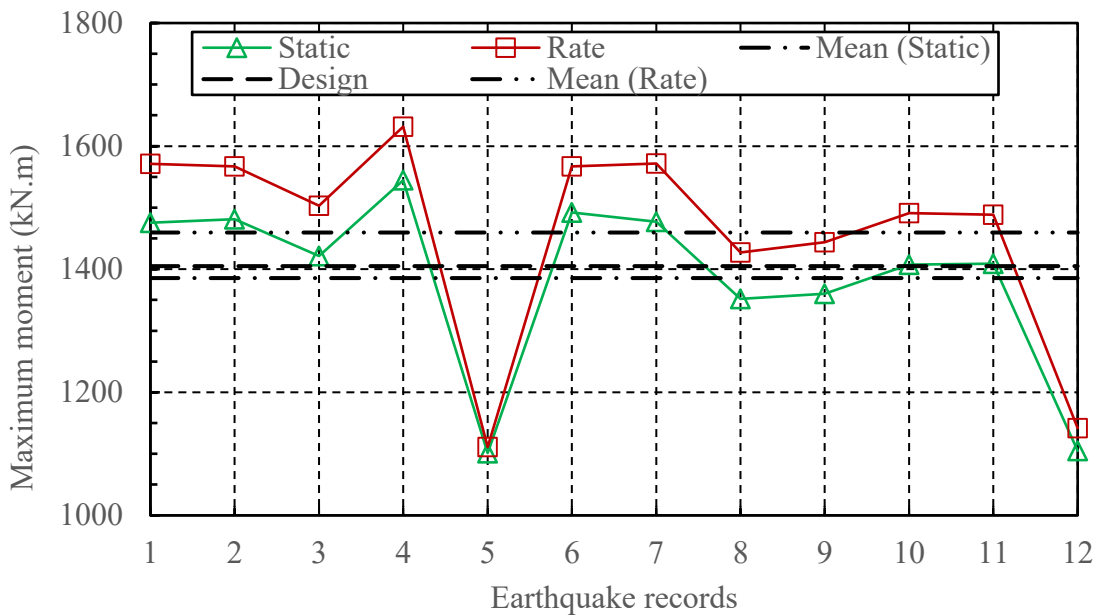


Figure 5.9 Maximum moment at the first floor RBS center with and without strain rate dependent material properties for MATH at DBE hazard level

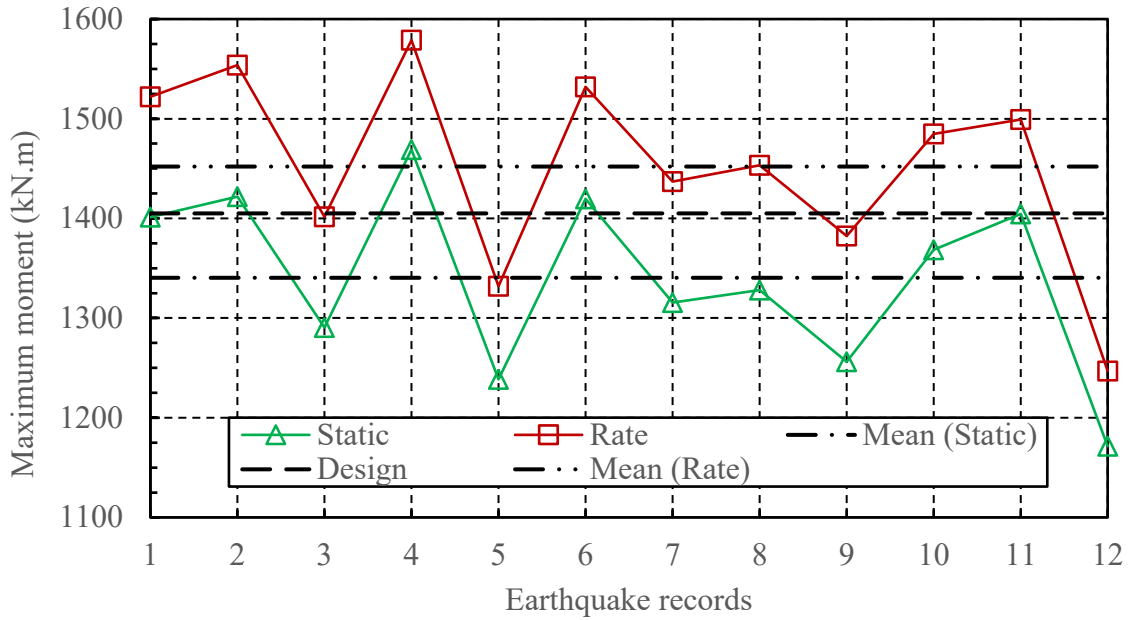


Figure 5.10 Maximum moment at the first floor RBS center with and without strain rate dependent material properties for MATG at MCE hazard level

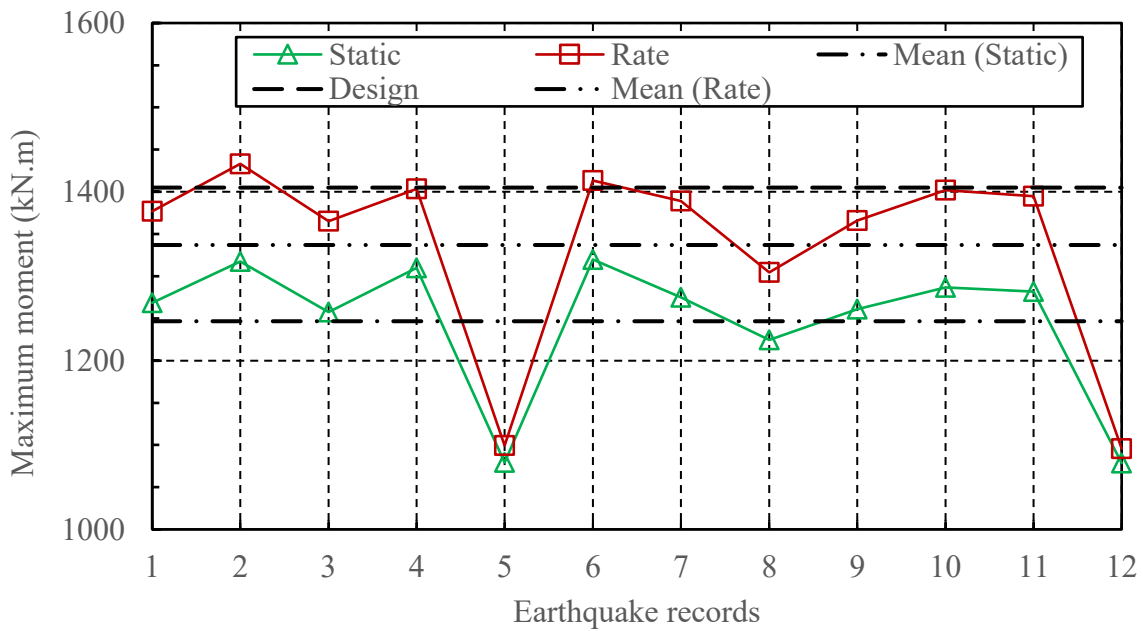


Figure 5.11 Maximum moment at the first floor RBS center with and without strain rate dependent material properties for MATG at DBE hazard level

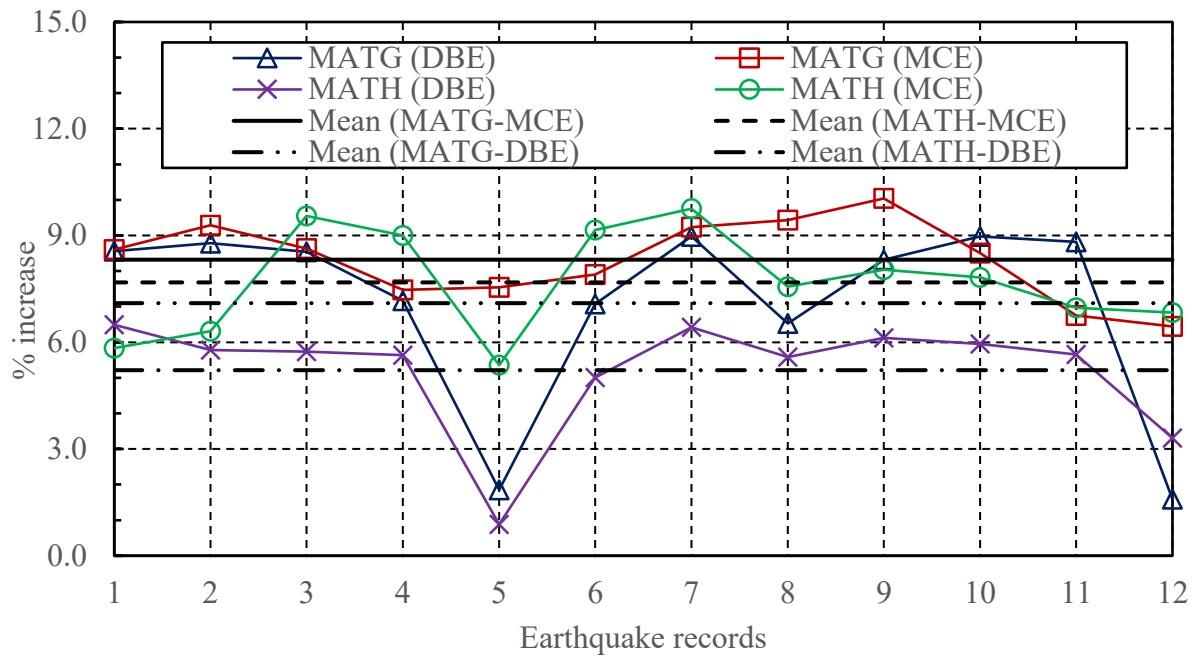


Figure 5.12 Increase (%) in the maximum moment with strain rate dependent material properties for MATG and MATH at first floor RBS center at DBE and MCE hazard levels.

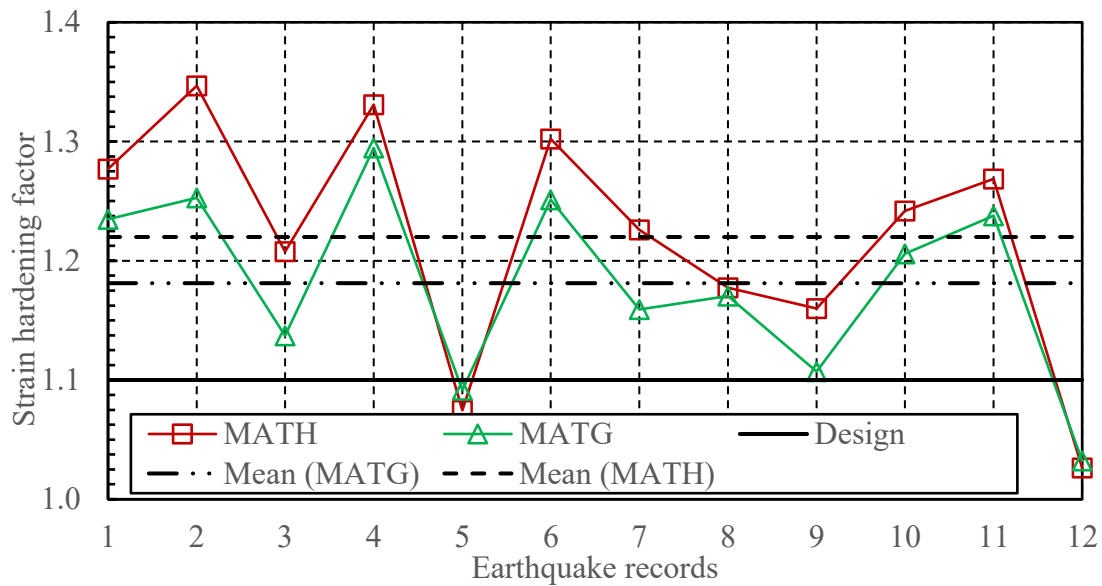


Figure 5.13 Predicted strain hardening factor at the first floor RBS center for MATG and MATH with static material properties at MCE hazard level

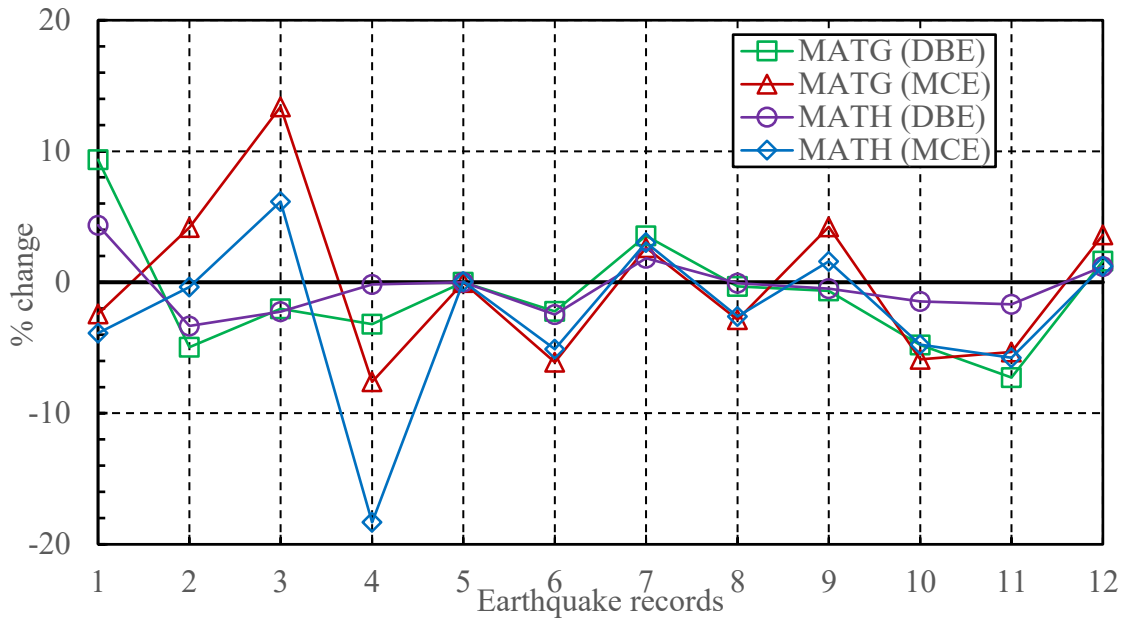


Figure 5.14 Percentage change in the peak inter-storey drift for first storey with strain rate dependent material properties for MATG and MATH at DBE and MCE hazard levels.

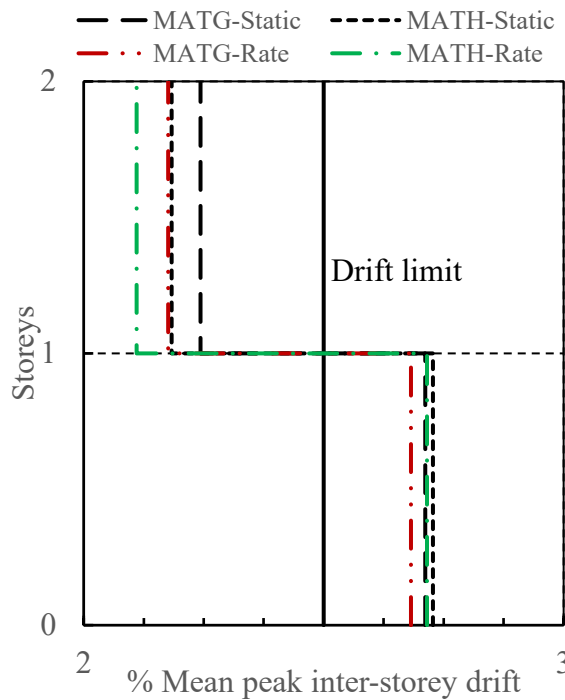


Figure 5.15 Average peak inter-storey drift with and without rate dependent properties for MATG and MATH at DBE hazard level

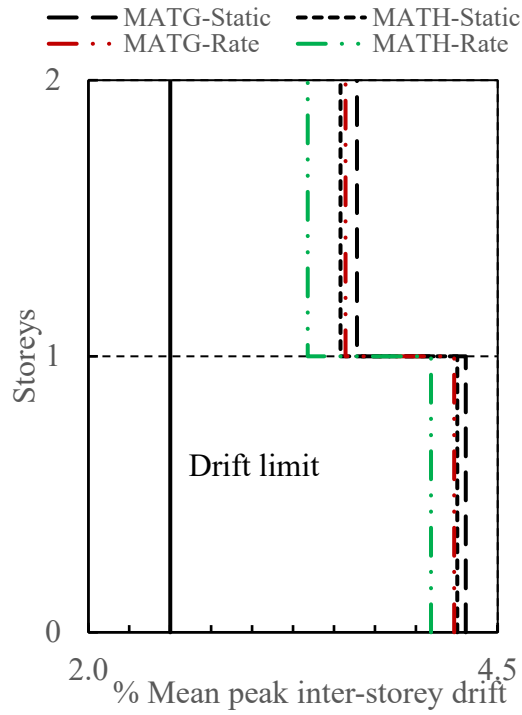


Figure 5.16 Average peak inter-storey drift with and without rate dependent properties for MATG and MATH at MCE hazard level

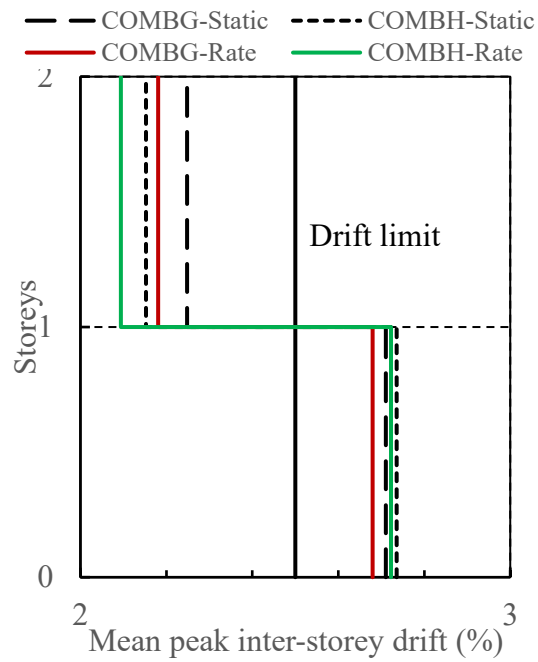


Figure 5.17 Average peak inter-storey drift with and without rate dependent properties for the suite of earthquake for COMBH and COMBG at DBE hazard level

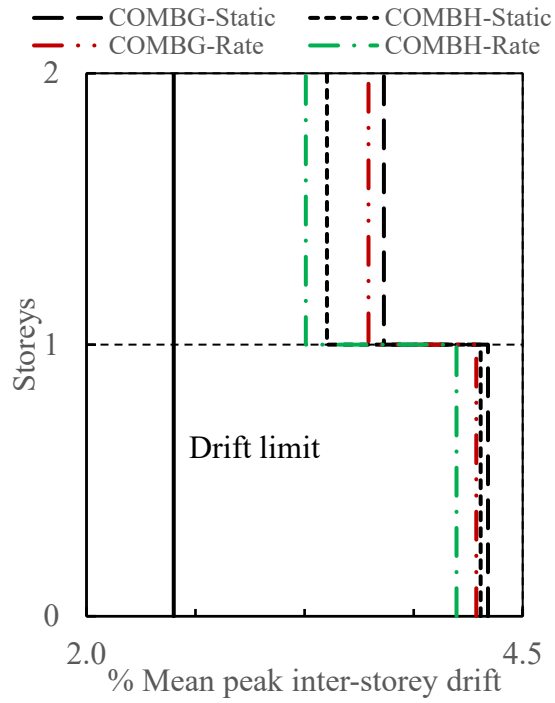


Figure 5.18 Average peak inter-storey drift with and without rate dependent properties for the suite of earthquake for COMBH and COMBG at MCE hazard level

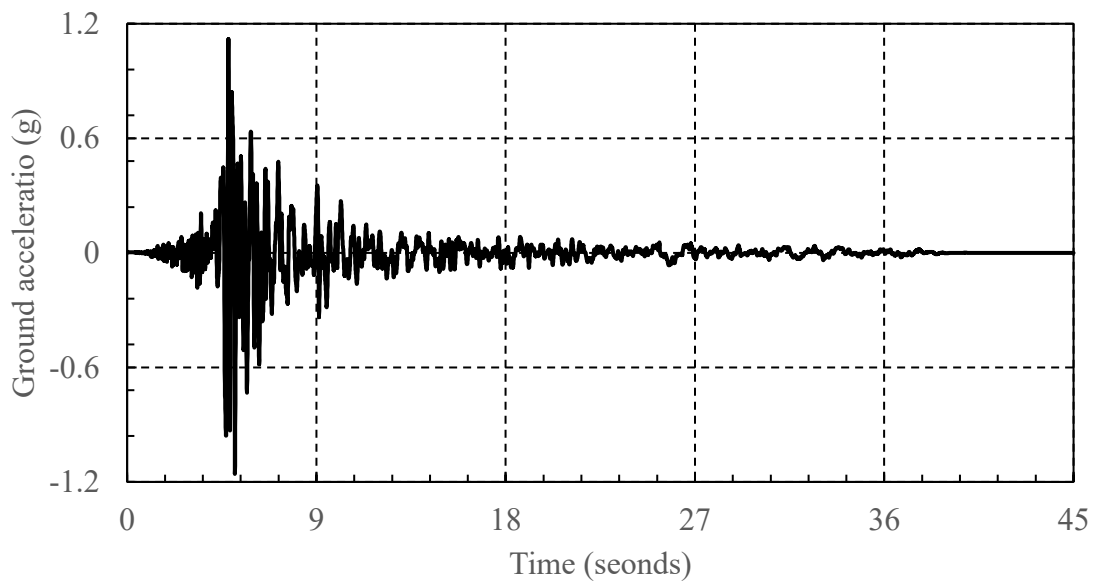


Figure 5.19 Ground acceleration time history for ground motion record 7 at MCE hazard level

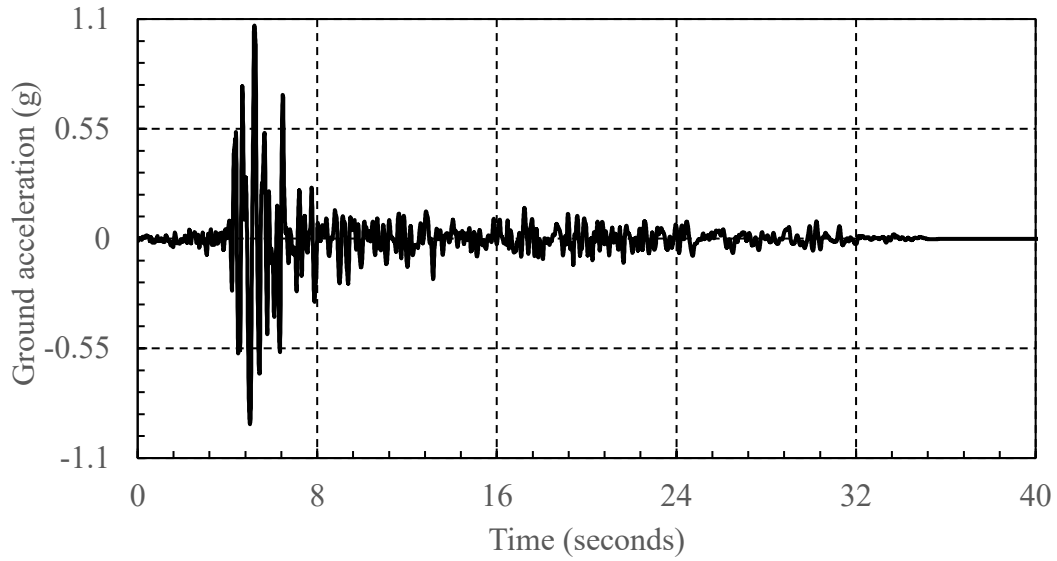


Figure 5.20 Ground acceleration time history for ground motion record 8 at MCE hazard level

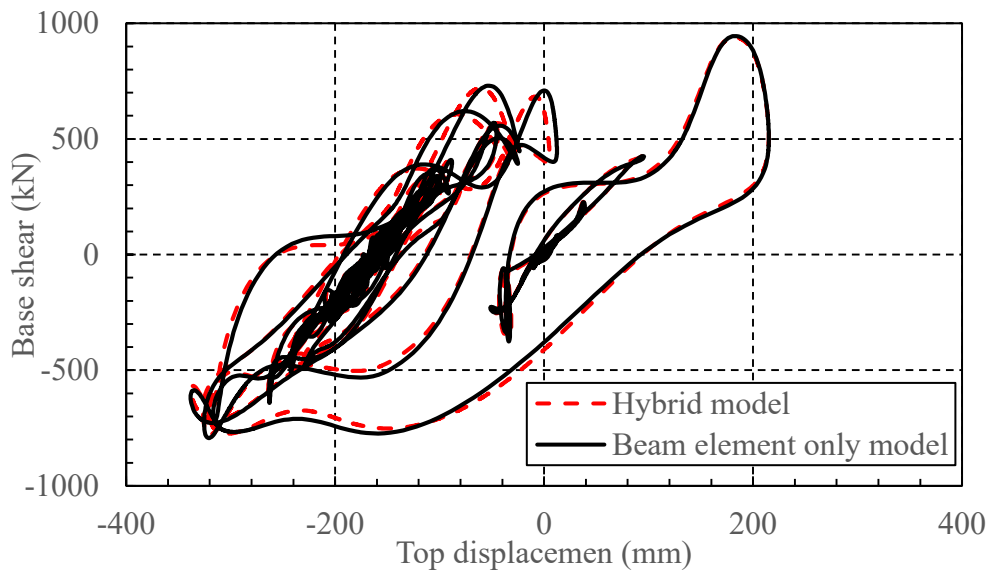


Figure 5.21 Comparisons of base shear versus roof displacement for hybrid and beam element only models for acceleration time history shown in Fig. 5.19

Chapter 6: Conclusions and Recommendations for Future Studies

6.1 Conclusions

The following conclusions can be drawn from the study.

1. In a combined hardening model, the flow stress is a combination of isotropic yield stress and back stress. Strain rate mainly affects isotropic hardening while kinematic hardening is independent of strain rate. However, back stress versus plastic strain curves generated using kinematic hardening parameters can affect the shape of isotropic yield stress versus plastic strain curves at different strain rates. A hump may occur in the calculated isotropic yield stress versus plastic strain curve when only a small number of kinematic hardening terms are used to generate back stress versus plastic strain curve. This study shows that the hump in the isotropic stress versus plastic strain curve can become less distinct or be eliminated as more kinematic hardening terms are used to better represent the back stress evolution.
2. Cowper-Symonds (1957) proposed an equation based on power-law relationship defined in Eq. (2.12) to provide the amplification factor that relates the yield stress as a ratio to the static yield stress at different strain rates. Tests conducted by Chen (2010) and Walker (2012) showed that the amplification factor is higher at the initial stage of strain hardening and decreases with strain. However, Eq. (2.12) is independent of plastic strain. The absence of plastic strain term in this equation can lead to the under-estimation of stress amplification at small plastic strain while over-estimating the amplification at large plastic strain. Hence, a modified Eq. (2.12) has been proposed in this study to model the reduction in the amplification factor on the isotropic yield stress with increasing plastic strain.

3. A procedure has been developed to generate static isotropic yield stress versus plastic strain curve and isotropic yield stress versus plastic strain curves at different strain rates that can be used as material properties input for strain rate dependent behaviour in the numerical simulations with the mixed-mode hardening model by Lemaitre and Chaboche (1979). Generated curves have been validated through numerical simulations against results of monotonic tensile and cyclic tests of round steel coupons (specimens) of ASTM A572 grade 50 and CAN/CSA G40.20/21 300W steel by Chen (2010) and Walker (2012).
4. Numerical modelling of the moment resisting frame (MRF) with reduced beam section (RBS) using a combination of shell and beam elements (hybrid model) and using beam only element have been explored in this study. In the hybrid model, the RBS is modelled using shell elements while in the beam element only model, the RBS is modelled with beam elements of varying flange width to approximate the flange profile of the RBS. Even though beam element only model cannot replicate the non-uniform stress across the flange at the RBS, it is found that there is not a significant difference in the results between the hybrid model and beam element only model. On the other hand, the hybrid model requires considerably more computational effort and time ($\sim 10\times$) to perform non-linear dynamic analyses with rate dependent material properties compared to the beam element only model.
5. The maximum strain rate produced at the first floor and roof RBS centers of the MRF has been determined in the study using non-linear dynamic analyses. It is observed that the MRF with RBS connections can experience a maximum strain rate up to 0.30 s^{-1} . The maximum strain rate is affected by the intensity of earthquakes with the maximum strain rate ranges from 0.09 s^{-1} to 0.30 s^{-1} at MCE hazard level and ranges from 0.03 to 0.21 s^{-1}

at DBE hazard level. The difference in the maximum strain rate in the MRF with different material strengths is quite small. Moreover, there is also not much difference in the predicted maximum strain rate between analyses conducted with and without strain rate dependent material properties. Hence, the maximum strain rate can be taken to be independent in the range of material strength and strain rate sensitivity considered in this study.

6. The mean maximum moment at the column centerline, column face and RBS center at the first floor and roof increases when rate dependent material properties are considered in the non-linear dynamic analyses. The rate of increase can be as high as 8%. The rate of moment increase is higher in the frame with a weaker strength material in the beam because isotropic yield stress amplification with strain rate is higher for a material with weaker strength. The increase in the mean maximum moment due to strain rate dependent material properties is higher at MCE hazard level as compared to DBE level due to higher strain rate developed with higher intensity ground motions. The moments and forces derived from the analyses using static material properties should be multiplied by a factor of 1.08 to account for the effects of material properties strain rate dependency.
7. The predicted maximum moment at the RBS center is higher for a frame with the beams composed of stronger material. For the MRF composed of material H, which has the static yield stress closer to the probable yield strength, the predicted maximum moment at the first floor RBS center at MCE hazard level ground motions with and without strain rate dependent material properties exceeds the design probable maximum moment by up to 16%. When strain rate dependent material properties are considered, the design probable maximum moment at the first floor RBS center is also exceeded by the mean predicted

maximum moment for MRF with material G (at close to nominal yield strength) subjected to MCE hazard level ground motions and with material H subjected to DBE hazard level ground motions. Thus, the probable maximum moment in the design specified in S16-14 (CSA 2014) for ductile moment resisting frame should be increased by at least 10% when inter-storey drift limit is ignored in the design.

8. The strain hardening factor at the first floor and roof RBS center with static material properties subjected to MCE hazard level ground motions has been found to be significantly higher than the factor 1.1 specified in the design specification for ductile moment resisting frame. The mean predicted strain hardening factor is close to 1.2 at the first floor RBS center due to the possibly the large cyclic deformation range experienced by the MRF when it is designed only for strength. Thus, a strain hardening factor (at close to 1.2) should be considered for a ductile moment resisting frame when inter-storey drift limit is ignored in the design.
9. Overall, there is a slight reduction in the inter-storey drift when strain rate dependent material properties are included in the analyses. This decrease is slightly higher at MCE hazard level as compared to DBE level. Nevertheless, inter-storey drift can be considered to be independent of strain rate sensitivity of the material strength.
10. There is an increase in the mean predicted maximum base shear of up to 7% when strain rate dependent material properties are used in the non-linear dynamic analyses. However, there is a big difference between the predicted and design base shear. The mean predicted maximum base shear is still much larger than the design base shear even at DBE hazard level ground motions for material G without including strain rate dependent material properties. Further study is required to investigate the big difference.

6.2 Recommendations

1. Current study only considers two materials. Additional study should be carried out for different material strength and strain rate sensitivity. Instead of actual material tests, the procedure established in the current study can be used to generate stress versus strain curves for materials of different strengths and strain rate sensitivity as the input in the dynamic analyses.
2. The reduction of the flange width at the center of RBS is greater than 40% in this study. Analyses can be carried out to assess effects of strain rate dependent material properties on RBS with different percentage of flange width cut as this affects the plastic hinge and strain localization
3. There are three types of seismic ground motions depending on the source of crustal, sub-crustal and subduction earthquakes. The earthquakes from these sources affect the building at different time periods. As noted by Mario (2015), subduction earthquake has greater influence on the structures with the time period greater than 1.5s while the contribution from crustal and sub-crustal earthquakes is dominant for structures with the time period less than 0.7s. Hence, a parametric study can be conducted to study effects of strain rate material properties dependency on Seismic Force Resisting Structures (SFRS) for different buildings and earthquakes types.
4. The MRF in this study has been subjected to scaled ground motions from a simple method which scales the median of a suite of ground motion records at the fundamental time period. A more detailed scaling using the procedure in NBCC (2015) can be used to scale the ground motions for different time periods that contribute to the dynamic response of a structure.

5. Currently only one bay of ductile moment resisting frame is considered in the study. A more realistic design with multiple bays of moment resisting frame should be considered. Besides ductile moment resisting frames, moderately ductile moment resisting frames and limited ductile moment resisting frames should be considered in future studies.
6. Shake table tests can be carried out on a moment resisting frame with reduced beam section to provide data to assess and validate the findings on the behaviour and response of the frame due to material properties strain rate dependency. Results of dynamic analysis of the MRF have not been validated against any experimental data.

References

1. Aksoylar, N. D., Elnashai, A. S., and Mahmoud, H. (2011). The Design and Seismic Performance of Low-Rise Long-Span Frames with Semi-Rigid Connections, *Journal of Constructional Steel Research*, 67(1), 114-126.
2. Alexandrou, M. (2015). Difficulties in FE-modelling of an I-Beam subjected to Torsion, Shear and Bending, MSc. Thesis, The Department of Civil and Architectural Engineering, Royal Institute of Technology (KTH), Stockholm, Sweden
3. ANSI/AISC 358-16, Prequalified Connections for Special and Intermediate Steel Moment Frames for Seismic Applications, American Institute of Steel Construction, USA, 2016.
4. Armstrong, P.J. and Frederick, C.O. (1966). A Mathematical Representation of the Multiaxial Bauschinger Effect, CEGB Report, RD/B/N/731, Berkeley Nuclear Laboratories, R&D Department, California, USA
5. Bhowmick, A.K., Driver, R.G. and Grondin, G.Y. (2009). Seismic Analysis of Steel Plate Shear Walls Considering Strain Rate and P-Delta Effects. *Journal of Constructional Steel Research* 65, no. 5, pp 1149-1159
6. Bruneau, M., Uang, C.M., and Whittaker A. (1996). *Ductile Design of Steel Structures*. First edition, McGraw-Hill, USA.
7. Canadian Standards Association: *Design of Steel Structures*, CAN/CSA-S16-14, Mississauga, Ontario, Canada, 2014.
8. Chaboche, J.L., Dang Van, K. and Cordier, G., (1979). Modelization of the Strain Memory Effect on the Cycle Hardening of 316 Stainless Steel, *Transaction of IASMiRT* 5, vol. L, L11/3

9. Chang, K.C. and Lee, G.C. (1987). Strain Rate Effect on Structural Steel under Cyclic loading. *Journal of Engineering Mechanics* 113, no 9 (1987), 1292-1301
10. Chen, J. (2010). An Experimental Study of Strain Rate Effects on Mild Steel, Masc. thesis, The Department of Civil and Environmental Engineering, Carleton University, Ottawa, ON, Canada,
11. Chen, S., Yeh, C.H., and Chu, J.M. (1996). Ductile Steel Beam-To-Column Connections for Seismic Resistance, *Journal of Structural Engineering*, 122(11), 1292-1299.
12. Chopra, A.K. (2012) *Dynamics of Structures: Theory and Applications to Earthquake Engineering*. 4th Edition,
13. Christopoulos, C., and Filiatrault, A. (2006). *Principles of Passive Supplemental Damping and Seismic Isolation*
14. Chun, B.K., Jinn, J.T. and Lee, J.K. (2002). Modeling the Bauschinger Effect for Sheet Metals, Part I: Theory. *International Journal of Plasticity*, 2002 Oct 1; 18 (5-6), p 571-595.
15. Clarke, K.D., Comstock, R.J., Mataya, M.C., Tyne, C.J., and Matlock, D.K. (2008). Effect of Strain Rate on the Yield Stress of Ferritic Stainless Steels. *Metallurgical and Materials Transactions A: Physical Metallurgy and Material Science*, vol. 39, no. 4, p 752-762
16. Couque, H., Boulanger, R. and Bornet, F. (2006). A modified Johnson-Cook model for strain rates ranging from 10⁻³ to 10⁴ s⁻¹. *J. Phys. IV* 134, p 87-93. (doi:10.1051/jp4:2006134015)
17. Couque, H. (2014). The use of the direct impact Hopkinson pressure bar technique to describe thermally activated and viscous regimes of metallic materials. *Phil. Trans. R. Soc. A* 372:20130218

18. Cowper, G.R. and Symonds, P.S. (1957). Strain-Hardening and Strain-Rate effects in the Impact Loading of Cantilever Beams. Division of Applied Mathematics, Brown University, Providence, R.I. USA
19. Drucker, D.C. and Prager, W. (1952). Soil Mechanics and Plastic Analysis for Limit Design. Quarterly of Applied Mathematics, Vol 10, No. 2, p 157-165
20. EC-8, Part 3: Design of Structures for Earthquake resistance. Assessment and Retrofitting of the buildings. EN 1998-3: June 2005E.
21. Elghazouli, A.Y, Broderick, B.M., Goggins, J., Mouzakis, H., Carydis, P., Bowkamp, J., and Plumier, A. (2004). Shake Table testing of Tubular Steel Bracing Members, Structures and Buildings, 229-241.
22. Engelhardt, M.D. (1999). The 1999 T.R. Higgins Lecture: Design of Reduced Beam Section Moment Connections, Chicago, IL, USA
23. Fazileh, F. (2011). Displacement-Based Seismic Design of RC Wall-Frame Buildings and Asymmetric Plan Buildings, PhD. Thesis, The Department of Civil and Environmental Engineering, Carleton University, Ottawa, ON, Canada
24. Federal Emergency Management Agency [FEMA] (2009). Quantification of Building Seismic Performance Factors, FEMA-P695. Washington DC: Federal Emergency Management Agency.
25. Gohlich, R.J. (2015). Development of an Innovative Hybrid Timber-Steel Moment-Resisting Frame for Seismic-Resistant Heavy Timber Structures. Masc. Thesis, The Department of Civil and Environmental Engineering, Carleton University, Ottawa, ON, Canada.

26. Gonzalez, M.A.G. (2017). Seismic Response of Tall Buildings using Ground Motions Based on National Building Code Canada 2015. Masc. Thesis, The Faculty of Graduate and Postdoctoral Studies (Civil Engineering), The University of British Columbia, Vancouver, British Columbia, Canada.
27. Grubs, K. V. (1997). The effect of the Dog-bone Connection on the Elastic Stiffness of Steel Moment Frames. M.S. Thesis, Department of Civil Engineering, University of Texas at Austin, Austin, Texas
28. Hailu, D., Zekaria, A., and Kinde, S. (2005). A Multiple Constraint Approach for Finite Element Analysis of Moment Frames with Radius-cut RBS Connections, pp 1-10
29. Hibbler, R.C. (2016). Engineering Mechanics: Static & Dynamics, 14th Edition, Pearson Education Inc., Upper Saddle River, NJ, USA.
30. Humar, J.L. (2002). Dynamics of Structures. 2nd Edition, A.A. Balkema Publishers, Tokyo, Japan.
31. Johnson, G.R., and Cook, W.H. (1985). Fracture Characteristics of Three Metals subjected to Various Strains, Strain Rates, Temperatures and Pressures, Engineering Fracture Mechanics, Vol 21, No 1, pp 31-48
32. Kelly, P. (2013). Solid Mechanics Lecture Notes- An Introduction to Solid Mechanics. Auckland: The University of Auckland.
33. Kitjasateanphun, T., Shen, J., Srivanich, W., and Hao, H. (2001). Inelastic Analysis of Steel Frames with Reduced Beam Sections, Structural Design Tall Buildings, 10, pp 231-244

34. Krempl, E. (1979). An Experimental Study of Room-Temperature Rate-Sensitivity, Creep and Relaxation of AISI Type 304 Stainless Steel, *Journal of the Mechanics and Physics of Solids*, 27(5-6): 363-375
35. Kudu, F.N., Ucak, S., Osmancikli, G., Turker, T., and Bayraktar, A (2015). Estimation of Damping Ratios of Steel Structures by Operational Modal Analysis Method. *Journal of Constructional Steel Research*, Volume 112, p 61-68.
36. Lau, D. (2017). *Structural Design Lecture Notes- An Introduction to Structural Design*. Ottawa: Carleton University.
37. Lee, C. H., & Kim, J. H. (2004). Seismic Design of Reduced Beam Section (RBS) Steel Moment Connections with Bolted Web Attachment. *Journal of the Earthquake Engineering Society of Korea*, 8(3), 87-96.
38. Lee, K., Goel, S.C., and Stojadinovic, B., *Boundary Effects in Welded Steel Moment Connections*. Research Report No. UMCEE 97-20.
39. Lemaitre, J. and Chaboche, J.-L. (1990). *Mechanics of Solid Materials*, Cambridge University Press, Cambridge.
40. Li R., Samali, B., Tao, Z. and Hassan, M.K. (2017). Cyclic Behaviour of Composite Joints with Reduced Beam Sections, *Engineering structures*, 136, pp 329-344
41. Liu, J. (1997). *Earthquake Analysis of Steel Moment Resisting Frame Structures*, Master's. Thesis, The Department of Civil and Environmental Engineering, Carleton University, Ottawa, ON, Canada
42. Logan, D.L. (2012). *A First Course in Finite Element Method*, 5th Edition, Cengage Learning India Private Limited, New Delhi, India.

43. Manjoine, M.J. (1944). Influence of Rate of Strain on Temperature on Yield Stresses of Mild Steel, Transactions of the American Society of Mechanical Engineers, Journal of Applied Mechanics, 66: A211-A218
44. Marie, L.A. (2014). Coupling of Beam and Shell Finite Elements for Rapid Analysis of Tubular Structures, MSc Thesis, School of Engineering and Computing Science, Durham University, Durham, United Kingdom.
45. Metten, A. and Driver, R. (2015). Structural Steel for Canadian Buildings, Third Edition, Library and Archives Canada Cataloguing in Publication, Canada
46. Meyers, M.A. (1994). Dynamic Behaviour of Materials, John Wiley & Sons, Inc., USA
47. Moment Connections for Seismic Applications, Canadian Institute of Steel Construction, Markham, Canada, Second Edition, 2016.
48. Moore, K.S., Malley, J.O. and Engelhardt, M.D. (1999), Design of Reduced Beam Section (RBS) Moment Frame Connections, Structural Steel Educational Council
49. Ngo, T., Mendis, P., Gupta, A. and Ramsay, J. (2007). Blast Loading and Blast Effects on Structures – An Overview, Electronic Journal of Structural Engineering Special Issue: Loading on Structures: 76-91
50. Nguyen, P. C., Doan, N. T. N., Ngo-Huu, C., & Kim, S. E. (2014). Nonlinear inelastic response history analysis of steel frame structures using plastic-zone method. Thin-Walled Structures, 85, 220-233.
51. Orban, F. (2011) Damping of Materials and Members in Structures. Journal of Physics: Conference Series. 268,012022.

52. Othman, R. (2015). A Modified Eyring Equation for Modelling Yield and Flow Stresses of Metals at Strain Rates Ranging from 10^{-5} to $5 \times 10^4 \text{ s}^{-1}$. *Advances in Materials Science and Engineering*, Volume 2015
53. PEER (2010). Technical Report for PEER Ground Motion Database Web Application. Berkeley, California: Pacific Earthquake Engineering Research Center.
54. Redwood, R. G., Lefki, L., & Amar, G. (1990). Earthquake resistant design of steel moment resisting frames, *Canadian Journal of Civil Engineering*, 17(4), pp 659-667.
55. Ritchie, C. B., Gow, M. I., Packer, J. A., & Heidarpour, A. (2017). Influence of elevated strain rate on the mechanical properties of hollow structural sections. *International Journal of Protective Structures*, 8(3), 325-351.
56. Salahi, A.A.A, and Othman, R. (2016). Constitutive Equations of Yield Stress Sensitivity to Strain Rate of Metals: A Comparative Study, *Journal of Engineering*, Volume 2016,
57. Shaw, R.E., and Malley, J.O. (2008). Design and construction standards for steel connections in seismic frames, 14th World Conference on Earthquake Engineering, Beijing, China.
58. Simulia (2017). Abaqus 2017, Dassault Systems Simulia Corp., Providence, Rhode Island, USA
59. Sofias, C.E., Kalfas, C.N., and Pachoumis, D.T. (2014). Experimental and FEM Analysis of Reduced Beam Section Moment Endplate Connections Under Cyclic Loading, *Engineering Structures*, 59, pp 320-329.
60. Song, Z. and Su, C. (2017). Computation of Rayleigh Damping Coefficients for the Seismic Analysis of a Hydro-Powerhouse. *Shock and Vibration*, Volume 2017, Article 2046345, 11 pages.

61. Soroushian, P. and Choi, K.B. (1987). Steel Mechanical Properties at Different Strain Rates, *Journal of Structural Engineering*, 113(4): 663-672
62. Sreenath, S., Saravanan, U. and Kalyanaraman, V. (2011). Beam and shell element model for advanced analysis of steel structural members, *Journal of Constructional Steel Research*, 67 (2011), pp 1789-1796
63. Suita K., Kaneta K. and Khozu I. (1992). The Effect of Strain Rate in Steel Structural Joints Due to High Speed Cyclic Loadings, *Earthquake Engineering*, Tenth world conference, Balkema, Rotterdam, Netherlands, pp 2863-2866
64. Tian, L., Wang, W., and Qian, H. (2014). The Effect Analysis of Strain Rate on Power Transmission Tower-Line System under Seismic Excitation, *The Scientific World Journal*, 2014
65. Tremblay, R., Tehebotarev, N., and Filiatrault, A. (1997). Loading Rate Effect and Influence of floor slab on the seismic performance of the RBS connection for steel moment resisting frame, *Annual Conference of the Canadian Society for Civil Engineering*, 419-428
66. Tuazon, B.J., Bae K.O., Lee, S.H. and Shin, H.S. (2014). Integration of a New data Acquisition/Processing Scheme in SHPB Test and Characterization of the Dynamic Material Properties of High-Strength Steels using the Optional Form of Johnson-Cook Model, *Journal of Mechanical Science and Technology*, 28 (9) (2014), pp 3561-3568
67. Vyas, P. (2016), Behaviour of Moment Resisting Frame and Shear wall- Frame Structure. *International Journal of Innovative and Emerging Research in Engineering*, Volume3, Issue 4

68. Wakabayashi, M., Nakamura, T., Iwai, S., & Hayashi, Y. (1980). Dynamic Loading Effects on the Structural Performance of Concrete and Steel Materials and Beams. Proc. 7th World Conference of Earthquake Engineering, Istanbul, Turkey Vol. 6, p 271-278.
69. Wakabayashi, M., Nakamura, T., Iwai, S., & Hayashi, Y. (1984). Effects of Strain Rate on the Behaviour of Structural Members Subjected to Earthquake Force. Proc. 8th World Conference on Earthquake Engineering, San Francisco, USA
70. Walker, A. (2012). An Experimental and Numerical Study of the Strain Rate Effects on Mild Steel for Cyclic Loading, Masc. Thesis, The Department of Civil and Environmental Engineering, Carleton University, Ottawa, ON, Canada
71. Wang, W. M., Li, H. N., Liu, G. H., & Tian, L. (2011). Strain Rate Effect on Transmission Tower-Line System under Earthquake, Advanced Materials Research, Vol. 243, pp. 5845-5848.
72. Wen, Z. (2012). Modeling of Ductile Fracture in Steel Structures for Monotonic and Cyclic Loading, PhD Thesis, The Department of Civil and Environmental Engineering, Carleton University, Ottawa, ON, Canada.
73. Zhang, H., and L, H.N. (2011). Dynamic Analysis of Reinforced Concrete Structure with Strain Rate Effect, Springer Berlin, p 213-216.

APPENDICES

Appendix A Design of Ductile Moment Resisting Frame with Reduced Beam Section

This appendix outlines the calculations and procedures used in the seismic design of the ductile moment resisting frame. National Building Code of Canada (NBCC 2015) has been used to calculate the dead, live, snow and seismic load acting on the MRF. The structural members of the MRF have been designed using CSA S16-14 (2014) for CAN/CSA G40.20/21 300W steel and RBS connections using prequalified connections from Moment Connections for Seismic Application (CISC 2014). A six storey building with moment resisting frames shown in Figs. A.1 and A.2 by Christopoulos and Filiatrault (2006) has been used as the basis to design the MRF with RBS connection. This building has been modified by keeping the same plan dimensions but with only two storeys each at 4.5m high in order to simplify the analysis. In addition, only one bay on each side of the perimeter has the moment resisting frame while remaining bays consist of simply supported beams. Figures A.3 and A.4 shows the plan and elevation of the modified building with the ductile MRF in the north-south direction being considered in the design (noted in Fig. A.3). The ductile MRF has been designed for Victoria, British Columbia with site class D as it has high seismic hazard level according to Seismic Hazard Map of Canada (Geological Survey of Canada, 2015) shown in Fig. A.5

A.1 Gravity Loads for Seismic Load Calculations

The dead load has been assumed given in Table A.1 based on a building by Metten and Driver (2015). Live load of 1.0 and 2.4 kPa has been considered at the roof and first floor respectively from NBCC 2015. The snow load is calculated using NBCC 2015 Clause 4.1.6.2 (1) as

$$S = I_s [S_s (C_b C_w C_s C_a) + S_r] \quad (A. 1)$$

where I_s is the snow load importance factor, S_s is 1 in 50-year ground snow load in kPa, S_r is 1-in-50-year associated rain load in kPa, C_b is basic roof snow load, C_w is wind exposure factor, C_s is slope factor and C_a is accumulation factor. Table A.2 shows the values of these parameters used to calculate the snow load for the proposed building in Fig. A.3.

The seismic weight of the building is calculated using the values in Tables A.1 and A.2 with 25% of the roof snow load. Hence, the total load on the roof is 1.87 kPa (1.60 + 0.27 kPa) and 3.32 kPa on first floor. For the building shown in Fig. A.3, the seismic weight are 1501 kN for the roof and 2665 kN for first floor respectively.

Seismic analyses for the design of MRF is carried out using equivalent static method specified in NBCC (2015). Site class D has been selected for the seismic design of MRF at Victoria, BC. The building is assumed to be of normal importance with both floors intended for office use. Using NBCC 2015 clause 4.18.4 (7), the design spectrum for Victoria, BC for site class D is calculated and shown in Fig. A.6 and Table A.3. Fundamental lateral period (T_a) of the MRF is based on expression $0.085 h_n^{(3/4)}$, where h_n is height of the MRF. The MRF has initial period estimated at 0.44 seconds.

A.2 Design Base Shear

NBCC 2015 Clause 4.1.8 gives the equation for calculating the base shear as

$$V = \frac{S(T_a)M_V I_e W}{(R_d R_0)} \quad (A. 2)$$

where $S(T_a)$ represents the spectral acceleration of the structure ($T_a = 0.44$ seconds, time period estimated for the ductile MRF), M_V represents the higher mode factor (taken as 1.0), R_d is the

ductility related force modification factor (5.0 for ductile MRF), R_0 is the overstrength related force modification factor (1.5 for ductile MRF), I_e is the importance factor taken as 1.0 for normal importance building and W is the seismic weight. The base shear calculated using Eq. (A.2) is 709 kN.

For moment resisting frame, the design base shear should not be lesser than

$$V > \frac{S(2.0)M_V I_e W}{(R_d R_0)} \quad (A.3)$$

and for seismic force resisting systems having R_d greater than or equal to 1.5, V should not be greater than the larger of the following values of

$$\frac{0.67 S(0.2) I_e W}{(R_d R_0)} \text{ or } \frac{S(0.5) I_e W}{(R_d R_0)} \quad (A.4)$$

The total base shear is distributed on along the height of the building according to the expression from NBCC Clause 4.1.8.11 (7) as

$$F_x = (V - F_t) \frac{W_x \times h_x}{\sum_i^n W_i h_i} \quad (A.5)$$

where F_x is the lateral force applied at level x , F_t represents the portion of design base shear to be concentrated at the top of the building taken as zero for structures with a time period less than 0.7 seconds, W_x and W_i seismic weight and h_x and h_i are the heights above the base of structure at levels x and i respectively. Table A.4 shows the storey shear distribution for MRF. Since the building is symmetrical with two MRFs in the north-south direction, half of these shear forces go to each MRF. Hence, the shear forces of 188 and 167 kN are applied to the roof and first floor of MRF respectively. Additional lateral forces also have to be considered for the accidental torsion due to seismic load acting at an eccentricity of 10 % of building dimension and notional loads for frame stability at 0.5% the gravity loads. It is assumed that the torsion due to eccentricity of the

seismic load is resisted entirely by the MRFs on the short side (north-south direction). Figure A.7 shows the shear forces due to seismic weight with and without accidental torsional effect and notional loads. The final applied loading on the MRF is shown in Fig. A.8. The analysis of this frame has been carried out with non-linear geometry to account for the second order effect of gravity load (P-delta). The maximum moment for the beam at the first floor is 1200 kN.m and at the roof is 292 kN.m. The maximum moment at the column centerline at the first floor is 1330 kN.m. At the center of RBS, the maximum moment is 1038 kN.m at the first floor and 226 kN.m at the roof. Final member sizes selected for the frame are shown in Fig. A.9 (a) and bending moment, shear force and axial force diagram in Fig. A.9 (b), (c) and (d), and sectional properties in Table A.5.

A.3 Reduced Beam Section

Moment Connections for Seismic Application by CISC (2014) is used to design the RBS for the ductile MRF shown in Fig. A.9. The capacity at the reduced section should safely resist the load combination for factored live, dead, snow and seismic loads. The trial values for the RBS dimensions, a (distance of the RBS cut from face of the column), s (length of the RBS cut) and c (depth of the cut at center of RBS) are chosen such that

$$0.5 b \leq a \leq 0.75 b \quad (A.6)$$

$$0.65 d_b \leq s \leq 0.85 d_b \quad (A.7)$$

$$0.1 b \leq c \leq 0.25 b \quad (A.8)$$

where b and d_b are the width and depth of the beam respectively. Figure A.10 shows the values of these parameters chosen for the RBS at the first floor and roof. Based on these dimensions, the plastic section modulus at the center of RBS (Z_e) is calculated as

$$Z_e = Z_b - 2ct_b (d_b - t_b) \quad (A.9)$$

where Z_b and t_b are plastic section modulus and flange thickness of the unreduced beam cross-section. The RBS plastic section moduli at first floor and roof are obtained as $3.32 \times 10^6 \text{ mm}^3$ and $8.3 \times 10^5 \text{ mm}^3$. Based on these values, probable maximum moment at the center of RBS (M_{pr}) is calculated as

$$M_{pr} = C_{pr} R_y F_y Z_e \quad (A.10)$$

where $C_{pr} = 1.1$ for ductile moment resisting frame (factor that accounts for the strain hardening), F_y is the yield stress, R_y is the factor applied to yield stress to estimate probable yield stress ($R_y = 1.1$). This gives probable maximum moment at RBS center of 1405 and 353 kN.m at the first floor and roof. The shear force can be calculated at the center of RBS at each end of beam using free body diagram shown in Fig. A.11. The shear force at the center of RBS (V_{RBS}) is calculated as

$$V_{RBS} = \frac{2 M_{PR}}{L_h} \pm \frac{wL_h}{2} \quad (A.11)$$

Figure A.12 gives the free body diagram of beam segment between RBS center at the first floor and roof. The calculated shear force at the center of RBS at the first floor is 515 kN and at the roof is 126 kN. The moment at the face of the column due to plastic hinging of the reduced beam section (M_{cf}) is calculated as (Fig. A.13(a))

$$M_{cf} = M_{pr} + V_{RBS} \left(a + \frac{s}{2} \right) \quad (A.12)$$

Equation A.12 yields the maximum moments of 1646 and 391 kN.m at the face of first floor and roof column. The moment at the column centerline (M_c) as shown in Fig. A.13(b) is calculated as

$$M_c = M_{pr} + V_{RBS} \left(a + \frac{s}{2} + \frac{d_c}{2} \right) \quad (A.13)$$

where d_c is the depth of the column. Maximum moments of 1841 and 439 kN.m are obtained at first floor and roof column centerline. The moment developed at the face of the column due to formation of plastic hinge at the center of RBS should satisfy

$$M_{cf} \leq \phi_d R_y F_y Z_b \quad (A.14)$$

where $\phi_d = 1.0$

Table A.6 summarizes the design values for the RBS at the first floor and roof of the ductile MRF.

The column is designed as the beam column such that the column can resist the apparent moment produced due to plastic hinge formation at the RBS such that the limit states of overall member strength and lateral torsional buckling strength are satisfied according to CSA S16-14 (CSA 2014) as

$$\frac{C_f}{C_r} + \frac{0.85 U_1 M_f}{M_r} \leq 1.0 \quad (A.15)$$

where C_f and M_f are the axial force and moment induced on the column centerline due to the loading and C_r and M_r are the factored compressive and moment resistances, and U_1 is the factor to account for the second-order effect due to axial force. The column is assumed to be transversely braced at the mid-height of the first-storey. Table A.7 summarizes the design of the column of the MRF. The frame has a fundamental time-period of 1.1 seconds and the inter-storey drift of 8.9% for first storey and 5.9% for the second storey. Figure A.14 summarizes the steps for the design of RBS.

The period obtained through empirical expression, $0.085 h_n^{(3/4)}$ is 0.44 seconds. This is likely a conservative estimate as the actual period of the MRF obtained is 1.1 seconds for the designed frame. Hence, the preliminary design forces obtained can be decreased using the actual

time period. However, NBCC (2015) Clause 4.1.8.11 (3) limits the period taken for design up to 1.5 times the time-period determined through $0.085 h_n^{(3/4)}$. Therefore, $S(T_a)$ used in Eq. (A.2) should be based on the fundamental period based at this upper limit of 0.66 seconds. The base shear obtained using Eq. (A.2) for time period of 0.66 seconds is 627 kN. This base shear is distributed at both the storeys according to Eq. (A.5). Since the time period is less than 0.7 seconds, F_t is taken as zero. Hence, no additional force is concentrated at the top of the MRF. Table A.8 shows the reduced lateral forces at the two storeys of the MRF including the accidental torsional effects and notional loads based on time period of 0.66 seconds. The lateral forces at the roof and first floor are reduced from the calculated forces for time period of 0.44 seconds by 26 and 23 kN respectively. Since, the reduction is not very large, it is decided not to update the design of the frame for reduced forces. The lateral force can be further reduced by using the actual time period of the MRF at 1.1 seconds. The base shear using Eq. (A.2) for time period of 1.1 seconds comes out to be 404 kN. This base shear is distributed at both the storeys according to Eq. (A.5) and listed in Table A.8. Since the time period is greater than 0.7 seconds, an additional concentrated force $F_t = 0.07t_a V$ is applied at the roof of the MRF. Table A.8 shows the base shear, distributed force at each storey, inter-storey drifts and maximum moment at the center of first floor RBS for the three time-periods of 0.44, 0.66 and 1.1 seconds. The reduction in the lateral force calculated at the fundamental time period of the MRF is purely an academic exercise as NBCC 2015 does not allow such reduction.

Table A.1 Seismic weight at roof and first floor (Metten and Driver 2015)

Roof (in kPa)		First Floor (in kPa)	
Roofing/Deck	1.00	Partitions	0.50
Mechanical/Electrical,	0.10	65 topping on 38mm deck	2.40
Steel beams, joists columns	0.30	Mechanical/Electrical	0.10
Partitions	0.20	Floor Joists	0.22
		Girders and tributary columns	0.10
Total	1.60	Total	3.32

Table A.2 Snow load

I_s , importance factor	1.00
S_s , ground snow load (kPa)	1.10
C_b , basic snow load factor	0.80
C_w , wind exposure factor	1.00
C_s , slope factor	1.00
C_a , accumulation factor	1.00
S_r , associated rain load (kPa)	0.20
S , total snow load (kPa)	1.08

Table A.3 Design spectrum for Victoria, British Columbia (site class D)

Time period	S_a (T)
0.00	1.28
0.20	1.28
0.50	1.28
1.00	0.82
2.00	0.51
5.00	0.17
10.0	0.06

Table A.4 Shear force distribution at each storey of MRF

Level	Area (m ²)	W_t/area	W_i	Height (m)	$W_i \times H$	$W_i h_i / \text{sum}$	V (kN)
Roof	802	1.87	1501	9.0	13509	0.53	376
First floor	802	3.32	2665	4.5	11992	0.47	333
Total					25501		709

Table A.5 Sectional properties

	Columns (W760×161)	First floor beam (W690×140)	Roof beam (W460×60)
Depth (mm)	758	684	455
Width of flanges (mm)	266	254	153
Thickness of flange (mm)	19.3	18.9	13.3
Thickness of web (mm)	13.8	12.4	8.00
Area (mm ²)	2.04×10^4	1.78×10^4	7.59×10^3
Moment of inertia, I_x (mm ⁴)	1.86×10^9	1.36×10^9	2.55×10^8
Moment of inertia, I_y (mm ⁴)	6.07×10^7	5.17×10^7	7.96×10^6
Section Modulus, Z_x (mm ³)	5.66×10^6	4.55×10^6	1.28×10^6
Torsional constant, J (mm ⁴)	2.07×10^6	1.67×10^6	3.35×10^5
Warping constant, C_w (mm ⁶)	8.28×10^{12}	5.72×10^{12}	3.88×10^{11}

Table A.6 Design summary of RBS at first floor and roof of the MRF

	First floor	Roof
Plastic section modulus at center of RBS, Z_e (mm ³)	3.32×10^6	8.30×10^5
Probable maximum moment at center of RBS, M_{pr} (kN.m)	1405	353
Shear force at the center of RBS, V_{RBS} (kN)	515	126
Maximum moment at the face of column, M_{cf} (kN.m)	1646	391
Column centerline maximum moment, M_c (kN.m)	1841	439
$\frac{M_{cf}}{\phi_d R_y F_y Z_b}$	0.94	0.80

Table A.7 Design of column

Limit state	Overall member strength	Lateral-torsional buckling strength
F_y (MPa)	350	350
C_f (kN)	1405	1405
M_f (kN.m)	1473	1473
C_r (kN)	6362	5604
M_r (kN.m)	1783	1779
U_1	1.00	1.0
$\frac{C_f}{C_r} + \frac{0.85 U_1 M_f}{M_r}$	0.92	0.96

Table A.8 Comparison of base shear, distributed force, elastic drift and moment at RBS center

Fundamental time period, t_a (seconds)	0.44	0.66	1.10
Building base shear (kN)	709	627	404
Additional concentrated force at roof, F_t (kN)	0.00	0.00	31.0
Base shear for single MRF (kN)	355	314	202
Force at roof, D_r (kN) (includes accidental torsion, notional loads)	230	204	123
Force at first floor, D_f (kN) (includes accidental torsion, notional loads)	210	188	116
$D_r + F_t$ (kN)	230	204	154
Maximum elastic drift (%) at first floor	8.94	7.99	5.61
Maximum elastic drift (%) at roof	5.90	5.30	3.81
Moment at the first floor RBS center (kN.m)	1038	923	660

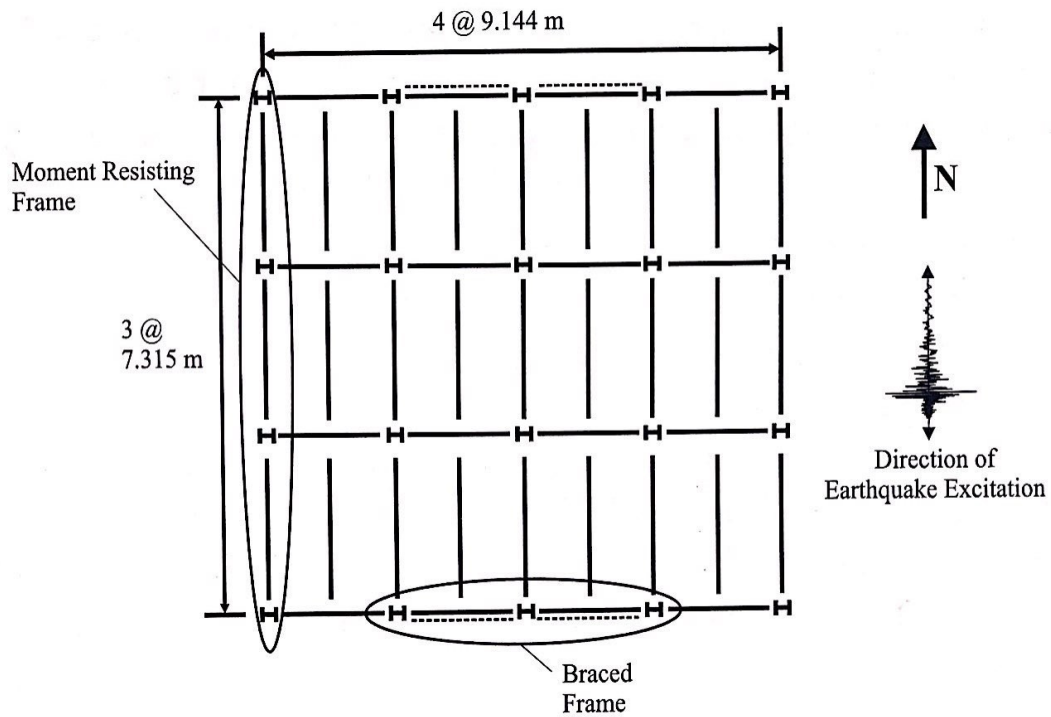


Figure A.1 Building plan dimensions from Christopoulos and Filiatrault (2006)

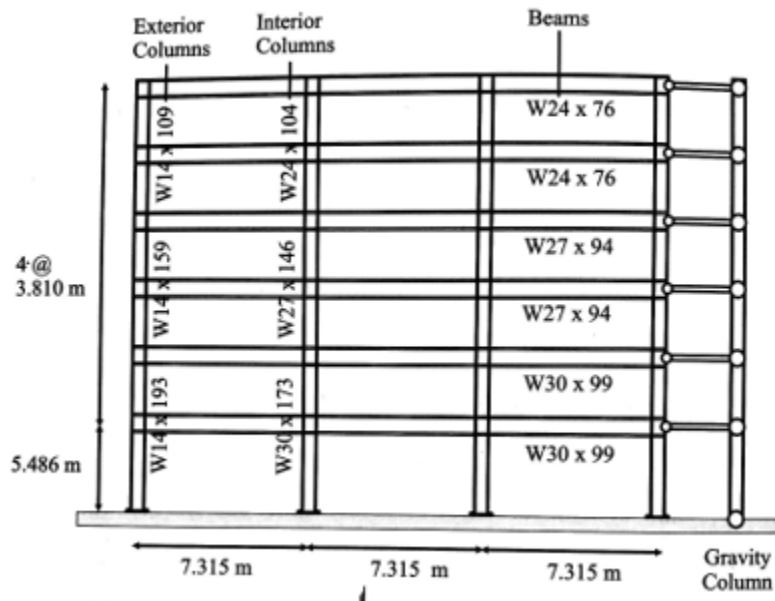


Figure A.2 Six-storey building elevation from Christopoulos and Filiatrault (2006)

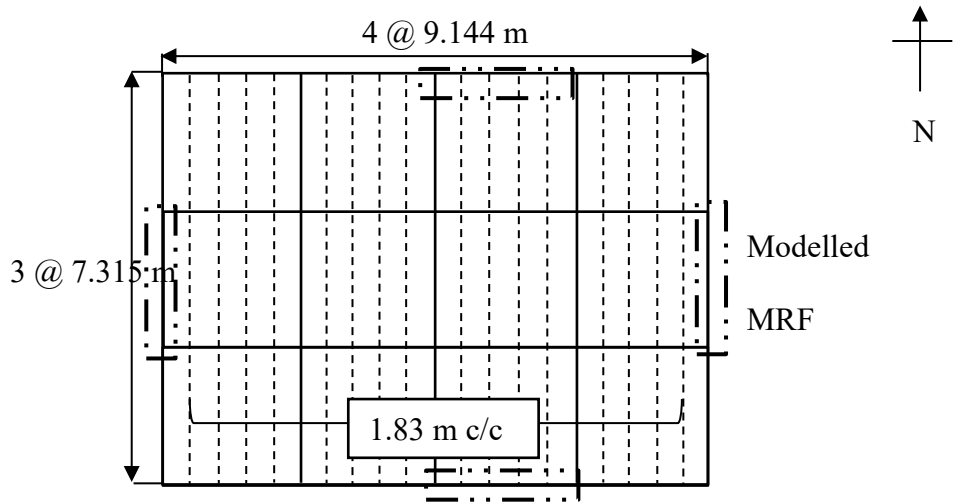


Figure A.3 Building plan dimensions

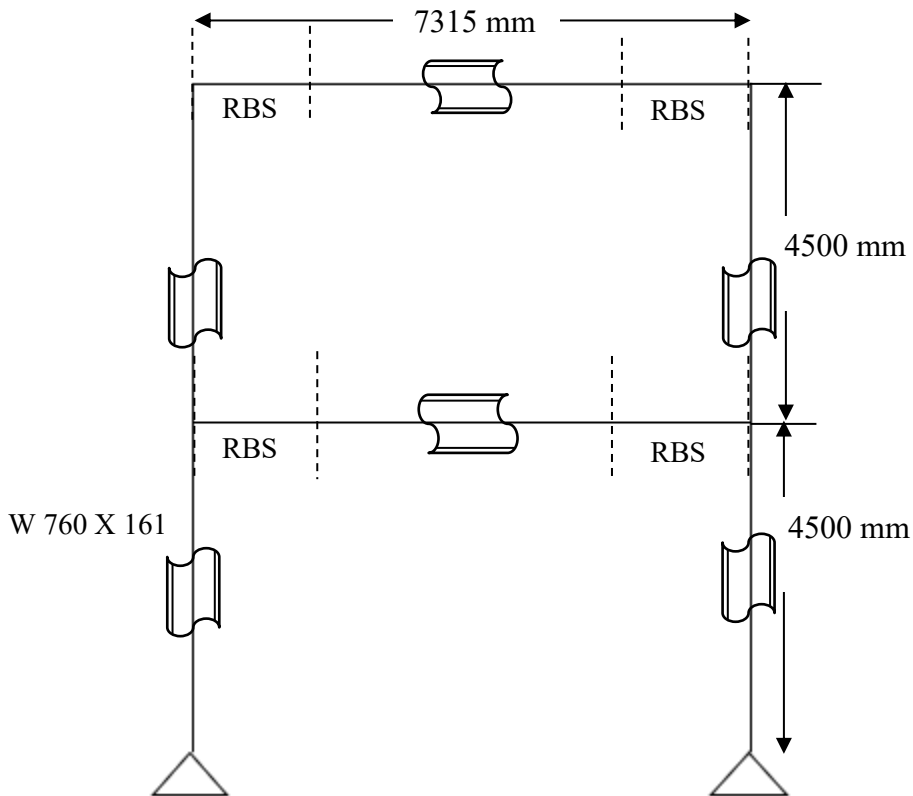


Figure A.4 Elevation view of the moment resisting frame of the modified building

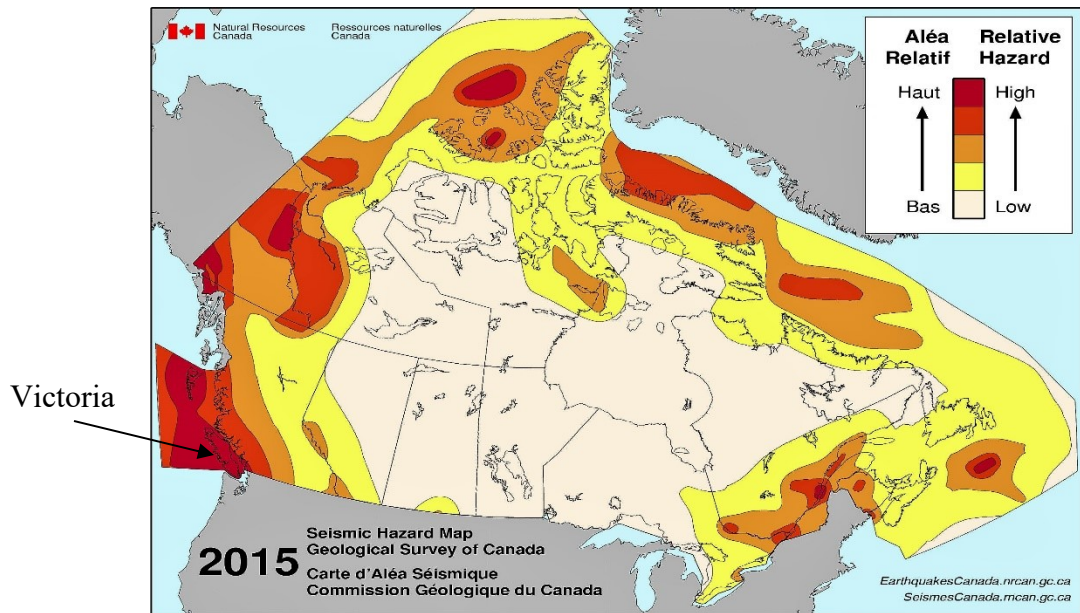


Figure A.5 Seismic hazard map (Geological Survey of Canada 2015)

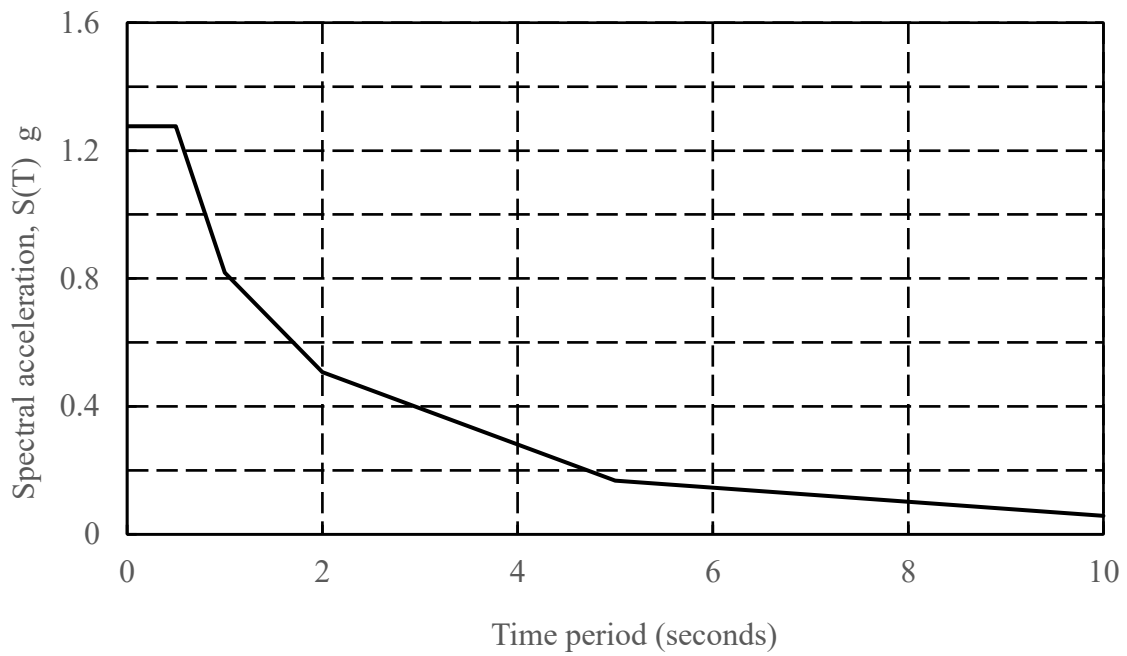


Figure A.6 Design Spectrum for Victoria, British Columbia for site class D

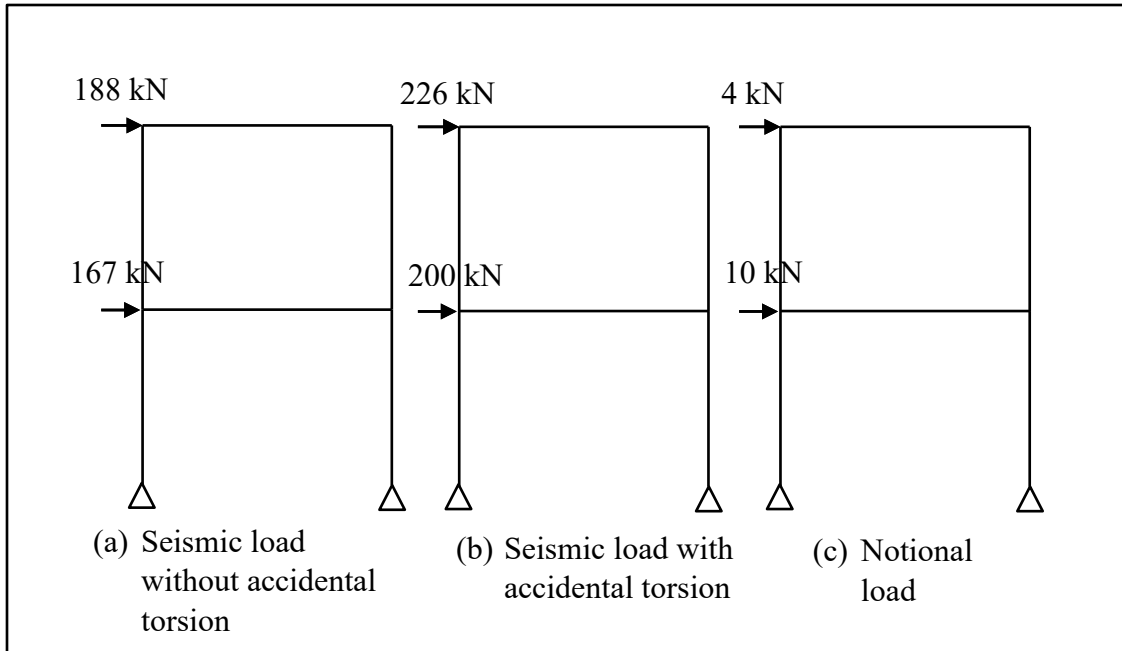


Figure A.7 Lateral forces on the ductile MRF

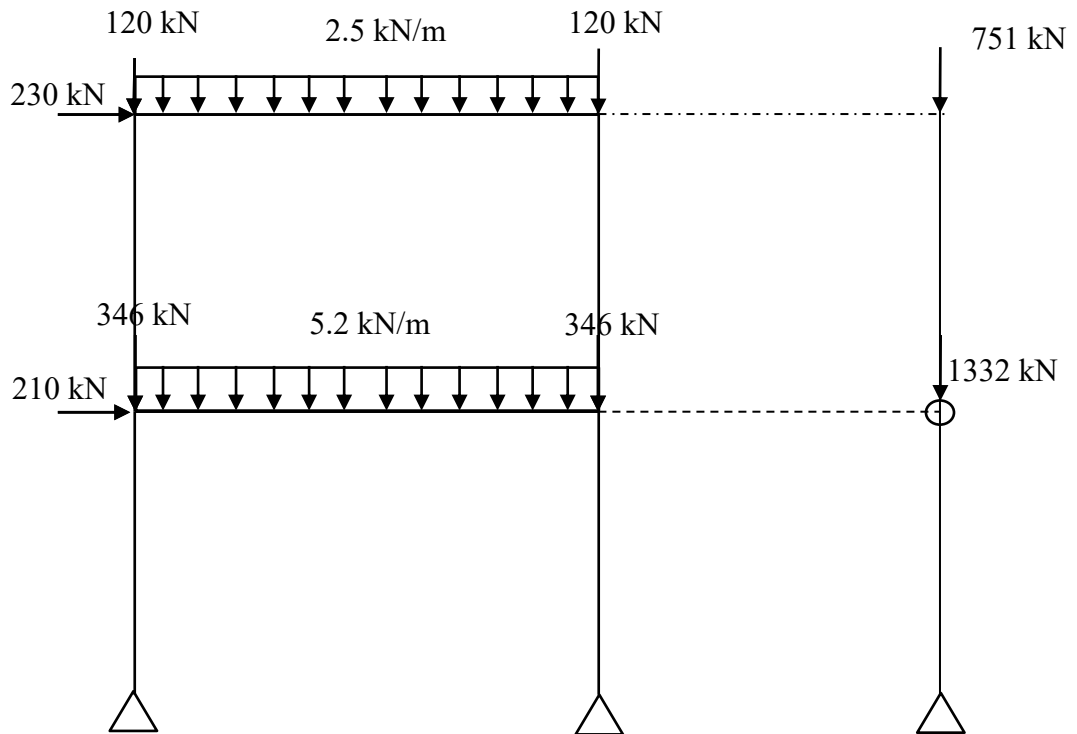
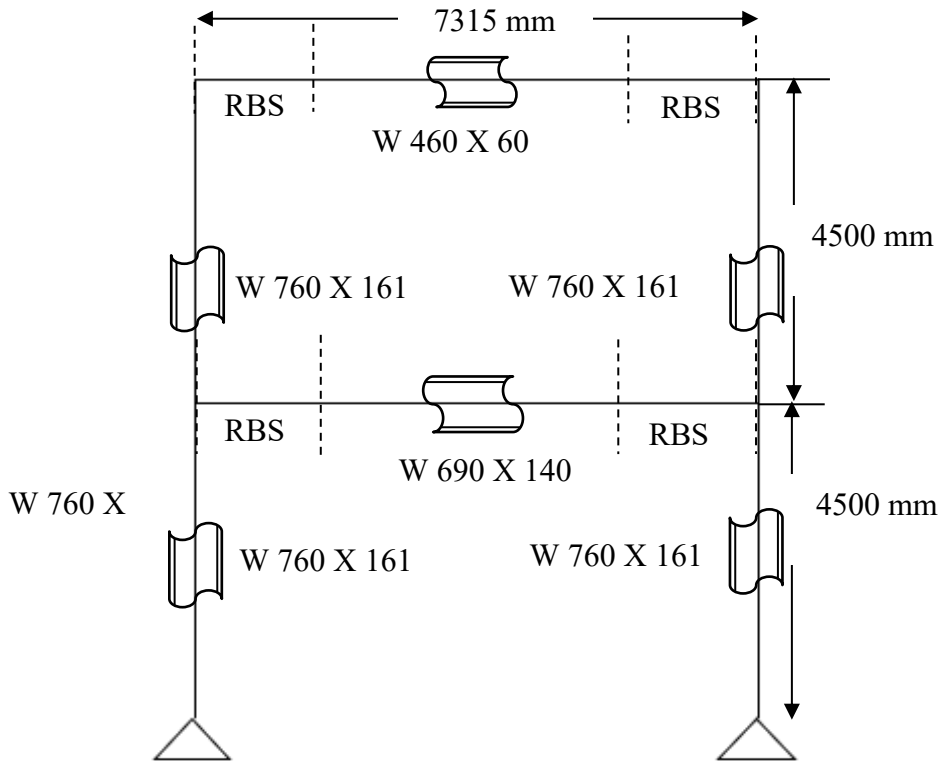


Figure A.8 The applied loads on the ductile MRF



(a) Final member sizes

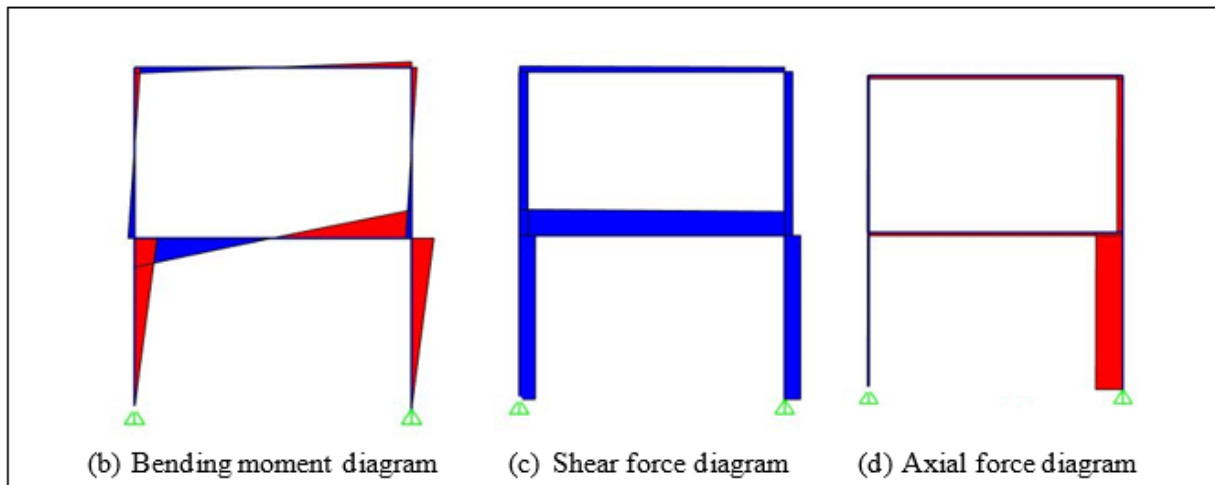
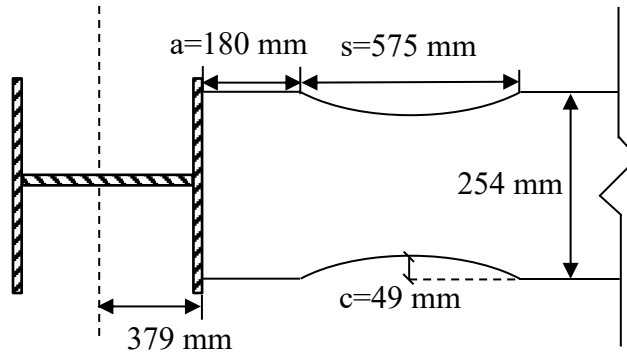
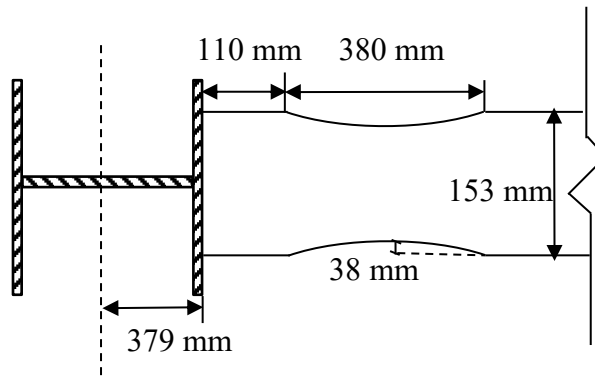


Figure A.9 (a) Final member sizes of ductile MRF (b) bending moment diagram (c) shear force diagram (d) axial force diagram



(a) Details of RBS at first floor



(b) Detail of RBS at roof

Figure A.10 Details of RBS connections

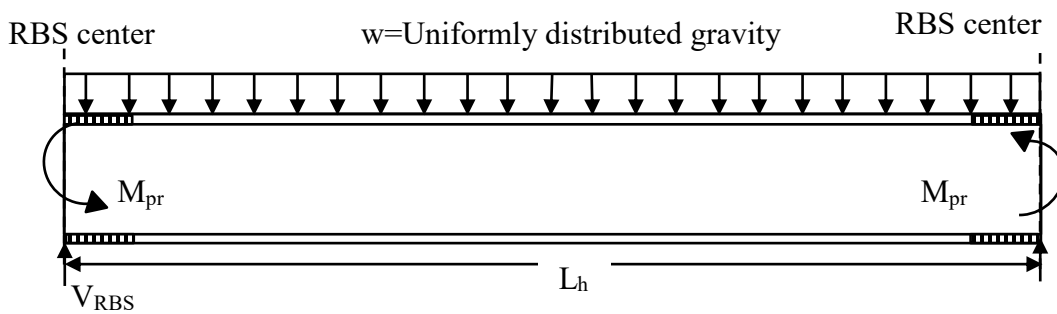
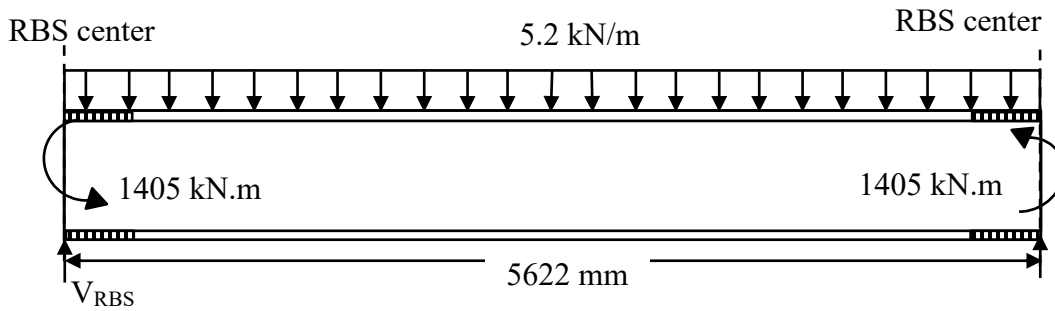
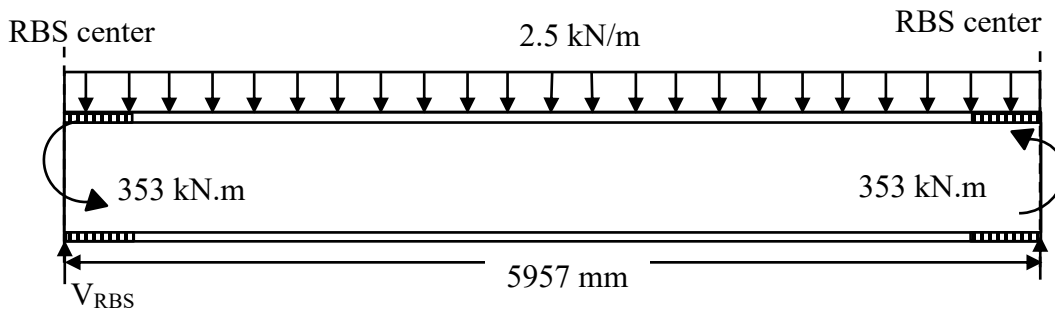


Figure A.11 Free-body diagram of beam segment between plastic hinges at RBS center



(a)



(b)

Figure A.12 Free body diagram of beam segment between RBS center at (a) first floor and (b) roof

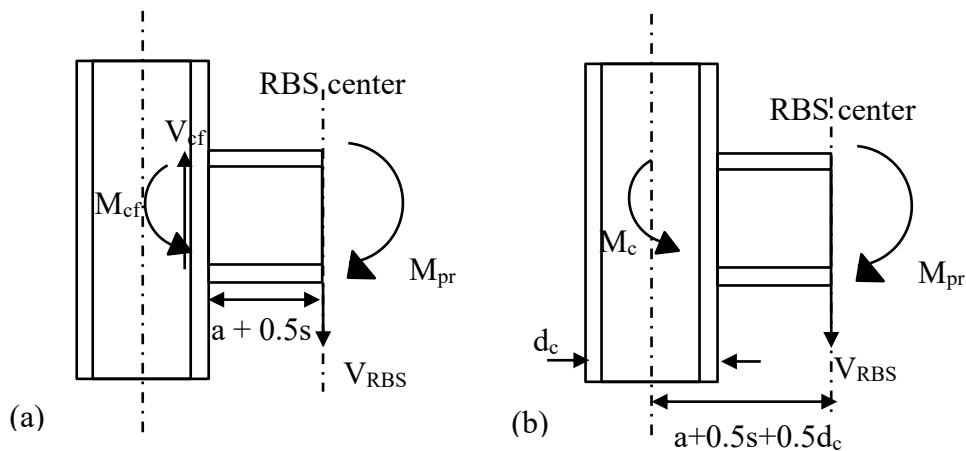


Figure A.13 Maximum moment due to plastic hinging of RBS at (a) column face (b) column centerline (Moment Connections for Seismic Application, CISC 2014)

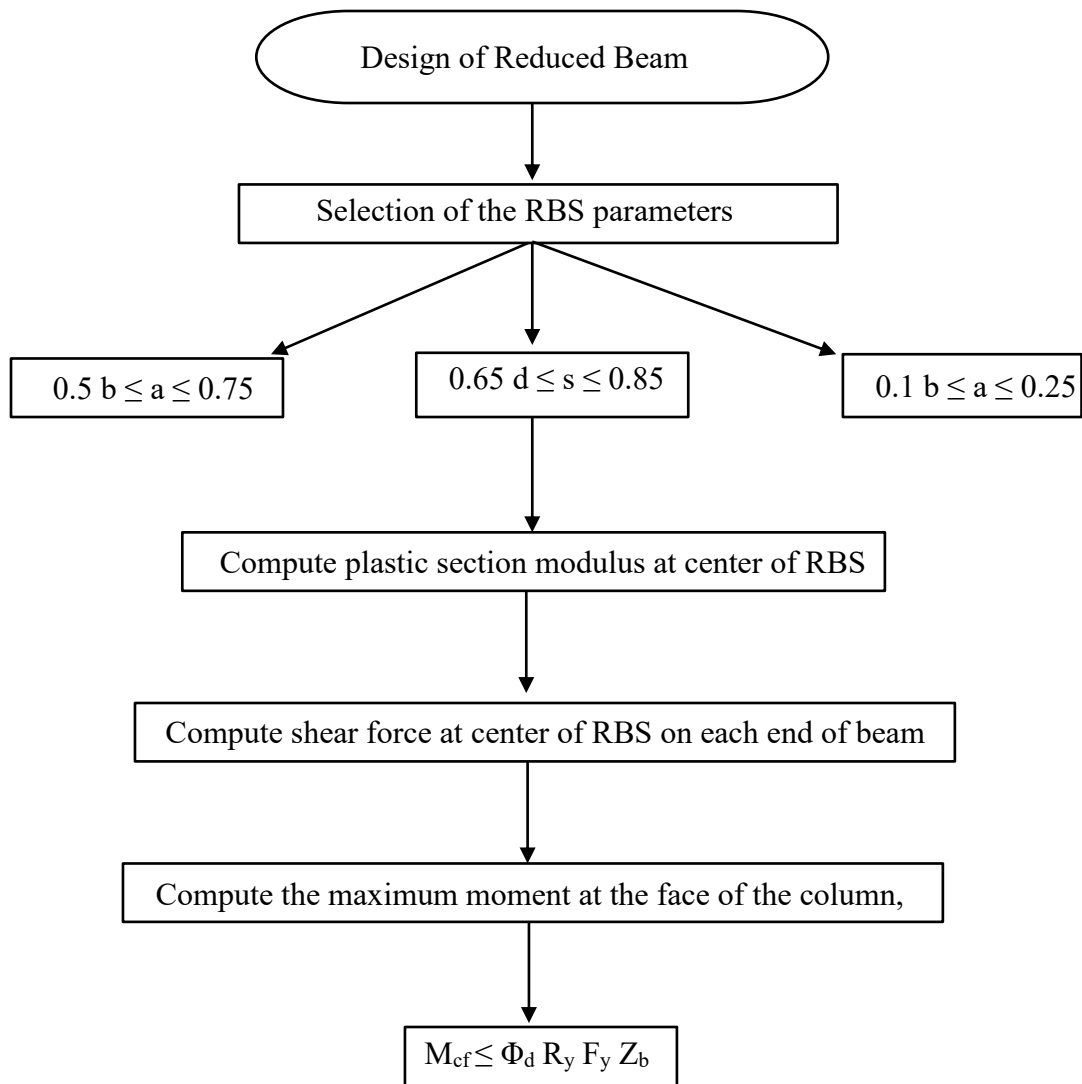


Figure A.14 RBS design summary

Appendix B Validation of the Shell and Beam Element Interface

A 5 meter W 610 × 174 ($d = 616\text{mm}$, $b = 325\text{mm}$, $t_w = 14\text{mm}$ and $t_f = 21.6\text{mm}$) cantilever beam of hybrid model and beam element only model have been considered in order to validate the shell and beam element interface. The hybrid model consists of 100 B31OS beam elements and 110 S4R shell elements of equal size in the longitudinal direction. In the cross-section of the shell segment, each flange is modelled with 10 shell elements of equal size and the web with 28 shell elements of equal size. The beam element only model consists of 200 equally spaced B31OS beam elements in the longitudinal direction. The hybrid model is referred as B-S4R and the cantilever beam model with entirely B31OS beam elements as B-B31OS. The beams are subjected to three separate loads of axial load of 100 kN, vertical load of 100 kN and bending moment of 100 kN.m at the free end. The material is considered to be elastic (elastic modulus of 200 GPa) for the analyses. The stresses from the loading are compared at different sections of the cantilever beam. These sections are referred to as S-5000, S-4500, S-4000, S-3500, S-3000 and S-2500, as shown in Fig. B.1. The section S-2500 is the section at shell and beam element interface in B-S4R. Comparisons of stresses corresponding to the three loads at various sections are shown in Figs. B.2 to B.4. There is good agreement between stresses for B-S4R and B-B31OS at sections S-4500, S-4000, S-3500 and S-3000. However, there is slight difference in the stresses at sections S-2500 and S-5000 as there are additional constraints against lateral deformation introduced for the shell elements at the fixed end and at the shell and beam element interface.

Table B.1 shows the vertical deflection and bending rotation at the middle of the web at section S-2500 and free end for B-S4R and B-B31OS loaded with a vertical force of 100 kN at the free end. There is a good agreement between the results from both models.

Table B.1 Vertical deflection and bending rotation at the middle of the beam at free end and section S-2500

	B-B31OS		B-S4R	
	Free end	S-2500	Free end	S-2500
Vertical deflection in mm	14.95	4.80	14.79	4.79
Bending rotation in rad	4.29E-3	3.21E-3.	4.23E-3	3.15E-3

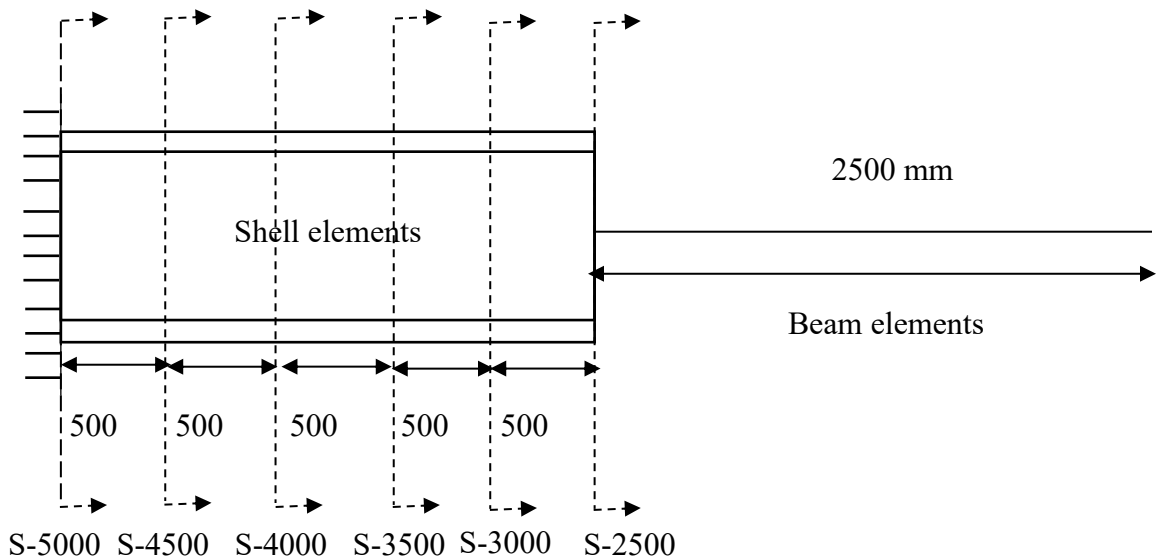
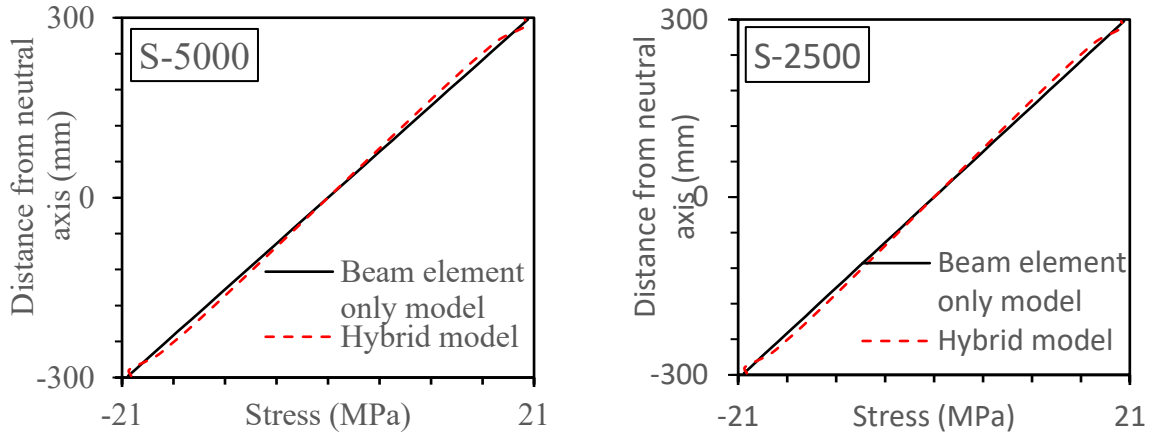
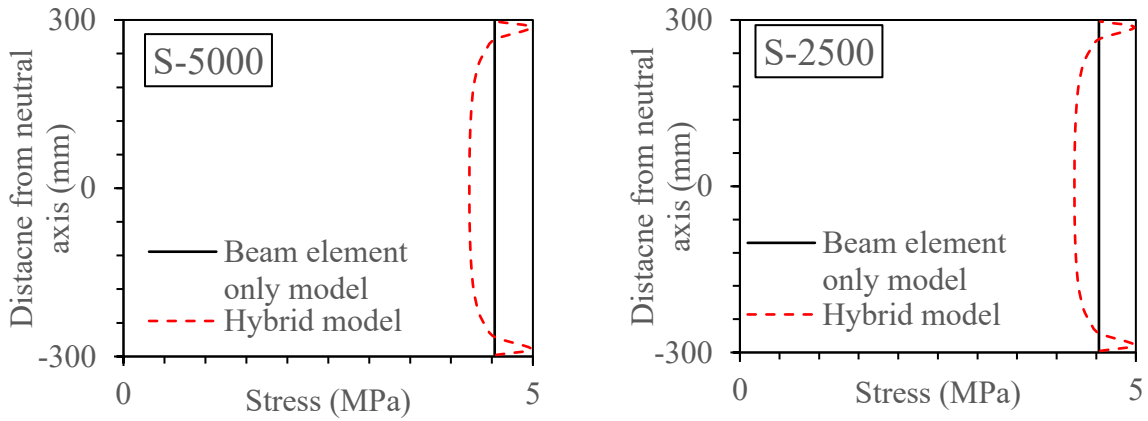


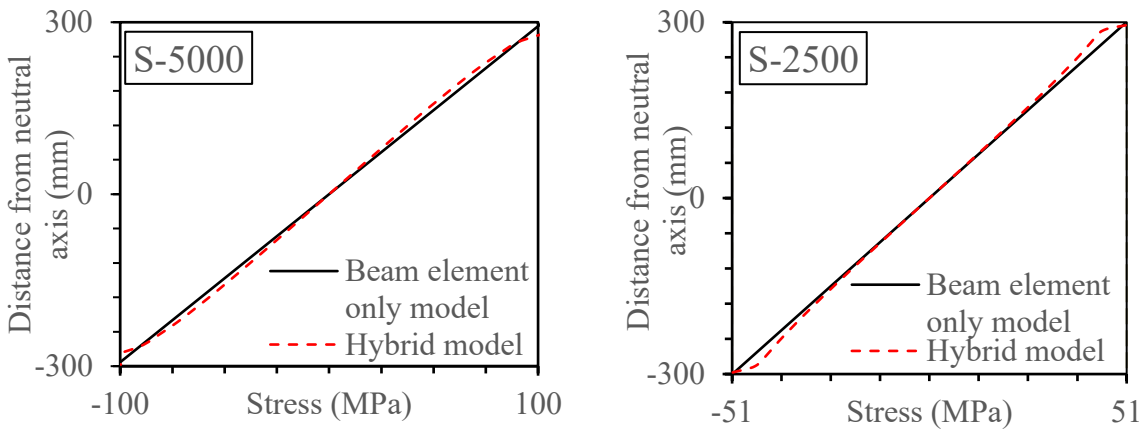
Figure B.1 Sections at which bending and axial stresses are evaluated



(a) Bending stress due to applied moment

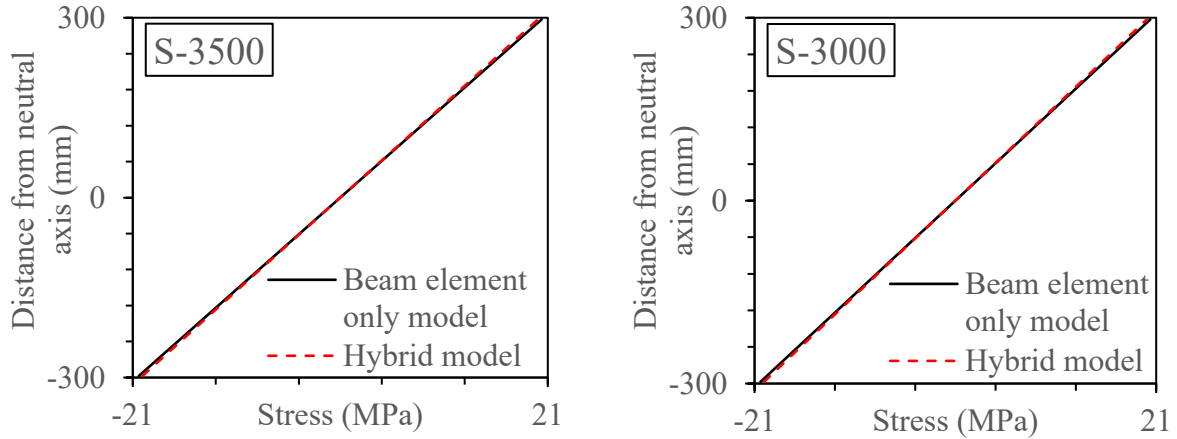


(b) Axial stress due to applied axial force

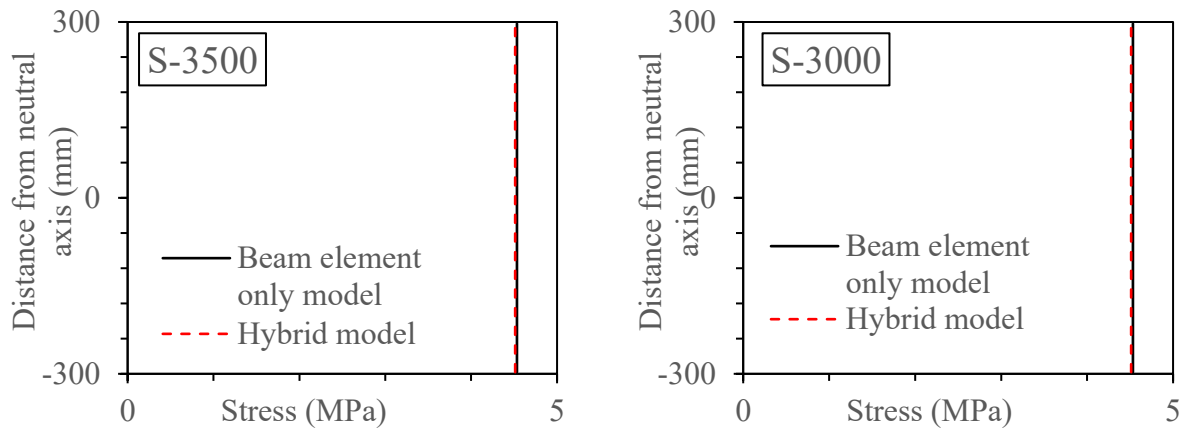


(c) Bending stress due to applied vertical force

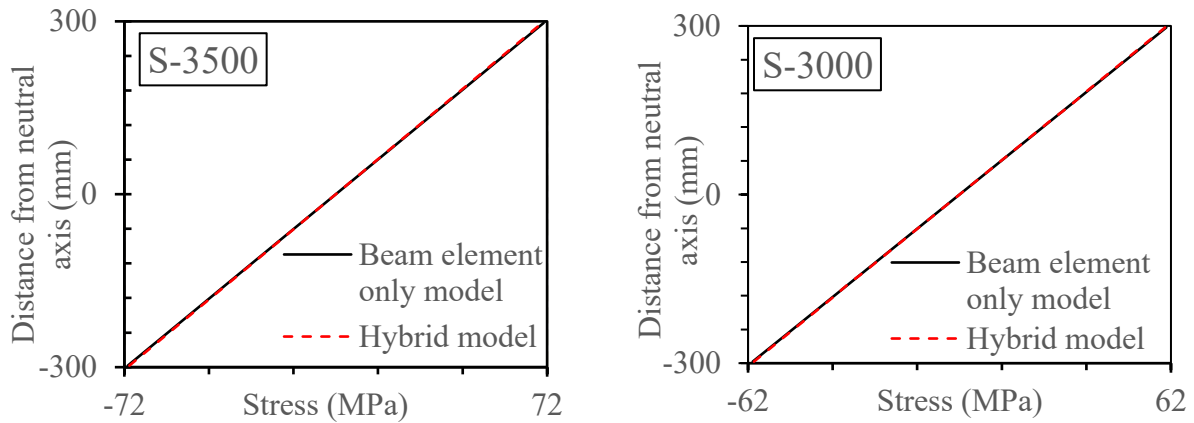
Figure B.2 Comparisons of stresses at section S-5000 and S-2500 of the cantilever beam for hybrid and beam element only models



(a) Bending stress due to applied moment

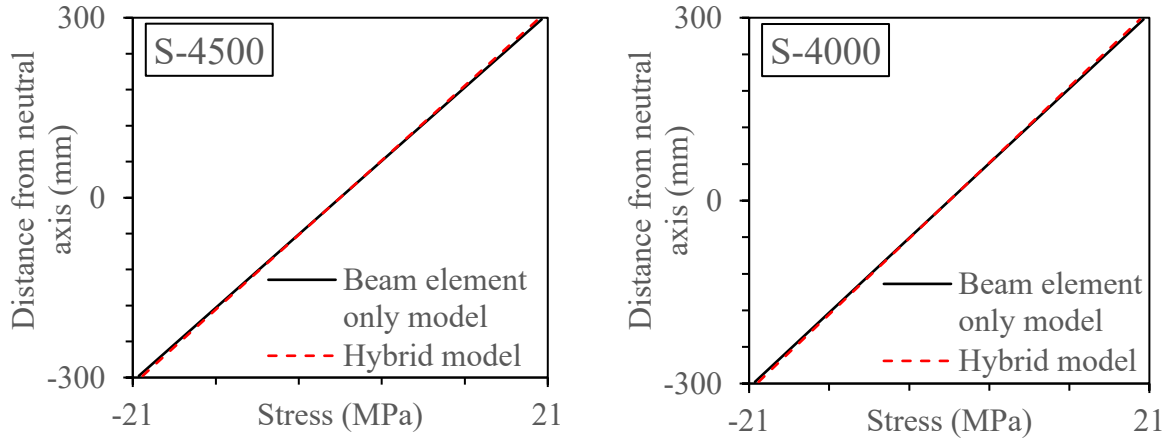


(b) Axial stress due to applied axial force

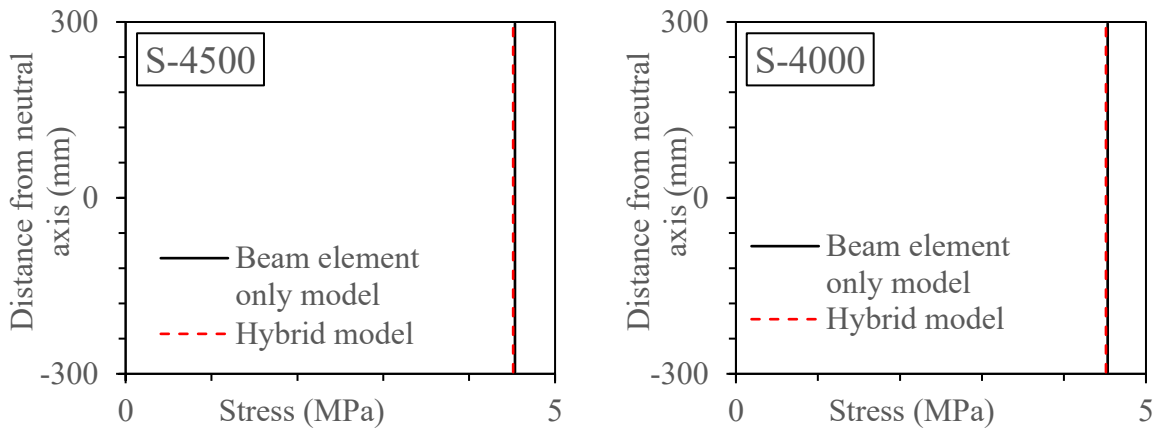


(c) Bending stress due to applied vertical force

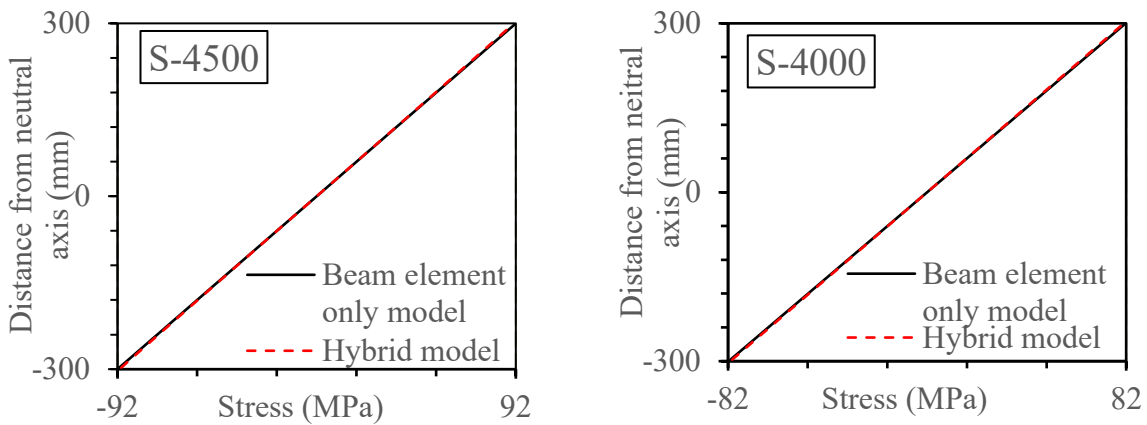
Figure B.3 Comparisons of stresses at section S-3500 and S-3000 of the cantilever beam for hybrid and beam element only models



(a) Bending stress due to applied moment



(b) Axial stress due to applied axial force



(c) Bending stress due to applied vertical force

Figure B.4 Comparisons of stresses at section S-4500 and S-4000 of the cantilever beam for hybrid and beam element only models

Appendix C Example of Moment Versus Curvature Curves

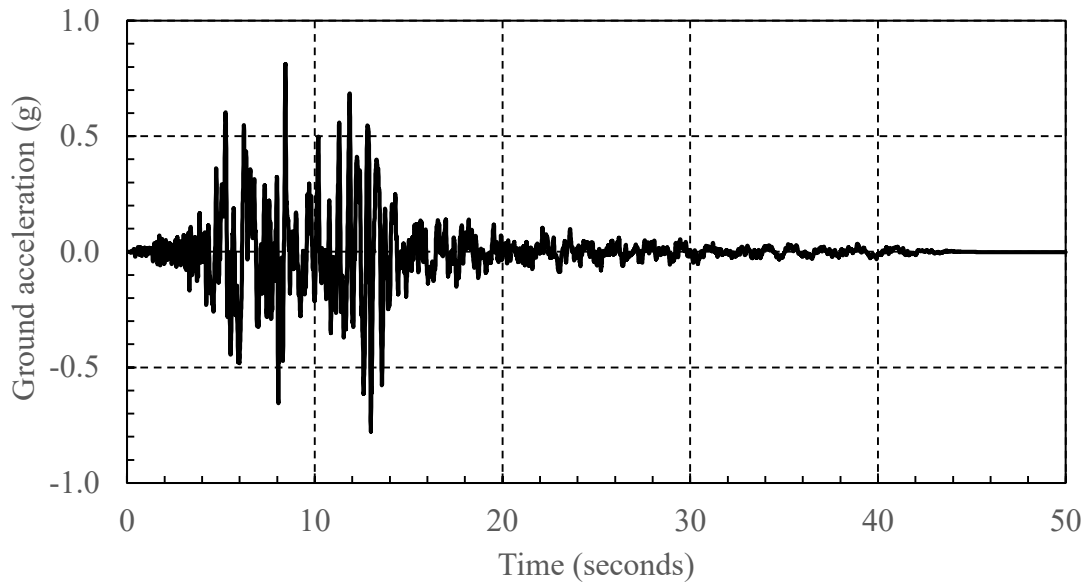


Figure C.1 Ground acceleration time history for earthquake record 4 at MCE hazard level

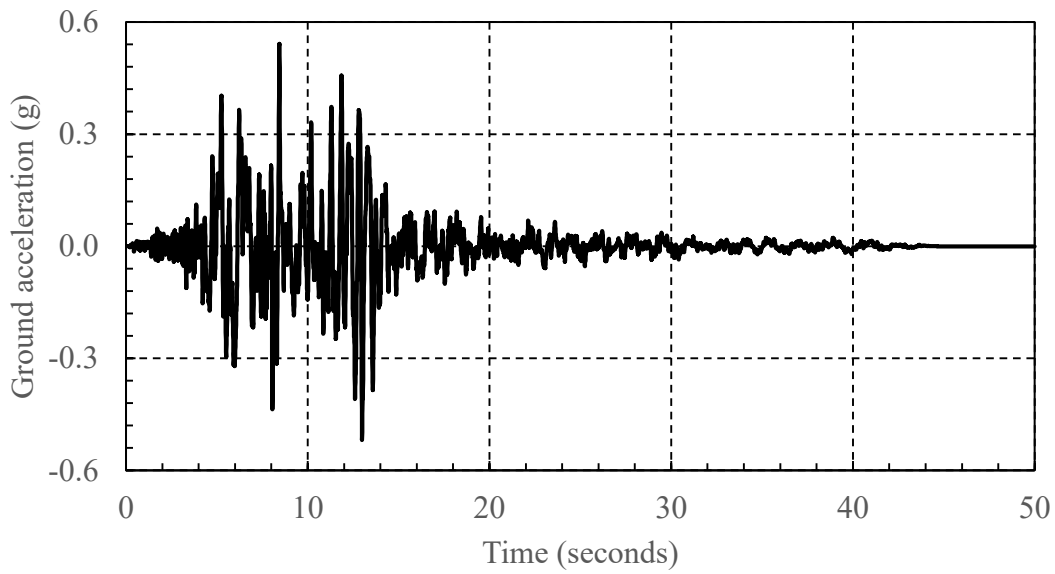


Figure C.2 Ground acceleration time history for earthquake record 4 at DBE hazard level

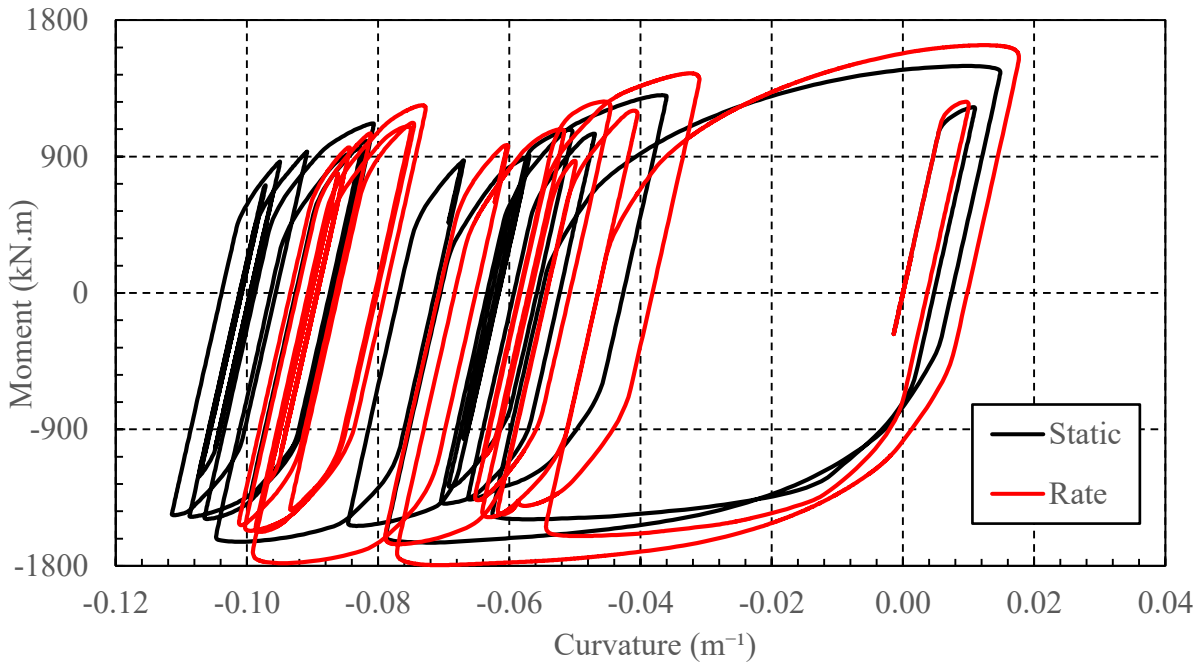


Figure C.3 Moment versus curvature at first floor RBS center for earthquake record 4 for MATH at MCE hazard level

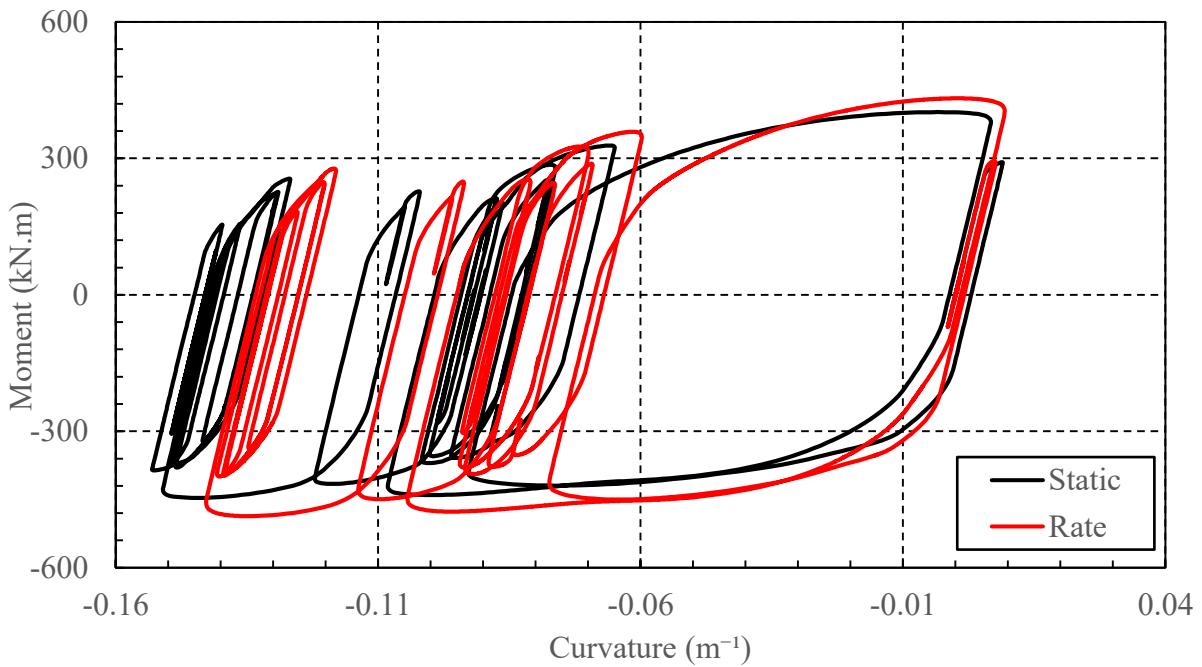


Figure C.4 Moment versus curvature at roof RBS center for earthquake record 4 for MATH at MCE hazard level

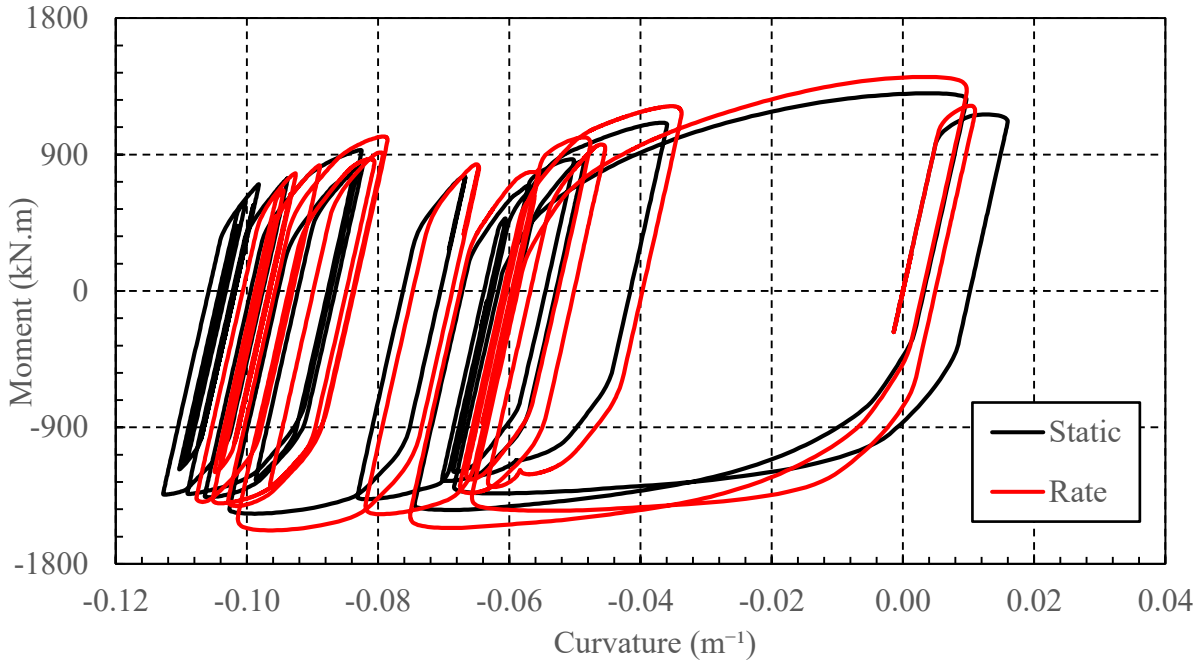


Figure C.5 Moment versus curvature at first floor RBS center for earthquake record 4 for MATG at MCE hazard level

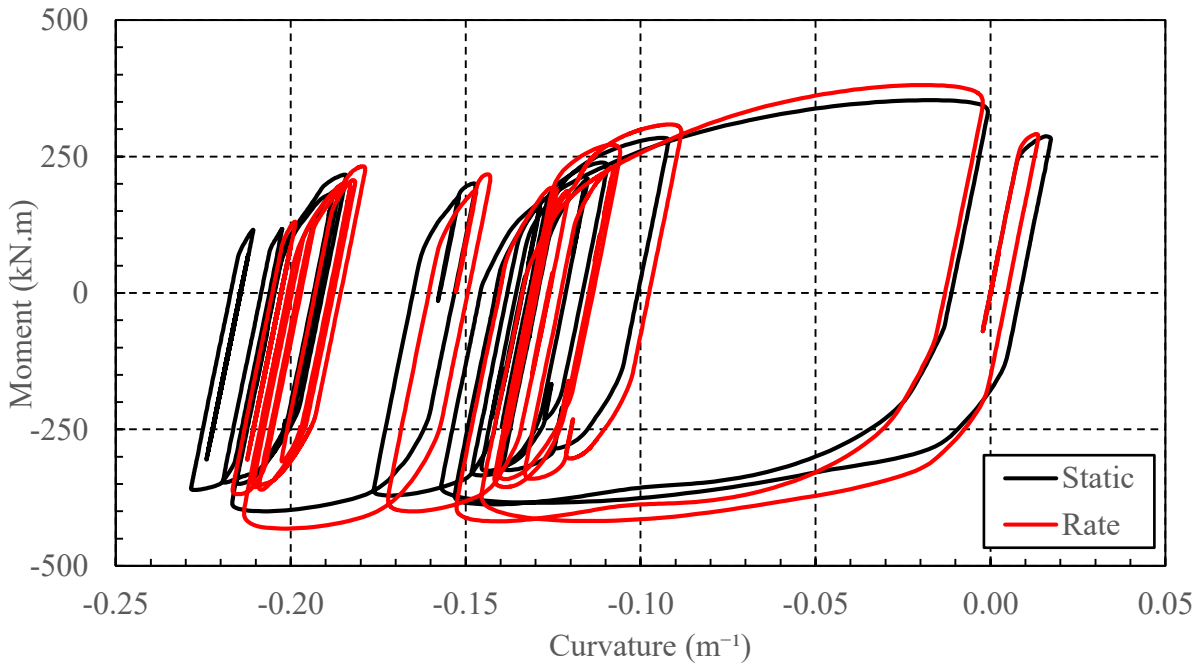


Figure C.6 Moment versus curvature at roof RBS center for earthquake record 4 for MATG at MCE hazard level

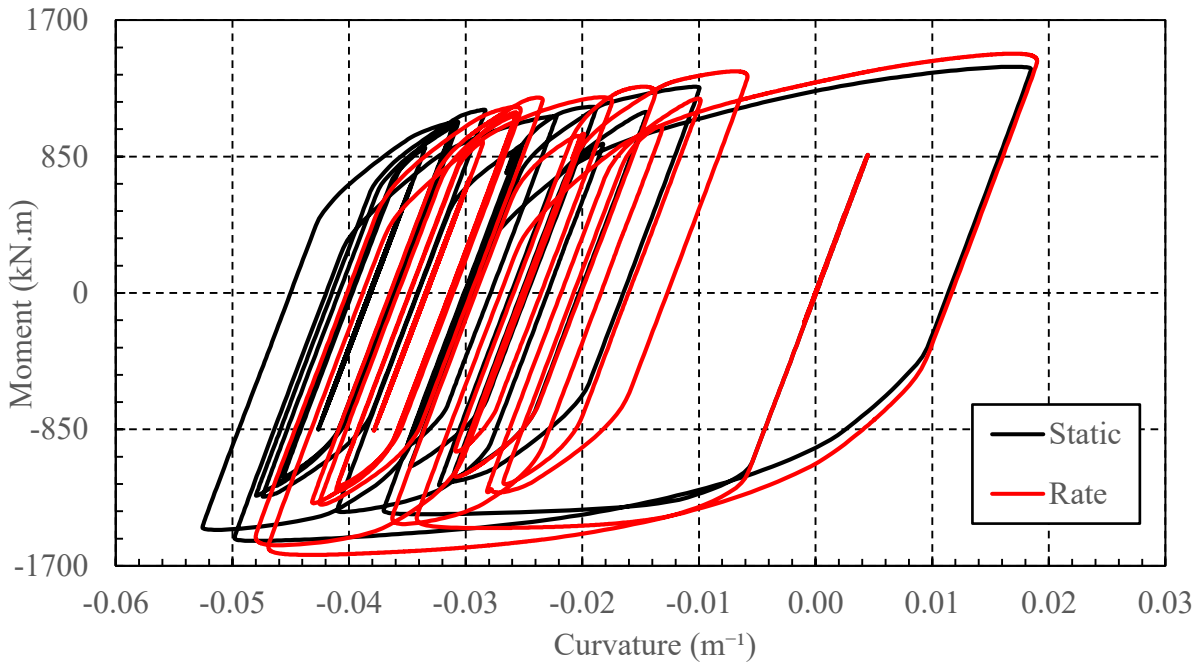


Figure C.7 Moment versus curvature at first floor RBS center for earthquake record 4 for MATH at DBE hazard level

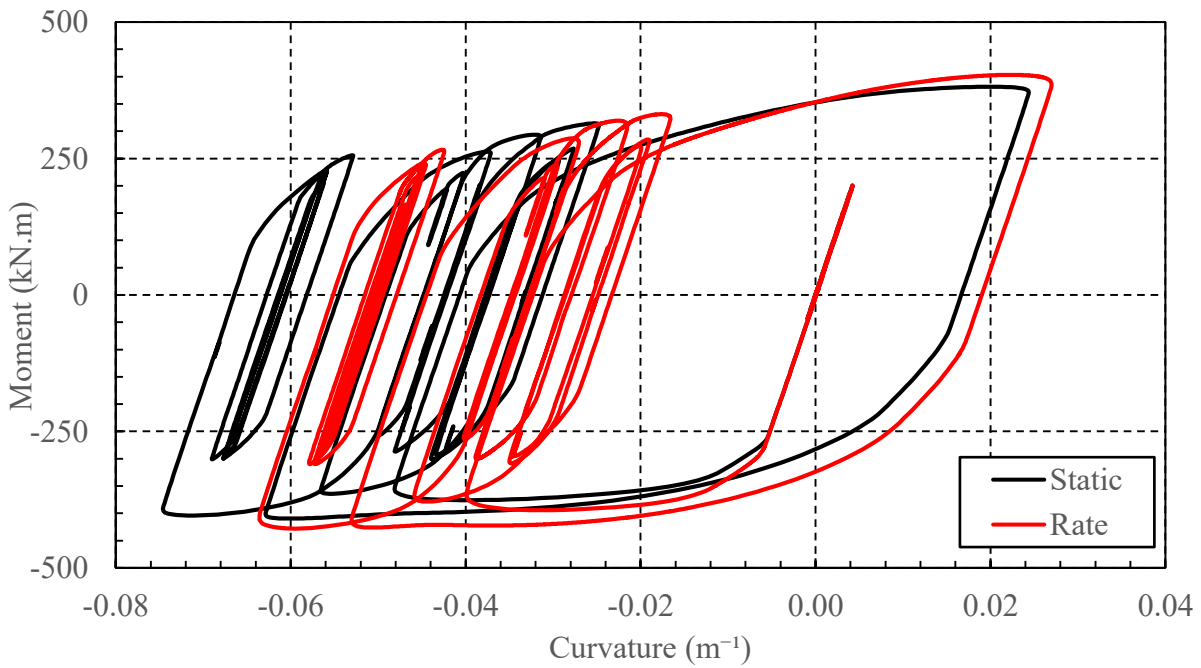


Figure C.8 Moment versus curvature at roof RBS center for earthquake record 4 for MATH at DBE hazard level

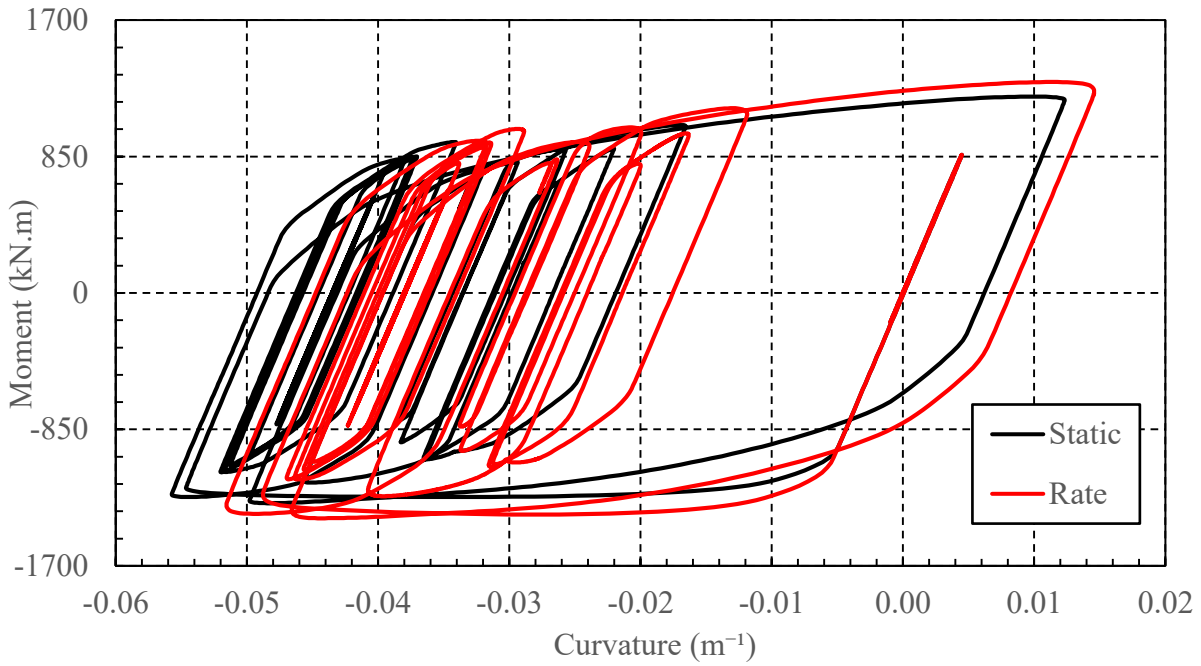


Figure C.9 Moment versus curvature at first floor RBS center for earthquake record 4 for MATG at DBE hazard level

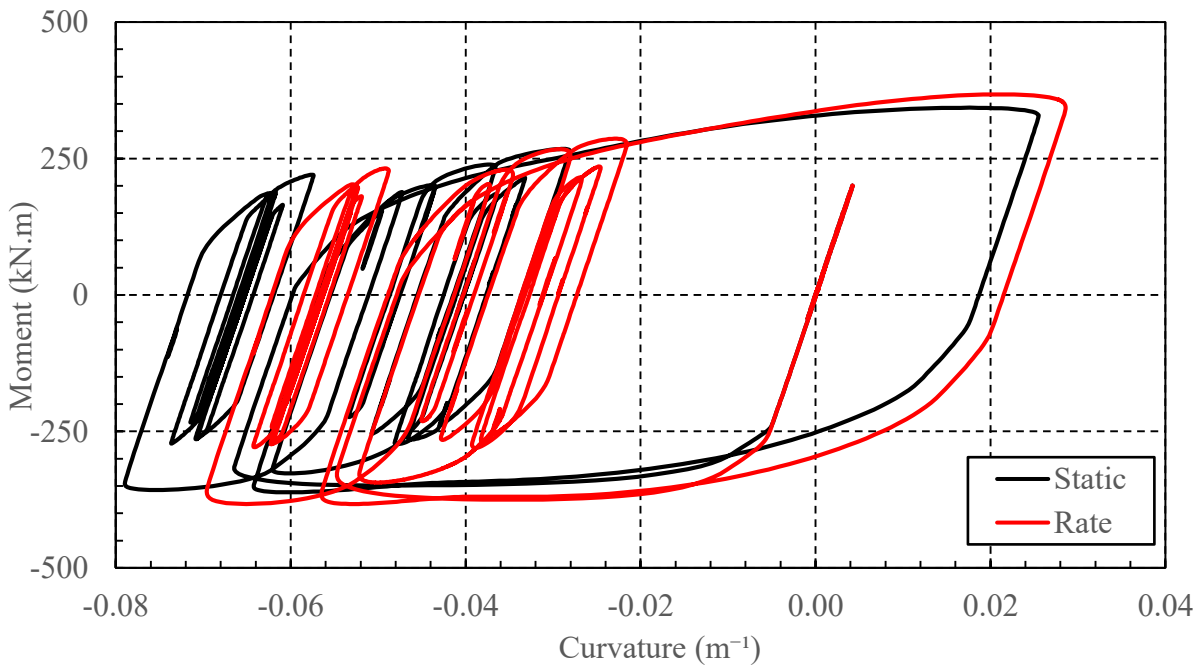


Figure C.10 Moment versus curvature at roof RBS center for earthquake record 4 for MATG at DBE hazard level